Development of high speed low noise InAs electron avalanche photodiodes

Pin Jern Ker

A thesis submitted for the degree of Doctor of Philosophy
Department of Electronic and Electrical Engineering
The University of Sheffield

October 2012

Acknowledgement

Abstract

This work aims at studying the impact ionisation properties of InAs for the exploitation of InAs avalanche photodiodes (APDs) in practical applications such as infrared sensing and optical fibre communications. It involved extensive experimental work in device fabrication, leakage current analysis, avalanche gain characterisation, excess noise and frequency response measurements.

Following an optimisation of wet chemical etching procedures for InAs diodes, surface passivation using different commercially available dielectrics was investigated. SU-8 was identified as the most suitable dielectric for surface passivation. It reduces the surface leakage current and increases the robustness of InAs diodes, which enabled further progress in the fabrication of high speed InAs diodes. Furthermore, dark current analysis shows that in the SU-8 passivated InAs APDs the bulk leakage current is diffusion-dominated at temperatures $\geq$ 200 K. However, the surface leakage current that appears to originate from surface generation-recombination becomes a more dominant dark current source at temperatures < 200 K and in small-area APDs. High quantum efficiency, either higher or comparable to that of commercial InAs photodiodes, and avalanche gain > 20 with low gain-normalised dark current density of ~ 5×10^{-6} A/cm^2 at 77 K demonstrate the potential of InAs APDs for infrared sensing applications.

As one of the first avalanche photodiodes from III-V semiconductors with single carrier multiplication characteristics, the effects of temperature, peak electric field and electric field gradient on the avalanche gain and excess noise of InAs APDs were investigated. Extremely low excess noise factors of ~ 1.45 - 1.6 were temperature- and gain-independent for avalanche gain > 3. A few unique impact ionisation properties of InAs, which are dissimilar from those of conventional APDs, were identified. These understandings of the ionisation properties are important in interpreting the avalanche characteristics when designing InAs APDs for practical

applications. The ability of InAs APDs to improve the sensitivity of a system was established by evaluating the APDs with a commercial low-noise pre-amplifier.

The frequency response of the high speed InAs APDs was studied. The 3-dB bandwidth was determined to be ~ 3.5 - 4 GHz and it remained unaffected by avalanche gain and temperature. Maximum avalanche gains of ~ 125 and ~ 165 produce record high gain-bandwidth products of 430 GHz and 580 GHz at room temperature and 77 K respectively. This is the very first practical demonstration of extremely high gain-bandwidth product using III-V semiconductors and it confirms the third ideal characteristics of InAs electron-APDs, besides the exponentially rising avalanche gain and extremely low excess noise independent of gain. Although the 3-dB bandwidth is limited to ~ 3.5 GHz, the InAs APDs with its high gain-bandwidth products were able to amplify the 15-GHz optical signal by ~ 23 dB above the noise floor. This is potentially useful for 20-Gbps applications.

List of publications

Journal publications

1. Andrew R. J. Marshall, Peter Vines, **Pin Jern Ker**, John P. R. David and Chee Hing Tan, "Avalanche multiplication and excess noise in InAs electron avalanche photodiodes at 77K," *IEEE Journal of Quantum Electronics*, vol. 47, no. 6, pp. 858-864, June 2011.

2. **Pin Jern Ker**, Andrew R. J. Marshall, Andrey B. Krysa, John P. R. David and Chee Hing Tan, "Temperature dependence of leakage current in InAs avalanche photodiodes," *IEEE Journal of Quantum Electronics*, vol. 47, no. 8, pg. 1123-1128, Aug. 2011.

3. Andrew Marshall, **Pin Jern Ker**, Andrey Krysa, John David and Chee Hing Tan, "High speed InAs electron avalanche photodiodes overcome the conventional gain-bandwidth product limit," *Optics Express*, vol. 19, no. 23, Nov. 2011. (**Published by *Laser Focus World Magazine*, vol. 47, issue 12, December 2011**)

4. **Pin Jern Ker**, Andrew R. J. Marshall, Andrey B. Krysa, John P. R. David and Chee Hing Tan, "Low noise high responsivity InAs avalanche photodiodes for infrared sensing," *Physica Status Solidi (c)*, vol. 9, no. 2, pp. 310-313, Dec. 2011.

5. Rajiv B. Gomes, Chee Hing Tan, **Pin Jern Ker**, John P. R. David and Jo Shien Ng, "InAs avalanche photodiodes for X-Ray detection," *Journal of Instrumentation*, vol. 6, P12005, Dec. 2011.

6. **Pin Jern Ker**, John P. R. David and Chee Hing Tan, "Temperature dependence of gain and excess noise in InAs electron avalanche photodiodes," *Accepted for publication in Optics Expressed on* 10th Dec. 2012.

7. Ian C. Sandall, Jo Shien Ng, Shiyu Xie, **Pin Jern Ker** and Chee Hing Tan, "Temperature dependence of impact ionization in InAs," *Submitted to IEEE J. Sel. Topic in Quantum Electronics on* 1st Dec. 2012.

Conference publications

1. **Pin Jern Ker**, Andrew R. J. Marshall, Andrey B. Krysa, John P. R. David and Chee Hing Tan, "Temperature dependence of leakage current in InAs avalanche photodiodes," *UK compound semiconductors conference*, Sheffield UK, July 2010.

2. I. C. Sandall, **P. J. Ker**, S.Xie, J.Xie and C. H. Tan, "Avalanche gain characteristics in $AlAs_{0.56}Sb_{0.44}$," *Semiconductor and Integrated Opto-Electronics (SIOE) conference*, Cardiff UK, April 2011.

3. S. Xie, J. Xie, X. Zhou, **P. J. Ker** and C. H. Tan, "$AlAs_{0.56}Sb_{0.44}$ avalanche photodiodes with weak temperature dependence," *Semiconductor and Integrated Opto-Electronics (SIOE) conference*, Cardiff UK, April 2011.

4. **Pin Jern Ker**, Andrew R. J. Marshall, Andrey B. Krysa, John P. R. David and Chee Hing Tan, "Low noise high responsivity InAs avalanche photodiodes for infrared sensing," *38th International Symposium on Compound Semiconductor (ISCS 2011)* Berlin, Germany, May 2011.

5. I. C. Sandall, **P. J. Ker**, S. Xie, J. Xie, A. S. Idris and C. H. Tan, "Temperature independent multiplication in $AlAs_{0.56}Sb_{0.44}$," *UK compound semiconductors conference*, Sheffield UK, July 2011.

6. Rajiv B. Gomes, **Pin Jern Ker**, Chee Hing Tan, John P. R. David and Jo Shien Ng, "InAs avalanche photodiodes for X-Ray detection," *IEEE Nuclear Science Conference*, Valencia Spain, Oct. 2011.

7. **Pin Jern Ker**, Andrew Marshall, Rajiv Gomes, John Paul David, Jo Shien Ng, and Chee Hing Tan, "InAs Electron-Avalanche Photodiodes: From leaky diodes to extremely low noise avalanche photodiodes," *IEEE Photonics Conference 2011*, Arlington Virginia US, Oct. 2011 (**Invited talk/paper**).

8. **Pin Jern Ker**, John P. R. David and Chee Hing Tan, "Temperature dependence of gain and excess noise in InAs electron avalanche photodiodes," *Semiconductor and Integrated Opto-Electronics (SIOE) conference*, Cardiff UK, April 2012.

9. **Pin Jern Ker**, Andrew Marshall, Andrey Krysa, John David and Chee Hing Tan, "InAs electron avalanche photodiodes with 580 GHz gain-bandwidth product," *17th OptoElectronics and Communications Conference (OECC 2012)* Busan, Korea, July 2012. (***Best Student Paper Award***)

10. **Pin Jern Ker**, Andrew Marshall, Andrey Krysa, John David and Chee Hing Tan, "Exploiting the characteristics of InAs electron avalanche photodiodes for unlimited gain-bandwidth product," *39ᵗʰ International Symposium on Compound Semiconductor (ISCS 2012)* Santa Barbara, CA USA, Aug. 2012.

11. **Pin Jern Ker**, Ian Sandall, Jo Shien Ng, John P. R. David and Chee Hing Tan, "Low noise InAs electron avalanche photodiodes for imaging applications," *Photon 12 conference*, Durham UK, Sept. 2012.

12. I. Sandall, **P. J. Ker**, J. S. Ng, J. P. R. David and C. H. Tan, "Planar InAs photodiodes fabricated using ion implantation," *Photon 12 conference*, Durham UK, Sept. 2012.

13. S. Butera, R. Warburton, I. Sandall, **P. J. Ker**, C. H. Tan, G. Buller and P. Vines, "Towards single photon avalanche diode detectors using narrow bandgap InAs," *Photon 12 conference*, Durham UK, Sept. 2012.

14. Shiyong Zhang, **Pin Jern Ker**, John P. R. David and Chee Hing Tan, "Background doping reduction in MBE grown InAs for electron avalanche photodiodes," *17ᵗʰ International conference on Molecular Beam Epitaxy (MBE 2012)*, Nara Japan, Sept. 2012.

Journals in preparation

1. "Fabrication and surface passivation of InAs diodes," *in preparation*.

Glossary of terms

APD	Avalanche photodiode
ξ	Energy
λ	Wavelength
f	Frequency
EM	Electromagnetic
h	Planck's constant (6.626068×10^{-34} m^{2}kg/s)
c	Speed of light (3×10^8 ms^{-1})
E_g	Bandgap energy
EHP	Electron-hole pair
λ_c	Cut-off wavelength
SNR	Signal to noise ratio
PMT	Photomultiplier tube
UV	Ultraviolet
SWIR	Short wave infrared ($1.4 - 3$ µm)
MWIR	Mid wave infrared ($3 - 5$ µm)
MCP	Microchannel-plate
CCD	Charge-coupled device
HPT	Heterojunction phototransistor
GBP	Gain-bandwidth product
LWIR	Long wave infrared ($8 - 12$ µm)
NIR	Near infrared
FPA	Focal plane array
SAM	Separate absorption and multiplication
α	Electron ionisation coefficient
β	Hole ionisation coefficient
k	Ionisation coefficient ratio
F	Excess noise factor
M	Avalanche gain

e-APD	Electron-APD
V_b	Bias voltage
T	Temperature
MBE	Molecular beam epitaxy
W	Depletion width / avalanche region width
M_e	Pure electron initiated avalanche gain
M_h	Pure hole initiated avalanche gain
MOVPE	Metal organic vapour phase epitaxy
ξ_{th}	Threshold energy of impact ionisation
$<l>$	Mean ionisation path length
RPL	Random path length
M_i	Avalanche gain for a single ionisation event
F_e	Pure electron initiated excess noise factor
F_h	Pure hole initiated excess noise factor
q	Electron charge (1.602×10^{-19} C)
B	Bandwidth
N_A	Pre-amplifier's noise
$I_{ph,pr}$	Unmultiplied photocurrent
$I_{d,pr}$	Unmultiplied dark current
M_{opt}	Maximum exploitable avalanche gain
RC	Resistance-capacitance
P_e (P_h)	Ionisation probability of electron (hole)
d_e (d_h)	Dead space for electron (hole)
α^* (β^*)	Enabled electron (hole) ionisation coefficient
ξ_{the} (ξ_{thh})	Threshold energy of impact ionisation of electron (hole)
E	Electric field
S_e (S_h)	Probability a free electron (hole) does not impact ionise
r_n	Uniformly distributed number
l_e (l_h)	Random ionisation path length of an electron (hole)
n_t	Total number of trials
I-V	Current-voltage
SMU	Source measurement unit

I_F	Diode forward current
I_o	Diode saturation current
V_t	Voltage drop across the diode
n	Ideality factor
k_B	Boltzmann's constant ($1.3806503 \times 10^{-23}$ m^2 kg s^{-2} K^{-1})
R	Series resistance
r	Radius
I_{diff}	Diffusion current
I_{g-r}	Generation-recombination current
I_{tunn}	Band-to-band tunnelling current
n_i	Intrinsic carrier concentration
A	Cross section area
τ_{eff}	Effective carrier lifetime
m^*	Effective mass of electron
$\hbar$	Reduced Plank's constant (1.05×10^{-34} J.s)
α_T	Tunnelling parameter
I_{surf}	Surface leakage current
C	Capacitance
ε_r	Relative permittivity of dielectric
ε_o	Permittivity of vacuum
C-V	Capacitance-voltage
d	Diameter
N	Doping concentration
V_{bi}	Built-in voltage
I_{pr}	Primary photocurrent
I_{ph}	Photocurrent
PSD	Phase sensitive detection
LIA	Lock-in amplifier
f_{ref}	Reference frequency
PLL	Phase-lock-loop
RMS	Root-mean square
V_{p-p}	Peak-to-peak voltage

$V_{LIA, RMS}$	Voltage reading on lock-in-amplifier
R_{sense}	Sensing resistor
NFA	Noise figure analyser
GSG	Ground-signal-ground
Z	Impedance
$P_{dark,dB}$ ($P_{total,dB}$)	Noise power of the dark (dark + photo) current in dB
$P_{dark,watt}$ ($P_{total,watt}$)	Noise power of the dark (dark + photo) current in Watt
N_p	Noise power of the photocurrent
RF	Radio frequency
MTA	Microwave transition analyser
GPIB	General purpose interface bus
VNA	Vector network analyser
EAM	Electro absorption modulator
FFT	Fast-Fourier Transform
E_A	Activation energy
TLM	Transmission line method
SiN_x	Silicon nitride
SiO_2	Silicon dioxide
BCB	B-staged Bisbenzocyclobutene
I_{dark}	Total reverse leakage current
J_{bulk}	Bulk leakage current component (A/cm^2)
J_{surf}	Surface leakage current component (A/cm)
R_{system}	System resistance
$R_{measured}$	Measured resistance between 2 TLM pads
R_{pad}	Resistance between the TLM pad and semiconductor
$R_{semiconductor}$	Resistance along a certain length of the semiconductor
d_t	Distance
$R_{contact}A$	Contact resistance-area product
SEM	Scanning electron microscopy
FTIR	Fourier Transform Infrared Spectrometer
LIDAR	Light detection and ranging
R_dA	Dynamic resistance-area product

J_A	Leakage current density
ROIC	Read-out integrated circuit
D^*	Detectivity
$R_p(\lambda)$	Responsivity at a particular wavelength
Δ_{so}	Spin-orbit splitting of the valance band energy
N_b	Unintentional background doping concentration
N_D (N_A)	Doping concentration of the *n*-doped (*p*-doped) region
SIMS	Secondary Ion Mass Spectroscopy
UID	Unintentional doping
S_{amp}	Pre-amplifier's sensitivity
SHIP	Silicon Heterointerface Photodetector
v_{se} (v_{sh})	Saturation drift velocity of electron (hole)

Contents

Chapter 1 Introduction

1.1   Introduction to photodetectors
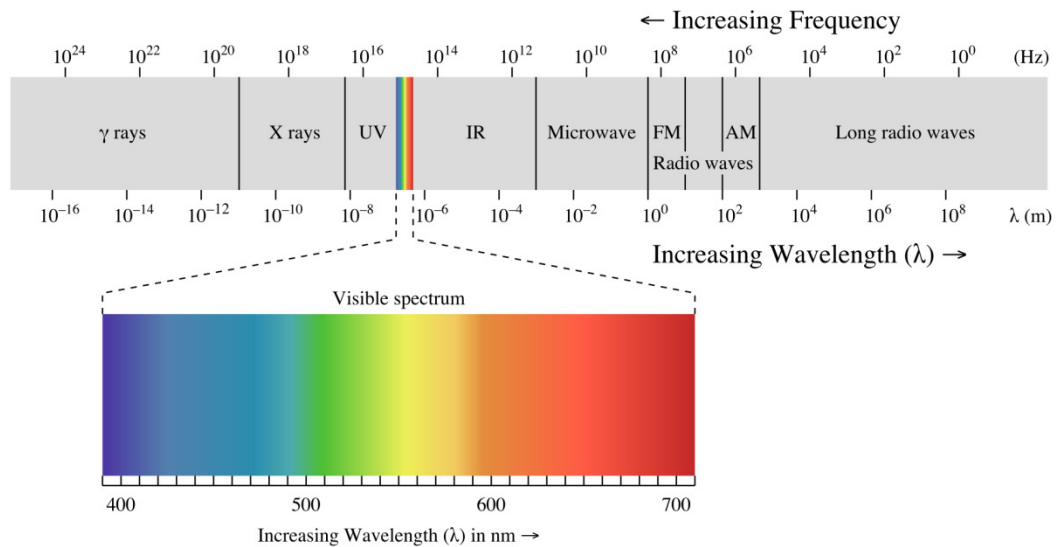
Figure 1.1 Schematic of the electromagnetic spectrum [1].

Semiconductor devices used to detect optical signals are called photodetectors. These optical signals consist of photons at an energy ξ, wavelength λ or frequency f. The semiconductor materials absorb the photons and convert them into electrical signal (either voltage or current). Figure 1.1 shows the electromagnetic (EM) spectrum from γ-ray to long radio waves, with a visible region from ~ 400 to 700 nm. Each λ and f corresponds to a particular energy by the equation

$$\xi = hf = \frac{hc}{\lambda}, \tag{1.1}$$

where h is the Planck's constant and c is the speed of light. For the ease of discussion, λ will be used to indicate the photon radiation energy throughout this

thesis. There is obviously no single photodetector that is usable for the entire range of EM spectrum. Depending on the applications, photodetectors are designed to be highly sensitive to a particular range of λ. For example, photodetectors for long-haul optical fibre communication are designed to respond to λ = 1300 to 1550 nm due to the low attenuation and dispersion in the optical glass fibre at these wavelengths.

The operation of a photodetector involves a few processes including the generation of free carriers upon absorption of photons, carrier transport and the extraction of carriers to contribute to an output current or voltage [2]. The free carriers here refer to the electrons in the conduction band or the holes in the valence band which can move freely. These processes are crucial in determining a few basic requirements of a photodetector:

i. ***Response to the radiation wavelength***

Photodetectors should be able to create as many free carriers as possible when the photons strike the semiconductors. Depending on the band structure and bandgap energy, E_g, of the semiconductor, a photon with energy more than E_g can be absorbed to create one electron-hole pair (EHP). In the event where the radiation energy is very high (in the X-ray or γ-ray), there can be more than one EHP per photon absorbed. Since the photon energy has to be > E_g, there will be wavelengths above which the photon will not contribute to an additional EHP in a semiconductor material, which is usually called the cut-off wavelength, λ_c, and can be related to E_g by

$$\lambda_c = \frac{hc}{E_g} \tag{1.2}$$

After the EHPs are created, they need to be transported within the photodetector to give rise to an additional output current. There are many mechanisms which are specifically designed to improve the carrier transport so that maximum current or voltage can be detected at the output terminal of the photodetectors. Different types of photodetectors employ different carrier

transport processes and they will be briefly described in the next section. Carrier generation and transport are important in determining the ability of a photodetector to respond to a particular radiation and they are usually measured in terms of responsivity and quantum efficiency.

ii. *Gain or amplification*

A photodetector can amplify or multiply the generated carriers internally. In applications that detect signals with very low photon flux, the internal gain is especially important since it can increase the responsivity of the photodetector. Therefore, besides creating large number of EHPs, a photodetector should also be designed to provide high internal gain in order to maximise the signal detected at the output of the photodetector. Examples of photodetectors with gain are described in section 1.2.

iii. *Low noise*

While it is important to maximise the electrical signal generated by a photodetector, it is equally essential minimising the noise as this determines the minimum detectable signal. It is for this reason that the signal to noise ratio (SNR) is often used as a measure of the sensitivity of a photodetector. There are many factors that contribute to the noise of a photodetector such as multiplication noise, background radiation noise and flicker noise. However, the 2 major noise contributions for a photodetector are usually the shot noise and thermal noise. Shot noise is closely associated to the dark current and photogenerated current of a photodetector. This noise originates from the statistical fluctuation of the generation and flow of discrete charges or electrons within a photodetector. Thermal noise is also commonly called the Johnson noise. This is an internal device noise of any resistive device that arises from the randomly agitated carriers due to thermal energy. Multiplication noise is an additional noise source in APDs. This is due to the random nature of the multiplication process that produces a fluctuation of gain around its mean value. Therefore, designing an APD also involves maximising the internal gain and minimising the multiplication noise.

iv. *Response speed*

The response speed of a photodetector is greatly influenced by the carriers transport and the gain mechanisms, in the case of APDs. Extremely high speed photodetectors are needed for the receiver module in optical fibre communication while moderate speed is acceptable for imaging applications. The speed limiting factors for photodetectors will be discussed in the following section.

In addition to the 4 major basic requirements mentioned above, there are other requirements which are more design and application-specific such as the spatial uniformity of photoresponse, the linearity of photodetectors for a wide dynamic range, the size of the photodetectors, power consumption, stability and reliability issues.

1.2 Types of photodetectors

This section aims at reviewing some of the major types of photodetectors and discussing briefly their operating principles. Based on the requirements discussed in the previous section, we shall also outline a few advantages and limitations of each photodetector.

1.2.1 *Photoconductor*

A photoconductor has a simple structure where it consists of a slab of semiconductor with two ohmic contacts at both ends. When the photons strike onto the semiconductor, carriers can be generated by band-to-band transitions. When a moderate electric field is applied across the two terminals, the electrons, with higher mobility, move quicker through the depletion region while holes move slower due to lower mobility. To maintain charge neutrality, more electrons are attracted into the depletion region. Depending on the hole lifetime, the amount of additional electrons and hence the amount of additional electrical signal is different. This mechanism is responsible for providing the internal gain of photoconductor up to 10^6 [2]. A

photoconductor is easy to fabricate and low in cost due to its simple structure. It is usually used for infrared detection and is suitable for high photon flux sensing. However, it has high leakage current and generally operates at a much lower speed than photodiodes making it unsuitable for applications which need low intensity detection at very high frequency.

1.2.2 Photomultiplier tube

A photomultiplier tube (PMT) consists of an input window, a photocathode, dynodes and an anode. Most of the photocathodes are made of compound semiconductors [3] and the operating wavelength of a PMT relies on the photocathode materials. The incoming photons excite the electrons in the photocathode and the generated electrons are channelled into a vacuum tube which has a number of dynodes. Dynodes are the electron multipliers where the electrons are multiplied before finally being collected at the anode. The internal gain is highly dependent on the voltage applied across the dynodes and the number of dynodes. One of the major advantages of the PMT is its ability to provide extremely high internal gain up to 10^7 with negligible multiplication noise. This has enabled PMTs to provide very high sensitivity and act as a very good photodetector for very low photon flux applications down to single photon detection from ultraviolet (UV) up to visible wavelengths.

However, the high operating voltages exceeding 1000 V has been a major issue, although there are currently PMTs with lower operating voltages < 1000 V [3] available in the market. Furthermore, the size of a PMT is much larger than that of other photodetectors due to the need for a long vacuum tube for the multiplication process. The quantum efficiency of commercially available PMTs is > 40 % only for λ between 400 and 700 nm. It drops to < 20 % for λ = 700 to 900 nm and the quantum efficiency is reduced further to < 2.5 % at λ = 900 to 1600 nm [3]. It can be expected that for short wave (SWIR) and mid wave infrared (MWIR) detections, it is difficult for PMTs to achieve a reasonable performance due to the inability of the photocathode to produce very low dark counts and high quantum efficiency. In addition, PMTs are not suitable for imaging purposes where small pixels with close

proximity are needed, typically < 30 µm. These issues have limited the use of PMTs to applications from the UV to the near infrared wavelengths and not for high-resolution imaging purpose. This has triggered research on photodetectors with similar gain mechanism to provide high internal gain with low multiplication noise.

Another type of PMT, that is different from the dynode PMT is the microchannel-plate (MCP) PMT. As the name implies, the difference is the gain mechanism. In this case the MCP, made of a thin disk with a 2-D arrays of glass capillaries with very small diameters (microchannel), typically between 6 and 20 µm diameters [3], is used to multiply the primary electrons. The inner wall of the microchannel has proper electrical resistance and secondary emissive properties to multiply the primary electrons. The MCP offers a faster response speed in hundreds of ps (compared to dynode PMT in the ns range) [4]. Furthermore, the MCP is usually more compact in sizeand allows position sensitive detection by substituting the single anode with an array of individual anodes. However, the MCP does have a few disadvantages in terms of its presumably shorter life-time and higher cost than dynode PMTs. It also has a lower current carrying capacity, which leads to smaller range of linear response to light intensity [5].

1.2.3 Phototransistor

The operating principle of a phototransistor is to optically generate a base current which is then amplified in the base-collector junction [6]. Arrays of Si phototransistors were initially fabricated for solid-state imaging but the invention of charge coupled devices (CCDs) has overshadowed the development of Si phototransistors. Since then focus has been shifted to utilising phototransistors for optical fibre communication, where the idea of a heterojunction phototransistor (HPT) was initially proposed. The HPT consists of an emitter with wider bandgap material than the base and collector to improve the injection efficiency [6].

HPTs generally have much lower operating voltages than APDs. Moreover, HPTs can provide gain up to ~ 100 [2] without the multiplication noise associated with the

avalanche effect in APDs. In the 1980s, HPTs were considered to have great potential as photodetectors in optical fibre communications due to the shift of optical fibre system to the 1300 and 1550 nm window with lower attenuation and dispersion [6]. One major disadvantage of HPTs is that the gain and speed reduce with increasing light intensity as the light intensity can alter the base potential. This has in turn caused the variation of gain-bandwidth product (GBP) with varying radiation power, with the highest reported GBP of ~ 10 GHz [6].

1.2.4 Charge-coupled devices

A CCD is a combination of many metal-insulator-semiconductors in an array, typically used for imaging purposes. There is no external dc-photogenerated current upon exposure to light and the photogenerated carriers are stored and transported in the form of a charge packet. As the name implies, a CCD transfers or couples the charge packet from one image sensor to another. Therefore the spacing between each pixel is typically < 10 µm to ensure the high charge transfer efficiency. The charge is converted to voltage at the output of the array and only one amplifier is needed. CCDs are made of metal-oxide-semiconductor with Si and SiO_2 as the semiconductor and oxide layer, respectively, due to the good interfacial properties of SiO_2.

Since the 1960s, CCDs have emerged as one of the main technologies for visible camera and imaging purposes. It has ~ 100 % quantum efficiency and its detection that integrates charge over a longer period also enables weak signal detection, obviously at the expense of slightly lower speed. Furthermore, it has very low dark current, low noise, low operating voltage and is robust.

Regardless of its maturity in terms of technology, CCDs have only limited use from visible up to near IR wavelengths as they are made of Si. For MWIR and long wave infrared (LWIR), there is work on CCDs with InSb [7] and HgCdTe [2] but not much success reported, possibly due to the inability of III-V and II-VI semiconductor materials to form high-quality oxide layer needed to minimise the gate leakage

current. In terms of its response speed, CCDs are limited to 10s of MHz to ensure high charge transfer efficiency, which is sufficient for imaging purpose but not for optical communication.

1.2.5 *Photodiode and avalanche photodiode*

A photodiode involves the transport of the minority carriers. There are several types of photodiodes including *p-n*, *p-i-n*, heterojunction, and metal-semiconductor junctions. Photodiodes employ a semiconductor junction to create a high electric field region that is depleted of charge. The light is absorbed within this depletion region and the high electric field separates the photogenerated EHPs, giving rise to additional current, which is generally called the photocurrent, flowing in an external circuit. Photodiodes are usually operated at 0 V or relatively low bias voltages and generally have very high quantum efficiency and short response time due to the carriers travelling at saturated velocity within the depletion region when biased appropriately. Furthermore, the design of the heterojunction photodiode has led to the reduction in dark current and ensures that the photons are absorbed in the high field region to obtain high quantum efficiency. The heterojunction photodiode uses two types of lattice-matched semiconductors with different E_g. The semiconductor with larger E_g is transparent to the radiation photons so that it acts as a window for radiation photons to reach the smaller E_g semiconductor in the undoped region. Depending on the applications, a different material can be used as the absorption region so that radiation at the wavelength of interest can be detected in the high-field region.

For long range or long haul detections, the level of photon flux can be quite low, causing a low level of photocurrent. Amplification of signal can be done using an external amplifier. However, at high bandwidth, commercially available amplifiers fail to provide high gain at low noise. Therefore APDs are used to provide internal gain to amplify the incoming signal prior to the amplifier. APDs are usually biased at much higher biases than photodiodes to produce sufficiently high electric fields in the depletion region. Provided that the energy gained from accelerating through the

electric field is higher than the threshold energy of impact ionisation, the photogenerated carriers can be multiplied through the impact ionisation process. This increases the photocurrent prior to the external amplifier circuit. However, the higher bias voltages will usually cause higher leakage current and the avalanche process is accompanied by the multiplication noise. The system sensitivity will improve only if the shot noise and excess noise from the APDs are lower than the noise from the external amplifier. Therefore the understanding of the characteristics of APDs with different semiconductor materials is crucial in designing APDs, so that the advantages of APDs can be fully exploited. A detailed theory of impact ionisation and APDs is provided in chapter 2.

1.3   Competing materials for infrared photodetectors

There has been an increasing attention on IR sensing and detection. This is because many applications, which are closely related to our daily lives, utilise the radiation spectra in the IR window. One of the very popular applications is imaging. While imaging with visible light can produce coloured pictures, imaging using IR can provide several features which are not achievable using visible camera. One clear example of images taken from visible and SWIR camera in a very dark night [8] is shown in figure 1.2. The SWIR camera utilises the night sky radiance reflected from the object to obtain much clearer images.

Figure 1.2 Comparison of the images taken from a visible (left) and SWIR (right) cameras at night [8].

Furthermore, SWIR imaging can also be used to obtain clear images in foggy conditions, detecting liquid level in a plastic container, food and fruits inspection, and biometrics verification [8]. The MWIR and LWIR sensors are excellent for heat leak detection, power line maintenance, and in detecting human activities which are pertinent for military applications.

In addition, environmental monitoring and gas sensing have become increasingly important and many gases in the atmosphere have high absorption in the IR window. For example, CO_2 and methane gases have high absorption at $\lambda = 2$ and 3.3 µm respectively. IR photodetectors with proper calibration can be employed for accurate gas sensing. In the medical field, IR detectors are also important because many biological molecules have distinctive absorption from near infrared (NIR) to MWIR [9]. For instance, the spectrum between 2 and 2.4 µm can be used for glucose level monitoring in the human body.

In this section a brief review of bulk semiconductors for infrared detection is presented. Quantum well, quantum dot, type II superlattice and impurity doped semiconductors are not included as they appear to be less promising for developing APDs. Research on InSb photodetectors started earlier than $Hg_{1-x}Cd_xTe$ photodiodes. InSb photodetectors can be grown on substrates with 7-cm diameter and can be used in focal plane arrays (FPAs) for MWIR [10]. To achieve satisfactory performance, InSb photodiodes are operated at 60 – 80 K [11] and to date there are very few reports on InSb APDs [12], possibly due to the difficulty in suppressing the dark current.

$Hg_{1-x}Cd_xTe$ photodiodes have been the dominant technology for IR sensing from MWIR to LWIR. This is because $Hg_{1-x}Cd_xTe$ offers bandgap tuning by varying its Hg and Cd compositions so that it can be tailored for optimised response at a particular IR region. However, $Hg_{1-x}Cd_xTe$ materials face several challenges related to the epitaxial growth, such as high production cost and availability of large-area lattice matched substrate [13]. Furthermore, the difficulty in growth is due to the high Hg pressure during growth, which causes problems in controlling the Hg and Cd

composition. The weak bonding of Hg atoms also causes $Hg_{1-x}Cd_xTe$ devices to be highly susceptible to process-induced damage [13]their use is limited to low-volume and high cost applications such as in the military sector.

Over the past 4 decades, the issues related to $Hg_{1-x}Cd_xTe$ photodiodes have motivated researchers to work on alternative materials to provide ease of growth, fabrication and better uniformity. These materials include the lead salt ternary compounds such as Pb(SnTe) and Pb(SnSe). Compared to $Hg_{1-x}Cd_xTe$, these IV-VI compounds are much easier to grow and they are more stable. However, they have a very high dielectric constant, causing large capacitance that limits the high frequency response. For example, the Pb(SnTe) alloy was reported to have a dielectric constant between 400 and 5800 [13]. Furthermore, the thermal expansion coefficient of these IV-VI compounds is much larger than that of the Si readout circuit (~ 20 times larger compared to InAs, InSb and $Hg_{1-x}Cd_xTe$, which is only ~ 2 times larger) [13].

1.4   Development of APDs

The development of APDs was initially driven largely by the demand of receivers for high speed long haul optical fibre communication [14]. This is because APDs can provide ~ 5 - 10 dB higher sensitivity than a normal *p-i-n* photodiodes [14]. In the first generation optical fibre system, which utilised λ = 800 to 900 nm, Si-based photodiodes and APDs undoubtedly have been the preferred choice because of the availability of the materials and its technological maturity. However, since E_g ~ 1.12 eV, corresponding to λ_c = 1.1 µm, the applicability of Si APDs is restricted to applications involving the visible and NIR region.

As the transmission window of optical communications migrated to λ = 1300 to 1550 nm, semiconductor alloys of groups III and V have been introduced as replacement for Si APDs. $In_{0.53}Ga_{0.47}As$ (hereafter as InGaAs) *p-i-n* photodiodes with E_g ~ 0.75 eV, have been extensively exploited in the optical fibre communication systems. However, the high tunnelling current at high electric fields has prevented it from being used as an APD. This issue has been addressed by having a heterojunction

separating the absorption and multiplication (SAM) regions of the APD structure [15]. InGaAs was used as an absorption layer while a wider bandgap and lattice-matched semiconductor such as InP was used as the multiplication region. This structure is commonly referred to as InGaAs/InP SAMAPD. Since then much efforts have been made to improve this InP-based APD, including having a planar structure, grading of the interface between InGaAs and InP, and design to increase the GBP and responsivity [14]. Furthermore, research on potential materials, such as $InAl_{0.52}As_{0.48}$ (here after as InAlAs) to substitute InP has been on-going to accommodate for a receiver module with bit-rate > 10 Gbps. However, there was not much success in exploring APDs suitable for 40 Gbps and the GBPs reported were all limited to below 340 GHz. GBPs of APDs will be reviewed and discussed in more detail in chapter 7.

Looking beyond the telecommunication aspect, there is recently a great demand for photodetectors to be utilised in other applications such as long range active imaging [16] and X-ray detection [17]. In general, besides having low dark current, APDs can provide much higher sensitivity or SNR if the multiplication noise is minimised. It is well understood that to reduce the multiplication or excess noise, the electron α or hole β ionisation coefficients ratio $k = \beta/\alpha$, must deviate as large as possible from unity [18]. To improve the performance of APDs, research on reducing the excess noise has been on-going for the past few decades.

Since k is material dependent [19], efforts to reduce the multiplication noise has been in characterising new materials and also optimising the electric field profiles. Si has very low k but its applications are limited due to its E_g. Most of the III-V semiconductors usually have $k > 0.3$, producing a very high multiplication noise. Fortunately, it was found that their multiplication noise reduces [20, 21] when the avalanche region was reduced to a very thin layer, typically < 1 µm [22]. This method exploits the effect of dead space, which is defined as the minimum distance a carrier needs to travel before attaining sufficient energy to impact ionise, to make the statistical ionisation process more deterministic. Among the III-V APDs which have successfully reduced their APDs noise through this method are InP [23], GaAs [24],

InAlAs [25] and $Al_xGa_{1-x}As$ [26]. This effect of dead space on impact ionisation is also commonly called the non-local nature of impact ionisation as the behaviour is no longer solely governed by the local electric field strength. Furthermore, it was predicted that [27] APDs can be designed with graded-bandgap in the multiplication region to enhance the impact ionisation of electrons or holes, so that k can deviate further from unity. The graded-bandgap allows the carrier to travel from a wider bandgap to a narrower bandgap with lower threshold energy. The highly energetic carriers from the wider bandgap material can impact ionise quickly and more readily, leading to an enhanced α or β. Campbell *et al.* has reported this bandgap engineering structure using InAlGaAs quaternary materials which are lattice-matched to InP substrates. They claimed that the APDs have lower excess noise factors F due to the suppression of ionisation of secondary holes and the localisation of electron ionisation events in the narrower bandgap materials [28]. However, there were several reports on the conduction band-offset, both observed through experiments [29, 30] and modelling [31] using $Al_xGa_{1-x}As$-GaAs. It was concluded that the additional energy an electron gains from the conduction band discontinuity is offset by the energy loss due to the higher phonon scattering rate [29-31].

It can be summarised that there are generally three ways to obtain low-noise APDs, which are i) having material with $k = 0$ properties; ii) exploiting the effect of deadspace to reduce multiplication noise in APDs with $k \sim 1$; and iii) using graded-bandgap although there are still doubts in the implementation of this bandgap engineering approach. Previous exploitation of the dead space effect is based on submicron scaling of the avalanche width. This has increased the tunnelling current of the APDs, causing higher shot noise. In addition, a thinner multiplication region also leads to a larger device capacitance, which limits the response speed of APDs. Hence, it can be suggested that research to discover potential materials with $k = 0$ and exploit this to achieve low-noise and high speed APDs is still the most beneficial approach.

Up until the early 2000s, only $Hg_{0.7}Cd_{0.3}Te$ was shown experimentally and conclusively to possess the $k = 0$ characteristics. $Hg_{0.7}Cd_{0.3}Te$ APDs show

exponentially rising avalanche gain M with increasing bias voltage while producing extremely low multiplication noise or $F \sim 1$. This class of APDs is commonly called electron-APD (e-APD) because only the electrons impact ionise to contribute to the avalanche gain. This characteristic is very much associated with the band structure of this material that has small E_g but large intervalley separation energies [14]. This has led to very small intervalley phonon scattering for electrons. The large difference between the effective mass of electron to hole also indicates that holes suffer from much higher scattering rate, causing the suppression of β. However, issues as mentioned in the previous section have inhibited the use of $Hg_{1-x}Cd_xTe$ photodiodes for daily and low cost applications.

In the late 2000s, InAs APDs were reported to offer low excess noise and produce gain at low voltages [32, 33] comparable to that of $Hg_{0.7}Cd_{0.3}Te$ APDs. With the mature III-V semiconductor growth technology, InAs with this HgCdTe-like e-APD behaviour can be a potential material for high-sensitivity photodetectors and infrared applications.

1.5   Review on InAs APDs

InAs with $E_g = 0.36$ eV at room temperature is certainly attractive for IR detections up to 3.6 µm. Due to its larger E_g than InSb and $Hg_{0.7}Cd_{0.3}Te$, InAs photodiodes promise a lower dark current and operating temperatures higher than 77 K, providing better sensitivity in its operating wavelengths. Furthermore, InAs possesses the $k = 0$ characteristics, low dielectric constant and high electron saturation velocity, which can produce low-noise and high GBP APDs for optical fibre communications.

In the early 1960s, Lucovsky [34] reported *p-n* junction InAs photodiodes fabricated by diffusing Cadmium into the *n*-type InAs layer. The diffused wafer was cut into 1 mm × 1 mm sample with Indium solders as the contacts. At 300 K, these photodiodes produced a reverse dark current of $\sim$ 10 mA at a reverse bias voltage V_b = 10 V. Further characterisation of these InAs photodiodes [35] showed that the photocurrent is multiplied at the same rate as the dark current at 300 K, with $M \sim 10$

at V_b = 10 V.

InAs *p-i-n* photodiodes with different *i*-layer thicknesses ranging from 0 (*p-n* junction) to 0.72 µm were reported by Lin *et al*. [36, 37]. It was reported that the surface and bulk leakage currents were reduced drastically with increasing the *i*-layer thickness. The low temperature measurement down to 40 K also showed that the total leakage current decreased by ~ 6 orders of magnitude compared to that at operating temperature, T = 300 K [37]. However, the InAs photodiodes were all operating at < 0.5 V, possibly due to high dark current at higher V_b. Furthermore, InAs photodiodes operating in the unity gain are also commercially available from Judson [38] and Hamamatsu [39].

Using Molecular Beam Epitaxy (MBE), Marshall *et al*. has successfully optimised the growth parameters and conditions such that epitaxially-grown InAs wafers with mirror-like surface can be obtained [40]. A lattice-matched wide bandgap material, $AlAs_{0.16}Sb_{0.84}$ was incorporated into the *p*-layer, aiming to reduce the bulk leakage current. The fabrication and processing of InAs diodes using wet chemical etchants were carried out and InAs diodes with reduced surface leakage current were reported [40]. A few different types of dielectric materials were used for surface passivation but were not successful in further reducing the dark current [41]. However, the unpassivated InAs diodes were reported to be able to operate at V_b > 10 V [40]. This has enabled the study of the impact ionisation properties of InAs.

At room temperature, the InAs diodes with a depletion width W = 3.5 µm were reported to provide avalanche gain at V_b > 0.5 V [32]. The pure electron initiated avalanche gain M_e was shown to be exponentially rising with increasing V_b up to ~ 10 V [32], without a classical avalanche breakdown. On the other hand, figure 1.3 shows that the pure hole initiated gain M_h ~ 1 up to 8 V, indicating a large difference between α and β. The excess noise measurement at room temperature also showed that the InAs APDs have F ~ 1.6 up to M_e ~ 7 [33]. This has confirmed that the InAs APD has the e-APD characteristics, since only the electrons can impact ionise.
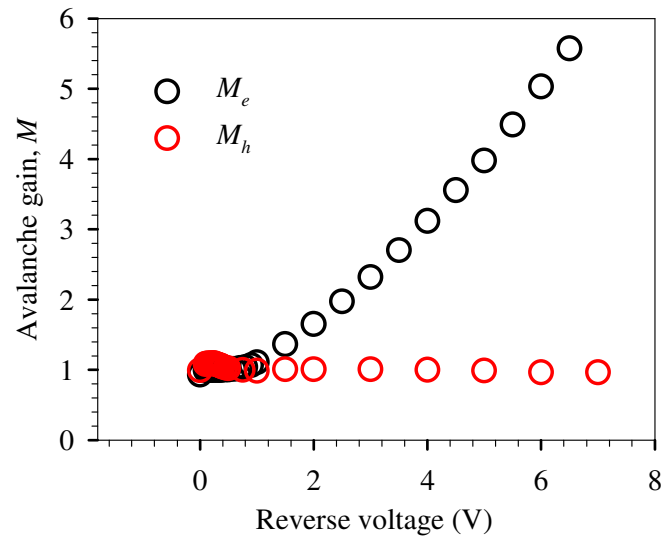
Figure 1.3 Pure electron and pure hole initiated avalanche gain at room temperature [32].

The characteristics of InAs APDs were also investigated at T = 77 K by Mikhailova *et al*. [42] and Marshall *et al*. [43]. Mikhailova *et al*. [42] has suggested that due to the spin orbit splitting being equal to the E_g of InAs at 77 K, band 'resonance' occurs and β becomes significantly larger than α. Marshall *et al*. however do not observe the impact ionisation of hole with M_h ~ 1 until the electric fields > 70 kV/cm [43]. M_e on the other hand is initiated at ~ 6 kV/cm at 77 K. At a particular V_b, the M_e of InAs APDs was shown to be lower compared to room temperature [43]. From the M_e data, α of InAs APDs at room temperature [44] and 77 K [43] were derived using the local model to allow the estimation of M_e for different structures of InAs APDs. The band-to-band tunnelling current of InAs APDs was also investigated and the electric field for the onset of tunnelling current was found to be ~ 60 kV/cm at 77 K [43].

1.6   Motivation / overview

From previous work, it was convincingly proven that InAs possesses very interesting impact ionisation properties which are ideal for an APD. Its λ_c, up to ~ 3.6 µm at room temperature, suits many different important applications. However, the leakage current at room temperature remains high and this has become a major obstacle for

further exploitation of InAs APDs for real practical applications.

The surface passivation of InAs diodes needs to be investigated to further reduce the leakage current. The bulk leakage current can be reduced by having higher crystal growth quality or decreasing the operating temperature of InAs APDs. Therefore, a detailed dark current analysis as a function of temperature is important. The study of the avalanche gain at temperatures between 77 K and room temperature are also crucial in determining the optimum operating temperature for InAs APDs. Besides, there have been contradicting results on the impact ionisation properties of InAs at 77 K [42, 43] and the uncertainty on the existence of band 'resonance' needs to be addressed as this can alter the mode of operation and design of InAs APDs.

Since the first two ideals of InAs APDs, which are the exponentially rising gain and very low excess noise, have been demonstrated, it is also equally important to exploit the characteristic of InAs APDs to exhibit the third ideal of APDs with $k = 0$ characteristics. The frequency response of InAs APDs shall be investigated and it can be hypothesised that the 3-dB bandwidth of the devices will not be limited by its avalanche gain, potentially providing extremely high GBP.

To further discuss the work carried out based on the above motivations, this thesis will therefore be organized as follows:

Chapter 2 discusses the background theories of impact ionisation in terms of the avalanche gain, excess noise and GBP.

Chapter 3 describes all the basic APD characterisation and experimental methods which are useful in carrying out all the work discussed in this thesis. In each experimental technique, the associated background knowledge and the steps to ensure the accuracy of the measurements will be discussed.

Chapter 4 revisits the fabrication steps of InAs diodes. The growth of InAs wafers using MBE and Metal Organic Vapour Phase Epitaxy (MOVPE) will also be briefly

described. The study on the etched mesa surface passivation using different dielectric materials and the fabrication of high speed InAs diodes using the best scheme of metal contacts will be presented.

Chapter 5 shows the temperature dependence of the leakage current in InAs APDs from 77 to 290 K. The detailed dark current analysis by separating the bulk and surface leakage current components has helped to identify the dark current mechanisms within the InAs APDs. Besides that, it also enabled the estimation of the leakage current for different dimensions of the InAs APDs at different temperatures. The responsivity and detectivity of the InAs diodes will also be discussed.

Chapter 6 examines the effects of temperature, depletion width, peak electric field and field gradient on the avalanche characteristics of InAs. The avalanche gain and excess noise characteristics are explained based on a few distinct impact ionisation properties of InAs. The measurements of M and F at different temperatures also allowed the investigation of band 'resonance' besides studying the variation of F with temperatures. Furthermore the incorporation of InAs APDs with a pre-amplifier has demonstrated the importance of low leakage current and pure electron injection to obtain high SNR.

Chapter 7 intends to demonstrate the unlimited GBP of InAs APDs due to its $k = 0$ characteristics. The fabrication of high speed InAs APDs allows the frequency response measurement to be carried out at 77 K and room temperature. It presents a record high GBP which clearly indicates that the avalanche build up time does not limit the 3-dB bandwidth of the devices. It is noted that the GBP is due to the highest achievable M of the prototype diodes, presenting experimentally one of the first extremely high GBP with $k = 0$ characteristics.

Chapter 8 summarises all the work presented in this thesis. Future work and possible areas to extend the work are suggested and proposed.

Appendices list the details of the InAs wafers used throughout this work, the high

speed InAs fabrication steps and a few detailed descriptions of the experimental steps which support the main content of this thesis.

References

[1] "http://en.wikipedia.org/wiki/File:EM_spectrum.svg."

[2] S. M. Sze and K. K. Ng, "Physics of semiconductor devices, 3rd. Edition," John Wiley and Sons Inc., 2007.

[3] K. K. Hamamatsu Photonics, "Photomultiplier Tubes: Basics and Applications," Aug. 2007.

[4] Becker&Hickl, idQuantique, and Hamamatsu, "Single photon counting APD, MCP and PMT detectors," *Boston Electronics Corporation,* 2006.

[5] J. R. Lakowicz, *Principles of fluorescence spectroscopy*. New York, NY: Springer, 2006.

[6] J. C. Campbell, "Chapter 5: Phototransistors for lightwave communications," in *Semiconductors and semimetals*. vol. 22, Part D: Photodetectors, W. T. Tsang, Ed.: Academic Press Inc., 1985.

[7] J. C. Kim, "InSb MIS structures for infrared imaging devices," in *International Electron Devices Meeting*, 1973, pp. 419-422.

[8] "http://www.sensorsinc.com/images.html."

[9] B. L. Carter, E. Shaw, J. T. Olesberg, W. K. Chan, T. C. Hasenberg, and M. E. Flatte, "High detectivity GaInAsSb pin infrared photodetector for blood glucose sensing," *Electron. Lett.,* vol. 36, pp. 1301-1303, 2000.

[10] A. Rogalski, "Infrared detectors: an overview," *Infrared Phys. & amp. Technol.,* vol. 43, pp. 187-210, 2002.

[11] A. Rogalski, "Infrared detectors: status and trends," *Prog. Quantum Electron.,* vol. 27, pp. 59-210, 2003.

[12] R. D. Baertsch, "Noise and Multiplication Measurements in InSb Avalanche Photodiodes," *J. Appl. Phys.,* vol. 38, pp. 4267-4274, 1967.

[13] A. Rogalski, "HgCdTe infrared detector material: history, status and outlook," *Reports on Progress in Physics,* vol. 68, p. 2267, 2005.

[14] J. C. Campbell, S. Demiguel, M. Feng, A. Beck, G. Xiangyi, W. Shuling, Z. Xiaoguang, L. Xiaowei, J. D. Beck, M. A. Kinch, A. Huntington, L. A. Coldren, J. Decobert, and N. Tscherptner, "Recent advances in avalanche photodiodes," *IEEE J. Sel. Top. Quantum Electron.,* vol. 10, pp. 777-787, 2004.

[15] N. Susa, H. Nakagome, O. Mikami, H. Ando, and H. Kanbe, "New InGaAs/InP avalanche photodiode structure for the 1-1.6-micron wavelength region," *IEEE J. Quantum Electron.,* vol. 16, pp. 864-870, 1980.

[16] I. M. Baker, S. S. Duncan, and J. W. Copley, "A low-noise laser-gated imaging system for long-range target identification," in *Proc. SPIE Infrared Technology and Applications, vol. 5406*, Orlando, FL, USA, 2004, pp. 133-144, 2004.

[17] M. Moszynski, M. Kapusta, M. Balcerzyk, M. Szawlowski, D. Wolski, I. Wegrzecka, and M. Wegrzecki, "Comparative study of avalanche photodiodes with different structures in scintillation detection," *IEEE Trans. Nuclear Sci.,* vol. 48, pp. 1205-1210, 2001.

[18] R. J. McIntyre, "Multiplication noise in uniform avalanche diodes," *IEEE Trans. Electron Devices,* vol. 13, pp. 164-168, 1966.

[19] J. P. R. David and C. H. Tan, "Material Considerations for Avalanche Photodiodes," *IEEE J., Sel. Topics Quantum Electron.,* vol. 14, pp. 998-1009, 2008.

[20] D. S. Ong, K. F. Li, G. J. Rees, G. M. Dunn, J. P. R. David, and P. N. Robson, "A Monte Carlo investigation of multiplication noise in thin p^+-i-n^+ GaAs avalanche photodiodes," *IEEE Trans. Electron Devices* vol. 45, pp. 1804-1810, 1998.

[21] X. Li, X. Zheng, S. Wang, F. Ma, and C. J. C., "Calculation of gain and noise with dead space for GaAs and $Al_xGa_{1-x}As$ avalanche photodiode," *IEEE Trans. Electron Devices,* vol. 49, pp. 1112-1117, 2002.

[22] S. A. Plimmer, J. P. R. David, and D. S. Ong, "The merits and limitations of local impact ionization theory [APDs]," *IEEE Trans. Electron Devices,* vol. 47, pp. 1080-1088, 2000.

[23] J. C. Campbell, S. Chandrasekhar, W. T. Tsang, G. J. Qua, and B. C. Johnson, "Multiplication noise of wide-bandwidth InP/InGaAsP/InGaAs avalanche photodiodes," *J. Lightwave Technol.,* vol. 7, pp. 473-478, 1989.

[24] K. F. Li, D. S. Ong, J. P. R. David, R. C. Tozer, G. J. Rees, S. A. Plimmer, K. Y. Chang, and J. S. Roberts, "Avalanche noise characteristics of thin GaAs structures with distributed carrier generation [APDs]," *IEEE Trans. Electron Devices,* vol. 47, pp. 910-914, 2000.

[25] C. Lenox, P. Yuan, H. Nie, O. Baklenov, C. Hansing, J. C. Campbell, J. A. L. Holmes, and B. G. Streetman, "Thin multiplication region InAlAs homojunction avalanche photodiodes," *Appl. Phys. Lett.,* vol. 73, pp. 783-784, 1998.

[26] B. K. Ng, J. P. R. David, G. J. Rees, R. C. Tozer, M. Hopkinson, and R. J. Airey, "Avalanche multiplication and breakdown in $Al_xGa_{1-x}As$ (x < 0.9)," *IEEE Trans. Electron Devices,* vol. 49, pp. 2349-2351, 2002.

[27] F. Capasso, T. Won-Tien, and G. F. Williams, "Staircase solid-state photomultipliers and avalanche photodiodes with enhanced ionization rates ratio," *IEEE Trans. Electron Devices,* vol. 30, pp. 381-390, 1983.

[28] J. C. Campbell, W. Shuling, Z. Xiaoguang, L. Xioawei, L. Ning, M. Feng, S. Xiaoguang, J. B. Hurst, R. Sidhu, A. L. Holmes, Jr., A. Huntington, and L. A. Coldren, "Recent developments in avalanche photodiodes," in *Conference on Optoelectronic and Microelectronic Materials and Devices*, 2002, pp. 53-58.

[29] C. K. Chia, J. P. R. David, G. J. Rees, P. N. Robson, S. A. Plimmer, and R. Grey, "Electron multiplication in $Al_xGa_{1-x}As$/GaAs heterostructures," *Appl. Phys. Lett.,* vol. 71, pp. 3877-3879, 1997.

[30] C. K. Chia, J. P. R. David, S. A. Plimmer, G. J. Rees, R. Grey, and P. N. Robson, "Avalanche multiplication in submicron $Al_xGa_{1-x}As/GaAs$ multilayer structures," *J. Appl. Phys.,* vol. 88, pp. 2601-2608, 2000.

[31] C. K. Chia, J. P. R. David, G. J. Rees, S. A. Plimmer, R. Grey, and P. N. Robson, "Impact ionization in $Al_xGa_{1-x}As/GaAs$ single heterostructures," *J. Appl. Phys.,* vol. 84, pp. 4363-4369, 1998.

[32] A. R. J. Marshall, C. H. Tan, M. J. Steer, and J. P. R. David, "Electron dominated impact ionization and avalanche gain characteristics in InAs photodiodes," *Appl. Phys. Lett.,* vol. 93, pp. 111107-3, 2008.

[33] A. R. J. Marshall, C. H. Tan, M. J. Steer, and J. P. R. David, "Extremely Low Excess Noise in InAs Electron Avalanche Photodiodes," *IEEE Photon. Technol. Lett.,* vol. 21, pp. 866-868, 2009.

[34] G. Lucovsky, "Electrical characteristics of diffused InAs p-n junctions," *British J. Appl. Phys.,* vol. 12, p. 311, 1961.

[35] G. Lucovsky and R. Emmons, "Avalanche multiplication in InAs photodiodes," in *IEEE International Solid-State Circuits Conference. Digest of Technical Papers.*, 1965, pp. 52-53.

[36] R.-M. Lin, S.-F. Tang, S.-C. Lee, C.-H. Kuan, G.-S. Chen, T.-P. Sun, and J.-C. Wu, "Room temperature unpassivated InAs p-i-n photodetectors grown by molecular beam epitaxy," *IEEE Trans. Electron Devices, ,* vol. 44, pp. 209-213, 1997.

[37] R.-M. Lin, S.-F. Tang, S.-C. Lee, and C. H. Kuan, "Improvement of current leakage in the InAs photodetector by molecular beam epitaxy," *J. Crystal Growth,* vol. 227-228, pp. 167-171, 2001.

[38] "InAs detectors J12 series datasheet, Judson Technologies, revised Jan. 2001."

[39] "InAs photovoltaic detectors P10090 series and P7163 datasheet, Hamamatsu, revised Apr. 2008."

[40] A. R. J. Marshall, C. H. Tan, J. P. R. David, J. S. Ng, and M. Hopkinson, "Fabrication of InAs photodiodes with reduced surface leakage current," in *Proc. SPIE Optical Materials in Defence Systems Technology IV*, Florence, Italy, 2007, pp. 67400H-9.

[41] A. R. J. Marshall, "PhD Thesis: The InAs electron avalanche photodiode and the influence of thin avalanche photodiodes on receiver sensitivity," in *Electronic & Electrical Engineering*: The University of Sheffield, 2009.

[42] M. P. Mikhailova, M. M. Smirnova, and S. V. Slobodchikov, "Carrier multiplication in InAs and InGaAs p-n junctions and their ionization coefficients," *Sov. Phys. Semicond.,* vol. 10, pp. 509-513, 1976.

[43] A. R. J. Marshall, P. Vines, P. J. Ker, J. P. R. David, and C. H. Tan, "Avalanche Multiplication and Excess Noise in InAs Electron Avalanche Photodiodes at 77 K," *IEEE J. Quantum Electron.,* vol. 47, pp. 858-864, 2011.

[44] A. R. J. Marshall, J. P. R. David, and C. H. Tan, "Impact Ionization in InAs Electron Avalanche Photodiodes," *IEEE Trans. Electron Devices,* vol. 57, pp. 2631-2638, 2010.

Chapter 2 Background theory

2.1   Impact ionisation in semiconductors

The process that gives rise to the avalanche gain in APDs is the impact ionisation. It is a process where the free carriers, either electrons or holes, obtain sufficiently high energy to promote an electron from the valence band to the conduction band, creating a new EHP [1]. To achieve this, the carriers are accelerated by an externally applied electric field and the minimum energy required for impact ionisation is commonly referred to as the threshold energy of impact ionisation, ξ_{th}.

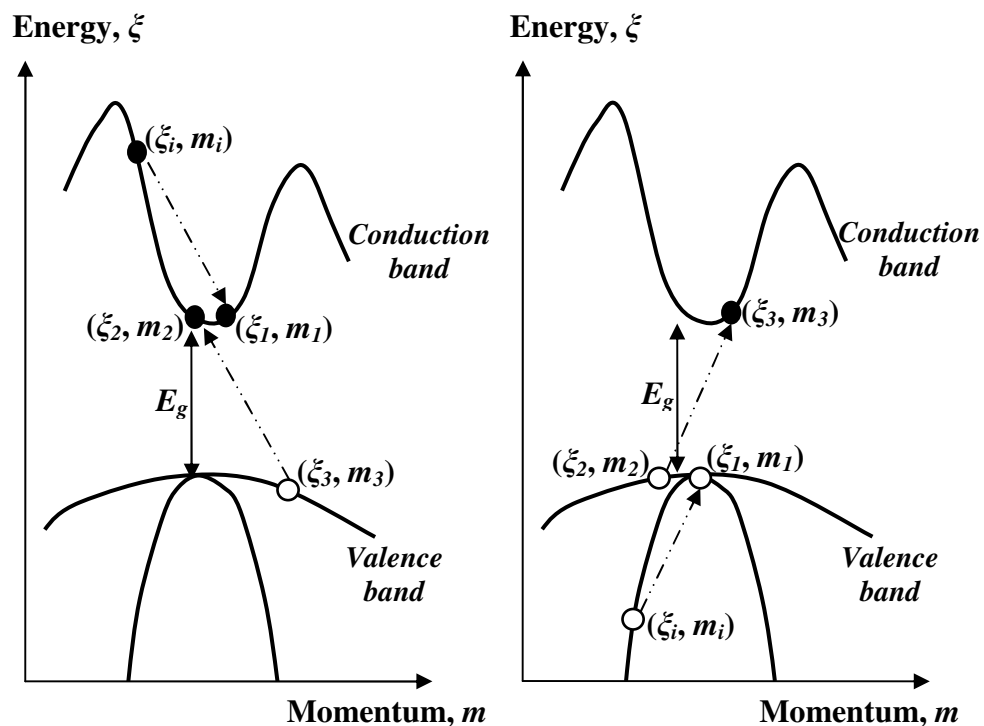Figure 2.1 Schematic diagram of the electron initiated (left) and hole initiated (right) impact ionisation process. The initial state is denoted by '*i*' and the subsequent final states are denoted as '*1, 2* and *3*'.

ξ_{th} depends largely on the band structure of the semiconductor material [1]. It is an important parameter which governs the impact ionisation rate of electrons and holes. Figure 2.1 illustrates the electron initiated and hole initiated impact ionisation process. It is clear that the conservation of energy requires $\xi_{th} \geq E_g$ for free carriers to impact ionise. The average numbers of ionisation events per unit distance travelled by the free carriers are often represented by α and β. The reciprocal of these ionisation coefficients will therefore provide the average distance a carrier needs to travel along the direction of electric field to produce a new EHP [1], which is often called the mean ionisation path length, *<l>*.

2.2   Avalanche gain

When a *p-n* or *p-i-n* semiconductor junction is biased at high voltage, it will produce a high electric field across the junction. If the free carriers are accelerated by the electric field to energies $> \xi_{th}$, a chain of impact ionisation events can occur. Figure 2.2 shows a series of ionisation events which the primarily injected electron and the secondary EHPs have travelled within the avalanche region from distance $x = 0$ to W. α and β are typically highly dependent on the electric field. Therefore, depending on the strength of electric field, different M is produced for a particular type of semiconductor.

The calculation of M using the current continuity equations are described in detail in [2]. From these equations, M_e at $x = 0$ can be written as

$$M_e = \frac{1}{1 - \int_0^{W_T} \left[\alpha(x) \, exp\left(- \int_0^x (\alpha(x) - \beta(x)) dx' \right) \right] dx} \qquad (2.1)$$

Similarly, M_h at $x = W_T$ can be expressed as

$$M_h = \frac{1}{1 - \int_0^{W_T} \left[\beta(x) \, exp\left(- \int_x^{W_T} (\alpha(x) - \beta(x)) dx' \right) \right] dx} \qquad (2.2)$$
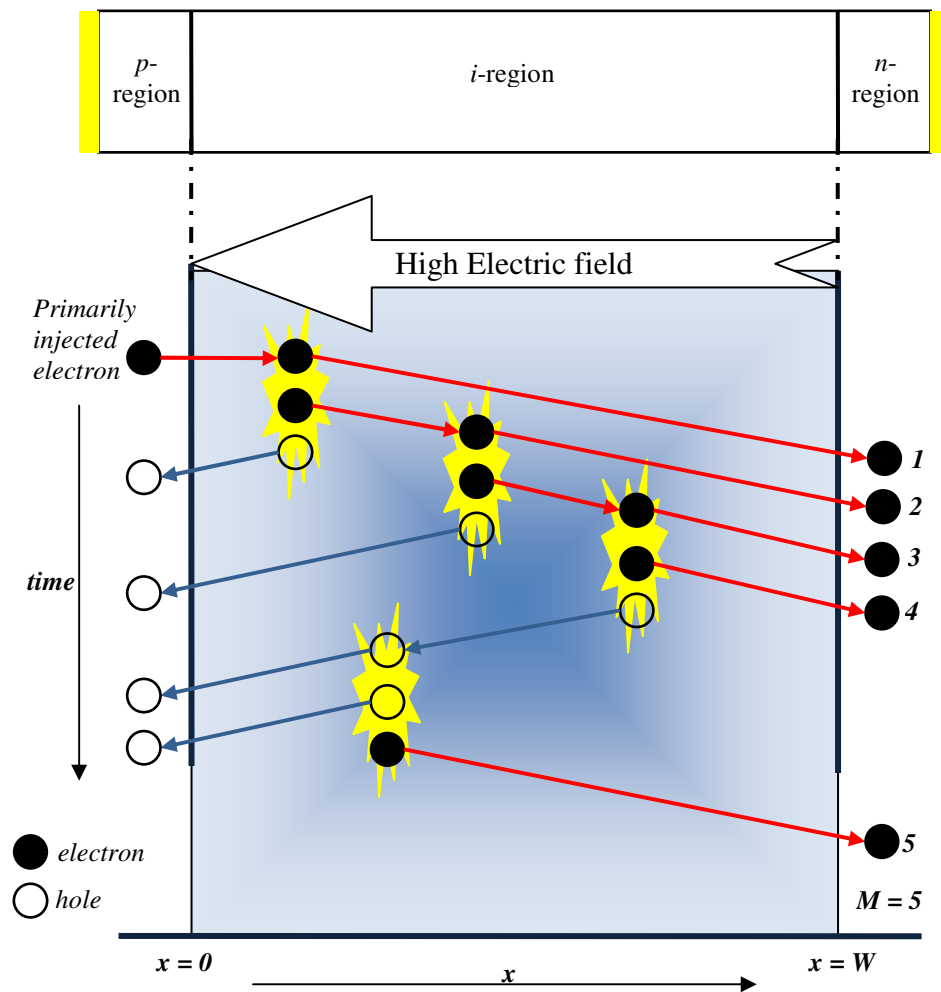
Figure 2.2 Illustration of the pure electron initiated avalanche gain within the high field regions with electrons travelling in the *x*-direction and holes travelling in the *-x*-direction.

It should be noted that equations 2.1 and 2.2 are based on the assumption that the impact ionisation probability depends only on the local electric field [3], but not the history of the carriers, which is commonly referred to as the local model. This is a convenient way of predicting *M* when the non-local effect due to the dead space is insignificant. There are many types of modelling techniques which incorporate the effect of the dead space, such as random path length (RPL) [4], lucky-drift [5], recurrence method [6], and Monte Carlo models which incorporate the full band structure [7] or simplified band structure [8]. The RPL model, which is used in

chapter 6, will be discussed briefly in section 2.5.

2.3 Excess noise

Thus far, the parameters, such as α, β and M, which are discussed in the previous two sections, are the average or mean values of the overall statistical process. Since the impact ionisation is a stochastic process, there is a fluctuation of gain around its mean or average gain. This will give rise to a certain level of noise that is usually called the excess noise or multiplication noise, which can be characterised by the excess noise factor. Since F is the standard deviation of the avalanche gain for a single ionisation event M_i, from the mean gain, it can be expressed as

$$F = \frac{\langle M_i^2 \rangle}{\langle M_i \rangle^2},$$ (2.3)

where $\langle M_i \rangle = M$ is the average value of M_i. Using the local model, Mcintyre [3] has shown that F can be expressed as a function of M and k, provided k is constant throughout the avalanche region. The pure electron initiated multiplication noise F_e can then be calculated from

$$F_e(M_e) = kM_e + \left(2 - \frac{1}{M_e}\right)(1 - k),$$ (2.4)

and the excess noise factor for pure hole injection F_h can be expressed as

$$F_h(M_h) = \frac{1}{k}M_h + \left(2 - \frac{1}{M_h}\right)\left(1 - \frac{1}{k}\right)$$ (2.5)

The noise associated to the impact ionisation process can arise from two mechanisms. Firstly, the secondary carriers are produced in random positions within the avalanche region. Secondly, the number of carriers generated by the chain of impact ionisation within the avalanche region is random. It is clear from equations

2.4 and 2.5, that to produce APDs with low F, the difference between α and β should be as large as possible, with the ideal case of either one of them to be 0. To obtain the lowest possible F for a particular APD, the carrier type with higher ionisation coefficient should be injected as the primary carrier to initiate the impact ionisation process.
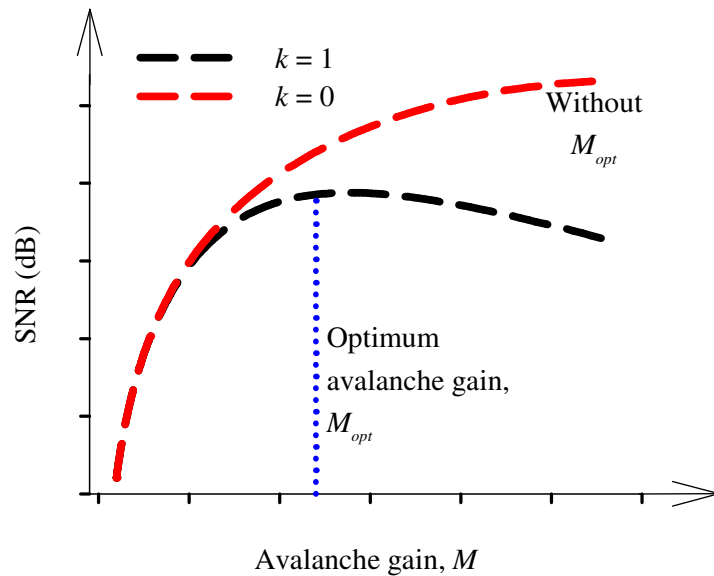

Figure 2.3 Illustration of SNR for a system consisting of an APD and a preamplifier for APDs with $k = 1$ and $k = 0$.

The multiplication or avalanche region plays an important role in determining the multiplication noise and GBP of an APD. The local model of impact ionisation has predicted that when k deviates extremely from unity with the ideal cases of $k = 0$ or ∞, multiplication noise can be reduced and higher GBP can be obtained [3, 9]. This k value has been widely used as a figure of merit of multiplication noise. Although it is valid only for local-model impact ionisation, k provides a good indication of the level of multiplication noise and it will be used throughout this thesis. To illustrate the effect of F on the overall SNR of a system, we will provide an example of the two extreme cases of impact ionisation where $k = 1$ and $k = 0$. Considering that a receiver module or system consists of an APD and a pre-amplifier, figure 2.3 shows the SNR of the two cases as a function of M. The SNR for an APD incorporated with a pre-amplifier can be calculated as

$$SNR = \frac{I_{ph,pr}^2}{2q(I_{d,pr} + I_{ph,pr})FB + \frac{N_A^2 B}{M^2}} \, , \qquad (2.6)$$

where q is the electron charge, B is the bandwidth, N_A is the amplifier's noise in A/(Hz)$^{1/2}$, $I_{ph,pr}$ and $I_{d,pr}$ are the unmultiplied photo and dark currents respectively.

Assuming the APDs have the same shot noise which is lower than the noise of the preamplifier and the same responsivity to the radiation, their SNRs are only affected by F. Figure 2.3 shows that there is a maximum exploitable gain M_{opt} for APDs with $k = 1$ because F is increasing at the same rate as M increases. For APDs with $k = 0$, the gain provided by the APD can continually increase the SNR as $F < 2$ independent on M. Similar trends and arguments apply for APDs with $0 < k < 1$, with the M_{opt} is extended to higher M value due to lower F than the case of $k = 1$.

2.4 Gain-bandwidth product

The GBP is the product of the avalanche gain and the 3-dB bandwidth of an APD. The 3-dB bandwidth of an APD is determined by the carrier transit time, the avalanche build up time and the resistance-capacitance *RC*-time of the APDs. To obtain high bandwidth, the *RC*-time should be short by reducing the series resistance and capacitance of the APDs, and therefore will not be the centre point of the discussion here. However, the carrier transit and avalanche build up time are mainly dependent on the design and material of an APD. The GBP is used to define the ability of an APD to respond to high frequency signals because there is a close relationship between M and the 3-dB bandwidth. In the previous section, it has been demonstrated that APDs with $k = 0$ have the lowest F, producing higher SNR. In the following discussion, it will be revealed that this characteristic is also highly desirable to obtain high GBP.

It was first reported by Emmons and Lucovsky [10] that the 3-dB bandwidth of

APDs is reduced at a particular value of *M*, depending on the material characteristic. Further theoretical work by Emmons [9] was done by relating the 3-dB bandwidth to *k*. He concluded that the frequency response is independent of *M* until the product of *kM* ~ 1. For *kM* > 1, the 3-dB bandwidth decreases with increasing *M* [9]. It is clear from here that the 3-dB bandwidth can be independent of *M* up to higher values of *M* with smaller *k*. A more detail discussion of bandwidth based on the current pulse using the time-dependent carrier transport equations can be found in [2].

In the ideal case of *k* = 0, there is no avalanche build up time limit for the APD where the 3-dB bandwidth is almost constant, independent of *M*. This is because with *β* (or *α*) = 0, the current pulse which results from the initially injected electron (or hole) increases during a time period which is essentially that of the transit time through the high-field region. Depending on *M*, the injected electron (or hole) will undergo multiple impact ionisation events during that particular transit through the depletion region. The current pulse then decreases to zero in approximately the hole (or electron) transit time. Thus, the current pulse will last only for a maximum of the sum of one electron and one hole transit times. Since the pulse-width is independent of the amount of multiplication events, there is no GBP limitation for any values of *M*.

2.5   Random path length model

The RPL model relies on the randomly chosen ionisation path lengths to determine the ionisation probability of a carrier [4]. From this stochastic process, the avalanche gain and excess noise factors can then be calculated. This simple model uses a hard dead space model where the ionisation probability of electron P_e is zero for an electron travelling a distance *x* in a uniform electric field, that is less than the dead space d_e. This is given by

$$P_e(x) = \begin{cases} 0 & , x < d_e \\ \alpha^* \exp[-\alpha^*(x - d_e)] & , x \geq d_e \end{cases}, \tag{2.7}$$

where α^* is the ionisation probability of the electron per unit distance, for a constant electric field, after d_e or the enabled electron ionisation coefficient. The hard threshold energy of electron ξ_{the} can be determined using the equation

$$d_e = \frac{\xi_{the}}{qE},$$ (2.8)

where E is the electric field. Following equation 2.7, the average distance between two electron ionisation events or $<l>$ will be

$$\int_0^\infty xP_e(x)dx = \frac{1}{\alpha^*} + d_e$$ (2.9)

Since $\alpha = 1/<l>$, it follows that

$$\alpha = \frac{1}{\frac{1}{\alpha^*} + d_e}$$ (2.10)

From equation 2.7, the probability a free electron does not impact ionise after travelling a distance x can be expressed as

$$S_e(x) = \begin{cases} 1 & , x \le d_e \\ \exp[-\alpha^*(x - d_e)] & , x > d_e \end{cases}$$ (2.11)

If we substitute $S_e(x)$ with a uniformly distributed number r_n with $0 < r_n < 1$, the random ionisation path length of an electron is

$$l_e = d_e - \frac{\ln r_n}{\alpha^*}$$ (2.12)

Similar derivation procedures for the expression of the hole random ionisation path length can be done by substituting $P_e(x)$, $S_e(x)$, α, α^*, d_e, ξ_{the} and l_e with $P_h(x)$, $S_h(x)$,

β, β^*, d_h, ξ_{thh} and l_h, respectively.

Each simulation trial j (with n_t being the total number of trials) is completed when all the carriers (electrons and holes) are no longer in the high field region. Then M and F can be calculated as

$$M = \frac{\sum_{j=1}^{n_t} m_j}{n_j},$$ (2.13)

and

$$F = \frac{\sum_{j=1}^{n_t} (m_j)^2}{n_j M^2}$$ (2.14)

References

[1]   F. Capasso, "Semiconductors and semimetals - Lightwave communications technology," in *Chapter 1: Physics of avalanche photodiodes*. vol. 22-D, W. T. Tsang, Ed.: Orlando: Academic Press Inc., 1985.

[2]   G. E. Stillmann and C. M. Wolfe, "Chapter 5: Avalanche photodiodes," in *Semiconductors and semimetals: Infrared detectors II*. vol. 12, R. K. Willardson and A. C. Beer, Eds.: Academic Press Inc., 1977.

[3]   R. J. McIntyre, "Multiplication noise in uniform avalanche diodes," *IEEE Trans. Electron Devices,* vol. 13, pp. 164-168, 1966.

[4]   D. S. Ong, K. F. Li, G. J. Rees, J. P. R. David, and P. N. Robson, "A simple model to determine multiplication and noise in avalanche photodiodes," *J. Appl. Phys.,* vol. 83, pp. 3426-3428, 1998.

[5]   B. K. Ridley, "Lucky-drift mechanism for impact ionisation in semiconductors," *J. Phys. C: Solid State Phys.,* vol. 16, p. 3373, 1983.

[6]   M. M. Hayat, B. E. A. Saleh, and M. C. Teich, "Effect of dead space on gain and noise of double-carrier-multiplication avalanche photodiodes," *IEEE Trans. Electron Devices,* vol. 39, pp. 546-552, 1992.

[7]   V. Chandramouli, C. M. Maziar, and J. C. Campbell, "Design considerations for high performance avalanche photodiode multiplication layers," *IEEE Trans. Electron Devices,* vol. 41, pp. 648-654, 1994.

[8] S. A. Plimmer, J. P. R. David, D. S. Ong, and K. F. Li, "A simple model for avalanche multiplication including deadspace effects," *IEEE Trans. Electron Devices, ,* vol. 46, pp. 769-775, 1999.

[9] R. B. Emmons, "Avalanche-Photodiode Frequency Response," *J. App. Phys.,* vol. 38, pp. 3705-3714, 1967.

[10] R. B. Emmons and G. Lucovsky, "The frequency response of avalanching photodiodes," *IEEE Trans. Electron Devices,,* vol. 13, pp. 297-305, 1966.

Chapter 3 Experimental methods

The performance of an APD needs to be evaluated in different aspects such as the associated noise contribution and the ability of the APD to respond to optical signals or photons. These assessments of APD can be carried out by different characterisation techniques which can provide useful information related to the key properties of an APD. The following sections will describe the implementation of these principle experimental methods and discuss how essential information can be extracted from the experimental results.

3.1   Current-voltage measurement

The most basic and fundamental characterisation of an APD is the current-voltage (*I-V*) measurement. This measurement can be carried out by applying a bias voltage across the diode and measuring the resulting current value. The *I-V* from the forward and reverse bias of a diode can provide a lot of information regarding the characteristics of a fabricated diode. Since the *I-V* measurement can be done easily with a Keithley 236 or Keithley 237 source-measurement unit (SMU) or HP4104 picoammeter, this characterisation is usually the first measurement after the fabrication.

An APD is operated at a high reverse bias to induce a high electric field region that facilitates the impact ionisation of carriers. However, information regarding the quality of the material, the formation of the junction and the quality of the contacts can be obtained from the forward *I-V*. To extract these information, the forward *I-V* I_F, can be fitted to an empirical equation [1],

$$I_F = I_o \left[exp \left(\frac{qV_t}{nk_BT} \right) - 1 \right],\tag{3.1}$$

where I_o is the saturation current, V_t is the total voltage drop across the diode, n is the ideality factor and k_B is the Boltzmann's constant. Usually the effect of series resistance and device heating will become significant at high forward current, hence an equivalent series resistance R is added to the equation,

$$I_F = I_o \left[exp\left(\frac{q(V_t - IR)}{nk_BT} \right) - 1 \right] \tag{3.2}$$

By fitting this equation to the experimental data, the value of R can be determined. An ideality factor of 1 signifies diffusion current whereas an ideality factor close to 2 indicates the current is due to generation and recombination of carriers.
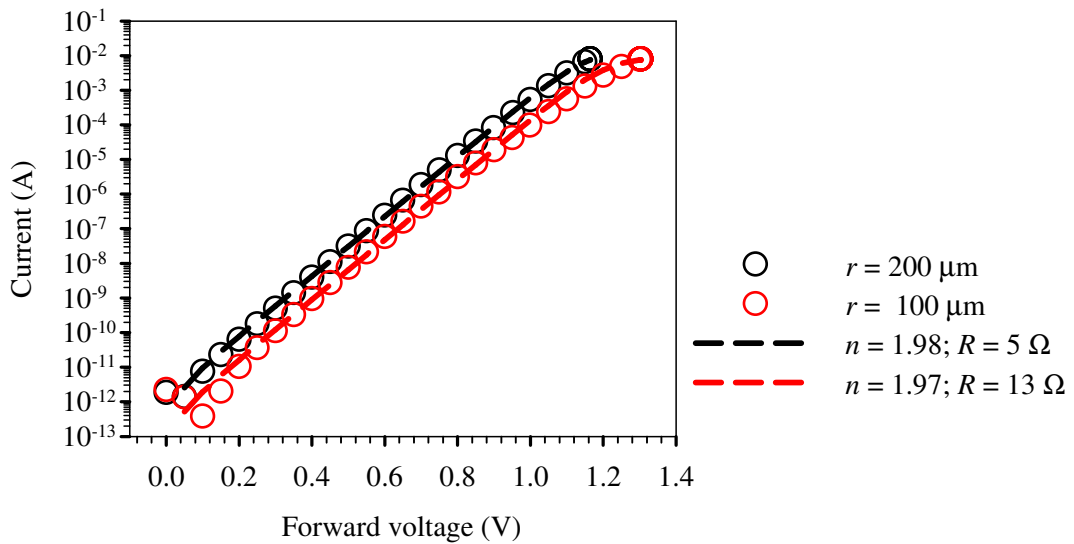

Figure 3.1 Measured and fitted forward *I-V* characteristics of GaAs diodes.

Figure 3.1 shows an example of the forward *I-V* of GaAs diodes with two different radii *r*. These *I-V*s are fitted with the diode's equation with n = 1.97 to 1.98, indicating it is generation and recombination current dominated and the crystal growth quality can further be improved. From this fitting, R which are largely contributed by the contact resistances between the metal and semiconductor can also be extracted. The contact resistance can be reduced by proper selection of metals as the *p*- and *n*-type contacts, and with an accurate scheme of the annealing

temperature. Moreover, the doping concentrations of the semiconductor that the metals are deposited on can also be increased to reduce the contact resistance. It is important to obtain low contact resistance because it will limit the maximum achievable gain and will impose an *RC*-time limit to the bandwidth of an APD.

In the reverse bias region, as *W* and *E* increase, a few mechanisms can take place and contribute to the increase in the leakage current or dark current. Since the leakage current will translate directly into shot noise that will degrade the SNR of an APD, the *I-V* at the reverse bias is important to evaluate the performance of an APD. Generally, the dark current can be divided into the bulk and surface leakage currents. The bulk leakage current consists of the diffusion I_{diff}, generation-recombination I_{g-r} and band-to-band tunnelling I_{tunn} components, given by the following equations [1].

$$I_{diff} = I_o \left[exp\left(\frac{qV}{k_B T}\right) - 1 \right], \tag{3.3}$$

$$I_{g-r} = \frac{q n_i A W}{\tau_{eff}}, \tag{3.4}$$

$$I_{tunn} = \frac{(2m^*)^{0.5} q^3 E V A}{4\pi^2 \hbar E_g^{0.5}} exp\left[-\frac{\alpha_T (m^*)^{0.5} E_g^{1.5}}{q\hbar E} \right], \tag{3.5}$$

where n_i is the intrinsic carrier concentration, *A* is the cross-sectional area of the junction, τ_{eff} is the effective carrier lifetime, m^* is the electron effective mass, $\hbar$ is the reduced Plank's constant, and α_T is a parameter dependent on the detailed shape of the barrier and is of the order of unity.

The surface leakage current I_{surf}, on the other hand, is caused by the conducting surface of an etched mesa. Depending on the surface condition and the mechanism that contributes to I_{surf}, it can either involve high complexity modelling, or a constant I_{surf} independent of V_b, or it can be a simple model that follows the Ohm's Law with
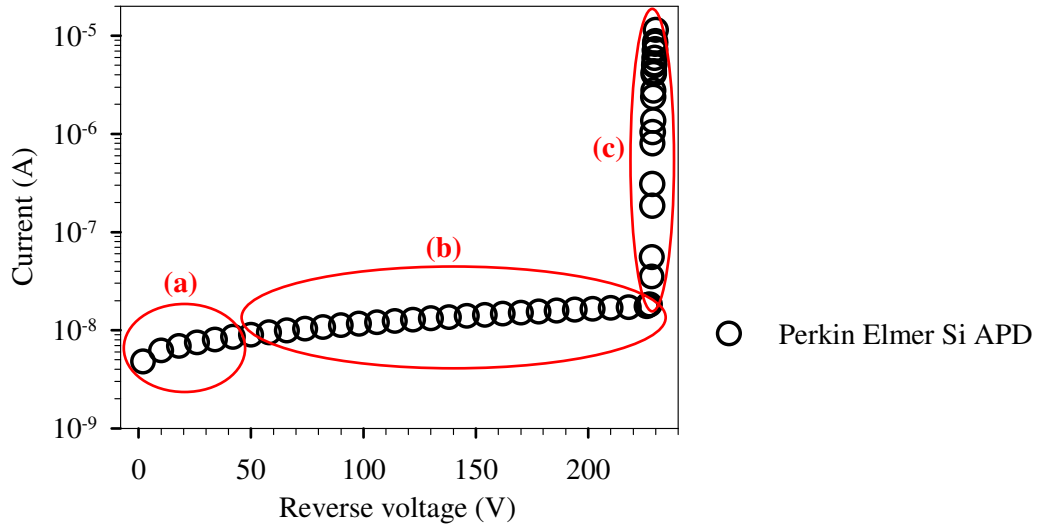
$$I_{surf} = \frac{V_b}{R} \tag{3.6}$$

Figure 3.2 Typical reverse *I-V* characteristic of the commercial Perkin Elmer Si APD at room temperature. The red circles indicate different current regimes, as discussed in the main text.

A typical *I-V* characteristic of a Si APD is shown as an example in figure 3.2. In region (a), the dark current rises rapidly with increasing V_b and saturates to a more constant value. It can be expected that the dominant current mechanisms are the I_{diff} and I_{g-r}. Region (b) shows that the current is multiplied by its avalanche gain as V_b increases. As *E* is sufficiently high in the region (c), the avalanche breakdown characteristic of this Si APD is shown. APDs do not always exhibit tunnelling current as it surfaces only at very high *E*. Generally, material systems with a large bandgap and APDs with wide *W* can be employed to suppress I_{tunn}.

3.2 Capacitance-voltage measurement

Two conductors which are separated by a dielectric will give rise to a capacitance *C*. This value depends on the relative permittivity of the dielectric ε_r, the area *A* of the

conductor, the thickness W of the dielectric layer, and they are related by the equation

$$C = \frac{\varepsilon_r \varepsilon_0 A}{W}, \tag{3.7}$$

where ε_o is the permittivity of vacuum. Similarly, the depletion region, formed between a *p-n* junction when a diode is reverse biased, will act as a dielectric separating two conductors. Capacitance-voltage (*C-V*) measurements therefore enable us to characterise the change in depletion width as the applied voltage increases. Throughout the work, the *C-V*s of the diodes were measured using the HP4275 LCR meter.
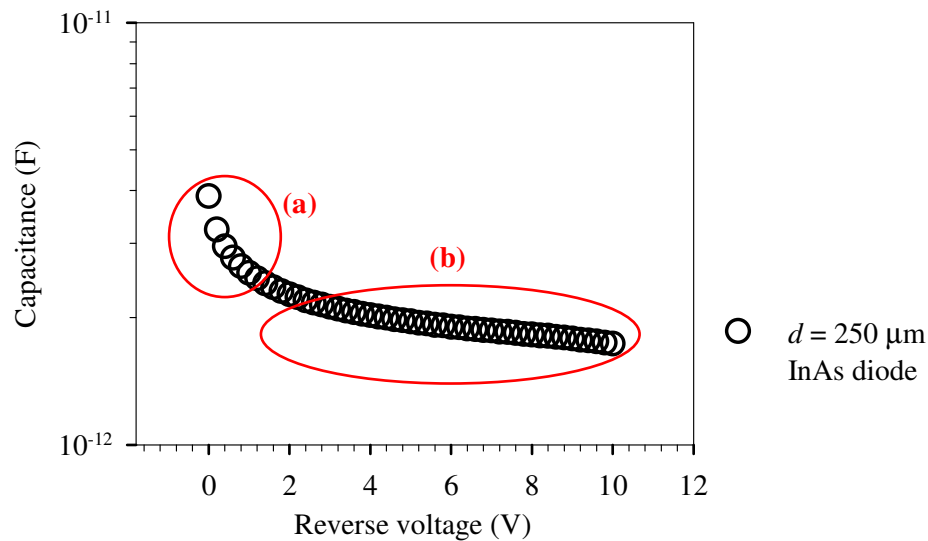

Figure 3.3 *C-V* characteristic of an InAs *p-i-n* diode with a diameter *d* = 250 µm at 77 K. The red circles identify two regimes in the *C-V* curve, as described in the text.

Figure 3.3 shows the *C-V* of an InAs *p-i-n* diode at 77 K. The *C-V* can be described by dividing it into two regions. Region (a) shows that the capacitance decreases rapidly with increasing V_b from 0 to 2 V. This is because W increases drastically due to the low background doping concentration in the *i*-layer. When W approaches the

n-layer at $V_b > 2$V in region (b), *C* decreases at a much slower rate as *W* increases more slowly due to higher doping concentration in the doped regions.

Besides extracting the total *W*, the doping concentration *N* at a certain depletion distance can be determined by

$$N(W) = \frac{2}{q\varepsilon_r\varepsilon_0 A^2}\left(\frac{dV_t}{d\left[\frac{1}{C^2}\right]}\right) \tag{3.8}$$

At equilibrium, a built-in potential or voltage V_{bi} is developed across any *p-n* junction. This potential can be obtained by plotting $1/C^2$ against V_b. Assuming an abrupt single sided junction with constant doping concentration, a straight-line graph is produced and the intercept at $1/C^2 = 0$ gives V_{bi}.
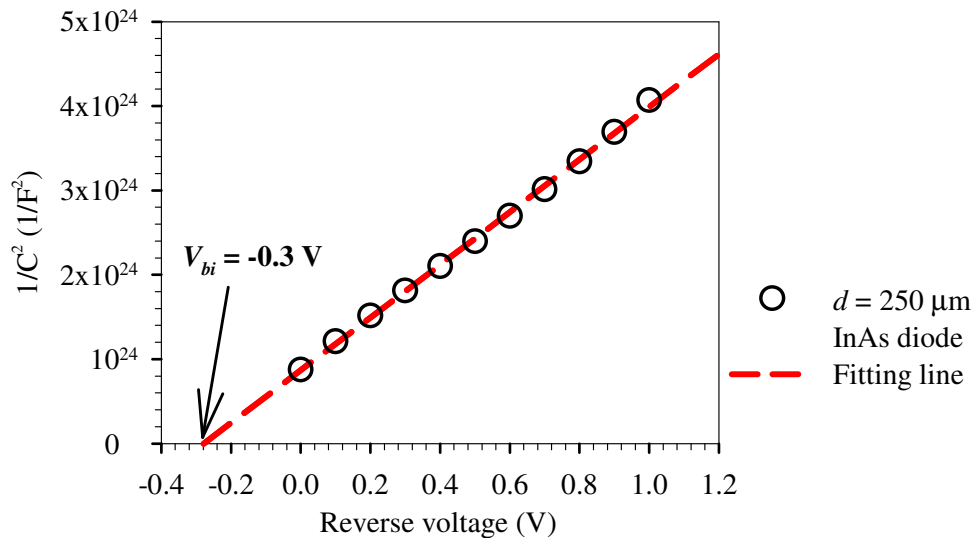

Figure 3.4 A plot of $1/C^2$ vs. reverse bias derived from the *C-V* measurement at 77 K on the InAs *p-i-n* diode.

To illustrate the way in which V_{bi} is determined, the $1/C^2$ vs. V_b graph is plotted using the *C-V* data from an InAs *p-i-n* diode, as shown in figure 3.4. It is worth noting that this way of deriving the V_{bi} is based on the assumption that the junction is formed by

a *p-n* junction with constant doping concentration in both the *p-* and *n*-layer. In figure 3.4, it can be seen that as the doping concentration in the *i*-layer increases when the depletion approaches the *n*-layer, the $1/C^2$ vs. V_b plot starts to deviate from the fitted straight line.

Furthermore, the *C-V* graph can also be fitted by an algorithm that uses the doping concentration for each region and the intrinsic region width as adjustable parameters. Based on these parameters, the algorithm calculates the electric field profile to obtain the depletion width that best fits the measured capacitance. The *i*-layer can also be divided into several regions to accommodate for the variation in doping concentrations. For a specific diode area and the relative permittivity, the capacitance can then be computed and fitted to the experimental results.

3.3   Photomultiplication measurement

Impact ionisation of carriers is an important process in APD operation. To characterise the APD gain due to the impact ionisation of carriers, photomultiplication measurements were carried out. The avalanche gain is calculated as

$$M(V) = \frac{I_{ph}(V)}{I_{pr}},$$

(3.9)

where *M(V)* is the avalanche gain at a specific voltage, I_{pr} is the primary photocurrent induced by the generation of primary carriers, which then diffuse into the high electric field region; $I_{ph}(V)$ is the photocurrent at a particular V_b. I_{pr} and $I_{ph}(V)$ are measured using a SMU or a lock-in amplifier, which will be discussed in the next section.

For this measurement, a laser was used as a radiation source and the laser spot was focused on top of a circular device. The photocurrent was measured under d. c. conditions to ensure that the dark current is adequately lower than the photocurrent.

To obtain a good SNR and to make sure *M* is calculated accurately, the photocurrent must be at least 2 orders of magnitude higher than the leakage current. Devices with high leakage current however will need the phase sensitive detection (PSD) technique to discriminate the photocurrent from the leakage current. InAs APDs are made from narrow bandgap material, thus producing high dark current at room temperature and the PSD technique is usually used. This is because the PSD technique using a Stanford Research Systems SR830 lock-in amplifier (LIA) can detect signals with a bandwidth as narrow as 0.01 Hz. Therefore the noise in the detection bandwidth is significantly reduced.

There are several set-ups available to carry out the PSD measurement, either using external or internal modulation of laser. The modulation frequency of the laser is usually kept very low, typically < 1 kHz, to avoid any undesirable effects, such as the inability of the device and measurement system to respond to high frequency signals. This can complicate the measurement and affect the accuracy of the measurement.

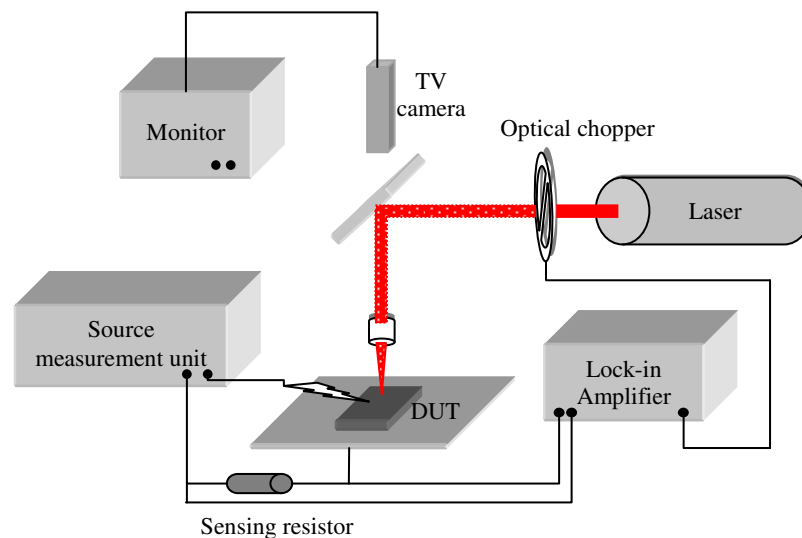### 3.3.1 PSD – External modulation

Figure 3.5 The photomultiplication measurement set-up with the external modulation of the laser using an optical chopper.

Figure 3.5 shows a typical measurement set-up, which utilises a SR830 LIA to measure the rise in photocurrent by measuring the voltage drop across the sensing resistor. The frequency of the optical chopper is fed into the LIA as the reference frequency f_{ref}. The phase-lock-loop (PLL) in the LIA actively tracks this external f_{ref} so that the measurement is not affected by any changes in f_{ref}. The LIA ideally responds to noise that is at f_{ref} and noise at other frequencies is removed by the low pass filter. This feature of "bandwidth-narrowing" is claimed to be the primary advantage of the LIA.

The LIA displays the Root Mean Square (RMS) value of a sine wave at f_{ref}. The optically chopped laser will give rise to a square-wave photocurrent output at f_{ref}. A square wave, $S(t)$ with a particular peak-to-peak voltage V_{p-p} consists of many components of sine waves at a multiple of the fundamental frequency with their amplitudes given as follow:

$$S(t) = \sum_{n=1,3,5\ldots} \frac{2V_{p-p}}{n\pi} \sin\left(n.2\pi f_{ref}t\right) \tag{3.10}$$

The LIA will detect and display only the amplitude of the first sine-wave component (or at f_{ref}) in RMS value. For example, for an input square wave with $V_{p-p} = 2$ V, the reading of the LIA ($V_{LIA, RMS}$) will be

$$V_{LIA,RMS} = \frac{2 \times 2V}{1 \times \pi} \times \frac{1}{\sqrt{2}} = 0.9\ V, \tag{3.11}$$

or

$$V_{LIA,RMS} = \frac{2 \times V_{p-p}}{\sqrt{2} \times \pi} \tag{3.12}$$

Consequently, the value of I_{ph} that is produced by a diode across the sensing resistor R_{sense}, is given by

$$I_{ph} = \frac{V_{LIA,RMS} \times \sqrt{2} \times \pi}{2} \times \frac{1}{R_{sense}} \approx \frac{V_{LIA,RMS}}{0.45 R_{sense}} \qquad (3.13)$$

Generally, it is not crucial to measure the absolute value of the photocurrent as the calculation of M is based on the relative value of the photocurrent at a particular V_b with respect to the I_{pr}. However, knowing the exact value of photocurrent will be essential in calculating the responsivity of a diode. By measuring the power of the laser incident on a diode (without chopping), the responsivity can then be calculated.

3.3.2 PSD – Internal modulation

The photomultiplication measurement set-up with internal modulation of the laser can be carried out using a laser which can be modulated internally at a certain frequency as shown in figure 3.6. All other measurement equipments were kept the same as the the case of using external modulation. During this work, the HP 8168C tuneable wavelengths laser was used because it could provide laser at λ = 1460 to 1600 nm and frequencies from 270 Hz to 10 kHz. Similarly, the modulation frequency was fed into the LIA as f_{ref}. Since the lasers in the infrared wavelengths are invisible, it is easier to focus the laser on the diodes using this method as the laser can be fibre-coupled.
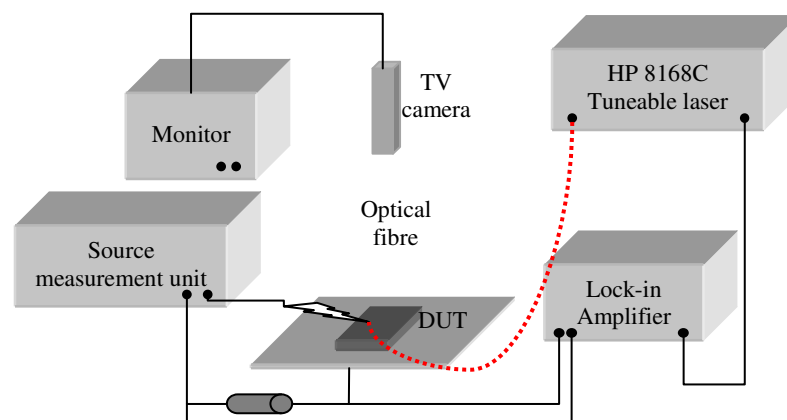

Figure 3.6 The photomultiplication measurement set-up with internal modulation of the laser.

For the photomultiplication measurements, either under d.c. condition or using PSD, there are a few main factors which need to be considered to ensure the accuracy of the results. Firstly, to accurately measure the avalanche gain that is initiated by one of the carrier type, either electron or hole, the purity of carrier injection into the high-field region is very important. The laser spot needs to be tightly focused on the *p*-type (or *n*-type) cladding layer for pure electrons (or pure holes) injection, so that no light is falling onto the mesa sidewalls. The absorption profile in the cladding layer will be different for lasers with different wavelengths. Hence, knowing the absorption coefficients and designing a thick enough cladding layer will also be crucial. To ensure the purity of carrier injections, measurements should be repeated with different sizes of devices and lasers with different λ.

Secondly, at high V_b, the power dissipation of the device will be high especially in devices with high leakage current such as InAs APDs. Since the impact ionisation process is temperature dependent, device heating can either overestimate or underestimate the real M of the devices. Repeating measurements with a range of photocurrents can help to check if device heating is an issue. In addition, devices can be biased for a longer period and a constant photocurrent over a certain period can be an indication that the devices are not heating up.

Thirdly, the series resistance in the circuit can cause inaccuracy in the measurement. It is usually due to the high contact resistance of the devices. At high M, the voltage drop across the resistor can be significant, causing the actual bias voltage across the diode to be lower than it is supplied by the SMU. Moreover, in the PSD measurement, R_{sense} should be selected such that the voltage drop across it is minimised while producing sufficiently high signal to noise ratio to be detected by the LIA. The difference in voltage across the diode needs to be taken into account so that M is not underestimated.

Finally, the photocurrent will increase as V_b increases either due to impact ionisation or the increase in collection efficiency of free carriers. The primary photocurrent shall be determined accurately by taking into account the increase in the depletion

width, which can increase the collection efficiency. It has been shown [2] that the increase in I_{pr} can be approximated by a straight line with the equation

$$I_{pr} = bV_b + e, \qquad\qquad (3.14)$$

where b is the slope and e is the *y*-intercept. The increase in I_{pr} at low V_b can be fitted with this equation and is extrapolated throughout the measured V_b range as shown in figure 3.7. *M* can then be calculated by dividing the photocurrent by the extrapolated I_{pr}. This technique is usually referred to as the base line correction. Due to the long electron and hole diffusion lengths of InAs, the photomultiplication measurements on InAs APD during this work do not involve the base line correction.
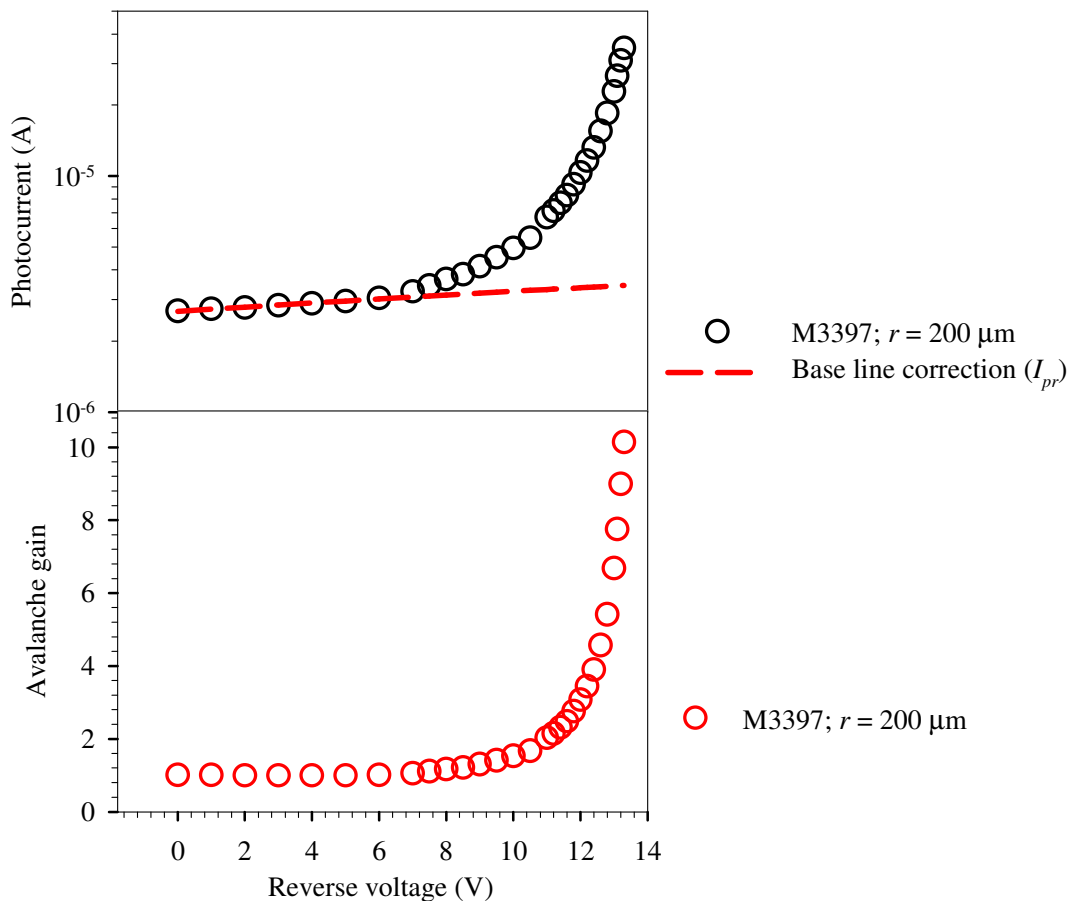

Figure 3.7 An example of base line correction method (top) to calculate *M* (bottom) in an InGaAs/InAlAs SAMAPD.

3.4   Excess noise measurement

During this work, the excess noise factor of InAs APDs was measured at temperatures below room temperature. Since the dark current was significantly reduced and the photocurrent was at least two orders of magnitude higher, the noise power could be measured directly from a noise figure analyser (NFA). As shown in figure 3.8, the experimental set-up for this noise measurement is similar to that used by Campbell *et al.* [3] but the noise figure meter was replaced by an Agilent 8973A NFA which allows measurements of the noise power at frequencies of 10 MHz to 3 GHz. The devices were probed using a 50 GHz ground-signal-ground (GSG) probe which was connected to a bias-tee through a well-shielded cable with SMA connectors at both ends. The d. c. bias voltage was applied to the APD via the bias-tee which also coupled the high frequency noise power generated by the APD into the NFA with an input impedance of $Z = 50\ \Omega$.
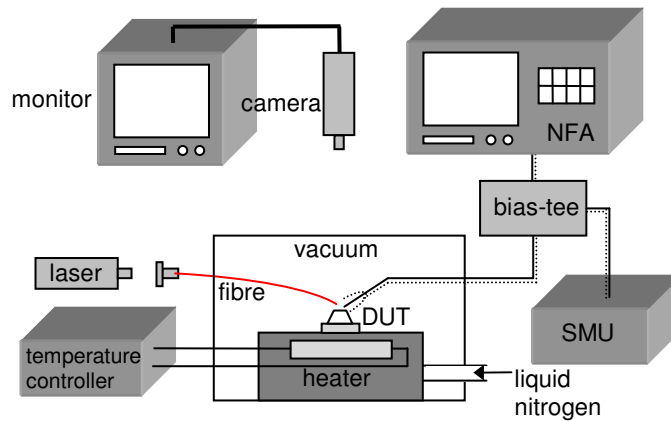

Figure 3.8 The experimental set-up for excess noise measurements using a noise figure analyser.

NFA measures and displays the noise power with respect to the thermal noise k_BT of the NFA at $T = 296.5$ K in units of dB. Each time before performing this measurement, the NFA was calibrated by connecting the input to a calibrated noise source (Model: Agilent 346B; Serial number: MY44420110). The details on the noise power at a particular frequency of this noise source and the step-by-step

calibration procedures are provided in Appendix B. To carry out the measurement, the noise power of the dark current ($P_{dark,dB}$) and the noise power of the dark and photocurrent ($P_{total,dB}$) of the diodes were measured. These two noise powers were converted into units of Watt ($P_{dark,watt}$, $P_{total,watt}$) using the equations

$$P_{dark,dB} = 10 \ \log \frac{P_{dark,watt}}{k_B T \Delta f} \tag{3.15}$$

$$P_{total,dB} = 10 \ \log \frac{P_{total,watt}}{k_B T \Delta f} \tag{3.16}$$

The noise power contribution of the photocurrent N_p was then calculated as

$$N_p = \left(10^{\frac{P_{total,dB}}{10}} - 10^{\frac{P_{dark,dB}}{10}} \right) \times k_B T \Delta f \tag{3.17}$$

F was then determined by the equation
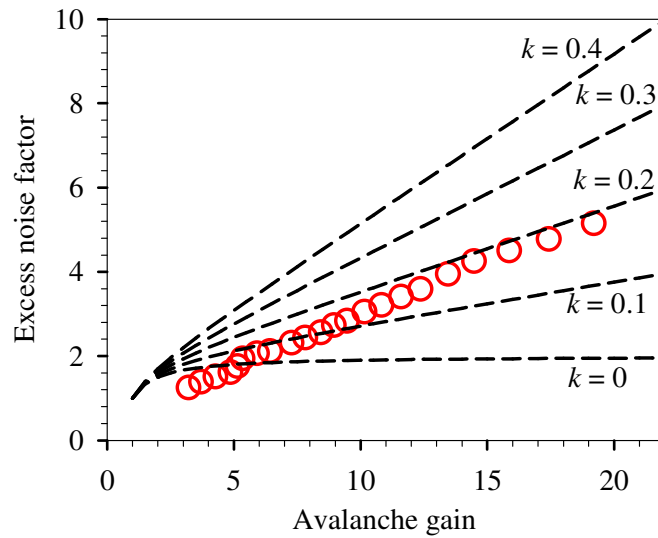
$$N_p = 2q I_{pr} M^2 F Z \Delta f \tag{3.18}$$

Figure 3.9: The excess noise factors of an InGaAs/InAlAs SAMAPD at room temperature. Local model reference lines at $k = 0$ to 0.4 [4].

This set-up was tested by measuring the excess noise of an InGaAs/InAlAs SAMAPD. The results were as expected and as measured using a custom-built noise measurement set-up with PSD [5], following the local model reference line of $k \sim 0.2$. After verifying the accuracy of this measurement set-up, the excess noise factors of the InAs APDs were measured at low temperatures.

3.5   Frequency response measurement

In this measurement, a HP 83402B 1300 nm laser which can be modulated up to 6 GHz was used as the optical excitation source. The laser was modulated by a HP 8341B radio frequency (RF) signal generator and fibre-coupled onto the devices using a single mode or multimode fibre. This RF source generates signals from 10 MHz to 20 GHz. It was interfaced with a HP 70820A microwave transition analyser (MTA) through a General Purpose Interface Bus (GPIB) so that it could be controlled remotely by the MTA. The modulating power and frequency range of the laser was controlled using the MTA.
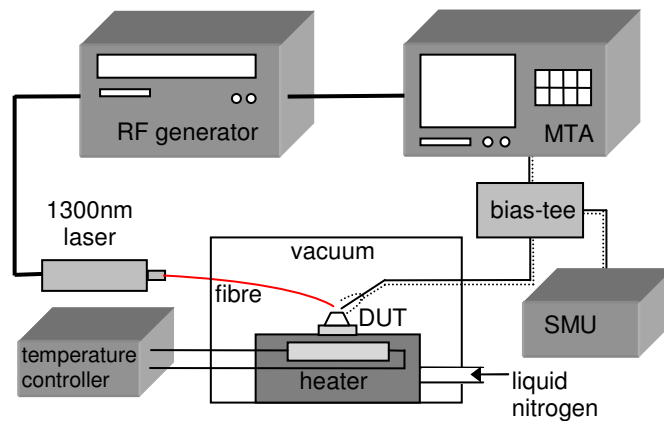

Figure 3.10 The experimental set-up for the frequency response measurements using the microwave transition analyser and radio frequency generator.

The fabricated devices were probed using a 50 GHz GSG probe. It was connected to a bias-tee using a well-shielded high speed cable with *V*-connector on one end and *K*-

connector on another. The devices were d. c. biased using a SMU and the resulting high-frequency photocurrent signal was fed into the MTA. The power of the signal was measured in units of dBm and was displayed on the MTA. The noise floor of this system, when the 50 GHz probe was open-circuited, was in the range of - 95 to - 85 dBm for frequencies of 100 MHz to 10 GHz. During the frequency response measurements, the power of the laser was adjusted such that the power transmitted by the devices was above - 75 dBm to ensure the accuracy of the measurements. The external connections and the procedures used for this set-up are in Appendix C.
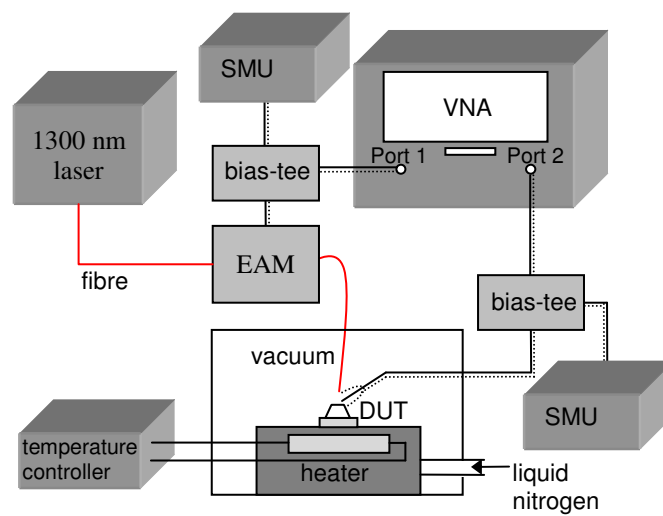
Figure 3.11 The experimental set-up for the frequency response measurements using the VNA and EAM.

The frequency response was also measured using the 2-port E8364B PNA Series vector network analyser (VNA) together with the 1.3 µm 40 Gbps Electro Absorption Modulator (EAM) from CIP Technologies (Model: 40G-IR-EAM-1300). The EAM needs to be terminated by a blocking capacitor and a broadband 50-Ω termination. This set-up was mainly used to measure the response at $f > 10$ GHz. The schematic diagram of the set-up is shown in figure 3.11. The EAM was d. c. biased using a SMU and was RF biased at a particular frequency using the RF source from port 1 of the VNA. The frequency response of the diodes was measured from Port 2 of the VNA, which is similar to that of the MTA mentioned above. Since the EAM

can modulate the signal up to 30 GHz with a 3 dB loss at this frequency, this set-up is only ideal for measurements at f < 30 GHz. The precautionary steps taken when using the EAM and VNA are listed in Appendix D.

It should be noted that at high frequencies, power or signal loss can occur throughout the measurement system. These losses can be originated from the cables, bias-tee, high speed connectors, laser and the high speed GSG probe. If the system is not properly calibrated, the losses are reflected on the frequency response of the device under test, resulting in an underestimation of the bandwidth of the device. Therefore, the system calibration is crucial in making sure that the frequency response measurement results are accurate. The calibration can be carried out using a 2-port VNA or it can be done using the MTA and RF generator. In section 7.5, the experimental calibration results will be discussed in detail since the results are only valid for a particular set of connectors, cablings and bias-tee. The way in which the losses are corrected will also be described. For different set of measurements using different components, the calibration needs to be repeated. All these losses were computed in units of dB, for a particular frequency in the low frequency range, such as 100 MHz.

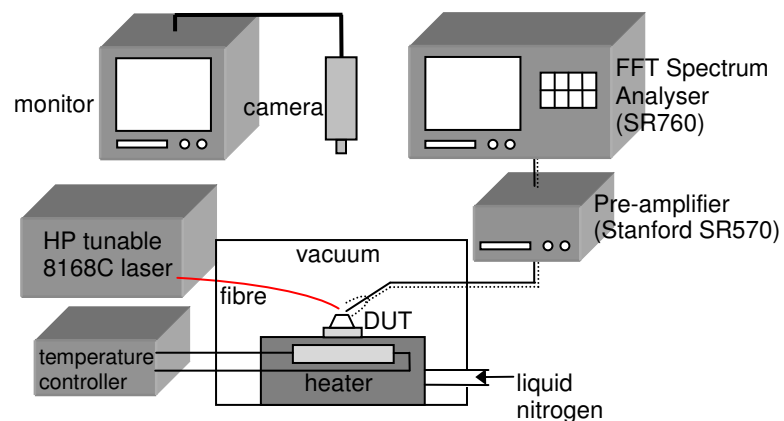## 3.6   Signal to noise ratio measurement

Figure 3.12 The experimental set-up to measure the signal to noise ratio of a system with a diode and an amplifier.

As discussed in section 2.3, the APD itself does not provide higher sensitivity if it is not operating in conjunction with an amplifier. Furthermore, the total noise of the system must be dominated by the noise of the amplifier for an APD to be useful. Figure 3.12 shows a simple receiver module which uses a low-noise Stanford SR570 pre-amplifier. The pre-amplifier can provide a d. c. bias up to 5 V and external supply such as battery can be added in series to increase the d. c. bias voltage. It has different sensitivities which define the gain of the pre-amplifier. The optical signal was provided by a HP 8168C tuneable laser at 1550 nm, which was modulated at a particular frequency. The photocurrent or electrical signal produced by the diode was amplified by the pre-amplifier before being channelled into the SR760 Fast Fourier Transform (FFT) Spectrum Analyser. The signal was displayed in the frequency domain and the signal's amplitude corresponding to the modulating frequency of the laser was recorded in RMS voltage. The total noise of the system can also be measured from the spectrum analyser. Using this experimental set-up, the change in the SNR with respect to increasing avalanche gain was investigated.

3.7   Low temperature characterisations

With thermal energy as one of the main sources of energy, many mechanisms taking place within an APD are inevitably related to temperature. Therefore, characterising APDs at temperatures lower or higher than room temperature is desirable and can provide significant knowledge on the behaviour of an APD. The activation energy E_A of a particular process or mechanism can also be calculated by using the Arrhenius Equation

$$B = B_0 \exp\left[\frac{E_A}{k_B T}\right], \tag{3.19}$$

where B and B_0 are constants.

To carry out the low temperature characterisation, a low temperature on-wafer probe station was used to cool the device to a desired temperature. Figure 3.13 shows the

Janis ST-500 series low temperature probe station with two d. c. probe arms, an optical fibre probe arm and a probe arm with the high speed GSG probe. The sample chamber was evacuated by the rotary and diffusion pumps to ~ 2×10^{-5} mBar before it was cooled by the flow of liquid nitrogen from a pressurised liquid nitrogen dewar. The steps and details of evacuating the chamber, cooling and shutting down the system are attached in Appendix E. The minimum achievable temperature for this set-up was approximately 77 K and the temperature of the sample chamber was monitored by a temperature controller. To achieve temperatures above 77 K, the heater of the temperature controller could be activated to heat the sample chamber up to a desired temperature.
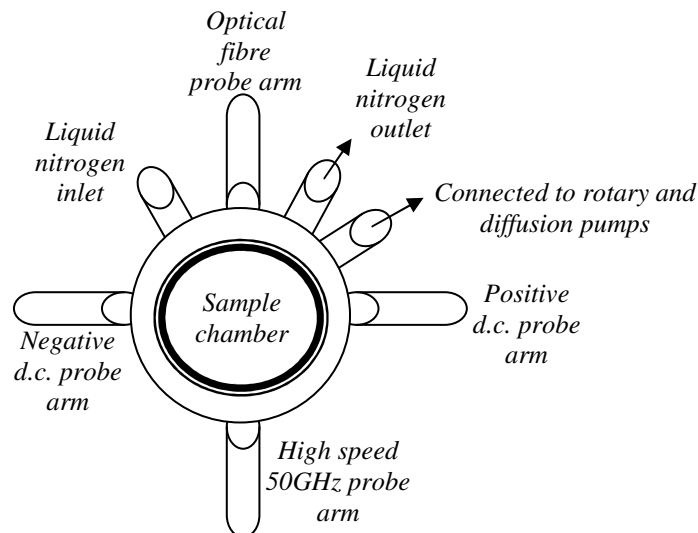

Figure 3.13 The Janis ST-500 series low temperature probe station set-up.

The *I-V* and *C-V* measurements were carried out using similar equipment as at room temperature. The devices were probed using the two d.c. probe arms of the low temperature probe station. At 77 K, the dark current of InAs APD decreases significantly compared to room temperature. Due to the high leakage current at room temperature, the *C-V* of InAs APDs was usually measured at 77 K.

When carrying out a photomultiplication measurement, the laser beam was coupled into a multimode fibre that was attached to the optical fibre probe arm. The

multimode fibre could transmit lasers from the visible up to 2 µm without significant attenuation. The core of the fibre has a diameter of 62.5 µm and depending on the distance between the core and the device, the laser spot diverges to diameters typically between 80 and 100 µm. Similar to the photomultiplication measurements which were discussed in section 3.3, this measurement can be carried out at low temperature, either under d. c. conditions or using the PSD technique.

The frequency response of the device at low temperatures was also measured using the Janis low temperature probe station. The probe arm connected with the high speed GSG probe was used for this purpose. The laser source used in this experiment has an output with FC/PC or FC/APC connectors. However, the multimode fibre was terminated with a SMA connector. To transmit the laser from a single mode fibre into the multimode fibre, an FC/PC to SMA connector was used.

References

[1]   S. M. Sze and K. K. Ng, "Physics of semiconductor devices, 3rd. Edition," John Wiley and Sons Inc., 2007.

[2]   M. H. Woods, W. C. Johnson, and M. A. Lampert, "Use of a Schottky barrier to measure impact ionization coefficients in semiconductors," *Solid-State Electron.,* vol. 16, pp. 381-394, 1973.

[3]   J. C. Campbell, W. T. Tsang, G. J. Qua, and B. C. Johnson, "High-speed InP/InGaAsP/InGaAs avalanche photodiodes grown by chemical beam epitaxy," *IEEE J. Quantum Electron.,* vol. 24, pp. 496-500, 1988.

[4]   R. J. McIntyre, "Multiplication noise in uniform avalanche diodes," *IEEE Trans. Electron Devices,* vol. 13, pp. 164-168, 1966.

[5]   K. S. Lau, C. H. Tan, B. K. Ng, K. F. Li, R. C. Tozer, J. P. R. David, and G. J. Rees, "Excess noise measurement in avalanche photodiodes using a transimpedance amplifier front-end," *Measurement Sci. Technol.,* vol. 17, p. 1941, 2006.

Chapter 4 Growth and fabrication of high speed InAs photodiodes

4.1 Background on growth and fabrication

The growth and fabrication of devices are crucial to reduce both the bulk and surface leakage currents in InAs diodes. The growth conditions of InAs using MBE have been optimised for substrate cleaning, growth rate and growth temperature to obtain a mirror-like surface morphology. It was reported that 470 $^{\circ}$C was the optimum growth temperature with a growth rate of ~ 0.83 ML/s (~ 2.512 Å/s) for MBE to produce wafers with very low surface defect density [1].

Due to its ability to produce high quality thick InAs wafers at a higher growth rate, MOVPE was also used to grow InAs wafers. Thick undoped InAs layers with very low background doping concentrations have been the priority to produce InAs diodes with very wide depletion widths. To obtain high quality InAs layers, surface oxide-cleaning at annealing temperatures of ~ 620 – 630 $^{\circ}$C was carried out prior to the growth. Growth conditions were optimised at a growth temperature of ~ 600 $^{\circ}$C with higher growth rate of ~ 10 – 14.6 Å/s for *p*- and *i*-layers, compared to ~ 7.5 Å/s for *n*-layers. A higher growth rate was used to minimise the diffusion of dopants from the highly-doped *p*- and *n*-cladding layers into the *i*-layer. Since InAs is a narrow bandgap material on which ohmic contacts with metals can be easily achieved, the doping concentrations of the *p*- and *n*- cladding layers are controlled so that they are not unnecessarily high.

All the InAs wafers used in this work were grown on InAs substrates, either *p*-doped, *n*-doped or undoped substrates. Hence, the problems related to lattice-mismatch do not exist. This is especially important for InAs APDs since thick structures are

necessary and they are operating at higher V_b and E.

Besides the bulk leakage current that is mainly related to the quality of the material, etched mesa diodes are highly susceptible to surface leakage current, especially in the case of narrow bandgap materials. It was reported that the free surfaces (vacuum-semiconductor interface) of InAs exhibit electron accumulation, resulting in the Fermi level to be pinned above the conduction band minimum [2, 3]. This conducting surface is believed to be the main source of surface leakage current. Therefore, proper surface treatment using optimised etching procedures are necessary to sufficiently suppress the surface leakage current for APD operation.

The fabrication of InAs diodes using wet chemical etching was reported by Marshall *et al.* [1]. The surface leakage current was significantly reduced to allow APD's characterisation. In this chapter, the fabrication of InAs diodes using wet chemical etching will be briefly discussed and the effect of the incorporation of wide-bandgap materials into InAs diodes will be investigated. Furthermore, the different surface passivations of the etched mesa sidewalls will be investigated to determine the most suitable dielectric for surface passivation. After identifying the optimised fabrication process, high speed InAs APDs are designed and fabricated to allow the frequency response measurements to be carried out.

4.2   Wet chemical etching

Before the optimisation of the surface passivation to reduce the surface leakage current, the fabrication using wet chemical etching was carried out as reported by Marshall *et al*. [1]. Ti/Au of about 20/200 nm was deposited as the *p*- and *n*-contacts of the InAs diodes. Neither of the contacts were annealed to avoid any diffusion of metal, especially gold into the semiconductor layers.

To avoid any contamination during the chemical etching process, the InAs samples were not mounted on glass slides using wax and dedicated glasswares were used specifically for the etching of InAs diodes. The InAs wafers were first etched using a

phosphoric acid-based etchant of $H_3PO_4:H_2O_2:H_2O = 1:1:1$ at an etching rate of ~ 1.1 μm/minute. It was followed by a finishing etch using a sulphuric acid-based etchant of $H_2SO_4:H_2O_2:H_2O = 1:8:80$ for 30 seconds [1]. Throughout the fabrication process, the samples were not exposed to $T > 100\ ^oC$ to avoid any surface degradation.

To ensure the repeatability of the fabrication process, two layers of InAs diodes, *n-i-p* (MR2560) and *p-i-n* (M3247), were fabricated using a NEWPIN mask. The NEWPIN mask design and the growth details of MR2560 and M3247 are in Appendix A1. Both the forward and reverse *I-V* of these diodes were measured to evaluate the quality of the fabricated diodes.
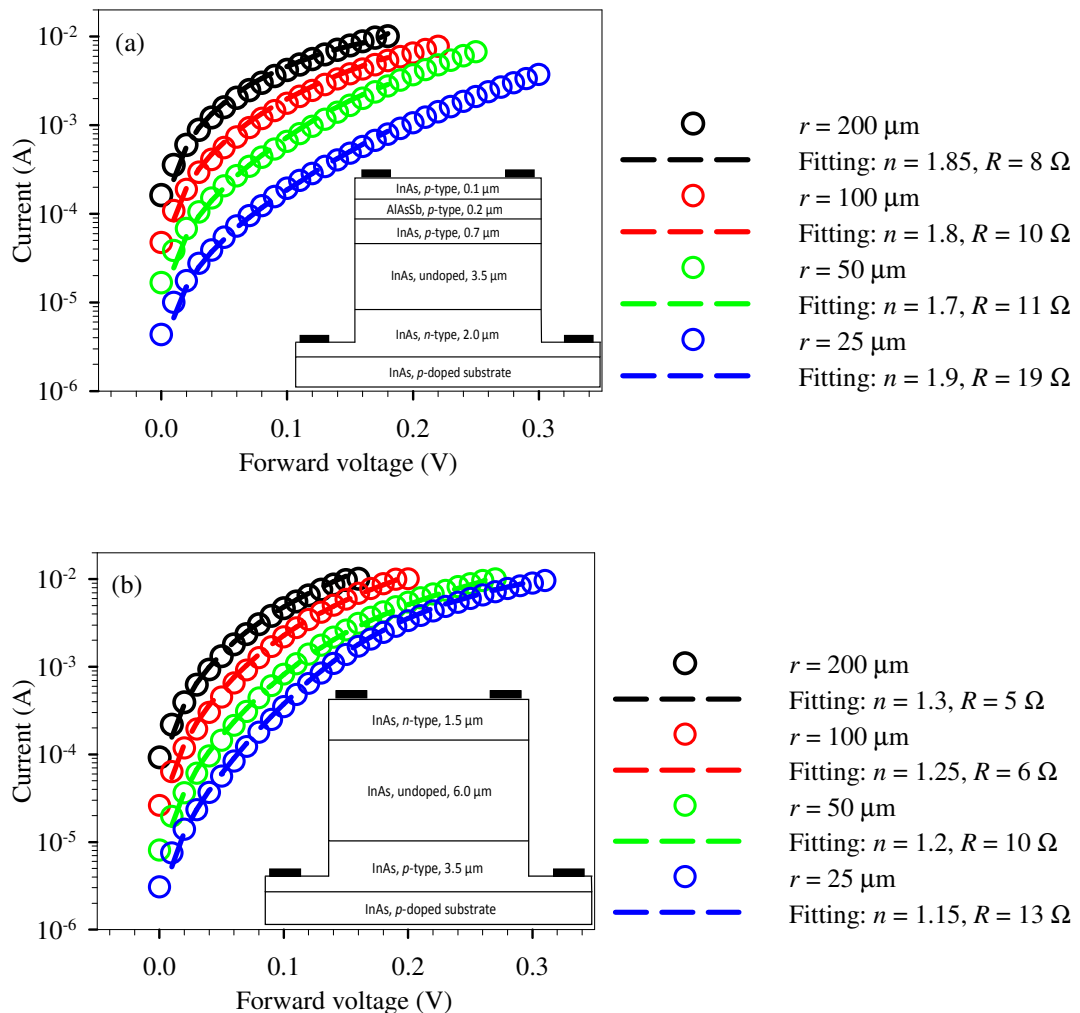

Figure 4.1 The forward *I-V* characteristics of (a) M3247 and (b) MR2560 together with the structures of the devices at room temperature.

Fig 4.1 shows the forward *I-V* characteristics from both InAs *p-i-n* (M3247) and *n-i-p* (MR2560) diodes together with the fitted parameters using equation 3.2 in section 3.1. For MR2560, *n* are between 1.15 and 1.3, very close to 1, suggesting a good *n-i-p* junction formed and there is more diffusion than generation-recombination current. The *p-i-n* diodes, however, show *n* closer to 2, probably due to the heterojunction formed between the InAs and $AlAs_{0.16}Sb_{0.84}$ blocking layer. This is because when the diode is forward biased, the diffused electrons from the *n*-layer to *p*-layer are blocked by the wide bandgap material. The accumulation of electrons (minority carriers in *p*-layer) enhances the recombination of electrons, causing higher recombination current. The series resistance, mainly due to the contact between the metal and the semiconductor, is higher for InAs *p-i-n* diodes because *p*-contact is proven to be more difficult to form a good ohmic contact with InAs. A more detailed discussion on contact resistance for InAs diodes is presented in section 4.5.1 with an explanation based on the transmission line method (TLM). It can be seen that the contact resistance is low enough for most of the APD applications even without thermal annealing because InAs is a narrow bandgap material. However, the contact resistance may become a major issue when very small InAs APDs are used for high speed applications where high resistance will impose an *RC* limit.
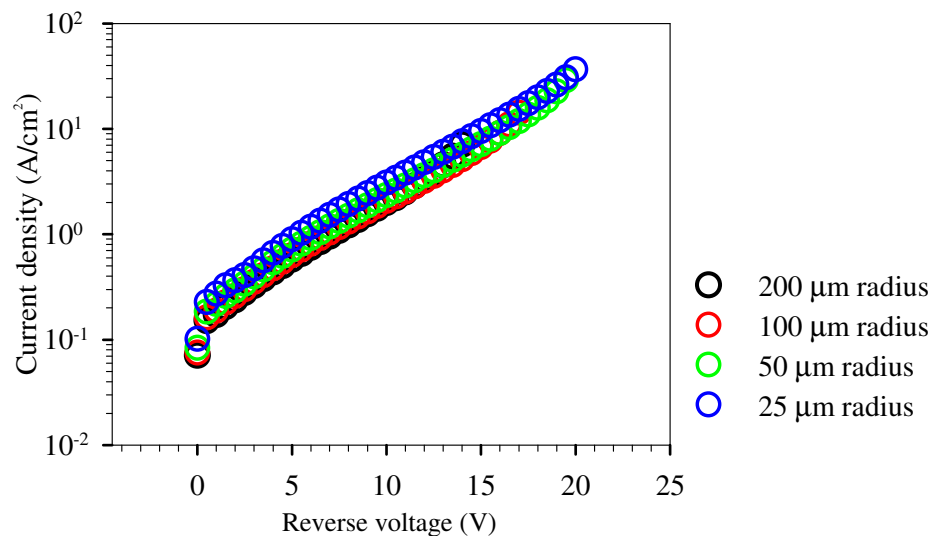

Figure 4.2 The dark current densities characteristics of MR2560.

The room temperature reverse *I-V* characteristics and leakage current densities for the InAs *n-i-p* APDs are shown in Fig 4.2. The *I-V* data are normalised to the device area and their respective current densities show good agreement with each other, indicating the bulk nature of the leakage current. A dark current density of ~ 100 mA/cm^2 was measured on these InAs diodes at room temperature [4]. Within the bias voltage range, there is no significant tunnelling current component observed and the non-scaling to device perimeter pointed out that the surface component is not the dominant leakage current component at room temperature.

Low temperature *I-V* characterisation can be another indication of the quality of the fabricated diodes. This is because the bulk dominated leakage current is due to either diffusion or generation-recombination current. Hence the bulk leakage current will reduce proportionally to the reduction of n_i or n_i^2 with decreasing temperatures. The surface leakage current, on the other hand, consists of mechanisms which are more uncertain, and its temperature dependence is usually less significant compared to the bulk leakage current. *I-V* measurements of the InAs diodes were therefore taken at 77 K.
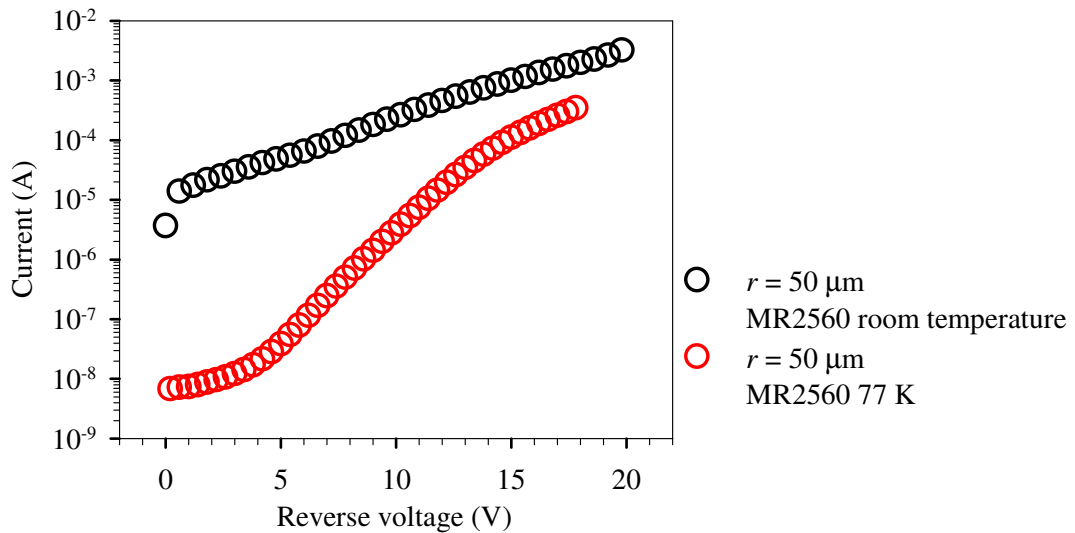

Figure 4.3 The *I-V* characteristic of a MR2560 diode with *r* = 50 µm at 77 K compared to room temperature.

Figure 4.3 shows an example of the leakage current in MR2560 diodes compared to that at room temperature. At $V_b < 1$ V, the leakage current reduces by > 3 orders of magnitude. I_{tunn} can be observed at $V_b > 5$ V. The existence of I_{tunn} can be confirmed by fitting the measured leakage current to the I_{tunn} equation. In addition, the leakage current due to tunnelling must exhibit strong dependence on the diodes' area to ensure its bulk dominated characteristic. As shown in equation 3.5, the I_{tunn} is highly dependent on E_g. As InAs has a narrow bandgap, I_{tunn} can happen even at low E, typically > 60 kV/cm [5]. To suppress this leakage current component, diodes with thicker W are needed to reduce the peak electric field.

Throughout the work reported in this thesis, many layers of InAs wafers, either MOVPE or MBE grown, were fabricated, of which only those layers in Appendix A1 are with sufficiently high quality and low leakage current at high V_b, which will be reported in the subsequent chapters. InAs wafers with lower quality and high surface defect density are listed in Appendix A2 with some brief comments based on their *I-V*, *C-V* and avalanche gain characterisations at room temperature and 77 K.

4.3   Study on the incorporation of wide bandgap material

The incorporation of a wide bandgap material into a narrow bandgap material has been widely reported to reduce the dark current. To achieve room temperature operation for InSb, Ashley and Elliot incorporated a wide bandgap material at the interface of *p-* and *i*-regions to block the minority electrons flowing from the *p*-layer to the depletion region [6]. For InAs diodes, it was reported that the incorporation of a wide bandgap material, such as $AlAs_{0.16}Sb_{0.84}$, can block the electrons in the contacts from diffusing into the *p*-layer and depletion region, hence reducing the leakage current of the InAs diodes [1]. However, previous dark current comparisons were carried out based on different wafers grown by MBE and MOVPE. This has created an uncertainty whether the reduction of leakage current is due to the incorporation of a wide bandgap material or the difference in the quality of growth, which can also affect the leakage current level. While it served as an indication, InAs layers grown by different methods do not provide a very clear-cut comparison in

demonstrating the effectiveness of the $AlAs_{0.16}Sb_{0.84}$ layer in blocking the electrons from diffusing into the depletion region.
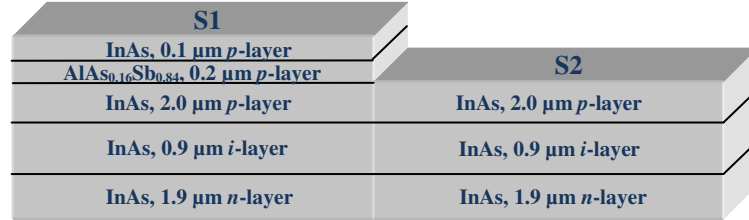

Figure 4.4 The cross section view of the M3279 InAs wafers with and without the $AlAs_{0.16}Sb_{0.84}$ blocking layer.

InAs M3279 layer was used to study the effect of the blocking layer. The details of this wafer can be found in Appendix A1. Half of the M3279 sample was masked with photoresist, and the top 100 nm of InAs and 200 nm of $AlAs_{0.16}Sb_{0.84}$ of the other half were etched, leaving a big sample with (S1) and without (S2) the blocking layer, as shown in figure 4.4. This sample was fabricated using the processing steps described in section 4.2 and was cleaved into two samples (S1 and S2) just before the final wet chemical etching process. The purpose of this was to ensure that these two samples went through a very similar fabrication process, whenever it was possible, so that the difference in the dark current, if any, will only be due to the blocking layer.

The room temperature *I-V* of S1 and S2 were measured and shown in figure 4.5. To ensure bulk dominated leakage current, the current densities shown in the figure were calculated based on the large area devices. There is a clear difference between S1 and S2 with S2 having ~ 4 times higher dark current density than S1. Figure 4.5 also present the dark current densities of a few other InAs wafers. All these InAs wafers without the blocking layer, either grown by MOVPE (MR2560) or MBE (M3884) show similar dark current densities as S2. Whereas, the reported dark current density of the M3247 with the $AlAs_{0.16}Sb_{0.84}$ blocking layer [1] shows similar leakage current level as S1. The reduction in dark current is believed to be mainly due to the

blocking layer which acts as a barrier that prevents the diffusion of electrons from the metal contact into the depletion region.
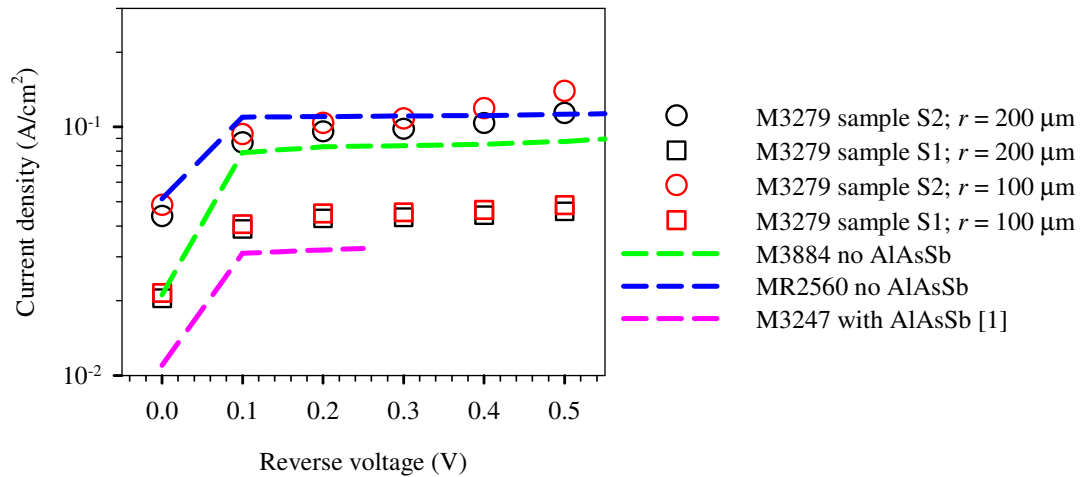

Figure 4.5 Dark current densities of S1 and S2, compared with the dark current densities of other MBE and MOVPE grown InAs wafers with and without the $AlAs_{0.16}Sb_{0.84}$ blocking layer.
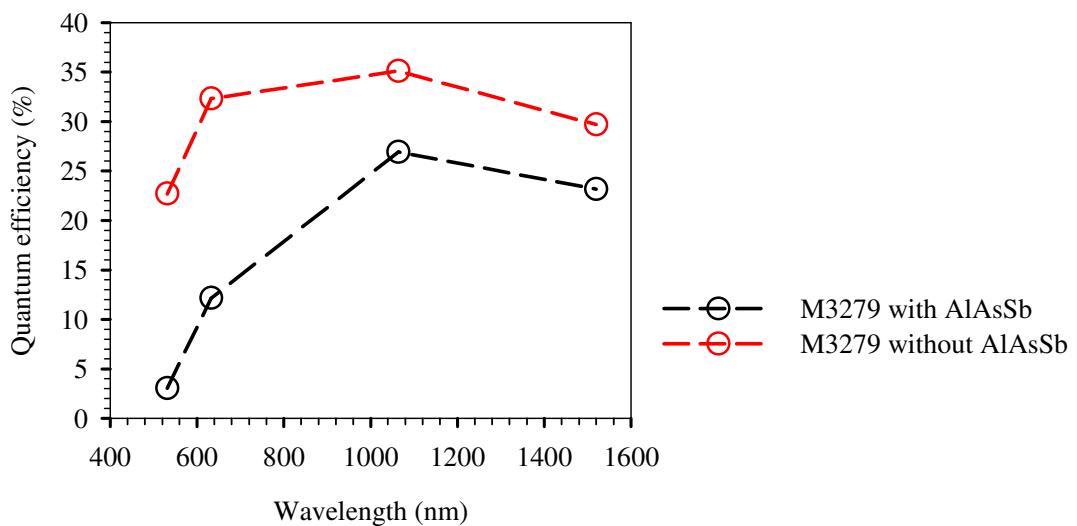

Figure 4.6 Measured quantum efficiencies of samples S1 and S2 at room temperature.

The responsivities of S1 and S2 were also measured at room temperature from $\lambda =$ 532 to 1520 nm. Figure 4.6 compares their quantum efficiencies and it is clear that the S2, without the wide-bandgap blocking layer, can provide higher responsivity. At radiation wavelengths of 1064 and 1520 nm, it is estimated that ~ 25 % of the carriers generated in the top 100 nm of the InAs layer are blocked by the $AlAs_{0.16}Sb_{0.84}$ layer, causing lower responsivity. Together with the dark current comparison in figure 4.5 this responsivity measurement also proves that minority electrons injected from the contacts are successfully blocked.

From this simple study, it is clear and conclusive that the bulk leakage current of InAs diodes can be reduced by incorporating a wide bandgap material in the *p*-layer to prevent the diffusion of the minority carriers from the contact. The design should be further optimised by studying the conduction and valence bands offset of other lattice-matched wide bandgap materials so as to further reduce the bulk leakage current. Besides that, wide bandgap materials which are not easily oxidised should be explored so that it does not need to be encapsulated by the InAs layer, which will reduce the quantum efficiency of the diode.

4.4   Passivation of InAs diodes

As discussed at the beginning of this chapter, the surface condition of an etched mesa diode is important to ensure low surface leakage current, especially in narrow bandgap semiconductor such as InAs. Besides a suitable etchant, surface passivation using an appropriate dielectric can be another important surface treatment that can prevent surface degradation that leads to surface leakage current. Ideally, the surface passivation should turn the semiconductor's etched surface into insulator-like material, which can completely eliminate the surface leakage current. A few commercially-used dielectrics such as silicon nitride (SiN_x), silicon dioxide (SiO_2) and B-staged Bisbenzocyclobutene (commonly referred to as BCB) were used to passivate InAs diodes but the results were not encouraging [7]. In fact, the surface was degraded and a much higher leakage current was observed in diodes which were passivated by SiN_x and SiO_2. BCB showed the best results among these passivation

dielectrics. A study on the different curing temperatures and time for BCB showed that the optimum condition for InAs diodes was at 300 ^{o}C for 1 minutes. However, the BCB passivated diodes did not show significantly lower dark current than the one which were not passivated [7].

Recently, the dark current density of the SU-8 passivated type-II InAs/GaSb strained layer superlattice detectors [8] was reported to reduce by 4 orders of magnitude at 77 K, compared to the unpassivated devices. SU-8 is a high contrast negative photoresist that is widely used for the fabrication of high aspect ratio MEMS devices and devices for optoelectronic applications [9]. It is designed to produce uniform thick films between 0.2 and 100 µm. SU-8 consists of bisphenol A novolac epoxy resin and a photoacid generator, which acts as the curing agent [9]. When SU-8 is exposed to UV, this curing agent generates a strong acid ($HCbF_6$) that causes the epoxy resin to form a solid structure with a high cross-linking density. This photo-polymerised SU-8 possesses good physical and chemical robustness. Furthermore, it is almost transparent to wavelengths > 350 nm, making it suitable for the passivation of infrared photodetectors [10].

Since it involves only spin-coating and UV exposure, the passivation technique using SU-8 can be incorporated easily into the fabrication process of InAs diodes. The passivation process also does not involve high temperature, which is crucial to avoid any possibility of contact diffusion and surface degradation. However, SU-8 has not been used as the surface passivation for InAs diodes. Therefore, SU-8 was used to passivate the InAs diodes in order to investigate the effectiveness of this dielectric material for surface passivation.

The freshly etched MR2558 InAs *n-i-p* sample was cleaved into two pieces, one acting as the reference sample and the other one was passivated using SU-8 5 using the steps listed below:-

   i.   Bake the sample for 1 minute at 100 ^{o}C to completely dehydrate the surface.

   ii. Spin SU-8 5 for 30 seconds at 3000 rpm to produce a film of ~ 5 µm, covering the whole sample. The thickness of the film can be varied by using

different spin speed, with thicker film at lower spin speed. The estimated film thickness can be referred to in [10].

iii.   Pre-bake the sample at 65 ^{o}C for 1 minute, followed by a soft bake at 95 ^{o}C for 3 minute. The baking time for different thicknesses of film can be found in [10].

iv.   Photolithography and UV expose the sample for ~ 50 seconds using mesa mask. Note that SU-8 is a negative photoresist, hence the area which is exposed to the UV will be hardened, whereas the unexposed area will be developed.

v.   Post-exposure bake at 65 ^{o}C for 1 minute, followed by another bake at 95 ^{o}C for 1 minute. The baking time for different thicknesses of film can be found in [10].

vi.   Develop the sample in SU-8 developer for 1 minute and rinse the sample with isopropyl alcohol.

The room temperature *I-V* of both the reference and passivated samples were measured and shown in figure 4.7 (a). Both samples show a very similar level of dark current at room temperature. As the temperature decreases to 77 K, there is a clear difference in dark current between these two samples, as shown in figure 4.7 (b). At low V_b, there is a reduction of ~ 2 orders of magnitude for the SU-8 passivated sample. At V_b > 15 V, the reduction in dark current for the SU-8 passivated sample is more obvious, approaching > 3 orders of magnitude. Therefore, there is a significant suppression of dark current, mainly from the surface leakage current, when the InAs diodes are passivated by SU-8.

The SU-8 can be hard baked to obtain a more durable structured film on the diodes. However, since SU-8 has very good mechanical properties, hard bake or high temperature curing is usually not required. It is recommended [10] that the hard bake temperature should be between 150 and 200 ^{o}C but the exact baking time is not specified. From the previous experience in fabricating InAs diodes, the surface can be degraded if the sample is exposed to high temperatures. Therefore, an additional SU-8 passivated sample was used to carry out the hard bake process at 150 ^{o}C for 20

minutes. The hard curing of SU-8 did not turn out well for the InAs diodes as they showed almost short-circuit like room temperature *I-V* immediately after the curing process. After ~ 24 hours, the surface settles down and it shows diode-like characteristics at room temperature but with a little higher dark current than the reference sample, as shown in figure 4.7 (a).
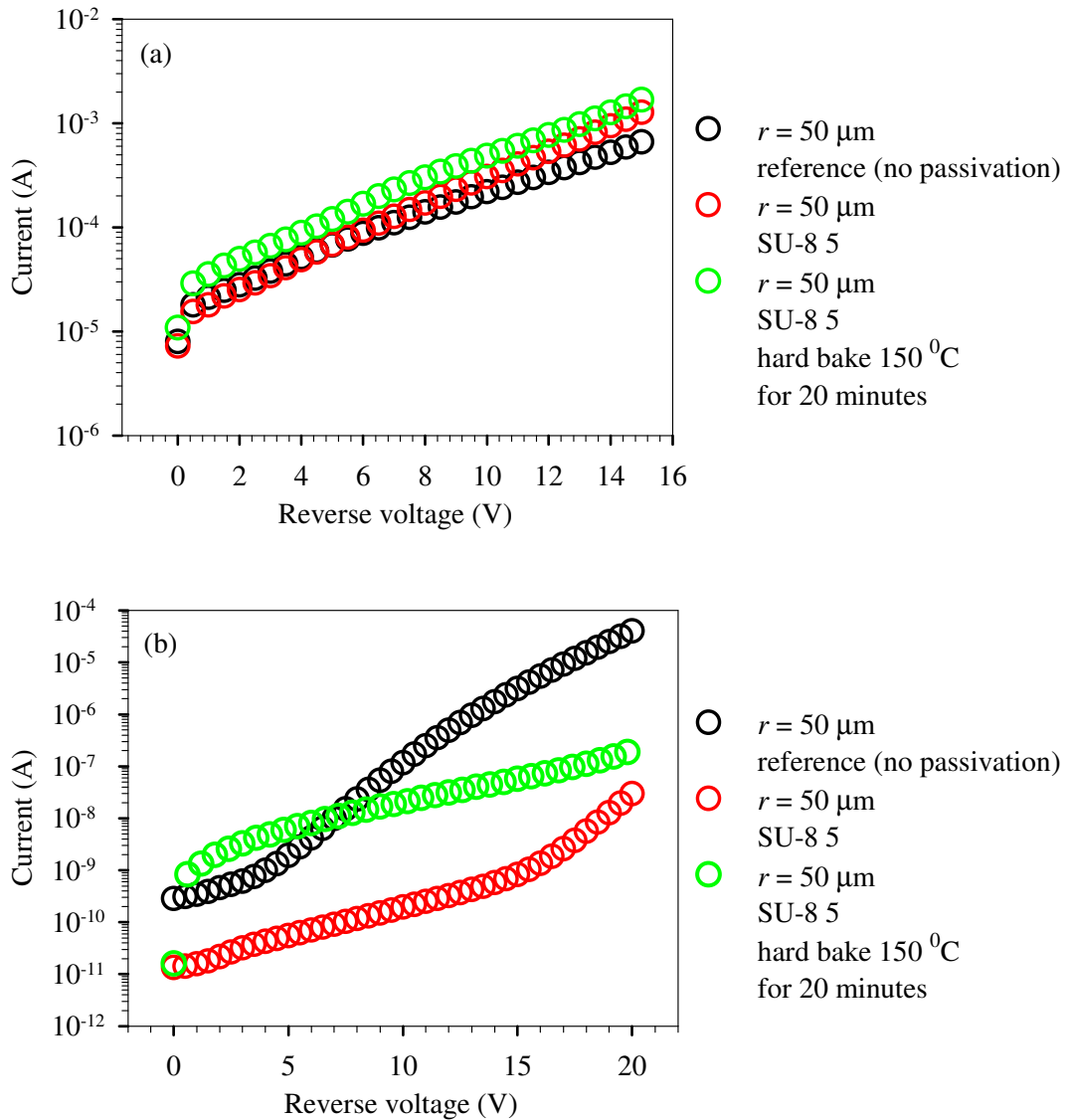

Figure 4.7 The *I-V* characteristic of the MR2558 reference diode with 50-µm radius compared with those passivated by SU-8 with and without hard bake at (a) room temperature and (b) 77 K.

The *I-V* measurement at 77 K revealed that the surface of the etched mesa was degraded by the hard bake or hard curing process. From figure 4.7 (b), the diodes show constantly higher leakage current than those which are not hard baked. At low V_b, the leakage current is even higher than the reference sample. Therefore, it is suggested that the hard curing process is not needed as it does not improve but degrade the etched mesa surface.
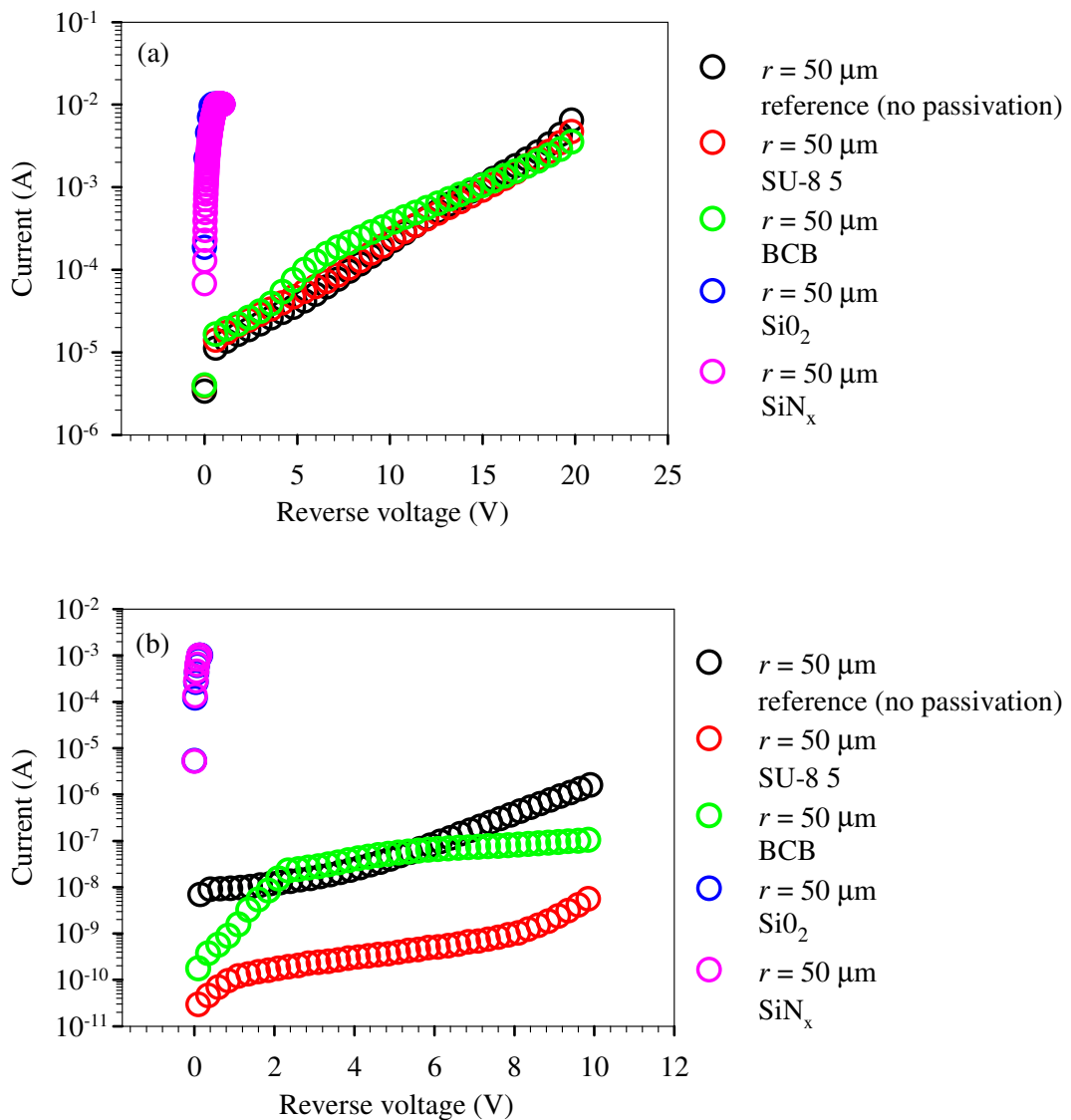

Figure 4.8 The *I-V* characteristic of a MR2560 50-µm radius reference sample, samples with SU-8, BCB, SiO_2 and SiN_x passivations at (a) room temperature and (b) 77 K.

To study and investigate the difference between all the four passivation dielectric materials, namely SiO_2, SiN_x, BCB and SU-8, one big sample from MR2560 was fabricated. To eliminate the possibility of surface degradation due to the fabrication and wet chemical etching, this sample was cleaved into 5 smaller samples just before the surface passivation was carried out. Each of them was passivated by SiO_2, SiN_x, BCB, SU-8 and the last one was left as reference sample. The processing steps for the surface passivation using BCB are detailed in Appendix F. Since they were all fabricated through exactly the same process before surface passivation, the difference in diodes' performance is mainly due to the different surface passivations.

The *I-V*s of all the samples were measured at room temperature and presented in figure 4.8 (a). The reference, SU-8 and BCB passivated samples show very similar leakage current levels at room temperature. The SiO_2 and SiN_x passivated samples have significantly high dark currents, similar to those reported previously [7].

The low temperature *I-V* characteristics were also investigated at 77 K. From figure 4.8 (b), the leakage current of the SiO_2 and SiN_x passivated samples is shown to be very high, reaching 10 mA within 0.5 V. The surface degradation due to these two passivations is so significant that the diodes have almost a conductor-like surface regardless of the operating temperature. At 0 V, the BCB and SU-8 passivated samples show a lower dark current than that of the reference sample. Unfortunately, the dark current of the BCB passivated diodes increases rapidly with increasing V_b, to a level close to that of the reference sample. SU-8 passivated diodes are still the ones with the highest performance, consistently having > 2 orders of magnitude lower dark current than the reference and BCB passivated samples.

Since the SU-8 passivated sample showed the lowest dark current, the *I-V* characteristic at a few temperatures between 77 K and room temperature was investigated. The reference sample was also measured concurrently and again used for comparison. The dark current of both samples were analysed by separating the bulk and surface leakage components. This was done using the equation [11]

$$I_{dark}(T,r) = \pi r^2 J_{bulk}(T) + 2\pi r J_{surf}(T) \qquad (4.1)$$

At each temperature, the total leakage current I_{dark}, of the InAs diodes with different r = 200, 100, 50 and 25 µm were measured. The bulk leakage component $J_{bulk}(T)$ in A/cm^2 and surface leakage component $J_{surf}(T)$ in A/cm were extracted using the fitting equation. The details on how to separate these two current components will be described in section 5.3. $J_{bulk}(T)$ and $J_{surf}(T)$ are plotted against the inverse of temperature, 1000/T, in figure 4.9.

$J_{bulk}(T)$ of both samples are very similar, as expected. This is because $J_{bulk}(T)$ should be highly dependent on the quality of the grown sample, and not on the fabrication and passivation process. Since they are from the same wafer, their values of $J_{bulk}(T)$ are comparable. The $J_{surf}(T)$ of the samples, on the other hand, become different as the temperature reduces from 295 to 77 K. At 295 K or room temperature, their $J_{surf}(T)$ are similar, hence showing almost equal I_{dark} as shown in figure 4.8 (a). As T decreases, the $J_{surf}(T)$ of the SU-8 passivated sample reduces at a quicker rate, as can be seen in figure 4.9, therefore producing I_{dark} which is ~ 2 orders of magnitude lower at 77 K.
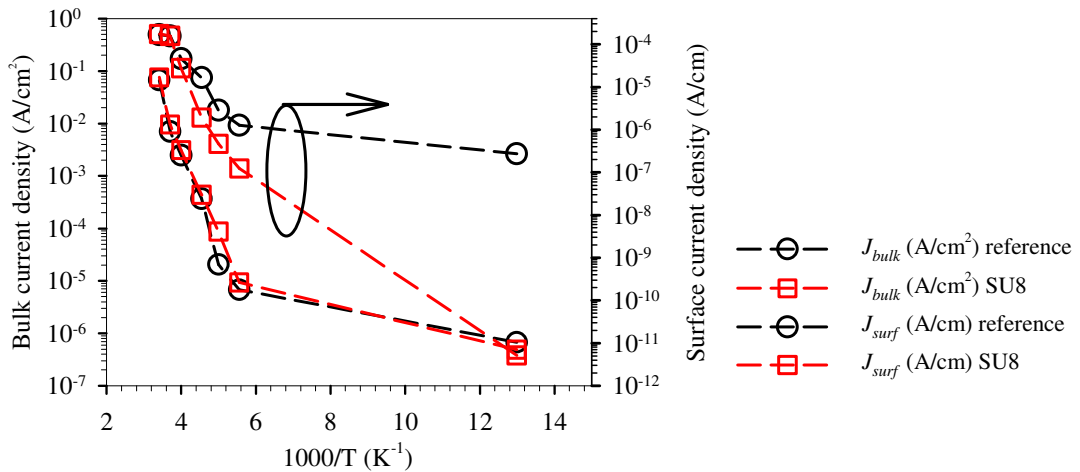

Figure 4.9 $J_{bulk}(T)$ and $J_{surf}(T)$ of the MR2560 reference and SU-8 passivated sample against 1000/T.

Besides having a lower dark current, the SU-8 passivated diodes are also more robust. They can be biased at higher V_b and can be measured several times without much surface degradation. This feature will be critical when the InAs diodes are used in practical applications where high gain and constant biasing of the diode are necessary.

From this study, the SU-8 dielectric has been identified as the most suitable dielectric for the surface passivation of InAs diodes, to date. UV curing of SU-8 which does not involve high temperature baking is proven to produce lower dark current than the InAs sample with SU-8 that is hard cured at 150 ^{o}C. The study of the bulk and surface current components versus temperature also clearly point out the effectiveness of SU-8 as a surface passivation dielectric that is able to reduce the surface leakage current. Furthermore, this passivation technique has also increased the robustness of the InAs APDs. This is especially crucial when higher reverse biasing is needed for high gain applications. Finally, it will be discussed later in section 4.5 that identifying the SU-8 as the passivation technique also serves as one of the important aspects in realising the fabrication of high speed InAs APDs.

4.5   Fabrication of high speed InAs APDs

The fabrication of high speed InAs APDs was made possible after identifying SU-8 as the most suitable dielectric material for etched mesa surface passivation. This is important as there is no semi-insulating substrate which is lattice-matched to InAs. Growing InAs diodes on lattice-mismatched substrate such as GaAs will inhibit high voltage operation of InAs diodes, causing huge difficulty in achieving APD operation. With this suitable dielectric, the GSG pads can therefore be deposited on the flat SU-8 film due to the lack of a lattice-matched semi-insulating substrate.

Before carrying out any device fabrication and frequency response measurement, a few experiments and calculations, such as contact resistance measurements using the TLM, *RC*-limited bandwidth calculation and transit time limited bandwidth calculation, were studied and investigated.

To achieve high speed operation, the limitation of bandwidth due to *RC* should be avoided by having a low contact resistance and junction capacitance. The *RC*-limited bandwidth is defined as

$$f_{RC} = \frac{1}{2\pi RC} \tag{4.2}$$

The diode junction capacitance can be calculated and estimated as discussed in section 3.2 using equation 3.7. However, the series resistance, which is mainly due to the contact resistance, cannot be computed in a straight forward manner. Therefore, the TLM is used to estimate the contact resistance.

4.5.1 Choice of metals for contacts

From previous InAs diode fabrication and measurements, it was found that the InAs *p*-contact has a different contact resistance from the *n*-contact, and the metal that is deposited should be chosen according to the lowest value of resistance without sacrificing the reverse leakage current characteristic. Besides the choice of metals, it should be noted that the doping concentration of the cladding layers that form the contact with the metal must be adequately high in order to minimise the contact resistance. In this aspect, all cladding layers of our InAs *p-i-n* and *n-i-p* structure wafers have doping concentrations $> 2 \times 10^{17}$ cm^{-3}, which is sufficient to produce a good ohmic contact for a narrow bandgap semiconductor.
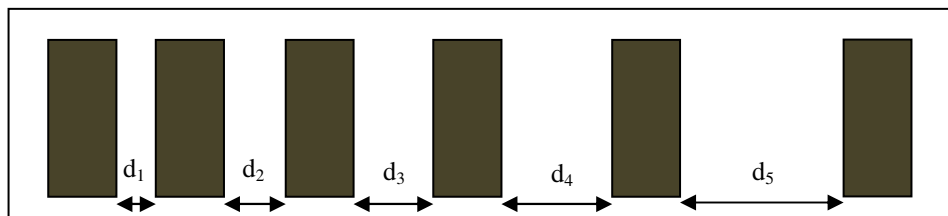

Figure 4.10 Contact resistance measurement using the TLM pads.

The TLM experiment was performed by depositing different metals on *p-* and *n*-layers on the 100×50 µm^2 TLM pads, as shown in figure 4.10. Ideally, an isolation etching should be done around the block of TLM pads to prevent leakage current from flowing through other additional paths. Then, the *I-V* between two TLM pads was measured for different distances (d_1, d_2, d_3, d_4, d_5).
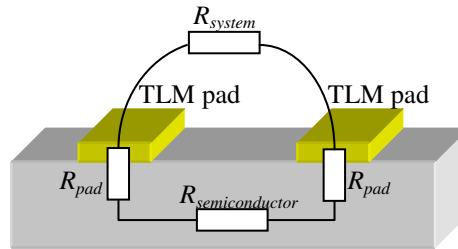

Figure 4.11 Different resistance components in the TLM measurement.
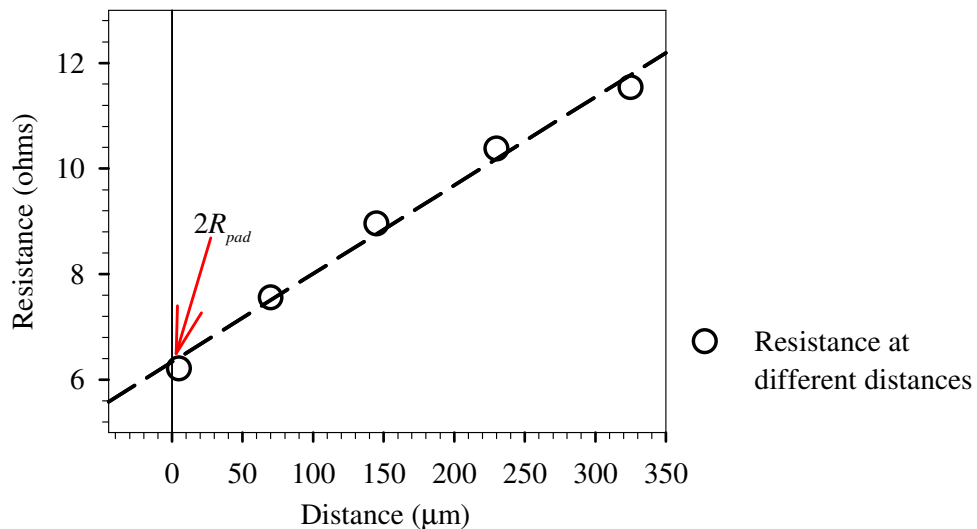
Figure 4.12 An example of *R* vs. d_t plot for a Ti/Au *n*-contact.

The set-up or system used for the *I-V* measurement needs to be calibrated in order to accurately calculate the contact resistance between the metal and semiconductor. To measure the system resistance R_{system} which includes the probes, cables and junction box, two probes were connected and the *I-V* was measured. The R_{system} was determined to be ~ 4.9 Ω. The resistances between two TLM pads $R_{measured}$ were

computed by dividing the voltage by the current. The total measured resistance between two pads can be written as

$$R_{measured} = 2R_{pad} + R_{semiconductor} + R_{system},\qquad(4.3)$$

where R_{pad} is the resistance between the TLM pad and the semiconductor, and $R_{semiconductor}$ is the resistance along the length of the semiconductor, as shown in figure 4.11.

An example of a plot of $R_{measured}$ vs. distance d_t based on the measurement of a Ti/Au n-contact is shown in figure 4.12. From the $R_{measured}$ vs. d_t plot and by extrapolating the graph to $d_t = 0$, that is with zero length of semiconductor, the $R_{measured}(d_t = 0) = 2R_{pad} + R_{system}$. Subtracting the R_{system}, R_{pad} can be obtained. Then the contact resistance-area product $R_{contact}A$, can be calculated by multiplying the R_{pad} by the area of each TLM pad. $R_{contact}$ for different sizes of device and contact area can then be computed.

A few different types of metals were used for both p- and n-contacts and the metals with the corresponding values of $R_{contact}A$ are listed in table 4.1 below.

Types of contact	Metal	Contact resistance-area product, $R_{contact}A$ (Ω/cm^2)
InAs p-contact	Au/Zn/Au	4.53×10^{-4} Ω-cm^2
	Ti/Au	3.73×10^{-4} Ω-cm^2
	Ti/Pt/Au	3.01×10^{-4} Ω-cm^2
InAs n-contact	InGe/Au	3.45×10^{-5} Ω-cm^2
	Ti/Au	3.48×10^{-5} Ω-cm^2
	Ti/Pt/Au	6.33×10^{-5} Ω-cm^2

Table 4.1 List of $R_{contact}A$ for p- and n-contacts with different metals.

To obtain a better ohmic contact with lower resistance, thermal annealing of the metal contact is always an option or alternative for high speed device fabrication. However, due to the narrow bandgap nature, InAs has quite a low contact resistance even without annealing. Thermal annealing however was done for experiment and observation purposes but it did not improve the contact resistance significantly. To make matters worse, the value of $R_{contact}$ was increased after annealing at a certain temperature. For instance, annealing the Ti/Pt/Au *p*-contact at 350 ^{o}C increased $R_{contact}$. This may be due to the enhanced out-diffusion of As atoms towards the metals, causing the formation of a TiAs/PtAs intermixing zone [12]. It was also shown in section 4.4, that baking the devices at 150 ^{o}C can degrade the performance of the InAs APDs. Thus, to prevent any surface degradation, to avoid any unnecessary metal diffusion from the contact into the semiconductor, and since annealing did not improve $R_{contact}$ significantly, thermal annealing of contacts was not carried out in the fabrication of high speed InAs APDs. Finally, from the data obtained through this TLM experiment, Ti/Pt/Au and Ti/Au were used for the *p*-contact and *n*-contact, respectively.

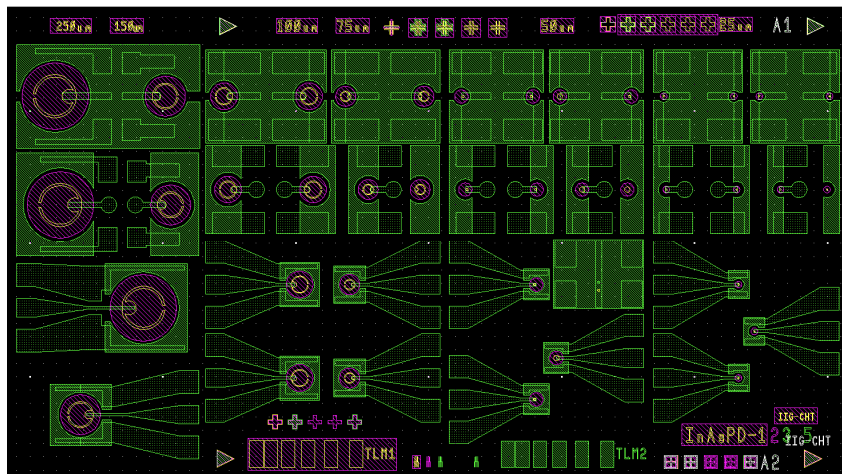### *4.5.2 Device fabrication and bondpad design*

Figure 4.13 Mask set design for high speed InAs APDs with different designs of GSG pads.

A new mask set was designed to fabricate the high speed InAs APDs, which could be measured and probed using a 50-GHz GSG probe. Before designing the mask set, a few experiments were carried out such as optimising the exposure time and baking time for SU-8 to develop into a thick, durable and hard planar film without sacrificing the yield of the smallest workable devices. Furthermore, investigating the effect of isotropic etching profiles of InAs diodes was proven to be significant because the sizes of the diodes became smaller as the etch depth went deeper. In addition, the isotropic etching profile was also dependent on the orientation of the wafer. This, if not properly designed, could cause the top contact to fall on the mesa sidewalls and the GSG tracks or pads not being able to make contact with the top and lower contacts. The experimental details and considerations regarding issues of the SU-8 exposure and baking time, and the isotropic etching profile were discussed with the aid of figures in Appendix G. Moreover, the *RC*-limited bandwidths of each size of devices were also calculated and estimated based on the values of *W* and $R_{contact}$.

The mask set consists of devices with diameters ranging from 25 to 250 µm. Since the *W* of the InAs diodes was large, contributing to lower *C*, a few larger size devices with *d* = 250 and 150 µm were included to investigate and demonstrate the *RC*-limited bandwidth. Besides that, GSG pads with different designs, as shown in figure 4.13, were included to investigate if there is any impedance mismatch between the 50-Ω measurement system and the GSG pads, and parasitic effects between the signal tracks and the conducting substrate.

Due to the long diffusion length of minority electrons in InAs, pure electron injection can be obtained even in diodes with an *n-i-p* structure, provided that the laser spot is accurately focused on the *p*-layer. Since most of the MOVPE grown *n-i-p* InAs diodes have a wider *W* than the *p-i-n* diodes due to thicker *i*-layer, the GSG pads for the *n-i-p* diodes have been designed to have a top metal cap, aiming to block the laser from falling onto the *n*- and *i*-layer. The design of the GSG pads for *p-i-n* and *n-i-p* diodes are shown in figure 4.14.
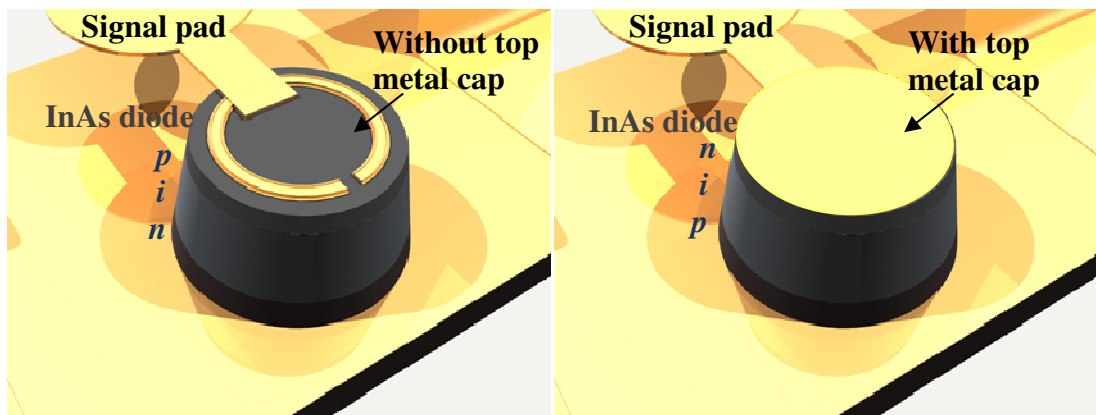
Figure 4.14 Design of high speed InAs *p-i-n* and *n-i-p* APDs to obtain pure electron injection. The metal cap on top of the *n-i-p* diode is to prevent light from falling onto the *n-* and *i*-layers.
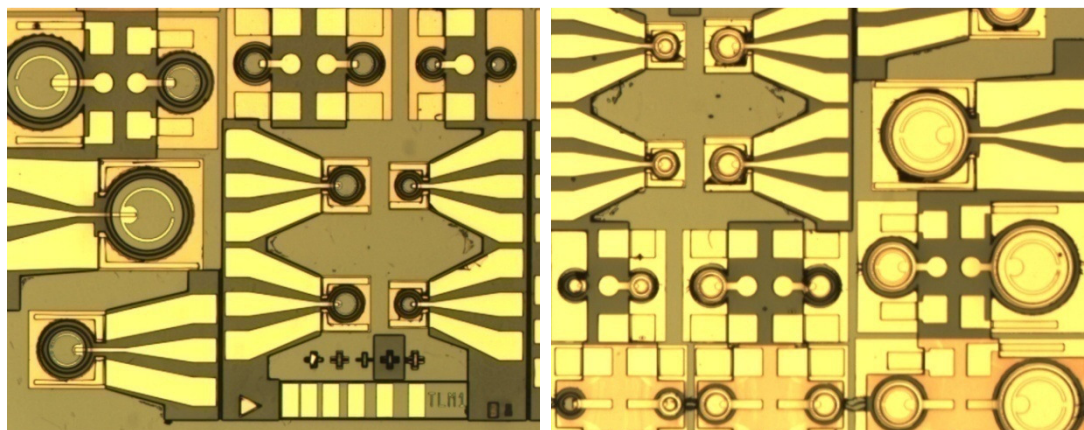
Figure 4.15 High speed InAs *p-i-n* APDs (left) and InAs *n-i-p* APDs (right) with top metal cap.

Using this newly designed high speed mask set, the InAs *p-i-n* (MR2538) and *n-i-p* (MR2558) APDs were fabricated using the metal contacts as mentioned in section 4.5.1. The etched mesa surface were passivated by ~ 10 µm thick SU-8 before depositing the GSG pads with 30/400 nm Ti/Au. The 10-µm thick SU-8 can cause problem to the deposition of GSG pads as the metals travel through the interception point between areas with and without SU-8. To overcome this problem, 2 coils containing Ti and 2 coils containing Au were used to enable the deposition of Ti and

Au from opposite directions. This problem can also be solved by depositing the GSG pads metals using a metal sputterer machine which will rotate the samples while sputtering metals. The pictures of the fully fabricated InAs *p-i-n* and *n-i-p* APDs are shown in figure 4.15.

The fabricated high speed devices were also inspected under the scanning electron microscopy (SEM). Figure 4.16 shows the overview and the cross section of a diode. It was observed that the GSG pads were able to extend through the 10-µm SU-8 slope and make contact with the lower contact. Furthermore, the SU-8, with the optimised UV exposure and baking time, was able to fully protect the etched mesa surface.

The room temperature *I-V* of the high speed InAs APDs was measured. The forward and reverse *I-V* characteristics of the diodes are shown in figure 4.17.
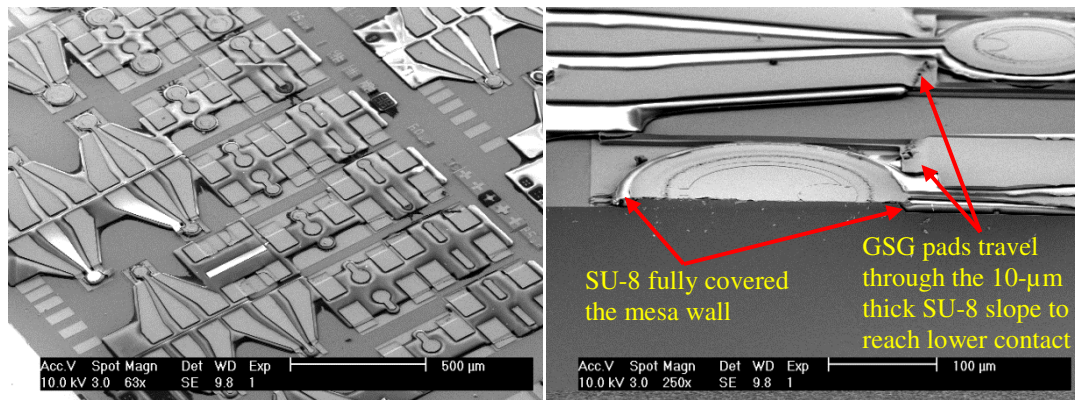
Figure 4.16 Top view (left) and cross section view (right) of the high speed InAs APDs under SEM.

For clarity, only forward *I-V*s of selected device sizes are shown in figure 4.17 (a). The forward *I-V* shows that the high speed diodes have higher series resistance than the NEWPIN diodes. For example, the 250-µm diameter high speed diode has a series resistance of 20 Ω, whereas a 50-µm radius NEWPIN diode has only 13 Ω. This can be attributed to two factors. Firstly, the lower metal contact of the high

speed diode has a smaller area contact, whereas the NEWPIN diode has a large-area lower contact on the *p*-substrate of the wafer. Secondly, the thin and long GSG pads deposited on the SU-8 can also contribute to the higher contact resistance.
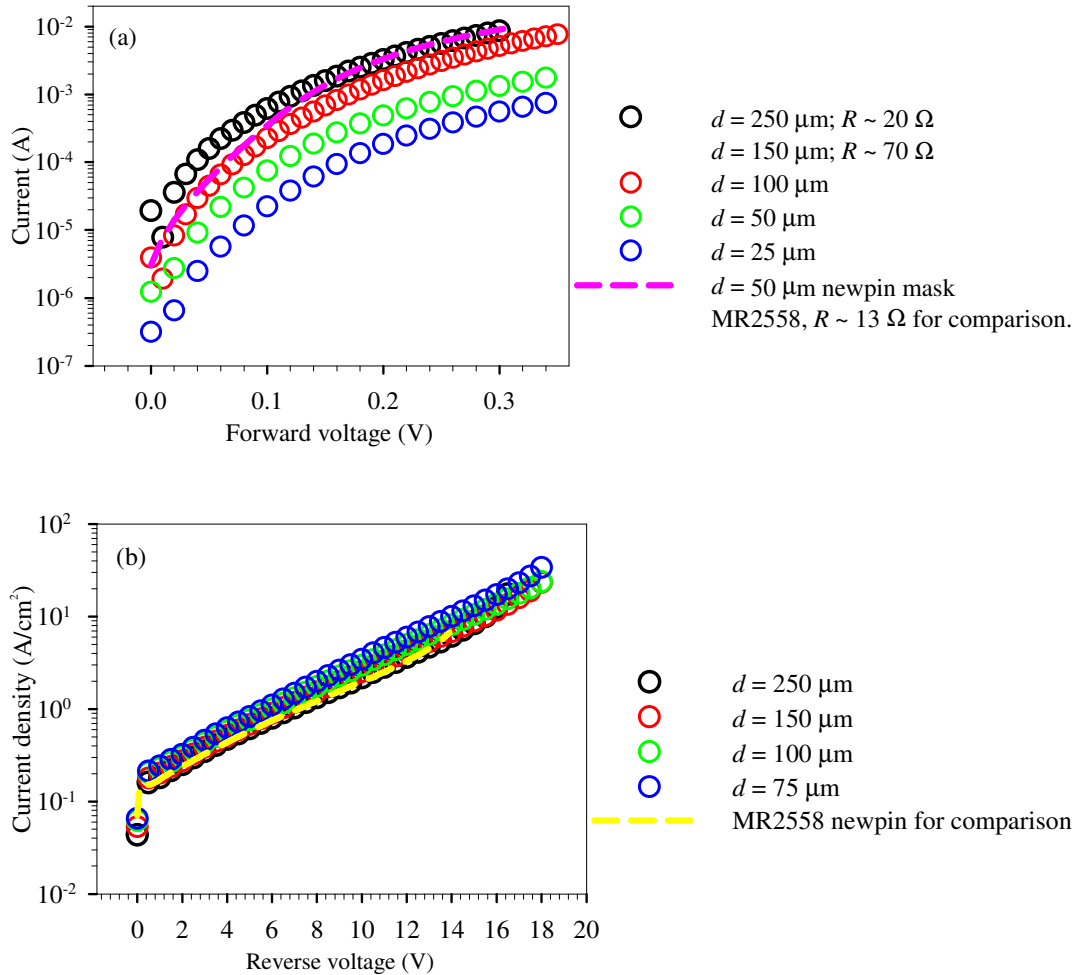
Figure 4.17 (a) The forward *I-V* characteristic and (b) the reverse current densities of the MR2558 high speed InAs APDs. The forward *I-V* and reverse current density of MR2558 diodes fabricated using NEWPIN mask is also shown for comparison.

The reverse leakage currents of the diodes with nominal diameters of 250, 150, 100, 75, 50 and 25 µm were all scaled with their area. Due to the isotropic etching profile, the diameters of these devices were effectively reduced by about 15 µm. The current densities of the diodes are plotted in figure 4.17 (b). It is clear that the high speed InAs APDs have very similar dark current densities to that of APDs fabricated using

the simpler NEWPIN mask. This has shown that the additional processing steps involved in the fabrication of high speed devices are well controlled such that the performance of the high speed APDs is not compromised at room temperature.

4.6   Temperature dependence of the spectral response

InAs is a III-V binary semiconductor compound which can provide good quantum efficiency up to the mid-infrared wavelengths. Other well established semiconductor technologies, such as Si, GaAs and InGaAs can be used for applications up to wavelengths of 1.7 µm. Therefore, InAs is a good candidate for applications which require detection at ≥ 2 µm. As temperature decreases, the leakage current of InAs APDs reduces. However, this is accompanied by an increase in E_g, causing the λ_c to decrease.

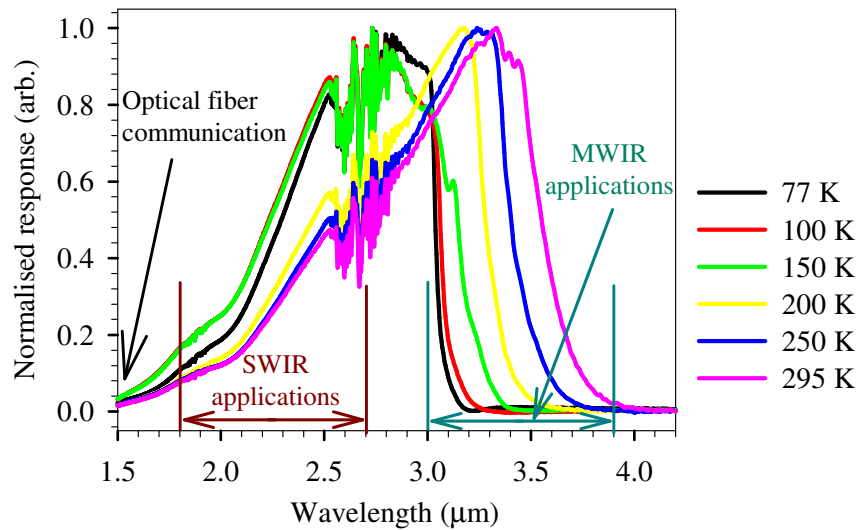Figure 4.18 The spectral responses of a homojunction InAs *n-i-p* diode at 77, 100, 150, 200, 250 and 295 K.

The temperature dependence of the spectral response was measured on a packaged homojunction InAs MR2775 *n-i-p* diode using the Fourier Transform Infrared Spectrometer (FTIR). The normalised spectral responses from 77 to 295 K are shown in figure 4.18. It is worth noting that the figure shows the peak-normalised response

in arbitrary unit. The FTIR set-up has a standard ceramic light source that is able to transmit radiation from 1.7 to 25 µm [14]. Therefore, it can be expected that for $\lambda <$ 2.0 µm, the radiation power is very low, resulting in very low response at 1.5 µm and this should not be regarded as the short wavelength cut-off. In section 5.6, it will be shown that the InAs diodes are able to provide ~ 50 % quantum efficiency even down to λ = 1.3 µm. However, this measurement is primarily aimed at investigating the long wavelength cut-off of the InAs diodes which are at $\lambda >$ 3 µm. The λ_c, which is taken at the 50 % of the peak response, at each temperature were determined from the spectral responses. These values were compared with the reported equation of the temperature dependence of the InAs bandgap energy, $E_g(T)$, by Fang *et al*. [13]

$$E_g(T) = 0.415 - \left[\frac{2.76 \times 10^{-4}\ T^2}{T + 83} \right] \tag{4.4}$$

The comparison between the measured λ_c and the $\lambda_c = E_g/1.24$ calculated from the equation are presented in table 4.2. The measured and calculated λ_c show good agreement and λ_c ranges from 3 to 3.55 µm as T increases from 77 to 295 K.

Temperature (K)	50 % λ_c (µm)	Reported λ_c (µm)
77	3.036	3.065
100	3.061	3.103
150	3.146	3.195
200	3.279	3.300
250	3.402	3.416
295	3.552	3.530

Table 4.2 Comparison between the 50% λ_c observed from the spectral responses and the λ_c calculated from $E_g(T)$ by Fang *et al*. [13].

References

[1]   A. R. J. Marshall, C. H. Tan, J. P. R. David, J. S. Ng, and M. Hopkinson, "Fabrication of InAs photodiodes with reduced surface leakage current," in *Proc. SPIE Optical Materials in Defence Systems Technology IV*, Florence, Italy, 2007, pp. 67400H-9.

[2]   D. C. Tsui, "Observation of Surface Bound State and Two-Dimensional Energy Band by Electron Tunneling," *Phys. Rev. Lett.,* vol. 24, pp. 303-306, 1970.

[3]   L. F. J. Piper, T. D. Veal, M. J. Lowe, and C. F. McConville, "Electron depletion at InAs free surfaces: Doping-induced acceptorlike gap states," *Phys. Rev. B,* vol. 73, p. 195321, 2006.

[4]   P. J. Ker, A. R. J. Marshall, A. B. Krysa, J. P. R. David, and C. H. Tan, "Temperature Dependence of Leakage Current in InAs Avalanche Photodiodes," *IEEE J. Quantum Electron.,* vol. 47, pp. 1123-1128, 2011.

[5]   A. R. J. Marshall, P. Vines, P. J. Ker, J. P. R. David, and C. H. Tan, "Avalanche Multiplication and Excess Noise in InAs Electron Avalanche Photodiodes at 77 K," *IEEE J. Quantum Electron.,* vol. 47, pp. 858-864, 2011.

[6]   T. A. a. C. T. Elliott, "Operation and properties of narrow-gap semiconductor devices near room temperature using non-equilibrium techniques," *Semicond. Sci. Technol.,* vol. 6, p. C99, 1991.

[7]   A. R. J. Marshall, "PhD Thesis: The InAs electron avalanche photodiode and the influence of thin avalanche photodiodes on receiver sensitivity," in *Electronic & Electrical Engineering*: The University of Sheffield, 2009.

[8]   H. S. Kim, E. Plis, A. Khoshakhlagh, S. Myers, N. Gautam, Y. D. Sharma, L. R. Dawson, S. Krishna, S. J. Lee, and S. K. Noh, "Performance improvement of InAs/GaSb strained layer superlattice detectors by reducing surface leakage currents with SU-8 passivation," *Appl. Phys. Lett.,* vol. 96, pp. 033502-3, 2010.

[9]   M. Shaw, D. Nawrocki, R. Hurditch, and D. Johnson, "Improving the process capability of SU-8," *Microsystem Technol.,* vol. 10, pp. 1-6, 2003.

[10]   Microchem, "NANO^{TM} SU-8 Negative tone photoresist formulations 2-25 datasheet."

[11]   X. G. Zheng, J. S. Hsu, J. B. Hurst, X. Li, S. Wang, X. Sun, A. L. Holmes, Jr., J. C. Campbell, A. S. Huntington, and L. A. Coldren, "Long-wavelength In$_{0.53}$Ga$_{0.47}$As–In$_{0.52}$Al$_{0.48}$As large-area avalanche photodiodes and arrays," *IEEE J. Quantum Electron.,* vol. 40, pp. 1068-1073, 2004.

[12]   G. Stareev, "Formation of extremely low resistance Ti/Pt/Au ohmic contacts to p-GaAs," *Appl. Phys. Lett.,* vol. 62, pp. 2801-2803, 1993.

[13]   Z. M. Fang, K. Y. Ma, D. H. Jaw, R. M. Cohen, and G. B. Stringfellow, "Photoluminescence of InSb, InAs, and InAsSb grown by organometallic vapor phase epitaxy," *J. Appl. Phys.,* vol. 67, pp. 7034-7039, 1990.

[14]   "Varian 7000/7000e FT-IR spectrometers operational / hardware manual", Varian Australia Pty Ltd., March 2005.

Chapter 5 Temperature dependence of leakage current in InAs APDs

5.1   Introduction

In chapter 1, it has been discussed that InAs, with E_g = 0.36 eV, can be utilised in active imaging [1], gas sensing [2], free space communications [3] and satellite based environmental monitoring [4]. In these applications, the photon flux can be low and amplification of the signal is necessary. However external amplification can degrade the overall SNR especially when high gain at high frequency is required. Commercially available amplifiers that can provide high gain at high bandwidth with very low noise are unfortunately limited and expensive.

APDs can circumvent this problem since their internal gain mechanism can significantly improve the overall system sensitivity. For instance, HgCdTe APDs have been incorporated into FPAs to facilitate long range high sensitivity active imaging [1]. In chapter 1, we have reviewed that both HgCdTe and InAs APDs possess the ideal APDs characteristics of $k = 0$ with very low F. However, due to the narrow bandgap of InAs, InAs photodiodes exhibit higher room temperature dark current than photodiodes made from wider bandgap materials such as InGaAs. Consequently, to achieve the same dark current density as in InGaAs photodiodes, cooling is necessary. An additional challenge in InAs photodiodes is the difficulty in suppressing the surface leakage current [5]. Hence there is a need to understand the significance of both the surface and bulk leakage currents as a function of temperature.

Section 1.5 revisited a few fabrication and dark current analysis of InAs photodiodes by Lin *et al.* [6, 7]. However, the operating voltage of the InAs photodiodes is still

limited below 0.5 V. A detailed study on the dependence of surface and bulk leakage currents on high reverse bias and the dependence of these leakage current components on temperature have only been reported by this work [8].

In this chapter, we discuss a systematic study and analysis of the leakage current in MR2558 InAs APD as a function of temperature. The InAs APDs have a nominal 6 µm intrinsic layer, as well as a 1.5 µm *n-* and 3.5 µm *p*-cladding layers. These 11-µm thick structures impose stringent requirements on the fabrication and processing of the APDs. The surface of the mesa was sufficiently passivated by SU-8 to suppress the surface leakage current and ensure bulk dominated leakage current at room temperature. The dark current analysis encompassed a wide temperature range from 77 to 290 K. Analysis of the bulk and surface current components enables the extraction of activation energies. To obtain a desired dark current density for a specific application, the required operating voltage, operating temperature and the area of an InAs APD can also be determined from this analysis. The avalanche gain, responsivity and detectivity of the InAs APDs will also be discussed.

5.2   Temperature dependence of the leakage current

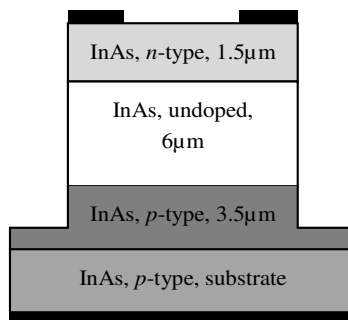Figure 5.1 Schematic cross section view of the MR2558 InAs *n-i-p* diode structure.

The MR2558 InAs *n-i-p* structure was grown on a *p*-type doped InAs substrate using MOVPE at a growth temperature of 600 °C. A schematic cross section view of the diode structure is shown in figure 5.1. The *p-* and *n*-type dopants were Zn and Si respectively. The details of this wafer can be found in Appendix A1. The fabrication

of circular mesa photodiodes, with 205, 105, 55 and 30-µm radii, was carried out as described in section 4.2. Since the SU-8 has been identified as the best surface passivation for InAs diodes to date, the etched mesa walls were passivated by depositing a layer of SU-8 [9]. The passivation technique and procedures have been explained in section 4.4. Due to the high room temperature leakage current at large reverse biases, the device capacitance was measured at 77 K and it confirmed that doping concentrations > 5×10^{17} cm^{-3} were obtained in both the *n-* and *p*-type cladding layers and unintentional doping concentrations varying between 7×10^{14} and 2×10^{15} cm^{-3} were obtained in the *i*-layer. Depletion widths up to 4.5 µm were achieved within the bias range reported.
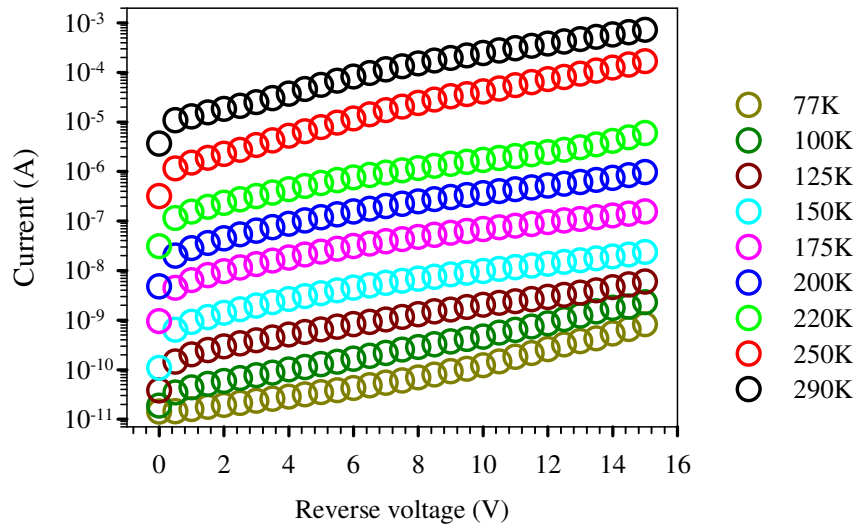

Figure 5.2 Reverse dark currents of the MR2558 InAs *n-i-p* diodes with *r* = 55 µm.

The forward and reverse *I-V* measurements were performed at *T* = 77 to 290 K using the Janis ST-500 series low temperature on-wafer probe station as described in section 3.7. At each temperature, all the 205, 105, 55 and 30-µm radii devices were tested and the data were recorded. The dark currents for photodiodes with *r* = 55 µm are shown in figure 5.2. Clearly, the surface leakage current is sufficiently suppressed that the reverse leakage current decreases with decreasing temperatures. The Ti/Au metal formed good contact with all of the InAs photodiodes since the series resistances for all sizes of the photodiodes were found to be between 5 and 12

Ω at room temperature. The ideality factor is ~ 1.1, suggesting relatively good quality *n-i-p* junctions.

To investigate and analyse the temperature dependence of the total leakage currents, dark currents at 0.3 V, prior to the onset of avalanche gain, were plotted against 1000/*T*. The temperature dependence of the dark current was modelled using the following current expressions

$$I_1 = A exp\left[\frac{-E_g(T)}{2k_B T}\right],$$ (5.1)

$$I_2 = B exp\left[\frac{-E_g(T)}{k_B T}\right],$$ (5.2)

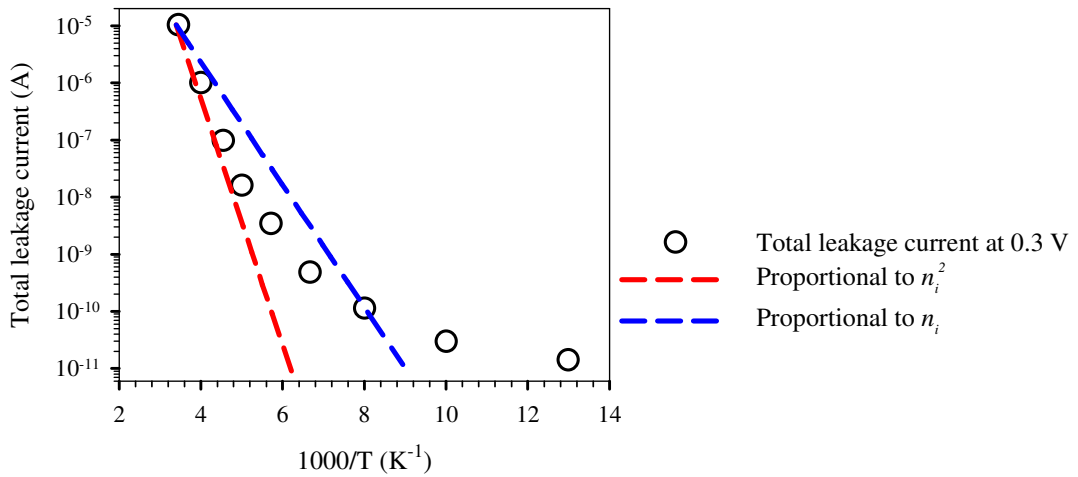where *A* and *B* are adjustable constants, and $E_g(T)$ is the temperature dependent bandgap of InAs [10].

Figure 5.3 The fittings of I_1 and I_2 to the temperature dependent total leakage current of a diode with *r* = 55 µm at 0.3 V.

Since the intrinsic carrier concentration is given by

$$n_i \propto exp\left[\frac{-E_g(T)}{2k_BT}\right], \tag{5.3}$$

I_1 and I_2 are proportional to n_i and n_i^2, respectively. Both I_1 and I_2 were used to fit the total leakage current across the range T = 77 to 290 K. However, we were unable to achieve a satisfactory fit using a single expression from I_1 or I_2. Figure 5.3 shows the fittings of I_1 and I_2 to the total leakage current of a diode with r = 55 µm at 0.3 V.

5.3   Dark current analysis

Since the total leakage current consists of the bulk and surface leakage current components, further analysis of the dark current was carried out by separating the total leakage current into J_{bulk} and J_{surf} across the range of applied bias from 0 to 15 V [11]. The dark currents at a fixed voltage for photodiodes with different radii were fitted with equation 4.1 [11].
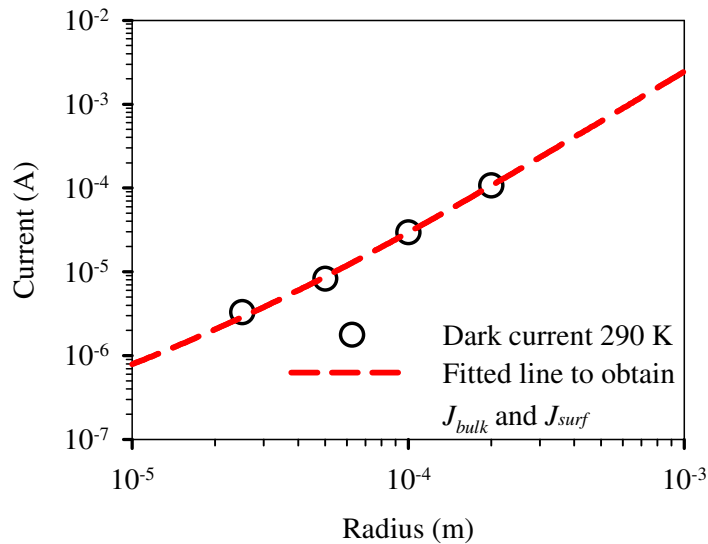

Figure 5.4 An example on how to extract J_{bulk} and J_{surf} using the fitting technique at T = 290 K and V_b = 0.3 V.

The measured *I-V* data from diodes with r = 30 to 205 µm at T = 77 to 290 K were used as the input parameters for an algorithm that searches for the best combination

of the $J_{bulk}(T)$ and $J_{surf}(T)$ to fit the measured $I(T)$. An example of the fitting is shown in figure 5.4 at $T = 290$ K and $V_b = 0.3$ V, with the fitted $J_{bulk} = 96$ mA/cm^2 and $J_{surf} = 46$ µA/cm.
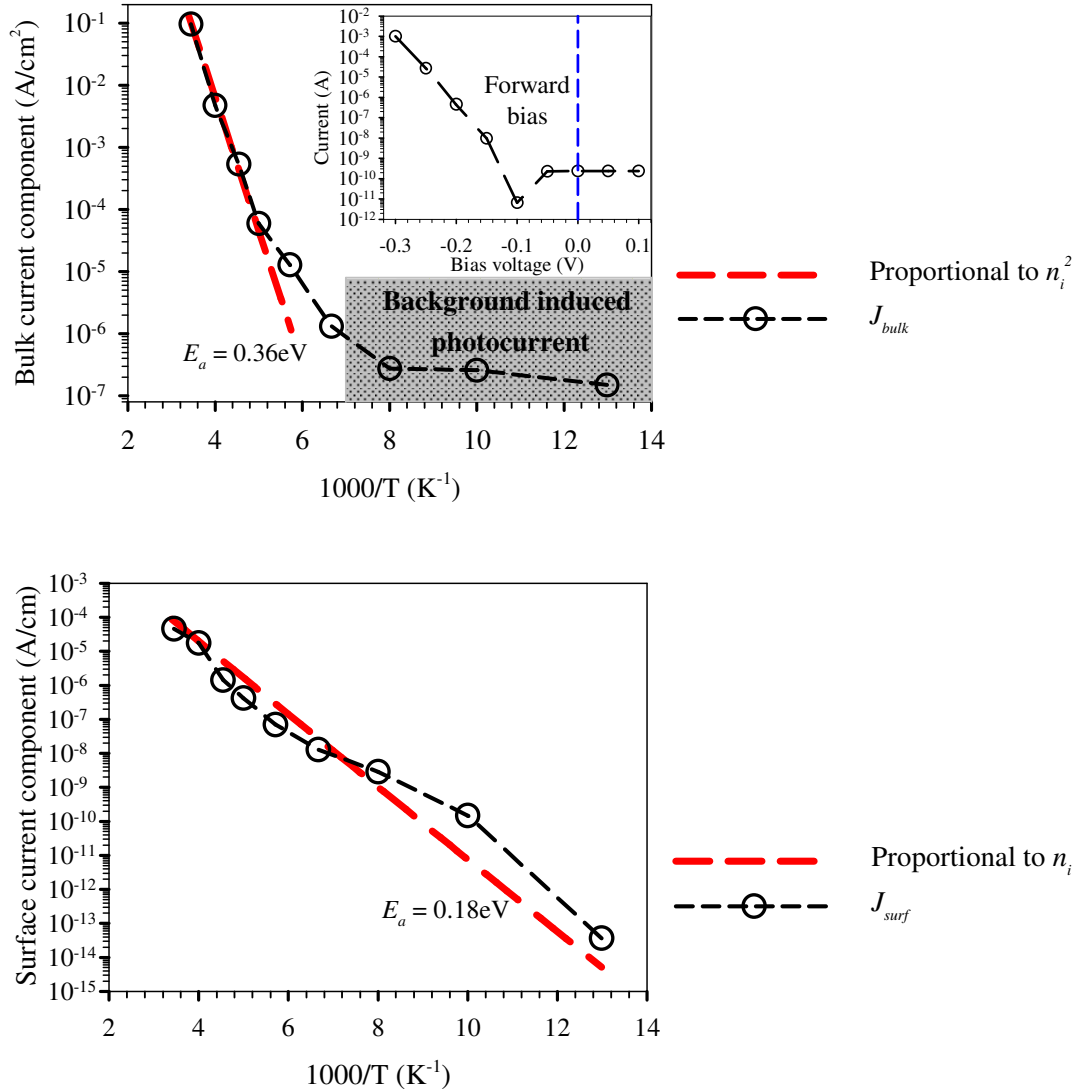

Figure 5.5 Comparison between the area normalised bulk current J_{bulk} (top) and the perimeter normalised surface current J_{surf} (bottom) with modelled components proportional to n_i^2 and n_i. The inset shows the forward I-V at 77 K with the background-induced photocurrent.

J_{bulk} and J_{surf} at 0.3 V were then plotted against 1000/T in figure 5.5. It is clear that

J_{bulk} is well modelled by I_2 for the temperatures between 200 and 290 K, whereas J_{surf} can be fitted by I_1 for the entire temperature range measured. Therefore, J_{bulk} is proportional to n_i^2 while J_{surf} is well described by n_i. $E_A = 0.36$ eV for J_{bulk} and $E_A = 0.18$ eV for J_{surf} were calculated using the Arrhenius equation, as discussed in section 3.7.

Figure 5.5 shows that the bulk component is proportional to n_i^2 for temperatures $\geq$ 200 K, indicating that J_{bulk} is dominated by the diffusion of carriers from the cladding layers. It is worth noting that the J_{bulk} saturates at $T < 125$ K while J_{surf} continues to decrease with decreasing temperature. Closer inspection of the forward *I-V* below 125 K, as in the inset of figure 5.5, shows that this saturated J_{bulk} is due to the background-induced photocurrent owing to insufficient shielding. On the other hand, J_{surf} is directly proportional to n_i for the entire temperature range reported indicating that the surface current is due to generation and recombination at the surface. The value of $E_A = 0.18$ eV, which is one-half of the bandgap energy, indicates that there are energy states or energy traps in the mid-bandgap energy level which act as generation and recombination centres along the etched mesa surface [12].
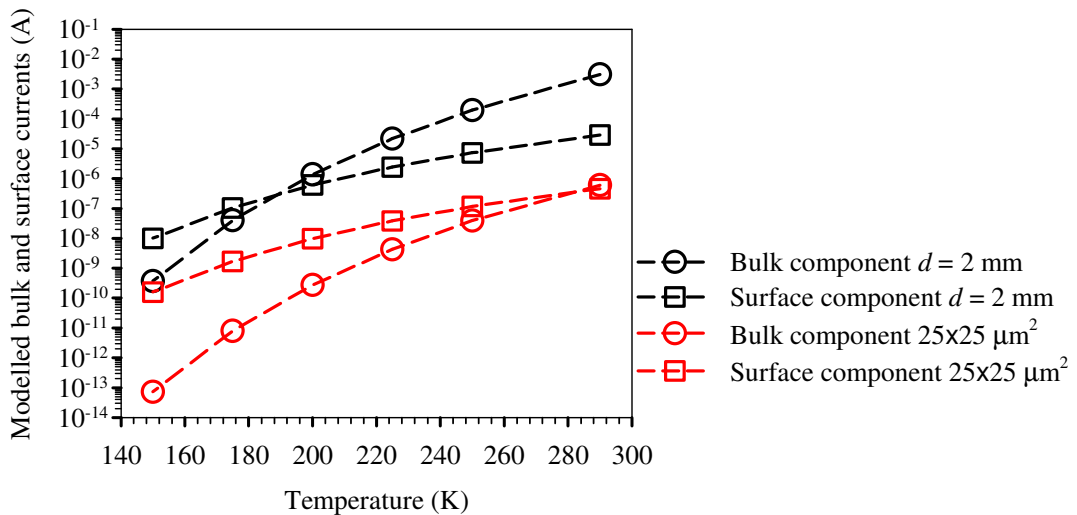

Figure 5.6 Modelled bulk and surface leakage currents of a 2 mm-diameter device and a 25×25 µm^2 pixel in the absence of the background induced photocurrent from 150 to 290 K.

To estimate the significance of J_{bulk} and J_{surf} in devices with different dimensions, the bulk leakage currents and surface leakage currents for a large area 2 mm-diameter device and a small 25×25 µm^2 device were modelled using I_1 and I_2 in the absence of the background induced photocurrent. The large area photodetector would be of interest for light detection and ranging (LIDAR) and gas sensing purposes while the small 25×25 µm^2 device corresponds to a typical pixel dimension in imaging FPAs. From figure 5.6, it can be seen that in the 2 mm-diameter device, the bulk leakage current dominates over the surface leakage current at $T > 200$ K. However, surface leakage current is more significant for a small pixel indicating that more effort is needed to reduce the surface current component if the InAs APD is targeted for FPAs.

5.4   Dark current comparison
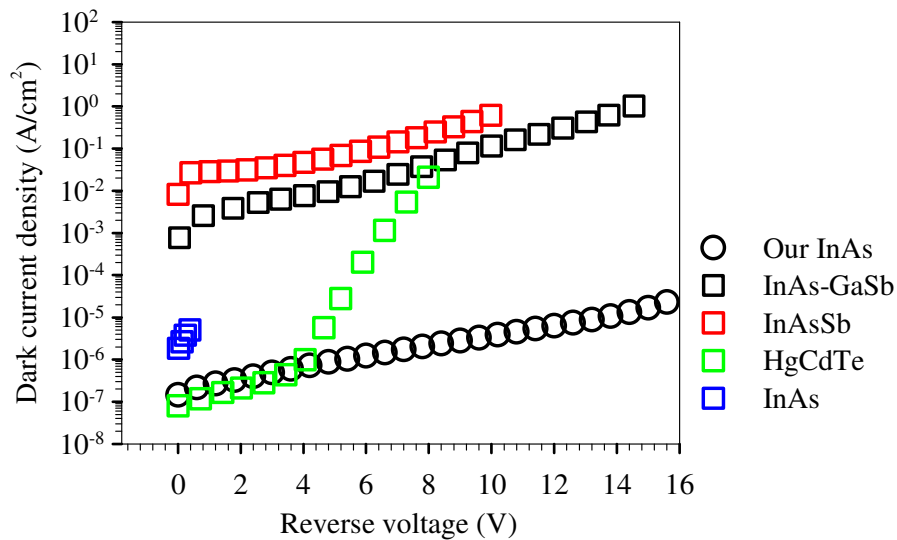
Figure 5.7 Reverse dark current densities reported by Ghosh *et al*. for InAs/GaSb APDs ($\lambda_c = 4.14$ µm at 77 K) [13], InAs$_{0.89}$Sb$_{0.11}$ photodetectors by Gao *et al*. ($\lambda_c = 4.64$ µm at 295 K) [14], HgCdTe APDs by Rothman *et al*. ($\lambda_c = 4.8$ µm at 77 K) [15], and InAs photodiodes by Lin *et al*. [7], compared with the result reported here for an InAs APDs at 77 K.

In this section, the leakage current of the InAs APDs are evaluated by comparing

them to other reported results. To facilitate the comparison, the current densities for all the APDs were calculated using the total leakage currents and the device areas. In figure 5.7, the dark current density comparison at 77 K shows that the InAs diodes have much lower dark current than other competing technologies, except the HgCdTe APDs. However, at $V_b > 4$ V, it is clear that the tunnelling current of our InAs APDs is better suppressed than that of the HgCdTe APDs. This is because the HgCdTe APDs have a $W \sim 0.5$ µm while our InAs APDs are designed to have $W > 3$ µm so that E is much lower.
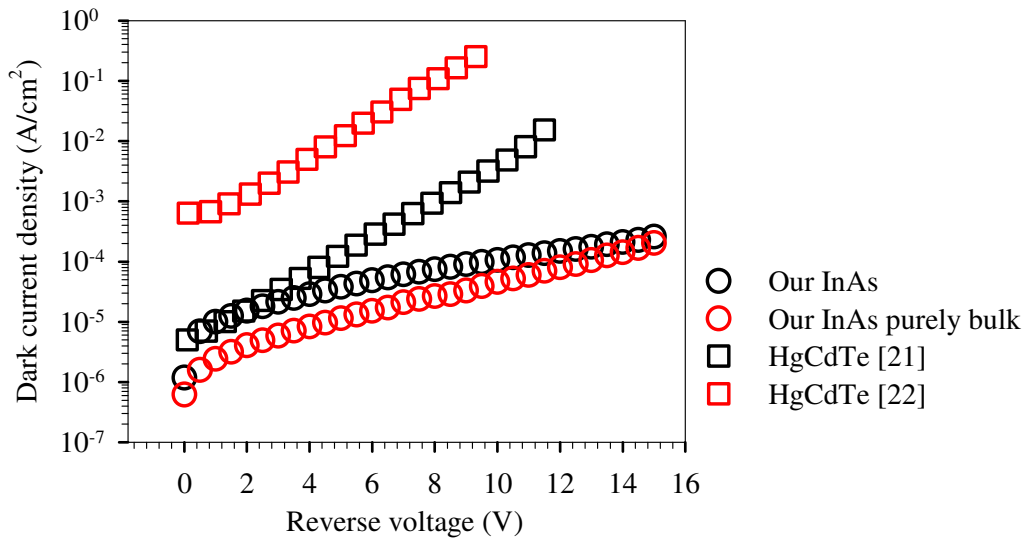
Figure 5.8 Reverse dark current densities reported by Reine *et al*. ($\lambda_c = 4.06$ µm at 160 K) [16] and Perrais *et al*. ($\lambda_c = 5$ µm at 77 K) [17] for planar MWIR HgCdTe APDs, compared with the result reported here for an InAs APD and the extracted InAs APD purely bulk current density at 150 K.

Figure 5.8 compares the dark current densities calculated for the InAs APDs reported here at 150 K with the MWIR planar HgCdTe APDs from Reine *et al*. at 160 K and Perrais *et al*. at 150 K. These APDs have $\lambda_c = 4.06$ µm and $\lambda_c = 5$ µm at temperatures of 160 and 77 K respectively. It is clear that the dark current density of the mesa-etched InAs APD is lower than that from Perrais *et al.* and is comparable to that of the planar MWIR HgCdTe APD from Reine *et al*. at $V_b < 4$ V. At higher V_b, the InAs APDs showed significantly lower leakage. Moreover, the pure bulk current density

extracted from our result is lower still, indicating that planar InAs APDs, fabricated either by ion implantation or diffusion of dopants, could potentially yield lower dark current by eliminating the surface current component.
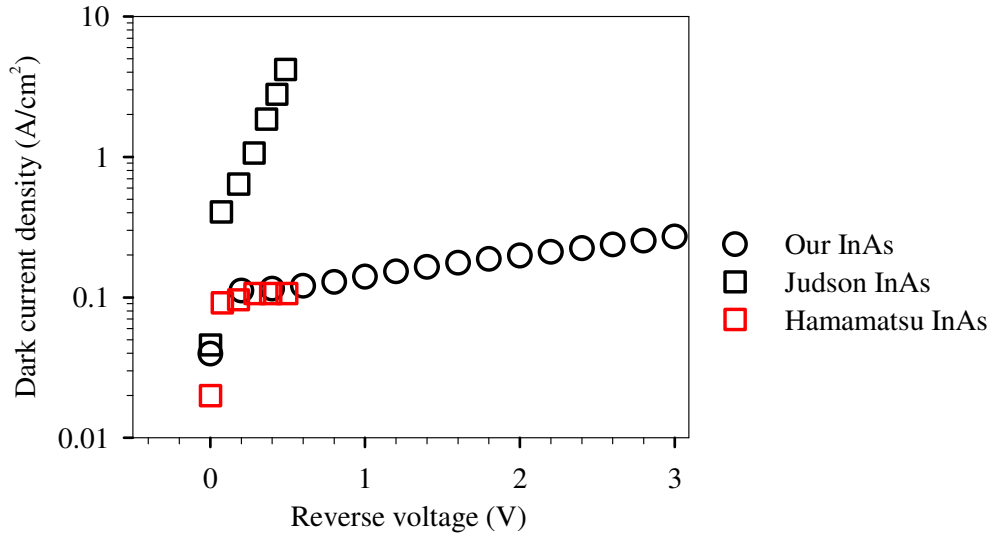
Figure 5.9 Reverse dark current densities of the commercial InAs photodiodes from Judson [18] and Hamamatsu [19], compared with the result reported here for an InAs APD at room temperature.

The dark current density of our InAs diodes is plotted together with those from other commercial Judson and Hamamatsu InAs photodiodes in figure 5.9. Both the commercial photodiodes have $V_b < 0.5$ V, suggesting high leakage current at higher V_b. On the contrary, our InAs diodes have the advantage of having low dark current even at higher V_b up to 20 V to provide avalanche gain. Even at low V_b, our InAs diodes have much lower dark current density than the Judson InAs photodiodes while having comparable dark current to the Hamamatsu InAs photodiodes.

5.5   Avalanche gain and dynamic resistance-area product

With our improved growth, fabrication and passivation techniques, the leakage current of the InAs APDs has been well suppressed. The band-to-band tunnelling current was not observed at $V_b < 15$ V at all temperatures due to the low

unintentional background doping of $\sim 7 \times 10^{14}$ cm^{-3} and hence low peak electric field. This has allowed the avalanche gain of the InAs e-APDs to be measured up to high V_b.

Figure 5.10 shows the avalanche gains and the gain-normalised dark current densities of the InAs APDs at 290 and 77 K. A predominantly electron injection profile was obtained by focusing a 633-nm laser onto the *p*-layer. The position of the laser spot was optimised to obtain the maximum avalanche gain. However there was a small amount of unintentional hole injection through the absorption at the mesa side walls. Despite the contamination of hole injection which decreases the avalanche gain, the InAs e-APD can provide a useful gain of 25 at 13 V and 19.5 V, at 290 and 77 K respectively. The measurement was also checked using 3 different incident light powers ranging between 10 and 100 µW to ensure that there is no heating effect which can cause the avalanche gain to vary.

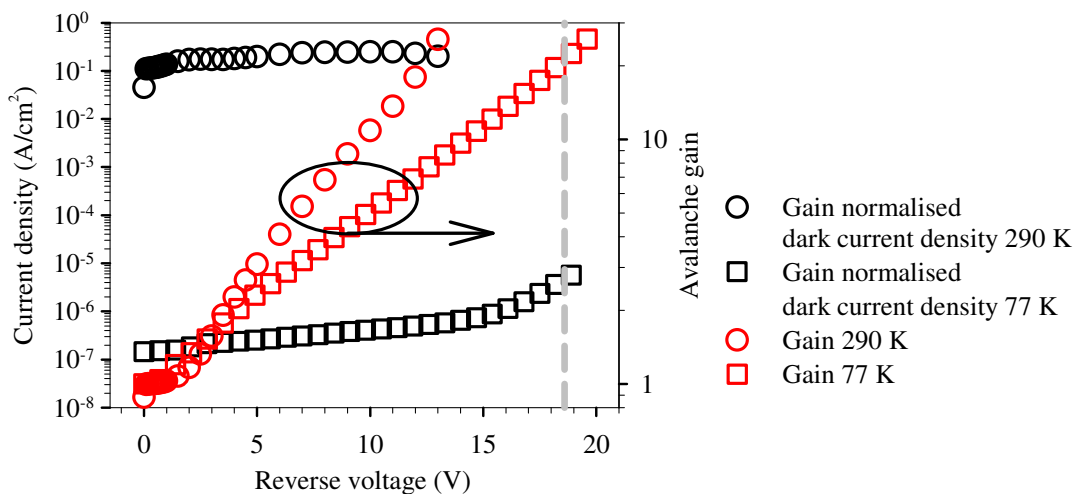Figure 5.10 Avalanche gain and the gain-normalised dark current densities at 290 and 77 K.

The temperature dependent dark current discussed in section 5.2 and the avalanche gain characteristics presented here, show that lowering the operating temperature of these InAs APDs to 77 K can reduce the leakage current substantially. However, this is accompanied by an undesirable reduction in the avalanche gain at a given V_b [20],

as evident in figure 5.10. At 77 K, although the bulk diffusion and surface generation current components were suppressed at low V_b, the total leakage current was dominated by the band-to-band tunnelling above 15 V. However, M as high as 22 can still be obtained at 18.6 V when a gain-normalised dark current density of ~ 5×10^{-6} A/cm^2 was assumed to be the maximum acceptable value. The peak electric field was calculated to be ~ 60 kV/cm at 15 V [20]. To further reduce the tunnelling current, lower *i*-layer background doping is necessary to reduce the peak electric field. A lower background doping will also yield wider W and therefore higher M at a given V_b [21].

Another parameter which is closely related to the performance and quality of an APD is the dynamic resistance-area product $R_dA = (dV_b/dJ_A)$ at a specific V_b, where J_A is the leakage current density and R_d is the dynamic resistance. From 0.1 to 15 V, the R_dA of our InAs APD was calculated to be between 34 and 0.6 Ω-cm^2 at room temperature. At 77 K, these values increased to 910 MΩ-cm^2 and 172 kΩ-cm^2.

R_dA of an APD is important when the APD is interfaced with other circuitry in a system. For instance, most of the commercially available readout integrated circuits (ROICs) for FPAs require a minimum R_DA of 1 kΩ-cm^2. The R_dA of an APD is mainly dependent on the rate of change of dark current with respect to V_b. From figure 5.2, it is shown that the total dark currents increase gradually with increasing V_b at each temperature. From 0.1 to 12 V, the R_DA of the InAs APDs was calculated to be between 3.7 and 1.1 kΩ-cm^2 at 200 K. It can be estimated, from figure 5.10, that the avalanche gain at 200 K is between 7 (77 K) and 18 (290 K) at V_b = 12 V. Therefore, the minimum R_DA requirement of the ROICs can be satisfied by operating the InAs APDs with useful avalanche gain at temperatures which can be achieved by thermoelectric coolers. The temperature dependence of the avalanche gain in InAs APDs will be discussed in more detail in chapter 6.

5.6   Responsivity and detectivity of InAs APDs

While the avalanche gain can amplify the incoming signal, the amount of free

carriers generated upon receiving the photon flux, which can be characterised by the responsivity, is equally important. The responsivity is a measure of the ability of a photodiode to respond to the incoming signal or radiation. It is calculated based on the amount of photocurrent induced per unit power, in units of A/W. Besides the dark current density, the responsivity is one of the important parameters that determine the figure of merit of a photodetector, which is the detectivity.

Figure 5.11 The responsivities of Judson [18] and Hamamatsu [19] InAs photodiodes compared with the responsivity reported here for an InAs APD at 77 and 295 K.

The responsivity measurement was carried out using discrete wavelength laser sources from 1.3 to 2 µm. Across the measured wavelengths, the InAs APDs achieved ~ 50 % quantum efficiency without antireflection coating. Due to the long minority carrier diffusion length of InAs, it can be predicted that the 50 % quantum efficiency can be extended to wavelengths close to the λ_c of InAs at different temperatures. The responsivity of the InAs diodes is also compared with the responsivity of the commercially available InAs photodiodes such as those from Judson [18] and Hamamatsu [19], as shown in figure 5.11. It can be seen that the InAs APD has comparable responsivity to Judson photodiodes and has about 15 % higher quantum efficiency than Hamamatsu photodiodes. It is worth noting that this InAs APD's structure is not optimised to provide high quantum efficiency. The diode

can be designed so that the photon source is illuminated near the high electric field region to further improve the diode's responsivity.
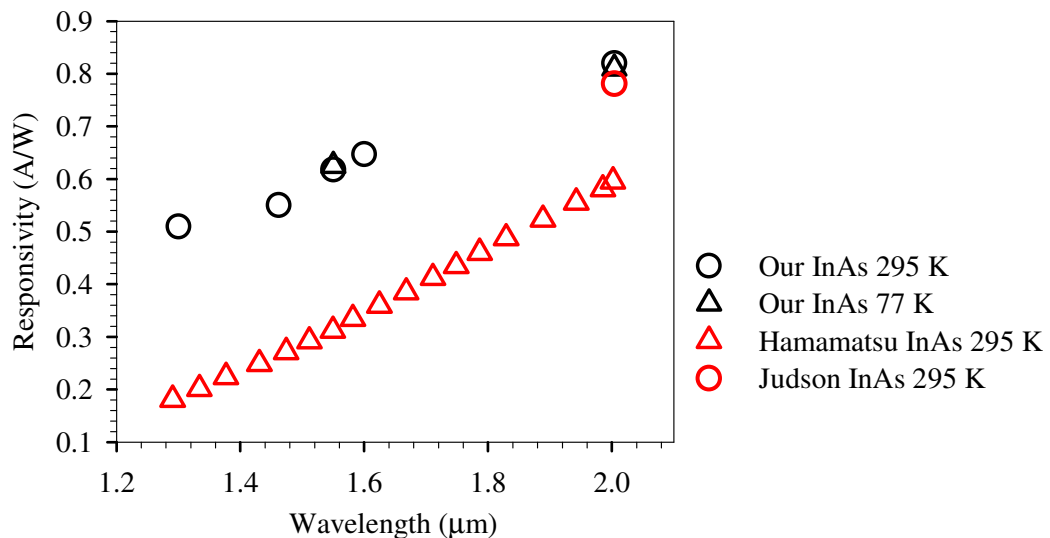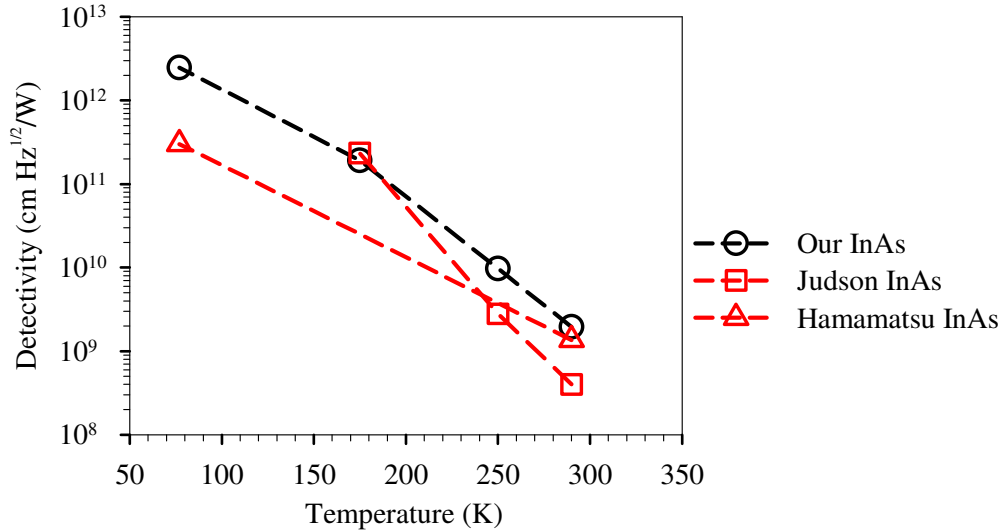

Figure 5.12 The detectivities of Judson [18] and Hamamatsu [19] InAs photodiodes at 1.55 µm compared with the detectivity reported here for an InAs APD from 77 to 295 K. (Lines are present to aid visualisation)

The detectivity D^* can be described by the ratio of the responsivity at a particular wavelength $R_p(\lambda)$ to the total noise current. In photodiodes, the total noise current is dominated by the shot noise and thermal noise as discussed in section 1.1. Hence the detectivity can be expressed as [22]

$$D^* = R_p(\lambda) \sqrt{\left[\frac{RA}{4k_B T + 2q I_{dark} R}\right]}, \tag{5.4}$$

Using the responsivity and dark current density data, the detectivity of the InAs diode was calculated at 1.55 µm from 77 to 290 K and is shown in figure 5.12. The responsivity at 1.55 µm is independent of T, hence the detectivity increases from 2×10^9 cmHz$^{1/2}$/W at 290 K to 2.5×10^{12} cmHz$^{1/2}$/W at 77 K owing to the reduction in dark current. A comparison with other commercial InAs photodiodes shows that the detectivity is comparable to that of the Judson InAs photodiode at 175 K and is

approximately 10 times higher than the detectivity of the Hamamatsu photodiode at 77 K. At room temperature, while Judson InAs photodiodes has comparable responsivity to our InAs diodes, its dark current density is much higher, causing its detectivity to be lower. On the other hand, from figure 5.9 and 5.11, although the Hamamatsu InAs photodiodes has similar dark current density to our InAs diodes at room temperature, its quantum efficiency is 15 % lower, leading to a lower detectivity than our InAs diode. Therefore, it is clear that both the responsivity and the dark current density are the important indicators for high detectivity and our InAs diodes have both of these advantages against the commercial InAs photodiodes. We believe that when it is operated in conjunction with a preamplifier, the InAs APDs can provide significantly better sensitivity than unity gain photodiode.

5.7 Conclusion

Although the SU-8 passivation has not completely suppressed the surface leakage current, it has reduced the surface current component sufficiently such that the temperature dependence of the leakage current in InAs APDs can be analysed. Relatively low dark current densities are achieved at both 77 and 290 K with R_dA = 910 MΩ-cm^2 at 77 K and R_dA = 34 Ω-cm^2 at 290 K at V_b = 0.1 V. Detailed dark current analysis, separating J_{bulk} and J_{surf} components, revealed that the bulk leakage current in these InAs APDs is carrier-diffusion dominated while the surface leakage current is caused by the mid-gap generation and recombination of carriers. Furthermore, this analysis allows the estimation of the total leakage current for a certain dimension or size of the InAs APD.

The dark current density comparison at 77 K shows that the design of our InAs diodes has successfully suppressed the tunnelling current at high bias voltages besides keeping a low dark current level. At 150 K, the comparison with other APDs technologies reaffirms the importance and potential of having improved mesa or planar InAs APDs to achieve minimum dark current levels and allow the potential benefits to be exploited fully.

Our InAs APDs have comparable or higher detectivity than the commercial InAs photodiodes due to high responsivity and low dark current density. The avalanche gain characteristic of the InAs e-APD has also been investigated. $M \sim 25$ was measured at 13 V and 19.5 V at $T = 290$ K and 77 K respectively. Low temperature operation can reduce the dark current density of the InAs APD substantially but at the expense of a lower M. However, the high responsivity, the low dark current density coupled with the ability to provide avalanche gain with very low F, have suggested that InAs APDs can be a promising photodetector for infrared sensing.

References

[1]   I. M. Baker, S. S. Duncan, and J. W. Copley, "A low-noise laser-gated imaging system for long-range target identification," in *Proc. SPIE Infrared Technology and Applications, vol. 5406*, Orlando, FL, USA, 2004, pp. 133-144, 2004.

[2]   A. Krier, H. H. Gao, and Y. Mao, "A room temperature photovoltaic detector for the mid-infrared (1.8-3.4 µm) wavelength region," *Semicond. Sci. Technol.,* vol. 13, pp. 950-956, May 1998.

[3]   M. Achour, "Free-space optics wavelength selection: 10 µm versus shorter wavelengths [Invited]," *J. Opt. Netw.,* vol. 2, pp. 127-143, 2003.

[4]   H. H. Gao, A. Krier, V. Sherstnev, and Y. Yakovlev, "InAsSb/InAsSbP light emitting diodes for the detection of CO and CO_2 at room temperature," *J. Phys. D: Appl. Phys.,* vol. 32, pp. 1768-1772, 1999.

[5]   A. R. J. Marshall, C. H. Tan, J. P. R. David, J. S. Ng, and M. Hopkinson, "Fabrication of InAs photodiodes with reduced surface leakage current," in *Proc. SPIE Optical Materials in Defence Systems Technology IV*, Florence, Italy, 2007, pp. 67400H-9.

[6]   R.-M. Lin, S.-F. Tang, S.-C. Lee, C.-H. Kuan, G.-S. Chen, T.-P. Sun, and J.-C. Wu, "Room temperature unpassivated InAs p-i-n photodetectors grown by molecular beam epitaxy," *IEEE Trans. Electron Devices, ,* vol. 44, pp. 209-213, 1997.

[7]   R.-M. Lin, S.-F. Tang, S.-C. Lee, and C. H. Kuan, "Improvement of current leakage in the InAs photodetector by molecular beam epitaxy," *J. Crystal Growth,* vol. 227-228, pp. 167-171, 2001.

[8]   P. J. Ker, A. R. J. Marshall, A. B. Krysa, J. P. R. David, and C. H. Tan, "Temperature Dependence of Leakage Current in InAs Avalanche Photodiodes," *IEEE J., Quantum Electron.,* vol. 47, pp. 1123-1128, 2011.

[9]   H. S. Kim, E. Plis, A. Khoshakhlagh, S. Myers, N. Gautam, Y. D. Sharma, L. R. Dawson, S. Krishna, S. J. Lee, and S. K. Noh, "Performance improvement of InAs/GaSb strained layer superlattice detectors by reducing surface leakage currents with SU-8 passivation," *Appl. Phys. Lett.,* vol. 96, pp. 033502-3.

[10] Z. M. Fang, K. Y. Ma, D. H. Jaw, R. M. Cohen, and G. B. Stringfellow, "Photoluminescence of InSb, InAs, and InAsSb grown by organometallic vapor phase epitaxy," *J. Appl. Phys.,* vol. 67, pp. 7034-7039, 1990.

[11] X. G. Zheng, J. S. Hsu, J. B. Hurst, X. Li, S. Wang, X. Sun, A. L. Holmes, Jr., J. C. Campbell, A. S. Huntington, and L. A. Coldren, "Long-wavelength In$_{0.53}$Ga$_{0.47}$As–In$_{0.52}$Al$_{0.48}$As large-area avalanche photodiodes and arrays," *IEEE J. Quantum Electron.,* vol. 40, pp. 1068-1073, 2004.

[12] S. R. Forrest, R. F. Leheny, R. E. Nahory, and M. A. Pollack, "In$_{0.53}$Ga$_{0.47}$As photodiodes with dark current limited by generation-recombination and tunneling," *Appl. Phys. Lett.,* vol. 37, pp. 322-325, 1980.

[13] S. Ghosh, S. Mallick, K. Banerjee, C. Grein, S. Velicu, J. Zhao, D. Silversmith, J. Rodriguez, E. Plis, and S. Krishna, "Low-Noise Mid-Wavelength Infrared Avalanche Photodiodes," *J. Electron. Materials,* vol. 37, pp. 1764-1769, 2008.

[14] H. H. Gao, A. Krier, and V. V. Sherstnev, "Room-temperature InAs$_{0.89}$Sb$_{0.11}$ photodetectors for CO detection at 4.6 µm," *Appl. Phys. Lett.,* vol. 77, pp. 872-874, 2000.

[15] J. Rothman, N. Baier, P. Ballet, L. Mollard, M. Fournier, J. Gout, and J. P. Chamonal, "High-Operating-Temperature HgCdTe Avalanche Photodiodes," *J. Electron. Materials,* vol. 38, pp. 1707-1716, 2009.

[16] M. B. Reine, J. W. Marciniec, K. K. Wong, T. Parodos, J. D. Mullarkey, P. A. Lamarre, S. P. Tobin, K. A. Gustavsen, and G. M. Williams, "HgCdTe MWIR back-illuminated electron-initiated avalanche photodiode arrays," in *Proc. SPIE Infrared and Photoelectronic Imagers and Detector Devices II*, San Diego, CA, USA, 2006, pp. 629403-12.

[17] G. Perrais, O. Gravrand, J. Baylet, G. Destefanis, and J. Rothman, "Gain and Dark Current Characteristics of Planar HgCdTe Avalanche Photo Diodes," *J. Electron. Materials,* vol. 36, pp. 963-970, 2007.

[18] "InAs detectors J12 series datasheet, Judson Technologies, revised Jan. 2001."

[19] "InAs photovoltaic detectors P10090 series and P7163 datasheet, Hamamatsu, revised Apr. 2008."

[20] A. R. J. Marshall, P. Vines, P. J. Ker, J. P. R. David, and C. H. Tan, "Avalanche Multiplication and Excess Noise in InAs Electron Avalanche Photodiodes at 77 K," *IEEE J. Quantum Electron.,* vol. 47, pp. 858-864, 2011.

[21] A. R. J. Marshall, J. P. R. David, and C. H. Tan, "Impact Ionization in InAs Electron Avalanche Photodiodes," *IEEE Trans. Electron Devices,* vol. 57, pp. 2631-2638, 2010.

[22] G. Rieke, "Detection of light", Cambridge University Press, 2003.

Chapter 6 Avalanche gain and excess noise of InAs APDs

6.1   Introduction

As discussed in section 1.4, in conventional APDs W is designed to be as thin as possible to increase the bandwidth and to reduce F at a given M. The effect of the dead space is exploited to produce lower F. While beneficial for noise reduction, the thinning of W increases the tunnelling current considerably leading to a higher shot noise, particularly in narrow bandgap semiconductors. Depending on E_g of the material, this imposes a minimum acceptable W so that the tunnelling current can be sufficiently suppressed. For detection at wavelengths beyond 1.8 µm, materials with $E_g < 0.68$ eV are needed. Thus, suppression of the tunnelling current will be a major challenge if W is reduced substantially to reduce F and to increase the bandwidth. This approach is impractical and it is necessary to identify semiconductor materials with disparate ionisation coefficients such that k is as small as possible [1].

InAs APDs were proven to provide M_e with very low F_e [2], but the high leakage current of InAs e-APDs at room temperature, due to its narrow E_g, produces high shot noise. Fortunately the dark current was found to reduce substantially when the InAs APDs were cooled from room temperature to 77 K [3]. In addition to the reduced dark current, Marshall *et al*. [4] reported reduced M_e at 77 K in contrast to most of the well-established APDs' technologies such as Si [5], GaAs [6], InP [7, 8] and InAlAs [7]. However, in their work, Marshall *et al.* attributed the reduced M to the reduced value of α without considering the influence of the variation of W with T. The depletion width of undoped InSb wafer was reported to increase from ~ 2 to 10 µm when it was cooled below 30 K [9], possibly due to the freezing of impurities which act as unintentional dopants. Due to larger E_g, this may happen in InAs at $T >$

30 K. Since for a given value of α, M_e increases approximately exponentially with W, it is important that the analysis of the temperature dependence of M_e is carried out, taking into account the possible variation of W with temperatures. Hence, the first objective of this chapter is to obtain an accurate temperature dependence of M_e from 77 to 295 K in InAs e-APDs taking into consideration the temperature dependence of W in InAs APDs.

Moreover there are only limited studies on the temperature dependence of F. Kanbe reported that the measured excess noise in Si APDs increased slightly with increasing temperatures but concluded that the variation is negligible [10]. For III-V semiconductors, both measured [11] and modelled [12] excess noise of InGaAs/InP APDs were also found to be decreasing with reducing temperatures, with their effective k varying from 0.42 to 0.53 as T changes from 240 to 360 K. $Al_xGa_{1-x}As$ APD with $x = 0$ to 0.4, on the other hand, were reported to have little variation of F within the accuracy of measurement as T changes [13]. The only low temperature excess noise of InAs APDs was reported at 77 K [4]. F_e at 77 K was measured to be lower than that at room temperature and it was attributed to the increase in ξ_{th} and d_e at 77 K. However Marshall *et al.* did not rule out the possibility of a measurement error in F_e. This is because for F_e to drop from ~ 1.6 (at 295 K [2]) to ~ 1.3 (at 77 K [4]), the increase in ξ_{th} ($\Delta\xi_{th}$) has to be significantly larger than the increase in E_g (ΔE_g) with decreasing T from 295 to 77 K. Therefore, in this work we will report the first comprehensive measurement of the excess noise over a wide range of temperatures to investigate the variation of F_e with T and address the discrepancy in the previous excess noise measurements in InAs APDs.

Besides the observed reduction in M_e, there appears to be contradicting results of the impact ionisation behaviour at 77 K. Mikhailova *et al.* reported that when the spin-orbit splitting of the valance band energy Δ_{so} is equal to the E_g of InAs at 77 K, band "resonance" occurs [14]. A similar phenomenon was also discussed by Norton [15] for the SWIR HgCdTe APDs with $E_g \sim 0.9$ eV. Grein *et al.* [16] predicted that this effect could produce an enhancement of β in AlGaSb, but only at low $E = 33$ kV/cm in his simulation. In contrast the reported M_e and F_e characteristics at 77 K by

Marshall *et al.* suggest that holes do not impact ionise until $E > 70$ kV/cm [4]. However, as T increases from 77 K to room temperature, E_g varies from 0.4 to 0.35 eV in InAs [17]. It is not obvious if the band "resonance" may occur as E_g shifts closer to the reported range of Δ_{so} at temperatures between 77 and 200 K [18] and whether this will change the value of $F_e < 2$ observed under pure electron injection in InAs e-APDs. Therefore, both the temperature dependence of M_e and F_e can also be used to verify whether the band "resonance" effect occurs in InAs.

In addition, it has been reported briefly that in InAs *p-i-n* APDs with uniform electric field profiles, thicker W can provide higher M at a particular V_b [19]. Hence the *i*-layer of the APD structure should be designed to be as thick as possible. However, to achieve $W > 3$ μm, unintentional background doping concentrations $N_b < 2 \times 10^{15}$ cm^{-3} are mandatory. InAs grown by liquid phase epitaxy and MBE have been reported to have *n*-type [20, 21] N_b between 1×10^{15} cm^{-3} and 6×10^{16} cm^{-3}. Therefore in APDs with thick W, a *p-n⁻* junction with a significant field gradient is likely to form prior to achieving a full depletion. The electric field gradient was reported to affect F in GaAs [22] and InAlAs [23] APDs but this effect is not well known in e-APDs. Unlike conventional semiconductors, e-APDs have α that is weakly dependent on E [24]. Consequently impact ionisation can occur at positions away from the vicinity of the peak electric field, at the *p-n⁻* junction. Thus, the effect of the peak electric field and field gradient on M_e and F_e for InAs e-APDs will also be investigated in this chapter. Finally, to demonstrate that the internal gain of InAs APDs can improve the system sensitivity, the InAs APDs were used with a pre-amplifier and the SNRs were calculated for increasing M. Furthermore, the importance of having low leakage current and pure electron injection profile for InAs APDs will also be illustrated through this SNR measurement.

To facilitate understanding for the subsequent sections, table 6.1 presents brief details of the wafers used throughout this chapter. More details on these wafers can be obtained in Appendix A1.

Wafers	Thicknesses (µm)	Electric field profiles
M3247	*p/i/n* : 1/3.5/1.9	Fully depleted *i*-region with uniform electric field
M3279	*p/i/n* : 2.3/0.9/1.9	
MR2537	*n/i/p* : 2/6/3	Undepleted *p-n*⁻ junction with peak electric fields and field gradients
MR2538	*p/i/n* : 2/6/2	
MR2835	*p/i/n* : 2/6/2	
MR2840	*p/i/n* : 2/6/2	
MR2558	*n/i/p* : 1.5/6/3.5	
MR2559	*n/i/p* : 1.5/6/3.5	

Table 6.1 Brief details of the wafers used.

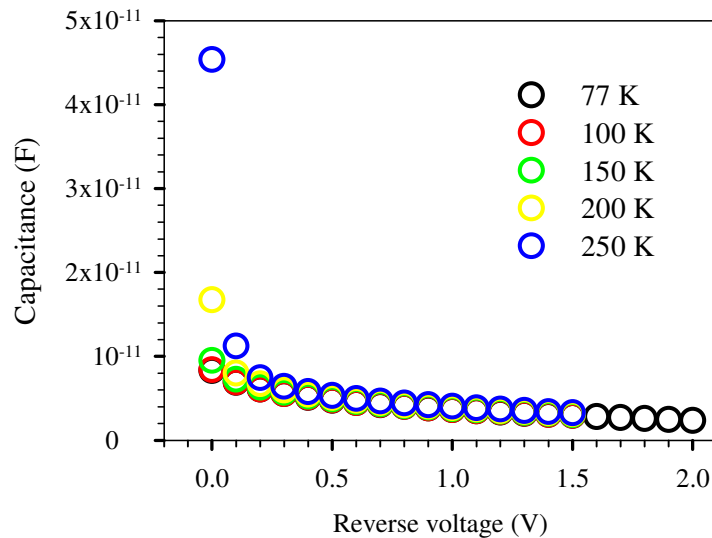## 6.2 Capacitance and built-in voltage

Figure 6.1 Capacitance-voltage of M3247 at 77, 100, 150, 200 and 250 K.

The *C-V* of M3247 was measured from $T = 77$ to 250 K using the set-up described in section 3.2 and 3.7. The temperature dependence of the *C-V* is crucial in investigating the change in *W* with *T*. Figure 6.1 shows the *C-V*s of M3247 with $d = 250$ µm at different *T*. It is clear that the *C-V*s converge to similar values for $V_b > 0.4$ V, indicating that *W* does not change significantly with *T*. Since M3247 has low $N_b \sim$

2×10^{14} cm^{-3} with $W \sim 3.5$ µm, a full depletion width was achieved at $V_b < 2$ V, forming a *p-i-n* junction with a uniform electric field.
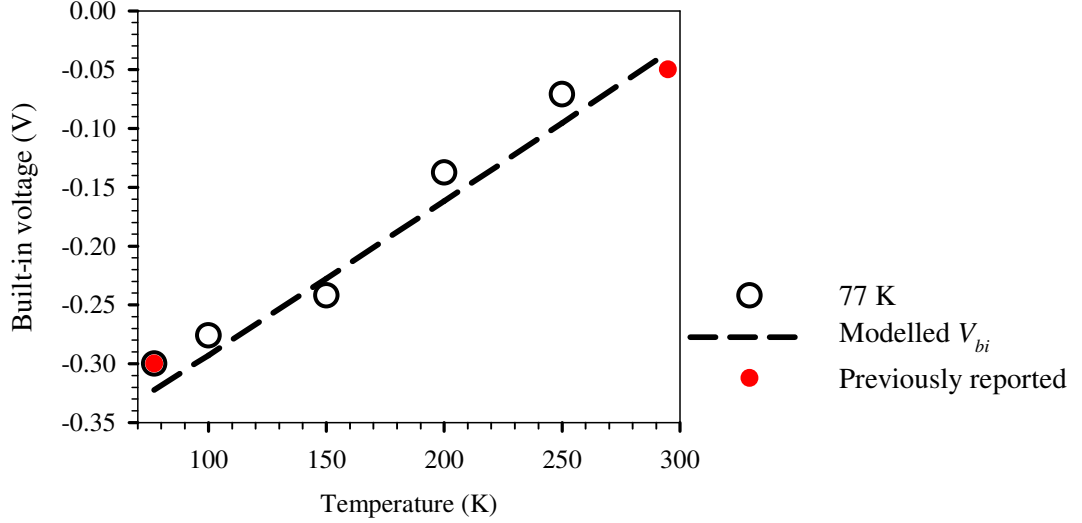

Figure 6.2 Derived V_{bi} at the measured temperatures and the previously reported V_{bi} at 77 and 295 K fitted with the modelled V_{bi} for M3247.

V_{bi} at each temperature were obtained by the extrapolation of the bias dependent $1/C^2$ curve to zero, as explained in section 3.2. These values vary from - 0.3 to - 0.07 V as *T* changes from 77 to 250 K, as shown in figure 6.2. Hence, the initial difference in *C* for $V_b = 0$ to 0.4 V is mainly due to the change in V_{bi} with *T*. The extrapolation of $1/C^2$, to extract V_{bi}, is valid prior to full depletion of the structure. The extracted V_{bi} agrees well with the modelled V_{bi} using the equation [25]

$$V_{bi} = \frac{k_B T}{q} ln \left[\frac{N_A N_D}{n_i^2} \right],$$
(6.1)

where N_A is the doping concentrations of the *p*-doped region and N_D is the doping concentrations of the *i*-region which was assumed to be *n*-type with an unintentional background doping, as reported for InAs grown by MBE [20, 21]. $N_A = 2 \times 10^{18}$ cm^{-3} and $N_D = 2 \times 10^{14}$ cm^{-3} deduced from Secondary Ion Mass Spectroscopy (SIMS) and

C-V were used to produce a good fit to the extracted and previously reported [26] V_{bi} as shown in figure 6.2.

To investigate the electric field profiles of a few different layers of InAs wafers, the *C-V* measurements at 77 K were also carried out for MR2835 and MR2840. Determination of the type of unintentional doping (UID) is crucial for the estimation of the electric field profiles. While the *n*-type UID has been widely reported for MBE-grown InAs [20, 21], there is very little literature reporting the UID type of MOVPE-grown InAs.
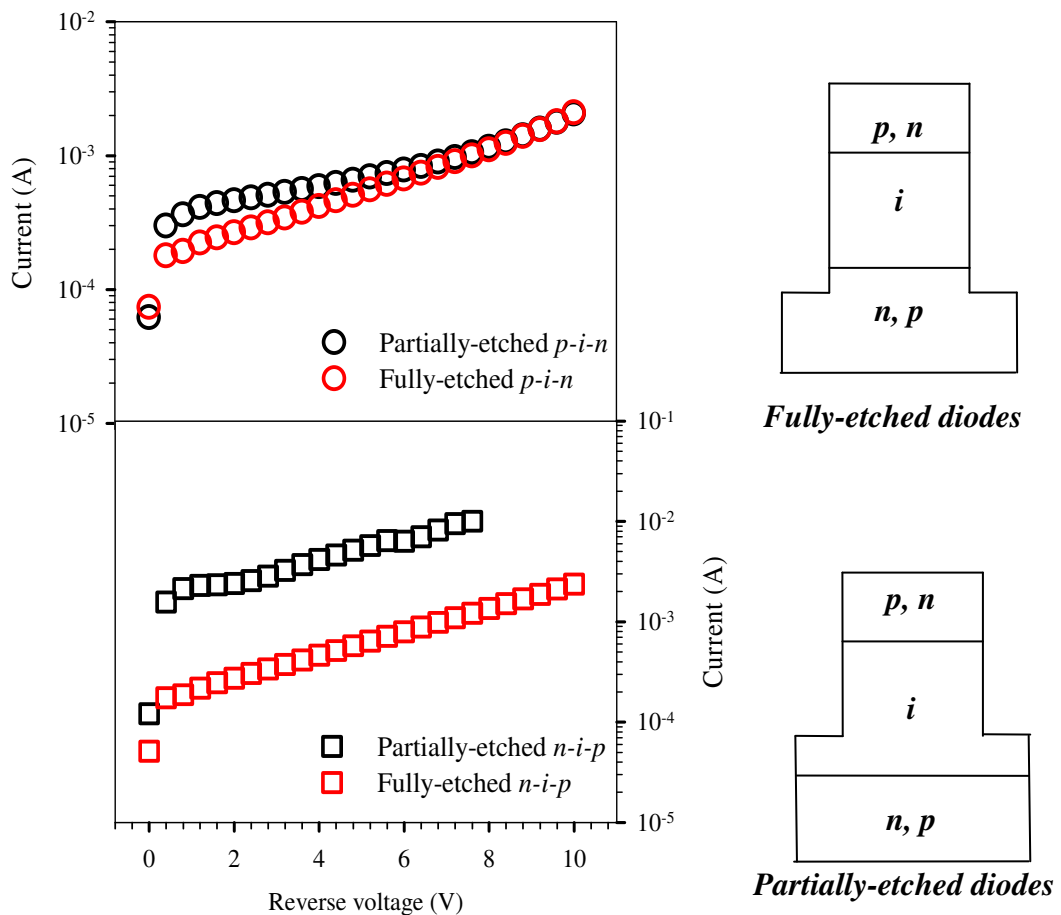

Figure 6.3 *I-V* characteristics of the fully- and partially-etched *p-i-n* and *n-i-p* InAs diodes.

The MOVPE grown *p-i-n* (MR2538) and *n-i-p* (MR2537) InAs diodes, both having nominal *i*-region thickness of 6 µm, were fully- and partially-etched as illustrated in figure 6.3. The room temperature reverse current of each diode was measured. For the *p-i-n* diodes no significant difference in the dark current was observed between the fully- and partially-etched diodes, whereas more than an order of magnitude difference was observed for *n-i-p* diodes. This trend can be explained by the presence of an *n*-type UID. In the *p-i-n* diode, the depletion width or junction starts to form at the *p-i* interface. Therefore the active area of the diode is defined once the etch depth reaches the *i*-layer, confirming the *n*-type UID. For the partially-etched *n-i-p* diode, the electric field is thought to spread across a much wider area at the bottom *i-p* junction producing much higher dark current than a fully-etched mesa diode.

Assuming the depletion starts from the *p-i* interface due to the *n*-type UID, the *C-V* was modelled to extract N_b, *W* and the *E* profiles. The *i*-region was divided into multi-regions to accurately model the *C-V* profiles. This multi-region *C-V* model can be found in [27]. The calculated *E* profiles at 12 V are shown in figure 6.4. M3247 was the only fully depleted *p-i-n* diode while the *i*-layers of MR2835 and MR2840 were not fully depleted due to higher N_b and thicker *i*-layers, producing *p-n⁻* junctions with non-uniform electric fields.
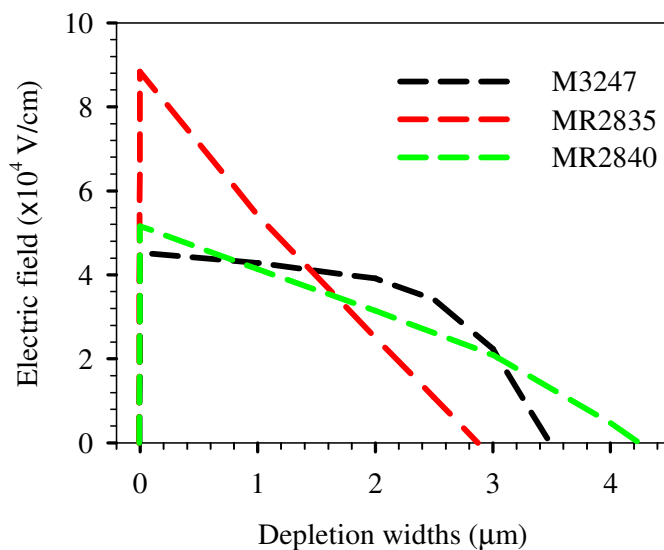

Figure 6.4 Electric field profiles of M3247, MR2835 and MR2840 at V_b = 12 V.
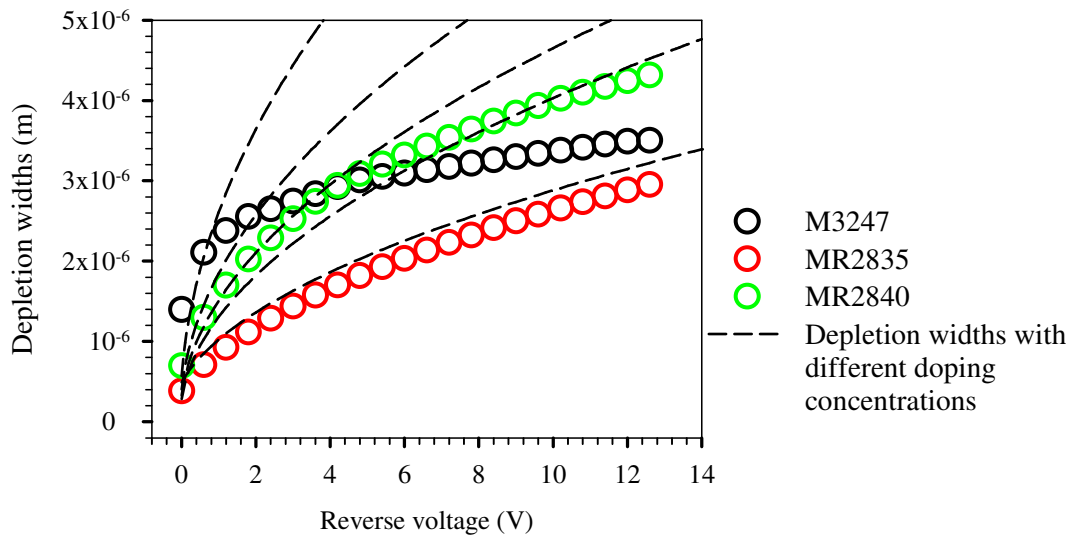
Figure 6.5 Depletion widths at different V_b for M3247, MR2835 and MR2840. Lines show the depletion widths for different background doping concentrations of 2×10^{15}, 1×10^{15}, 7.5×10^{14}, 5×10^{14} and 2.5×10^{14} cm^{-3}.

The extracted values of W as a function of V_b are shown in figure 6.5. At $V_b < 4$ V, M3247 and MR2835 have the largest and the smallest values of W, respectively. It can be seen that M3247 depletes very rapidly at $V_b = 0$ and 1 V, corresponding to a very low value of $N_b \sim 2\times10^{14}$ cm^{-3} while MR2835 and MR2840 appear to have $N_b \sim 2\times10^{15}$ cm^{-3} and $\sim 7.5\times10^{14}$ cm^{-3} respectively. At higher V_b, M3247 depletes more gradually as it approaches a full depletion of the undoped region.

6.3   Avalanche gain in InAs APDs

5 layers of InAs wafers, M3247, M3279, MR2835, MR2840 and MR2558 were used in the avalanche gain measurement. The details on these wafers are attached in Appendix A1. Photomultiplication measurements were carried out from $T = 77$ to 295 K on M3247 and M3279 using the PSD with an external modulation, as described in section 3.3.1. The PSD method was used so that M can be measured up to the highest possible electric field as this method could differentiate the photocurrent from the dark current.

During this photomultiplication measurement, all the factors, including pure carrier injection profile, device heating, series resistances and collection efficiency, which would affect the accuracy of this measurement, as described in section 3.3, were taken into account. Using the set-up described in section 3.7, the avalanche gain at different *T* was measured using 543- and 633-nm lasers. The measurements on M3247 and M3279 were repeated for *T* = 77, 100, 150, 200, 250 and 295 K, while *M* of MR2835, MR2840 and MR2558 were measured at 77 K. Since accurate sample temperatures were crucial in these measurements, the experiments were carried out only when the temperature of the sample chamber was kept constant at the desired temperature for > 20 minutes.
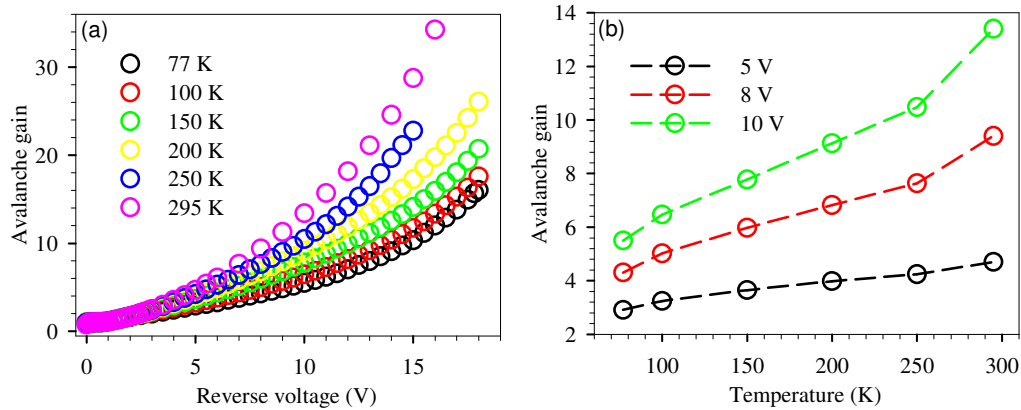
Figure 6.6 (a) Pure electron initiated avalanche gain of M3247 at 77, 100, 150, 200, 250 and 295 K. (b) Avalanche gain at V_b = 5, 8 and 10 V for different temperatures.

From figures 6.6 (a) and 6.7, both M3247 and M3279 exhibit exponentially rising M_e. It is clear that as *T* increases from 77 to 295 K, M_e at a given V_b increases. The confirmation of a constant *W* with *T* in the previous section is important because for *k* = 0 and under constant electric field, the local ionisation model predicts *M = exp* (αW). Since *W* is constant, the temperature dependence of M_e shown in figure 6.6 (a) and 6.7 are only dominated by the changes in the ionisation parameters.

Figure 6.6 (b) shows that from 77 to 295 K, M_e increases quite linearly with *T* at a given V_b. In wide bandgap semiconductors such as Si and GaAs, the reduced

temperature lowers the number of phonon scattering events leading to a larger population of hot carriers that increases the impact ionisation events. On the other hand in narrow bandgap materials, in which impact ionisation can occur at energies close to the E_g [28, 29], the role of minimum ionisation energy is more significant at low electric fields. Consequently in InAs, with large Γ-X and Γ-L valley separation energies reported to be $\geq 2E_g$ [18, 28, 30], it is reasonable to suggest that the temperature dependence of the electron ionisation threshold energy dominates over that of phonon scattering. Therefore, assuming that the ionisation threshold energy is proportional to E_g which increases with decreasing temperatures, the electron ionisation coefficient may be expected to decrease with temperatures, consistent with our measurement results on M3247 and M3279.
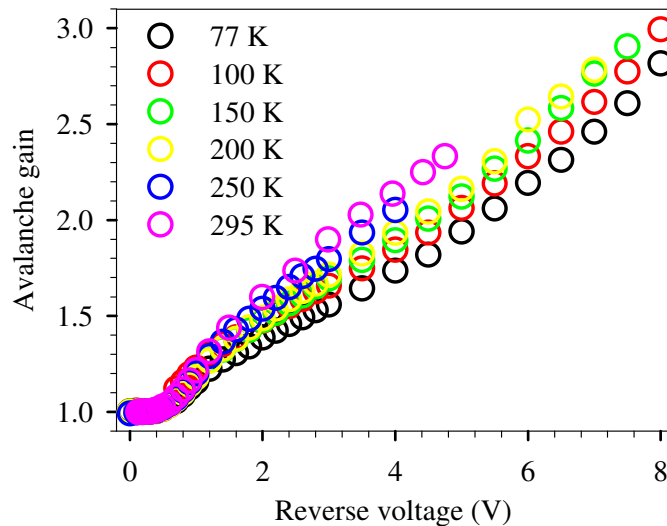
Figure 6.7 M_e of M3279 at 77, 100, 150, 200, 250 and 295 K.

Furthermore, it is also interesting to note that M3247 and M3279, with fully depleted and uniform electric field in the avalanche region, show the dependence of M_e on W, with higher M_e at a particular V_b when W is wider. On the contrary, in most of the well established semiconductors such as Si, GaAs, InP and InAlAs, APDs with thinner W can provide higher M at a particular V_b due to higher E. Figure 6.8 compares their M_e at 77 K and the trend of higher M_e with wider W remains for $T = $ 77 to 295 K. This characteristic has been reported briefly by Marshall *et al.* [19] at

room temperature. The $k = 0$ characteristic of InAs APDs and the weak dependence of α on electric field were considered to be the reasons for this phenomenon.

Figure 6.8 Comparison of the avalanche gain of M3247 and M3279 at 77 K.

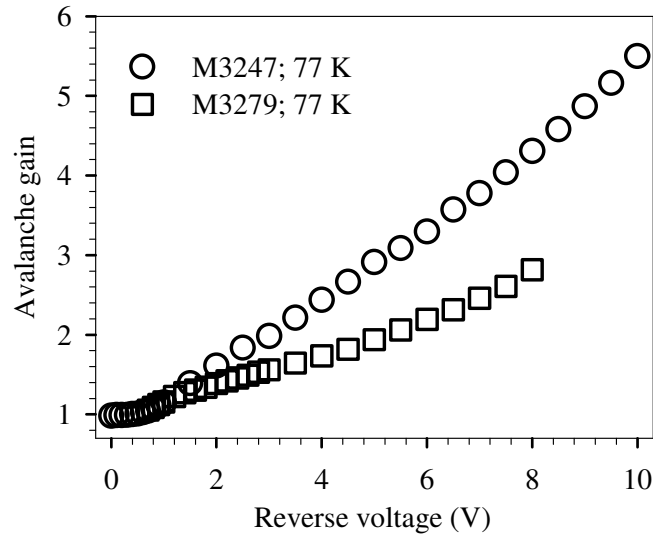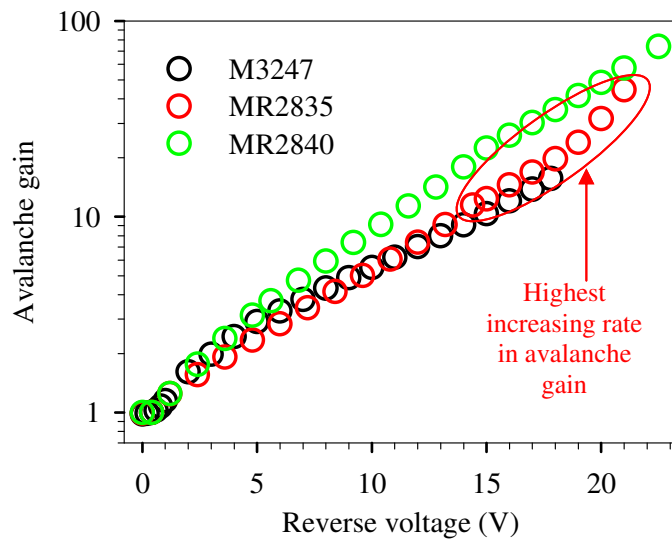Figure 6.9 Comparison of the avalanche gain between M3247, MR2835 and MR2840 at 77 K.

While the effect of W on M_e is understood for fully depleted *p-i-n* structures with almost uniform electric field, it is not clear that the same trend will be observed in *p-*

n^- junction with a peak electric field and field gradient throughout the avalanche region. As mentioned in section 6.1, a *p-n* junction field profile is likely to form if the *i*-layer of InAs APD is designed to be as thick as possible. The avalanche gain of MR2840 and MR2835 were therefore investigated and compared. Both of these InAs wafers have ~ 6 μm *i*-region but with different N_b ~ 7×10^{14} cm^{-3} for MR2840 and ~ 2×10^{15} cm^{-3} for MR2835, hence forming different peak electric fields and field gradients, as shown in figure 6.4. For comparison, figure 6.9 shows the avalanche gain of M3247, MR2835 and MR2840 at 77 K. Above 4 V, MR2840 produces the highest M_e at a given V_b. M3247 produces slightly higher M_e than MR2835 up to V_b = 12 V. At V_b > 17 V MR2835 exhibits a more rapid increase in M_e than the other two diodes.

At V_b > 4 V, figure 6.4 shows that MR2840 has the largest W at a given V_b. At each V_b, the M_e of MR2840 is higher than M3247 and MR2835. From the *C-V*s, the peak electric field of MR2835 is ~ 2 times higher than that of MR2840 at a given V_b. The difference in electric field gradients between MR2840 and MR2835 is also much larger than those between M3247 and M3279. However they are still showing the high dependency of M_e on W instead of the peak electric field. Besides the $\beta = 0$ characteristic of InAs e-APD and α is weakly dependent on the electric field, it is believed that this characteristic is also due to the onset of electron impact ionisation at very low E, typically < 5 kV/cm. Since there is only electron that impact ionises, a wider W would mean that the electron can travel longer within the high-field region, allowing the initially injected electron to impact ionise multiple times in a single transit, producing higher M_e. Therefore results from figures 6.4 and 6.9 show that in general InAs APDs with wider W produce higher M_e at a given V_b regardless of the E profile. The field gradient does not appear to have significant influence on M_e for E < 70 kV/cm.

However, for V_b > 12 V, MR2835 has the highest rate of increase of M_e with V_b. It is also noted that V_b > 12 V corresponds to peak fields > 80 kV/cm in MR2835. Consequently, this rapid rise in M_e could be attributed to two factors. First, from the

reported α for InAs at 77 K [4], it was shown that α increases more quickly for $E >$ 80 kV/cm. Second, the increase in M_e is accelerated by the onset of hole impact ionisation at $E > 70$ kV/cm. The change in the rate of increase in M_e with bias due to the onset of hole impact ionisation has also been observed in a Monte Carlo simulation of InSb devices [31].

To check the hole impact ionisation property of InAs at 77 K, MR2558 *n-i-p* InAs APDs were used. Pure hole injection was achieved by fibre-coupling 543- and 633-nm lasers onto the *n*-layer of the 200-µm radius devices. Figure 6.10 shows that $M_h > 1$ only at $V_b > 18$ V. This corresponds to peak electric fields > 70 kV/cm. 1150- and 1550-nm lasers were also used to show the increase in *M* for mixed injection profiles as they have only ~ 80 and ~ 70 % absorption [32] in the 1.5-µm *n*-layer, respectively. In figure 6.10, it also shows that the side injection onto the *p*-layer produces the highest gain, indicating the large difference between α and β.
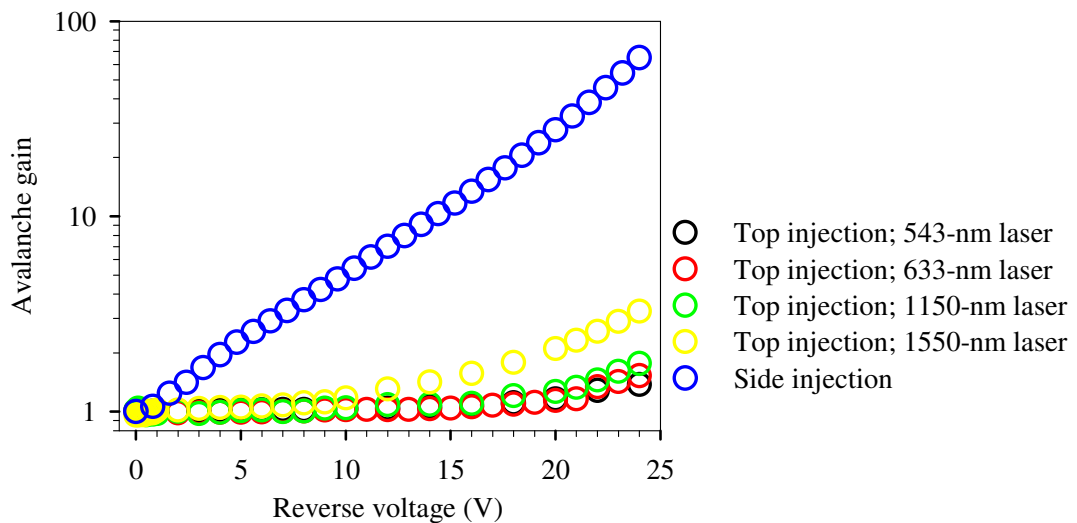

Figure 6.10 Comparison of avalanche gains for different carrier injection profiles.

6.4   Excess noise in InAs APDs

The noise power of the M3247, MR2835, MR2840 and MR2559 InAs APDs were measured from 77 to 250 K using the NFA. The details on the experimental set-up

and the calculations have been discussed in section 3.4. The fabrication of these InAs wafers into devices with GSG pads was described in section 4.5. Pure electron injection was achieved by fibre-coupling the 633-nm laser onto the 250 µm-diameter devices. Since this measurement set-up could not discriminate the photocurrent from the reverse leakage current, the photocurrent was kept to at least 2 orders of magnitude higher than the dark current. An example of the photocurrent and dark current of M3247 was shown in figure 6.11, together with its derived M_e at an intermediate temperature of 200 K.
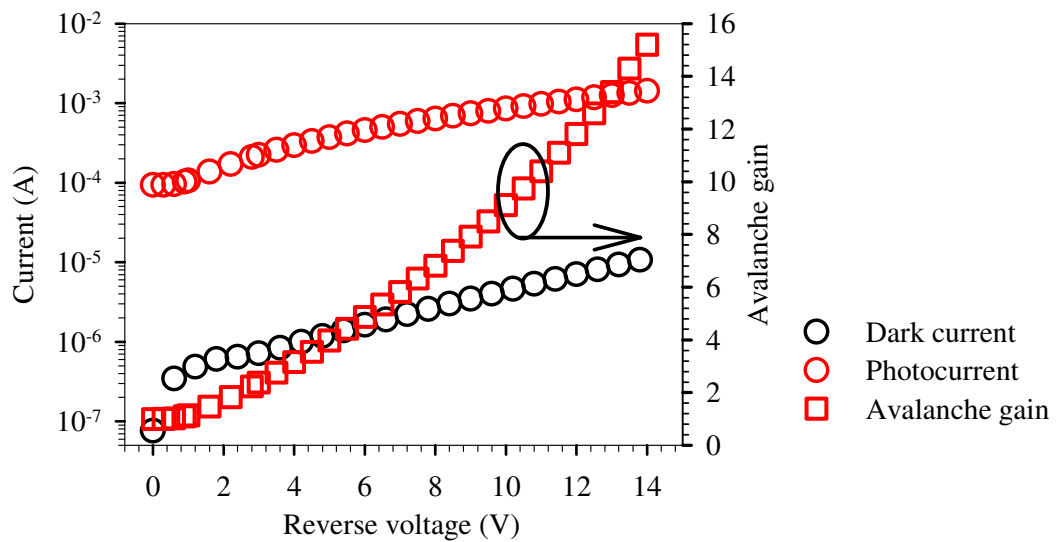
Figure 6.11 M_e, reverse leakage current and photocurrent measured on a $d = 250$ µm M3247 InAs diode under top illumination during the noise measurement at an intermediate temperature of 200 K.

Figure 6.12 shows F_e of M3247 from 77 to 250 K. They vary between 1.45 and 1.6 at $M_e > 3$ for this temperature range. Within the experimental errors, F_e is unaffected by the variation in T. The excess noise was not measured for $T > 250$ K due to higher leakage current in the InAs diodes and the photocurrent was comparable to the dark current.

F_e of InAs eAPDs is clearly lying below the lower limit corresponding to $k = 0$ in the local model [1]. This very low F_e can be attributed to the reduced randomness in the

ionisation path length due to the dead space effect. For APDs with $k = 1$, $<l>$ at high gain is comparable to W. Hence d_e (d_h) becomes comparable in length to $<l>$ only when W is thin, usually significantly less than 1 µm [33]. However, in the case of $k = 0$, $<l>$ is much shorter than W so that multiple ionisation events occur to build up the gain within a single transit time. As a result the dead space effect is dominant even in $W >> 1$ µm, such as in our InAs eAPD. Hence, αd_e, which is the ratio of d_e to $<l>$ (since $1/\alpha = <l>$), can be used as a measure of the dead space effect, with a higher value of αd_e indicating more deterministic ionisation behaviour [2, 34].
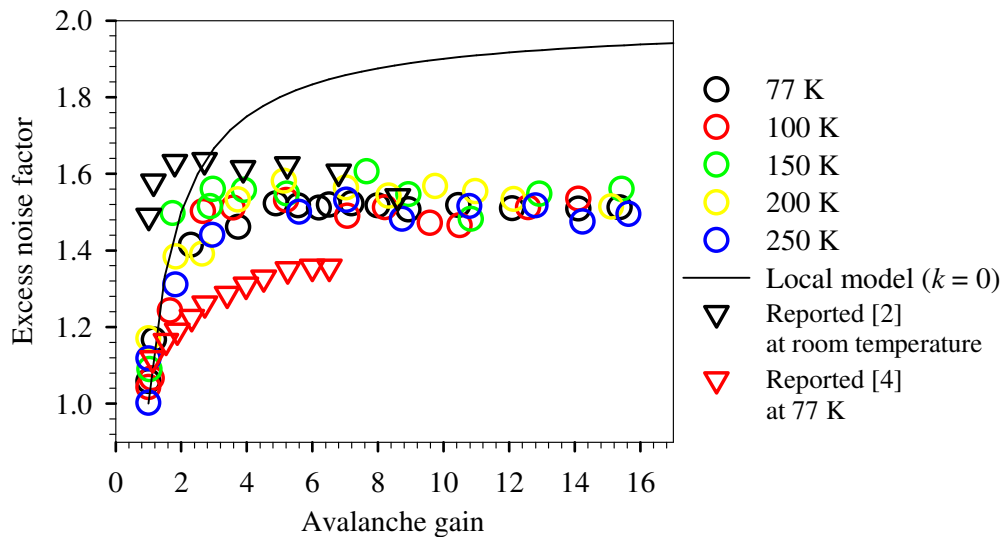
Figure 6.12 Pure electron initiated multiplication noise measured on M3247 at 77, 100, 150, 200 and 250 K under top illumination. The line shows the calculated valies with local model for $k = 0$.

The previously reported F_e of InAs APDs at room temperature [2] and 77 K [4] are also plotted in figure 6.12 for comparison. The room temperature F_e is measured using a custom-built set-up [35], which can differentiate the photocurrent from the dark current and the result is very similar to those reported here from 77 to 250 K. However, the previous 77 K result is clearly lower than our current result. The reduction in F_e at 77 K was attributed to the increase in ξ_{th} at lower temperature [4]. We strongly believe that the lower F_e is due to a few experimental errors, which are closely related to the measurement set-up used previously.

Previous 77 K noise measurement	Current low *T* noise measurement
Two DC-probes connected to a junction box. (DC-probes have 3 and 10 dB loss at 12 MHz and 30 MHz respectively)	GSG probe which can handles frequency up to 50 GHz.
BNC tri-axial and co-axial cables connected to co-axial cable with SMA connectors.	High frequency co-axial cable with SMA connectors (up to 20 GHz).
Measured noise power needs to be corrected / calibrated using a reference diode.	Measured noise power corresponds to the shot noise of the photocurrent at unity gain.
Devices are fabricated with designs for low-frequency measurements.	Devices are fabricated with designs for frequency response measurements up to GHz range.

Table 6.2 Comparison between the previous and current low temperature noise measurement set-ups.
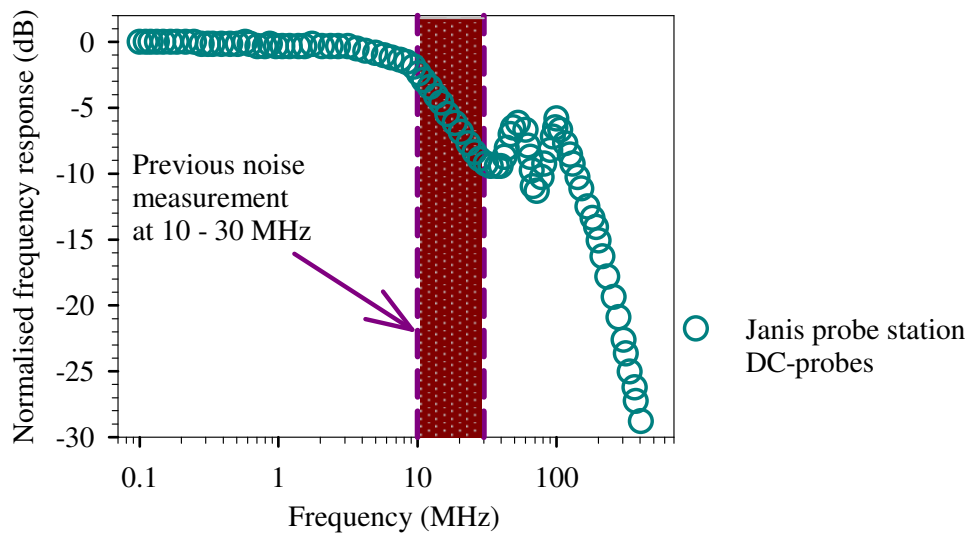

Figure 6.13 Normalised frequency responses of the DC-probes for the Janis ST-500 series low temperature probe station [36].

The major differences between the previous and current low temperature noise measurements are summarised in table 6.2. For the new measurement method, a few important aspects are improved such as having an APD design suitable for high

frequency measurements, the GSG probe, the high frequency cablings and elimination of junction box. These are crucial to ensure that the actual noise powers of the APDs are measured. More importantly from figure 6.13 the DC-probes have power losses of ~ 3 and ~ 10 dB at 12 and 30 MHz respectively. These were the frequencies at which the results were obtained for the previous 77 K measurements. Hence it is highly possible that this is the major factor that causes the underestimation of F_e.
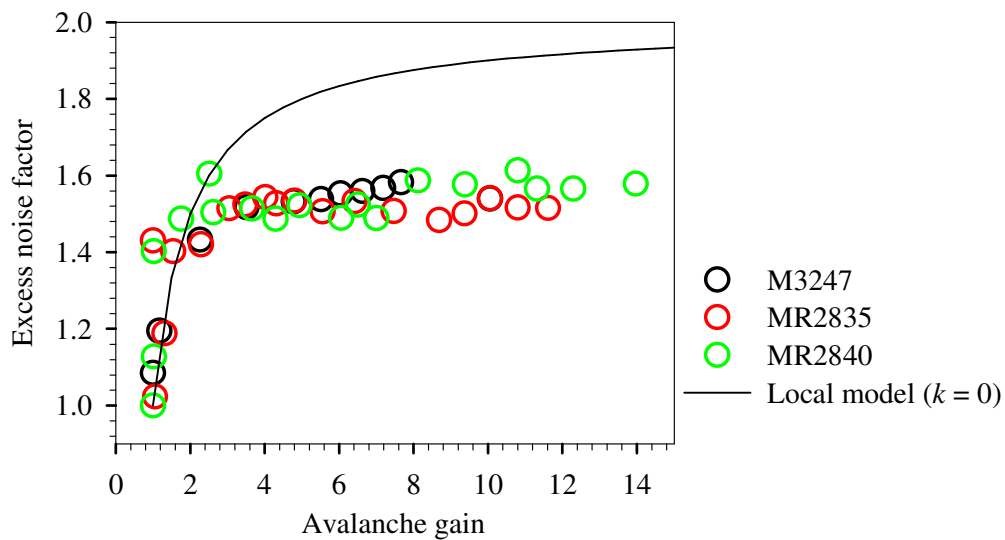
Figure 6.14 Pure electron initiated multiplication noise measured on M3247, MR2835 and MR2840 at 77 K under top illumination. The line shows the calculated valies with local model for $k = 0$.

The investigation on the effect of electric field gradient on excess noise was done by measuring F_e of MR2835 and MR2840 from T = 77 to 250 K. The excess noise results were very comparable to those from M3247, varying between 1.45 and 1.6. For comparison, figure 6.14 summarises an example of F_e for M3247, MR2835 and MR2840 at 77 K. These results show that F_e is independent of the electric field gradient. We believe that the lack of dependence on the field gradient in InAs e-APD is due to the very weak dependence of α on E and the impact ionisation of electrons can occur at very low E. Therefore the impact ionisation process can happen throughout the depletion widths of the APDs and is no longer confined in the high-

field region, as what observed in GaAs APDs [22]. This has led to a weak dependence of F_e on the field gradient.
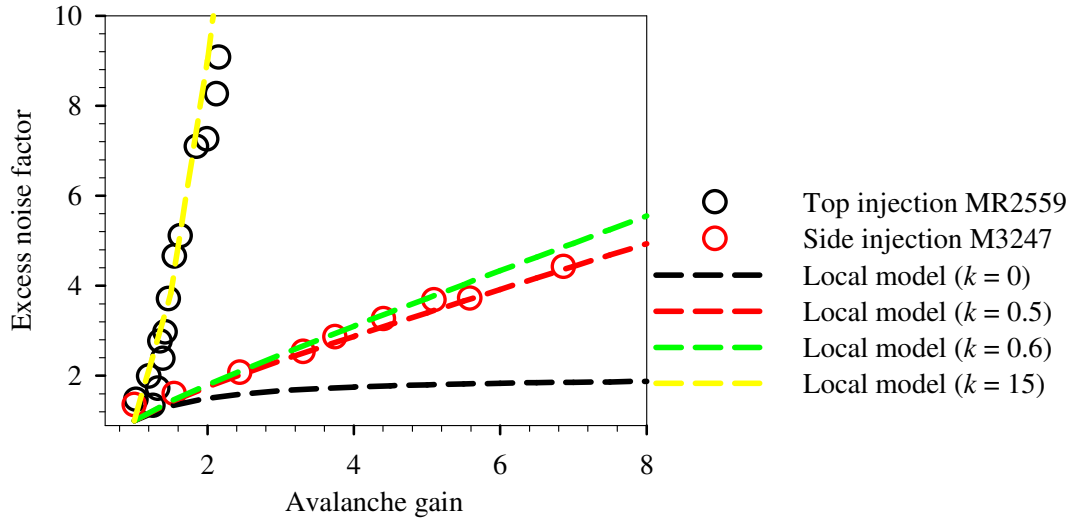
Figure 6.15 Excess noise characteristics measured on M3247 with illumination on the mesa sidewalls and hole-dominated excess noise factors on a 75-µm diameter MR2559 diode from 77 to 250 K. The line shows the calculated valies with local model for k = 0, 0.5, 0.6 and 15.

To further verify if the band "resonance" effect occurs, the excess noise measurements were also carried out with mixed-injection and hole-dominated injection profiles from 77 to 250 K. When the laser spot was focused near the mesa sidewalls of M3247, MR2835 and MR2840, where the carriers were largely generated in the depletion regions, a drop in M was observed at every V_b compared to the top illumination. This was also accompanied by an increase in F in which they were following the k = 0.5 - 0.6 lines as shown in figure 6.15. Hole-dominated injection profile was obtained by focusing the laser spot onto the top of 75-µm diameter MR2559 InAs *n-i-p* APDs. Due to the size of the laser spot, there was a contamination of electron injection. However, the domination of hole injection can be observed as M < 2 even at V_b > 10 V. The resulting F were measured to be extremely high, following the k = 15 line. Both mixed and hole-dominated injections show that $\beta << \alpha$ as M is much lower with much higher F. Hence it is clear that band

"resonance" effect which can greatly enhance β cannot be observed in InAs APDs at the reported temperatures.

6.5   Limitations of local model and hard dead space model

Values of α of the InAs e-APDs at room temperature [19] and 77 K [4] were previously derived and parameterised using the local model [1]. This model assumes that the effect of dead space is negligible in the impact ionisation process. However, it is evident from the excess noise measurements that the effect of dead space is significant in InAs e-APDs with thick W. While the previously derived α using the local model can predict M_e reasonably well [4, 19], this model is not appropriate for the prediction of F_e. Therefore, the nonlocal effect needs to be taken into account when modelling the InAs e-APDs regardless of its operating temperatures.
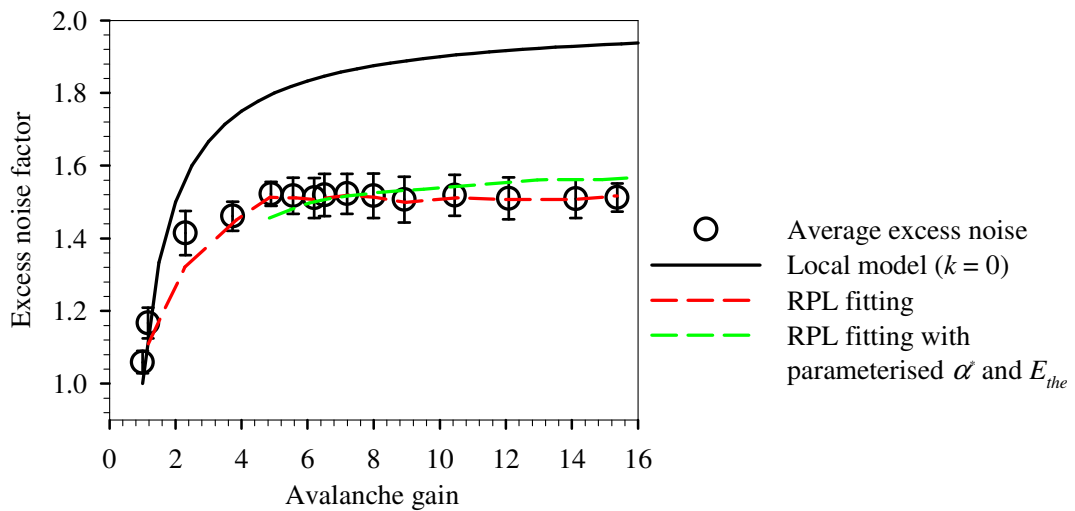
Figure 6.16 Average F_e of M3247 at 77 K with the associated error bars, the fittings using the RPL model to obtain α^* and d_e, and the RPL simulated F_e using the parameterised α^* and single effective ξ_{the}. The reference local model line of $k = 0$ is plotted for comparison.

We have attempted to fit the M_e and F_e results using the Random Path Length model. The details of this RPL model have been discussed comprehensively in [37] and

section 2.5. From this model, α^* and ξ_{the} can be determined and calculated using equation 2.8 [37].

Figure 6.16 shows the average values of F_e from a series of noise measurements on different devices at 77 K together with its associated error bars. Using the RPL model with E and W as fixed input parameters, we extracted α^* and d_e for each pair of the measured M_e and F_e at a given V_b. For the reported electric field range, $\beta = 0$ was used in this model as no impact ionisation of holes was observed. From figure 6.16, we found that the RPL model can provide excellent fit to the measured M_e and F_e only for $M > 4$. We believe this is because at $M < 4$, the measured F_e is more sensitive to the experimental errors.
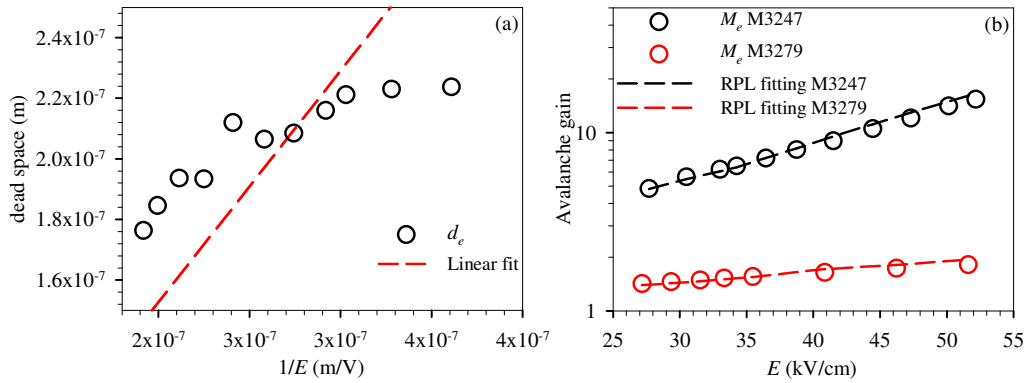
Figure 6.17 (a) Electric field dependent d_e that is used to determine ξ_{the}. (b) The comparison between the measured M_e on M3247 and M3279, and those modelled using the newly parameterised α^* and ξ_{the} at $T = 77$ K.

Using equation 2.8, ξ_{the} was obtained by a linear fitting to the d_e vs $1/E$ graph as shown in figure 6.17 (a). It can be seen that the single effective ξ_{the} using this ballistic model does not fit entirely to the simulated d_e. This results in ~ 17 % underestimation of d_e at high E and ~ 22 % overestimation of d at low E. α^* derived from the RPL model was parameterised with the equation

$$\alpha^* = A exp\left[-\left(\frac{B}{E}\right)^c\right], \tag{6.2}$$

where *A*, *B* and *c* are constants for a particular range of *E*. The parameterised $\alpha*$ and derived ξ_{the} were verified and cross-checked by modelling the M_e of M3247 and M3279, which have *W* ~ 3.5 and 0.9 µm respectively. Despite the use of a single effective ξ_{the}, figure 6.17 (b) shows that the simulated M_e using the parameterised $\alpha*$ can predict M_e with < 8 % deviation from the measured data of M3247 and M3279. Furthermore, the predicted F_e is still within the error bars of the measured F_e, as shown in figure 6.16.
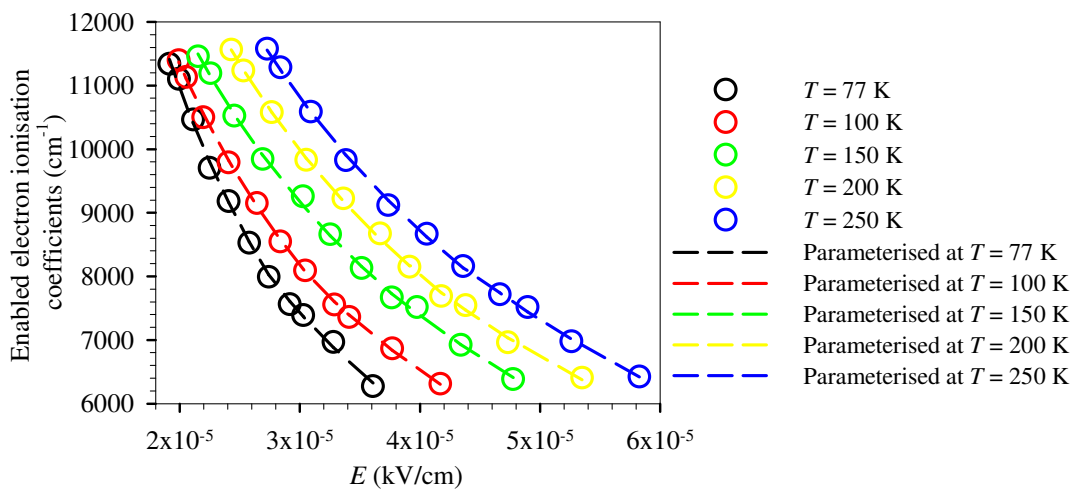
Figure 6.18 $\alpha*$ of InAs eAPD at 77, 100, 150, 200 and 250 K (symbols) and their parameterised $\alpha*$ (dashed lines).

Similar procedures were carried out to model the M_e and F_e results at 100, 150, 200 and 250 K. Figure 6.18 shows the extracted $\alpha*$ together with the fitted parameterised equations at each temperature. The *A*, *B* and *c* constants for a particular range of *E* and the values of ξ_{the} at each temperature are summarised in table 6.3. $\alpha*$ and ξ_{the} at each temperature was again verified by fittings to the experimental results. However, the deviation of the RPL simulated M_e from the experimental data increases as temperature increases from 77 to 250 K.

T (K)	A (cm^{-1})	B (V/cm)	C (arb.)	E (kV/cm)	ξ_{the} (eV)
77	3.7929×10^4	1.8459×10^5	0.339	27-33	0.764
	1.0418×10^5	6.2404×10^5	0.353	33-53	
100	3.3839×10^4	1.2900×10^5	0.345	23-31	0.676
	7.2097×10^4	4.0550×10^5	0.340	31-50	
150	3.3787×10^4	1.0064×10^5	0.365	20-27	0.596
	4.8753×10^4	1.8348×10^5	0.358	27-47	
200	3.2818×10^4	8.5080×10^4	0.370	18-24	0.531
	5.0244×10^4	1.6737×10^5	0.362	24-42	
250	3.8157×10^4	9.5240×10^4	0.374	17-22	0.472
	5.0173×10^4	1.4431×10^5	0.370	22-37	

Table 6.3 Newly parameterised α^* from 77 to 250 K for different electric field range and the effective ξ_{the}.
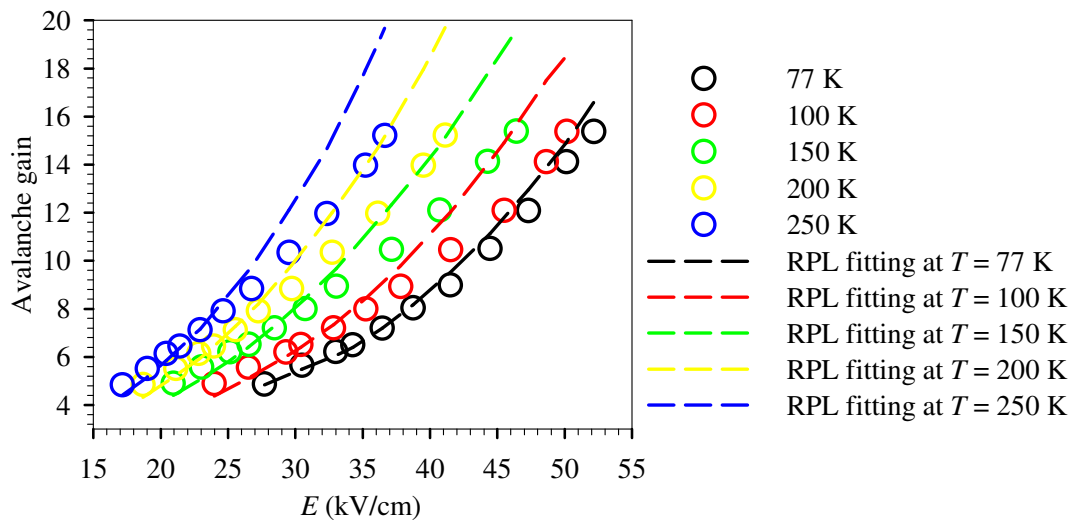

Figure 6.19 Electric field dependent avalanche gain and the RPL simulated M_e from 77 to 250 K.

As shown in figure 6.19, the RPL model could not provide reasonable fittings to the M_e of M3247 for $T > 77$ K. We believe that this is because the impact ionisation threshold of the semiconductor materials with small E_g but large Γ-X and Γ-L valley

separation energies such as InAs is soft [28]. Consequently the single effective hard threshold used in this model was unable to achieve satisfactory fittings. An analytical band Monte Carlo similar to [28] is therefore needed to provide a more accurate modelling of InAs e-APDs.

6.6   Signal to noise ratio

Although it is widely understood that an APD can provide internal gain to improve the overall sensitivity of a system, it is not obvious throughout this work that InAs APDs with excellent impact ionisation properties can improve the SNR unless they are operated in conjunction with a commercial amplifier. To investigate if the avalanche gain of the InAs APDs can provide better SNR due to low excess noise, the SNR measurements and calculations were carried out using the experimental set-up as discussed in section 3.6. The HP 8168C tunable laser was internally modulated at 1.13 kHz. Since the 3-dB bandwidth for the low noise SR570 pre-amplifier was > 20 kHz for pre-amplifier sensitivities S_{amp} > 10 µA/V, S_{amp} = 20 and 100 µA/V were used. Using a multimode fibre with a core's diameter of ~ 62.5 µm, the laser was fibre coupled onto the top of the d = 50, 75 and 150 µm devices and the measurements were carried out at 200 K due to high dark current at room temperature. The photocurrent signal was displayed on the SR760 FFT Spectrum Analyser at ~ 1.13 kHz while the noise was spread across the entire frequency range.

The SNR was first measured on the d = 150 µm MR2840 InAs APDs with S_{amp} = 20 and 100 µA/V. The SNR was calculated by taking the power ratio of the signal at 1.13 kHz to the noise level. At each sensitivity level, with the InAs APDs biased at 0.5 V (M ~ 1), the power of the laser was attenuated or reduced such that the photocurrent signal at 1.13 kHz was almost equivalent to the noise floor, producing SNR ~ 1. The SNR was measured and calculated for V_b = 0.5 to 14 V. The results are presented in figure 6.20.
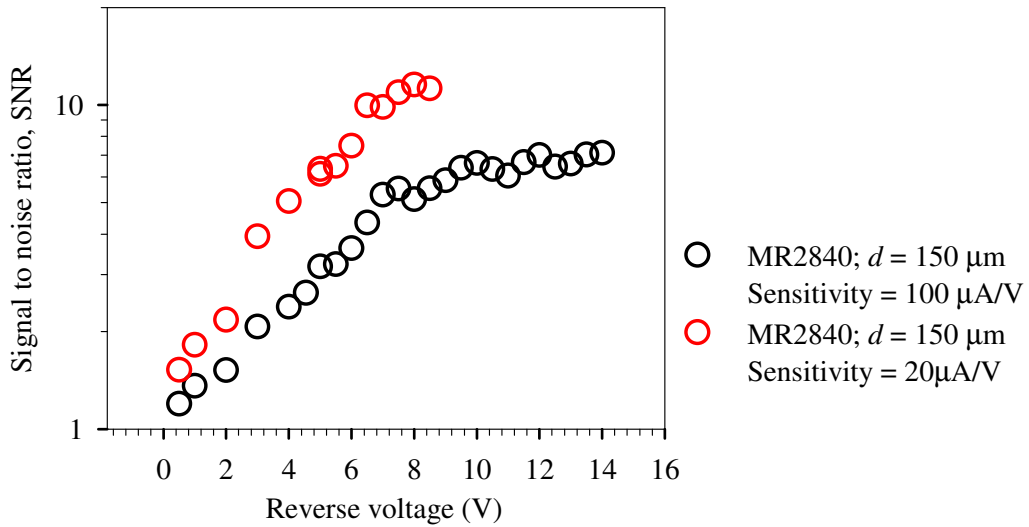
Figure 6.20 SNR for MR2840 InAs APDs with 150-µm diameter with S_{amp} = 20 and 100 µA/V.
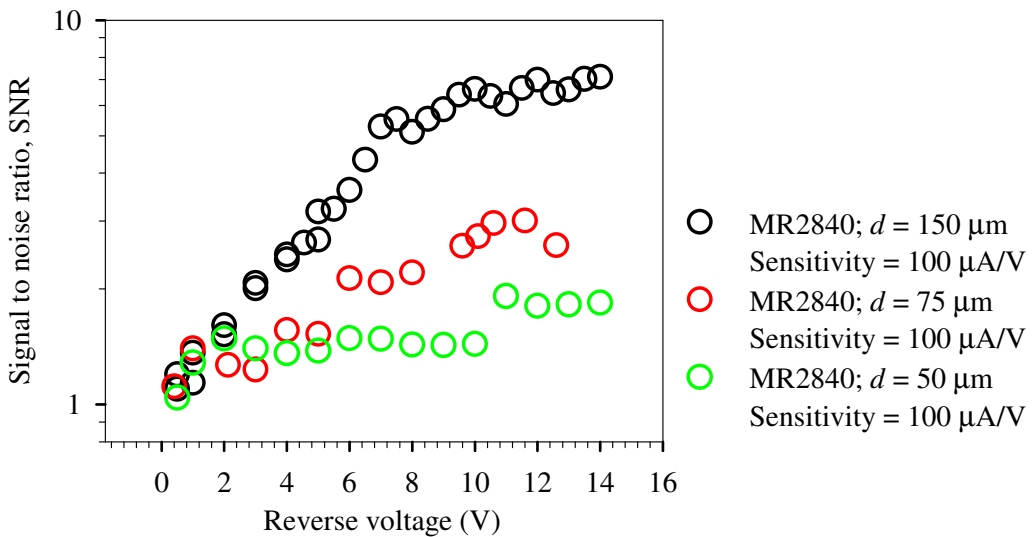
Figure 6.21 SNR for MR2840 InAs APDs with different diameters at S_{amp} = 100 µA/V.

At S_{amp} = 20 µA/V, the gain of the pre-amplifier is higher but at the expense of higher amplifier's noise [38]. Therefore, the InAs APDs were able to improve the SNR more significantly with its internal avalanche gain. On the other hand, the measurement with S_{amp} = 100 µA/V shows that the SNR increases slower when the

pre-amplifier gain and noise are lower. The SNR starts to increase slower when the contribution of noise by the dark current from the APDs is comparable to the pre-amplifier's noise at $V_b > 8$ V. It is clear that to improve the SNR of a system using an APD, the total system noise must be dominated by the amplifier's noise. It can be expected that as the bandwidth increases to the GHz range, as in the case of optical communication, the pre-amplifier's noise will be high. In this case, it will be even more advantageous in using an APD.

To obtain high SNR with its internal gain, it is equally crucial to ensure the primary carriers which initiate the avalanche gain in InAs APDs are the electrons. A brief study on the effect of the carriers' injection profile on the SNR was carried out by measuring the SNR of InAs APDs with different diameters at a fixed S_{amp}. Due to the size of the fibre core and the divergence of the laser spot, the laser spot falling on the devices was estimated to be ~ 90-µm diameter. Hence, mixed injection profile was obtained by measuring devices with diameters < 100 µm.

At S_{amp} = 100 µA/V, figure 6.21 shows the measured and calculated SNR for the InAs APDs with different diameters. Measurements on the InAs APDs with diameters from 150 to 50 µm show that the SNR increases at a slower rate for smaller devices. While the leakage current of the smaller devices is lower, the mixed injection profile causes M to reduce significantly with increasing V_b. Furthermore, as shown in figure 6.15, the excess noise increases quickly with increasing M for mixed injection, causing the degradation of the overall SNR.

The study on the effect of avalanche gain from the InAs APDs on the overall SNR shows that the internal gain can improve the SNR if the shot noise and avalanche noise from the APD are below the noise of the pre-amplifier. At low bandwidth, the pre-amplifier is able to provide very high gain with very low noise. However, as the bandwidth increases, the APDs are able to provide better SNR by amplifying the optical signal before channelling it into the pre-amplifier. Since the electrons in InAs are more readily impact ionise than holes, with $k = 0$, the injection profile is extremely crucial to ensure that maximum avalanche gain can be provided with

minimal excess noise. This study also demonstrates that for InAs APDs, pure electron injection is important to maximise the SNR and optimised APDs' structure is needed to ensure that the optical photons are fully absorbed in the *p*-layer of the InAs APDs in order to provide the highest *M* with lowest possible *F*.

6.7   Conclusion

To summarise the discussion, this chapter has experimentally concluded the followings:

   i.   The depletion widths of InAs APDs do not change for $T = 77$ to 250 K.

  ii.   The MOVPE-grown InAs has an *n*-type background doping.

 iii. M_e increases with rising temperature in InAs eAPDs.

 iv.   The field gradient and peak electric fields < 70 kV/cm do not have much influence on M_e. Instead, *W* is more critical in determining M_e, with higher M_e at a given V_b for wider *W*.

  v.   Within the accuracy of the measurement, F_e of InAs e-APDs do not change with temperatures and electric field gradients. The variation can be neglected in practical applications.

 vi.   The previously reported F_e at 77 K is lower than that newly reported here and the reason is attributed to the non-optimised measurement set-up and APD designs used previously.

 vii.   For semiconductor materials with $k = 0$ characteristics, the effect of dead space is significant even in APDs with thick *W*.

viii.   No band "resonance" was observed for $T = 77$ to 250 K.

 ix.   The local model is not appropriate in modelling InAs e-APDs due to the effect of the dead space. The non-local model which uses hard deadspace such as RPL was unable to produce a good fit to the avalanche gain results.

  x.   The SNR of a receiver system can be improved by using an InAs e-APD. Pure electron injection and low dark current are crucial in order to obtain the maximum SNR.

The excess noise and avalanche gain results also suggest that having a *p-i* InAs diode

with very thick and very lowly doped *i*-region is more desirable than a *p-i-n* structure with thinner *i*-region. Although not fully depleted, a structure with thick *i*-region can ensure the continuous increase in W with increasing V_b to achieve higher M_e. It is also important to maintain $E < 70$ kV/cm in the avalanche region to preserve the e-APD characteristics. Furthermore, maintaining $E < 70$ kV/cm will also ensure low I_{tunn}.

From the experimental results, a few distinct characteristics of InAs e-APDs are highlighted such as the weak electric field dependence of α, the positive temperature dependence of α, the onset of pure electron initiated avalanche gain at E as low as 5 kV/cm and the multiple electron impact ionisation events within a single transit through the avalanche region. These attributes are mostly opposite to the conventional behaviours of other III-V semiconductor APDs. Therefore it is important to not overlook these points because it may lead to an incorrect design and interpretation of the characteristics of InAs e-APDs.

References

[1] R. J. McIntyre, "Multiplication noise in uniform avalanche diodes," *IEEE Trans. Electron Devices,* vol. 13, pp. 164-168, 1966.

[2] A. R. J. Marshall, C. H. Tan, M. J. Steer, and J. P. R. David, "Extremely Low Excess Noise in InAs Electron Avalanche Photodiodes," *IEEE Photon. Technol. Lett.,* vol. 21, pp. 866-868, 2009.

[3] P. J. Ker, A. R. J. Marshall, A. B. Krysa, J. P. R. David, and C. H. Tan, "Temperature Dependence of Leakage Current in InAs Avalanche Photodiodes," *IEEE J. Quantum Electron.,* vol. 47, pp. 1123-1128, 2011.

[4] A. R. J. Marshall, P. Vines, P. J. Ker, J. P. R. David, and C. H. Tan, "Avalanche Multiplication and Excess Noise in InAs Electron Avalanche Photodiodes at 77 K," *IEEE J. Quantum Electron.,* vol. 47, pp. 858-864, 2011.

[5] D. J. Massey, J. P. R. David, and G. J. Rees, "Temperature dependence of avalanche multiplication in submicron silicon devices," in *Proc. 35th European Solid-State Device Research Conference*, 2005, pp. 245-248.

[6] C. Groves, R. Ghin, J. P. R. David, and G. J. Rees, "Temperature dependence of impact ionization in GaAs," *IEEE Trans. Electron Devices,* vol. 50, pp. 2027-2031, 2003.

[7]   L. J. J. Tan, D. S. G. Ong, J. S. Ng, C. H. Tan, S. K. Jones, Q. Yahong, and J. P. R. David, "Temperature Dependence of Avalanche Breakdown in InP and InAlAs," *IEEE J. Quantum Electron.,* vol. 46, pp. 1153-1157, 2004.

[8]   C. L. F. Ma, M. J. Deen, L. E. Tarof, and J. C. H. Yu, "Temperature dependence of breakdown voltages in separate absorption, grading, charge, and multiplication InP/InGaAs avalanche photodiodes," *IEEE Trans. Electron Devices,* vol. 42, pp. 810-818, 1995.

[9]   S. Hishiki, I. Kanno, O. Sugiura, R. Xiang, T. Nakamura, and M. Katagiri, "Undoped InSb Schottky detector for gamma ray measurements," in *IEEE Nuclear Science Symposium Conference Record*, 2004, pp. 937-940 Vol. 2.

[10] H. Kanbe, "Temperature dependence of multiplication noise in silicon avalanche photodiodes," *Electron. Lett.,* vol. 14, pp. 539-541, 1978.

[11] J. Yu, L. E. Tarof, R. Bruce, D. G. Knight, K. Visvanatha, and T. Baird, "Noise performance of separate absorption, grading, charge and multiplication InP/InGaAs avalanche photodiodes," *IEEE Photon. Technol. Lett.,* vol. 6, pp. 632-634, 1994.

[12] Y. G. Xiao and M. J. Deen, "Temperature dependent studies of InP/InGaAs avalanche photodiodes based on time domain modeling," *IEEE Trans. Electron Dev.,* vol. 48, pp. 661-670, 2001.

[13] X. G. Zheng, P. Yuan, X. Sun, G. S. Kinsey, A. L. Holmes, B. G. Streetman, and J. C. Campbell, "Temperature dependence of the ionization coefficients of $Al_xGa_{1-x}As$," *IEEE J. Quantum Electron. ,* vol. 36, pp. 1168-1173, 2000.

[14] M. P. Mikhailova, M. M. Smirnova, and S. V. Slobodchikov, "Carrier multiplication in InAs and InGaAs p-n junctions and their ionization coefficients," *Sov. Phys. Semicond.,* vol. 10, pp. 509-513, 1976.

[15] P. Norton, "HgCdTe infrared detectors," *Optoelectron. rev.,* vol. 10, pp. 159-174, 2002.

[16] C. H. Grein and H. Ehrenreich, "Impact ionization enhancements in $Al_xGa_{1-x}Sb$ avalanche photodiodes," *Appl. Phys. Lett.,* vol. 77, pp. 3048-3050, 2000.

[17] Z. M. Fang, K. Y. Ma, D. H. Jaw, R. M. Cohen, and G. B. Stringfellow, "Photoluminescence of InSb, InAs, and InAsSb grown by organometallic vapor phase epitaxy," *J. Appl. Phys.,* vol. 67, pp. 7034-7039, 1990.

[18] I. Vurgaftman, J. R. Meyer, and L. R. Ram-Mohan, "Band parameters for III--V compound semiconductors and their alloys," *J. Appl. Phys.,* vol. 89, pp. 5815-5875, 2001.

[19] A. R. J. Marshall, J. P. R. David, and C. H. Tan, "Impact Ionization in InAs Electron Avalanche Photodiodes," *IEEE Trans. Electron Devices,* vol. 57, pp. 2631-2638, 2010.

[20] M. Yano, M. Nogami, Y. Matsushima, and M. Kimata, "Molecular beam epitaxial growth of InAs," *Jap. J. Appl. Phys.,* vol. 16, pp. 2131-2137, 1977.

[21] J. F. Chen and A. Y. Cho, "Molecular beam epitaxy growth of InAs-AlSb-GaSb interband tunneling diodes," *J. Electron. Mater.,* vol. 22, pp. 259-265, 1993.

[22] S. A. Plimmer, C. H. Tan, J. P. R. David, R. Grey, K. F. Li, and G. J. Rees, "The effect of an electric-field gradient on avalanche noise," *Appl. Phys. Lett.,* vol. 75, pp. 2963-2965, 1999.

[23] S. C. T. M. Liew, C. H. Tan, Y. L. Goh, A. R. J. Marshall, and J. P. R. David, "Modeling of

avalanche multiplication and excess noise factor in $In_{0.52}Al_{0.48}As$ avalanche photodiodes using a simple Monte Carlo model," *J. Appl. Phys.,* vol. 104, pp. 013114-6, 2008.

[24] A. R. J. Marshall, C. H. Tan, M. J. Steer, and J. P. R. David, "Electron dominated impact ionization and avalanche gain characteristics in InAs photodiodes," *Appl. Phys. Lett.,* vol. 93, pp. 111107-3, 2008.

[25] S. M. Sze and K. K. Ng, "Physics of semiconductor devices, 3rd. Edition," John Wiley and Sons Inc., 2007.

[26] A. R. J. Marshall, "PhD Thesis: The InAs electron avalanche photodiode and the influence of thin avalanche photodiodes on receiver sensitivity," in *Electronic & Electrical Engineering*: The University of Sheffield, 2009.

[27] C. H. Tan, "PhD Thesis: Measurements of excess avalanche noise in sub-micron Si and $Al_{0.6}Ga_{0.4}As$ avalanche photodiodes," in *Electronic & Electrical Engineering*: The University of Sheffield, 2001.

[28] J. Bude and K. Hess, "Thresholds of impact ionization in semiconductors," *J. Appl. Phys.,* vol. 72, pp. 3554-3561, 1992.

[29] C. H. Tan, G. J. Rees, P. A. Houston, J. S. Ng, W. K. Ng, and J. P. R. David, "Temperature dependence of electron impact ionization in $In_{0.53}Ga_{0.47}As$," *Appl. Phys. Lett.,* vol. 84, pp. 2322-2324, 2004.

[30] J. R. Chelikowsky and M. L. Cohen, "Nonlocal pseudopotential calculations for the electronic structure of eleven diamond and zinc-blende semiconductors," *Phys. Rev. B,* vol. 14, pp. 556-582, 1976.

[31] D. C. Herbert, P. A. Childs, R. A. Abram, G. C. Crow, and M. Walmsley, "Self-consistent 2-D Monte Carlo Simulations of InSb APD," *IEEE Trans. Electron Devices,* vol. 52, pp. 2175-2181, 2005.

[32] S. Adachi, "Optical dispersion relations for GaP, GaAs, GaSb, InP, InAs, InSb, $Al_xGa_{1-x}As$, and $In_{1-x}Ga_xAs_yP_{1-y}$," *J. Appl. Phys.,* vol. 66, pp. 6030-6040, 1989.

[33] S. A. Plimmer, J. P. R. David, and D. S. Ong, "The merits and limitations of local impact ionization theory," *IEEE Trans. Electron Devices,* vol. 47, pp. 1080-1088, 2000.

[34] B. E. A. Saleh, M. M. Hayat, and M. C. Teich, "Effect of dead space on the excess noise factor and time response of avalanche photodiodes," *IEEE Trans. Electron Devices,* vol. 37, pp. 1976-1984, 1990.

[35] K. S. Lau, C. H. Tan, B. K. Ng, K. F. Li, R. C. Tozer, J. P. R. David, and G. J. Rees, "Excess noise measurement in avalanche photodiodes using a transimpedance amplifier front-end," *Measurement Sci. Technol.,* vol. 17, p. 1941, 2006.

[36] V. G. Luppov, "Low frequency probes," K. Pin Jern, Ed. Wilmington, MA: Janis Research Company, 2012.

[37] D. S. Ong, K. F. Li, G. J. Rees, J. P. R. David, and P. N. Robson, "A simple model to determine multiplication and noise in avalanche photodiodes," *J. Appl. Phys.,* vol. 83, pp. 3426-3428, 1998.

[38] S. R. System, "User Manual: SR570 Low-noise current preamplifier," 1997.

Chapter 7 Exploiting InAs e-APDs for extremely high GBP

7.1 Introduction / motivation

The development and advancement of APDs was initially driven by the optical fibre communications industry to improve the sensitivity of the receiver module. Due to the inability of Si APDs to respond to wavelengths suitable for second and third generation long-haul optical communication, InGaAs/InP APDs are the dominant APD technology in optical fibre communication receiver module. However, these InP-based APDs are mainly used for data rates up to 10 Gbps [1-4]. As data rates increase to accommodate the high volume of internet traffic, the sensitivity of the InP-based receiver is insufficient due to its limited GBP of ~ 100 - 170 GHz. For data rates > 10 Gbps, it is increasingly important to have APDs with very high GBP. Intensive research has been carried out to identify potential materials to replace InP such as InAlAs-based APDs.

Both InAlAs- and InP-based III-V optical communications APDs exploited the design of a thin avalanche region to obtain high GBP besides having low excess noise due to the effect of the deadspace [5]. However, there is a minimum tolerable *W* before the onset of tunnelling current. The optimum *W* of InP and InAlAs were reported to be ~ 200 nm [6] and ~ 150 nm [7], respectively. Yasuoka *et al.* [2] has reported a GBP of 170 GHz with 80 nm InP multiplication region at the expense of high tunnelling current. The reported GBPs for InAlAs-based APDs were also limited below 320 GHz [8-14]. The GBPs of the InP- and InAlAs-based APDs with different *W* reported to date are summarised in figure 7.1.
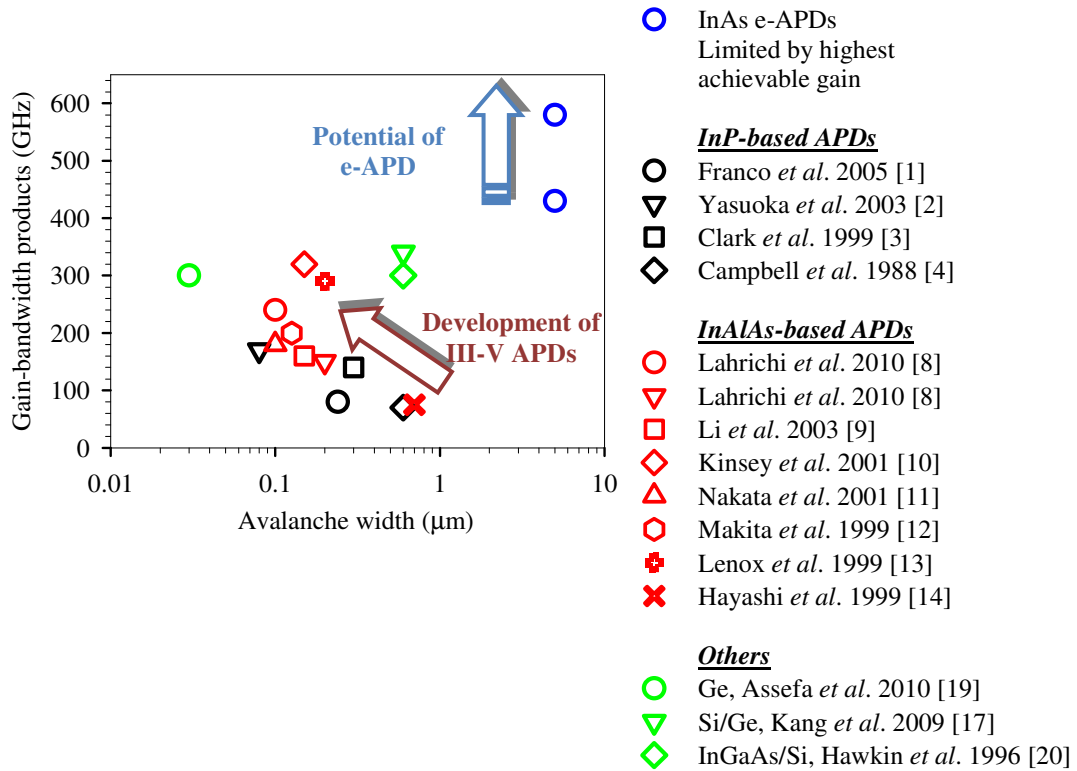
Figure 7.1 The reported GBP limits of the high bandwidth APDs with different material systems using different avalanche regions, compared to our InAs e-APDs with unlimited GBP.

It was pointed out since early theoretical work from Emmons [15] and Mcintyre [16] that the key material property that determines the GBP and excess noise of an APD is k, as discussed in chapter 2. Materials with lower k can produce higher APDs performance, with the ideal case of $k = 0$. Recently, Kang *et al.* has exploited this by using an APD incorporating a Ge absorption layer grown on a Si multiplication layer to achieve a high GBP of ~ 340 GHz, with $k = 0.09$ [17]. Zaoui *et al.* [18] further characterised these Ge/Si APDs at higher bias voltages and showed that the non local effect could increase the bandwidth but at the expense of a very high dark current. Furthermore, a Ge photodetector with avalanche region as thin as 30 nm was demonstrated to produce a GBP ~ 300 GHz [19]. The Silicon Heterointerface Photodetector (SHIP) which used the InGaAs absorption layer and Si multiplication layer was also reported to produce high GBP of ~ 300 GHz [20]. Although the characteristics of these APDs are encouraging, the GBP is still limited to a particular

value due to the impact ionisation of holes. The avalanche widths and GBPs of these APDs are also summarized in figure 7.1.

Chapter 1 has discussed that since early 2000s, APDs with $\beta = 0$ were demonstrated [21, 22] and due to their characteristics of deriving its avalanche gain from only the impact ionisation of electrons, they are referred to or classified as e-APDs. This ideal characteristic of APDs can be exploited to achieve an exponentially rising gain without a classical breakdown, very low excess noise or multiplication noise, and bandwidth that is unlimited by avalanche gain. The first two characteristics are now well established in practice as well as in theory, using the HgCdTe [21] and InAs [22-24] material systems. Perrais *et al*. have demonstrated the concept of infinite GBP by using the $Hg_{0.7}Cd_{0.3}Te$ e-APD which can provide GBPs of > 1 THz [25]. Due to the high leakage current, these e-APDs were operated at 77 K. Currently, the bandwidths of these $Hg_{0.7}Cd_{0.3}Te$ devices are limited to hundreds of MHz [25]. The motivation of this work is therefore to exploit $k = 0$ to achieve the third ideal characteristic of InAs e-APDs by obtaining extremely high GBP. This work is reported in [26].

7.2   High speed InAs e-APD structures

The fabrication of high speed InAs e-APDs was realised only after identifying the SU-8 as the most suitable surface passivation [27], as discussed in section 4.5. In addition, to achieve high GBP, the avalanche gain must be high before the onset of tunnelling current. The ability of the MOVPE to grow high quality InAs wafers with a thick *i*-layer and low unintentional background doping concentration is essential as InAs APDs with thick W can provide higher M at a particular V_b [28] and suppress the band-to-band tunnelling current.

High speed InAs *p-i-n* (MR2538) and *n-i-p* (MR2558) wafers were fabricated into vertically-illuminated APDs, as shown in figure 7.2. The details on the choice of metal, APDs design and device processing have been discussed in section 4.5.
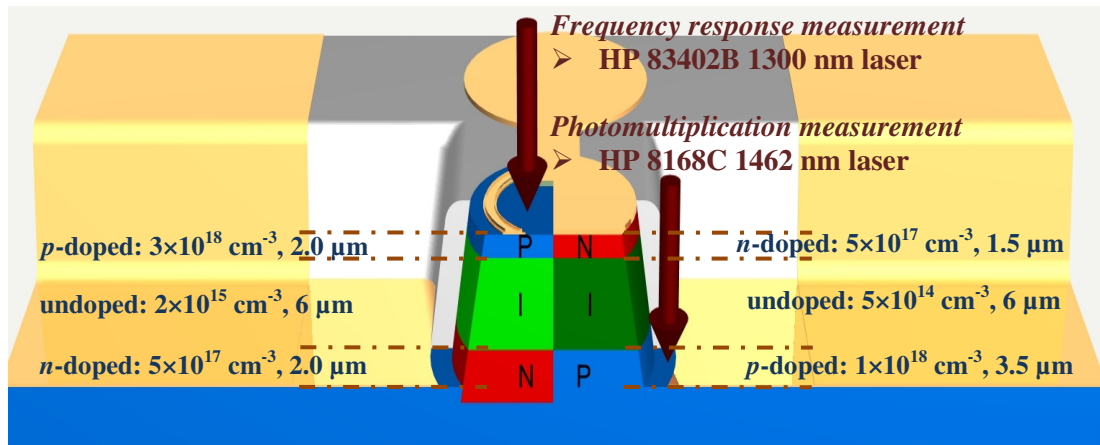
Figure 7.2 The cross-section views of the high speed InAs *p-i-n* and *n-i-p* e-APDs with their thicknesses and doping concentrations of the layers. The quoted background doping concentrations in the undoped regions are the minimum achievable doping. Also shown are the way in which the lasers are focused onto the *p*-layer during the photomultiplication and frequency response measurements to achieve pure electron injection [26].

These two InAs wafers were grown by MOVPE on InAs *p*-type substrates. The *p*- and *n*-cladding layers were highly doped to decrease the contact resistance. Due to the diffusion of dopants from the cladding layers to the *i*-layer, the background doping concentrations across the 6-µm *i*-layers are not uniform. The quoted values in figure 7.2 are the minimum achievable background dopings throughout the *i*-layers and they are derived from the *C-V* characteristics discussed in the next section.

7.3 *C-V* of high speed InAs e-APDs

In section 4.5, it has been shown that although the fabrication of high speed InAs e-APDs involves more processing steps, the *I-V* at room temperature is not degraded. However, to accurately measure the *C-V*, the leakage current must be low. Hence the *C-V*s of the InAs diodes were measured at 77 K. The *C-V*s of MR2558 devices with different diameters *d* are shown in figure 7.3. Due to the isotropic etching profile, the actual *d* of those devices were reduced effectively by ~ 15 µm. These effective *d* values of the diodes were measured under the microscope by estimating the

diameters of the active areas. Furthermore, based on the *C-V*s of the diodes, these effective values were deduced. The sizes of these high speed InAs diodes will be referred to by their effective *d* throughout this chapter.
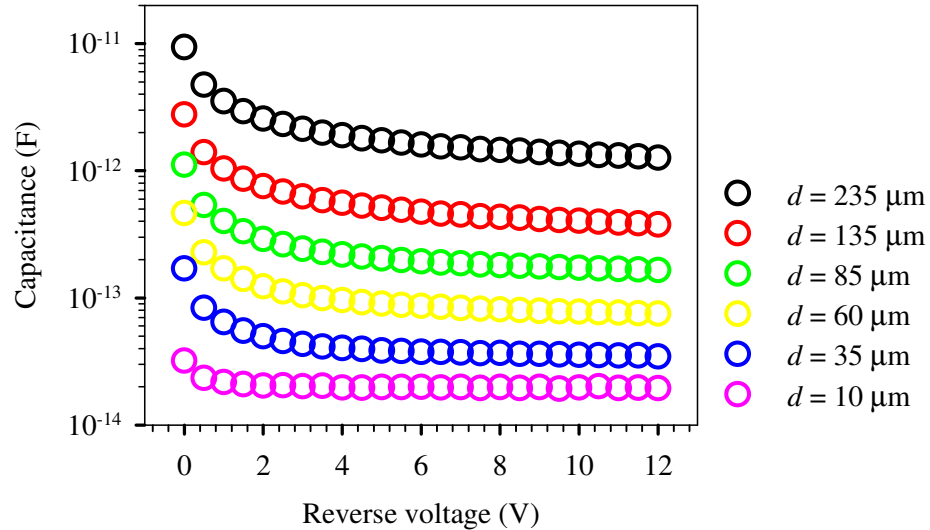

Figure 7.3 The *C-V*s of the MR2558 high speed APDs with different diameters at 77 K.
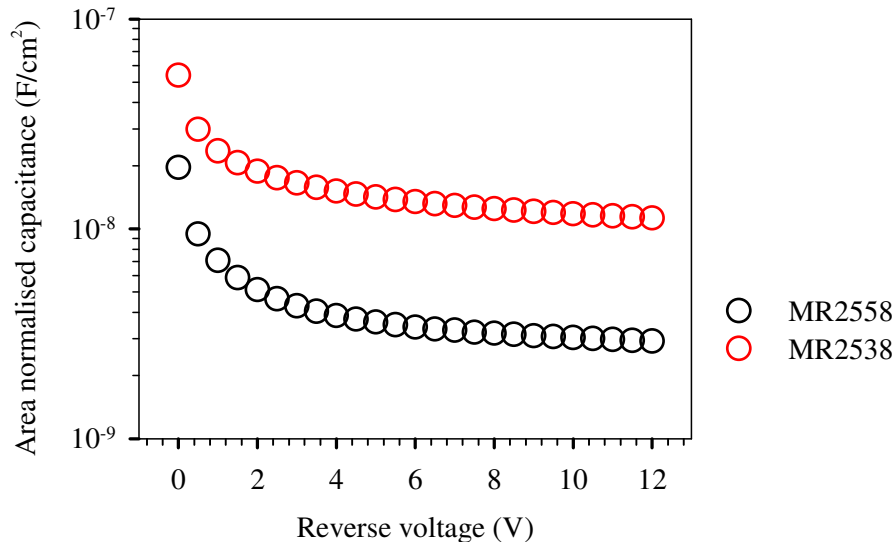

Figure 7.4 The area normalised capacitances of the MR2538 and MR2558 high speed InAs e-APDs.

Figure 7.3 shows that the capacitance of the smallest size device is limited by the parasitic capacitance, most probably due to the GSG pads. The capacitance saturates to ~20 fF for bias voltages > 1 V. Therefore, the capacitance per unit area or the area normalised capacitances of both the MR2538 and MR2558 were deduced based on the diodes with d = 60 to 235 µm. The area normalised capacitances are summarised in figure 7.4. From these values, the depletion widths and the background doping concentrations were derived. Due to the high background doping and thick *i*-layers, they are not fully depleted. MR2538 *p-i-n* diodes achieve W ~ 3 µm while MR2558 *n-i-p* diodes have W ~ 5 µm at 12 V.

7.4 Photomultiplication of high speed InAs e-APD
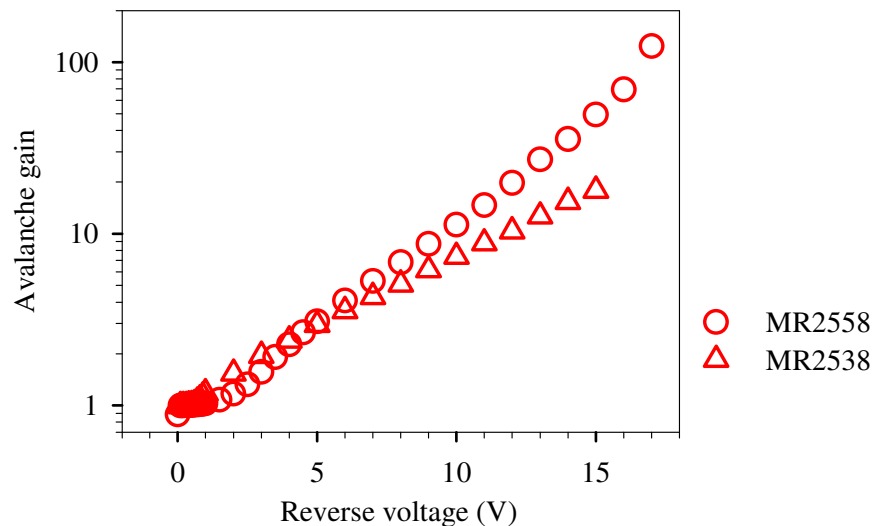
Figure 7.5 The avalanche gains of MR2538 and MR2558 high speed InAs e-APDs at room temperature.

The photomultiplication or avalanche gain of the high speed InAs e-APDs was measured using a HP8168C wavelength tuneable laser. The lowest wavelength, 1462 nm was used as this was the closest to the laser used for the frequency response measurement which will be discussed later in section 7.6. The 1462 nm laser was internally modulated at a frequency of 270 Hz using the measurement set-up described in section 3.3.2. Pure electron injection is important to obtain high

avalanche gain in InAs e-APDs, hence it is also crucial in obtaining high GBP. The designs of the InAs APD structures to achieve this for both *p-i-n* and *n-i-p* diodes are shown in figure 7.2.

The avalanche gain of the high speed InAs APDs was measured at room temperature. The pure electron initiated avalanche gains are shown in figure 7.5. It is clear that at a particular V_b, MR2558 which has a wider *W*, provides higher *M* than MR2538. In section 6.3, this effect of *W* on *M* has been discussed in more detail and it is proven to be true for fully depleted *p-i-n* junctions with uniform electric field and for single-sided depleting *p-n⁻* junctions with field gradient.

In the context of bandwidth, it can be expected that MR2558 with a wider *W* will produce lower bandwidth than MR2538 if the bandwidth is transit time dominated. This is because both the primary electron and secondary carriers will need to travel a longer distance through the depletion width, causing the current pulse to be longer. To achieve high GBP, high *M* and high bandwidth are necessary. It is therefore likely that there may be a trade-off between *M* and bandwidth in InAs e-APDs in the transit time limited bandwidth cases. However, since the carrier transit time and *M* increase linearly and exponentially with increasing *W*, respectively, it is expected that higher GBP can be obtained in InAs e-APDs with thicker *W*. Besides, wider *W* allows the measurement to be extended to higher V_b by suppressing the tunnelling current.

7.5   System calibration of the frequency response measurement

Due to the imperfect cables, bias-tee, high speed connectors, GSG probe and laser, there was power loss at different frequencies, as mentioned in section 3.5. Therefore this loss was taken into account when the frequency responses of the diodes were measured. The losses were extracted using a 2-port E8364B PNA Series VNA, as shown in figure 7.6. Port 1 is acting as a RF signal transmitter while port 2 is receiving and measuring the power. All the cables, bias-tee and high speed connectors were connected between the 2 ports and the power loss due to these components was measured.

Since the calibration of the system is very crucial so that the bandwidth of the device will not be under or overestimated, the power losses were also determined in a similar way by using the RF generating source and MTA. The RF generator transmits high-frequency signals and the MTA acts as the receiving end. The frequency responses of the calibration normalised to 100 MHz using these two methods are summarised in figure 7.7. It is clear that both the methods produce very similar results. This has confirmed and reassured that the calibration of the measurement system is accurate and reliable.
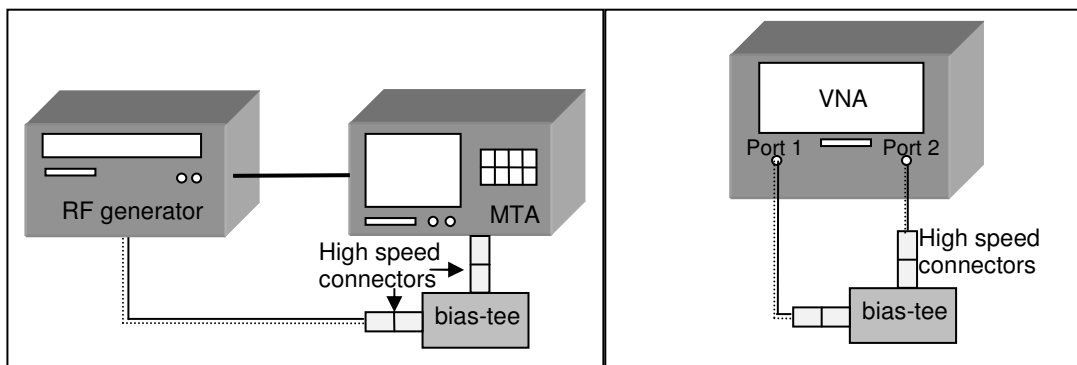
Figure 7.6 The calibration methods for the bias-tee, high speed cablings and connectors using the RF generator with MTA (left) and that using a VNA (right).
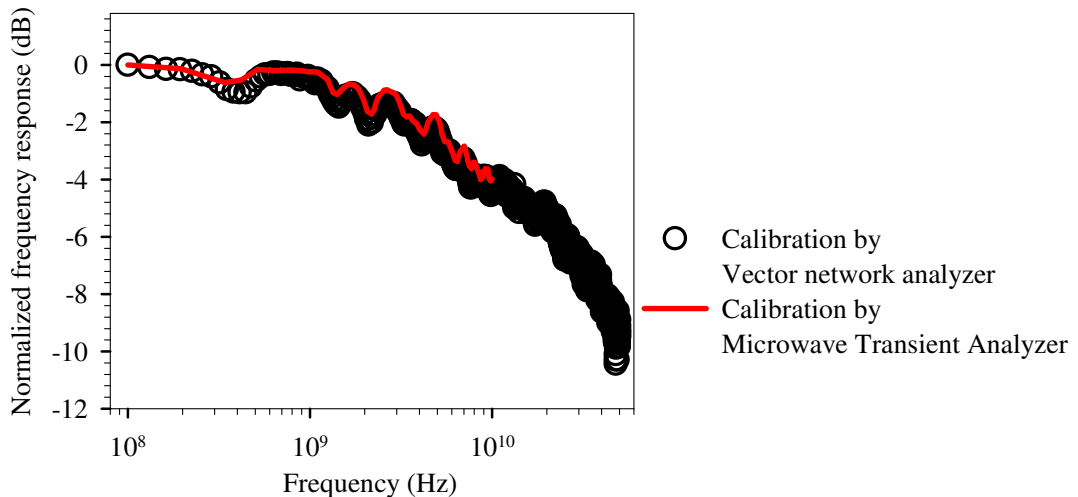
Figure 7.7 The normalised frequency response of the bias-tee, high speed cablings and connectors using the RF generator with MTA and that using a VNA.

The loss of the laser was measured by feeding the output of the laser source into an Agilent 86100B wide-bandwidth optical/electrical oscilloscope. The laser was modulated by the RF generator from 100 MHz to 10 GHz and the optical sine-wave signal was measured by the oscilloscope. The oscilloscope displayed the optical sinewave with the amplitude in units of V. It should be noted that the external trigger of the oscilloscope must be provided and an external timing reference must be connected to the trigger input connector. This is because the oscilloscope is not able to trigger directly on the test signal.

Figure 7.8 The calibration method for the 1300-nm laser using a wide-bandwidth optical oscilloscope.
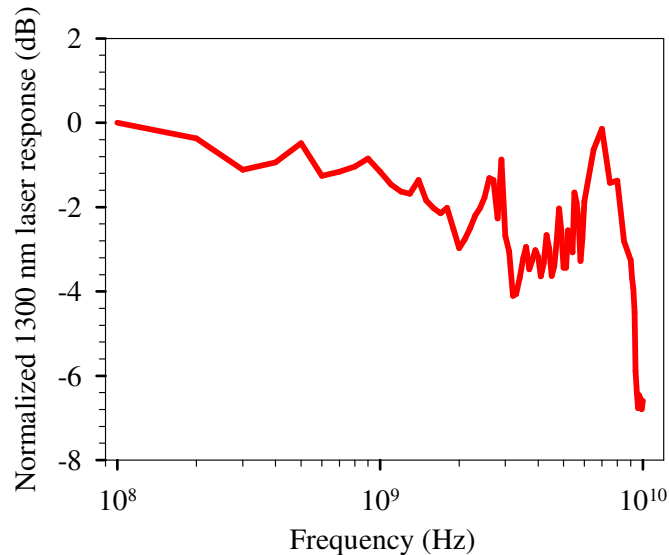
Figure 7.9 The normalised power loss of the 1300-nm laser.

The RMS voltage of the signal was measured across the frequency range and the corresponding power was calculated with a 50-Ω input impedance. The power in dBm can then be calculated and the power loss with respect to 100 MHz is computed and shown in figure 7.9.

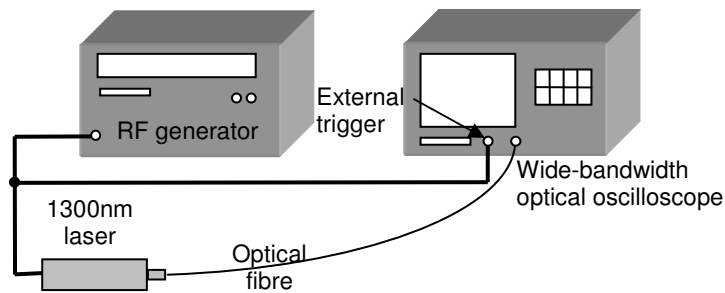Finally, the insertion loss of the 50-GHz GSG probe, which is less than 1 dB for the entire frequency range of 50 GHz, was taken from the datasheet of the Picoprobe by GGB Industries Inc. [29]. All the losses were added (in dB) with respect to 100 MHz. Throughout the frequency response measurement, which will be discussed in the next section, the same cables, bias-tee, high speed connectors, laser and GSG probe were used.

7.6   Frequency response and gain-bandwidth product

The frequency response measurement was carried out on both the MR2538 and MR2558 high speed InAs e-APDs. The equipments and measurement set-up have been described in detail in section 3.5. The system calibration results described in the last section were used to calculate the actual frequency response of the high speed InAs e-APDs.

Figure 7.10 The normalised frequency responses of the MR2538 and MR2558 high speed InAs e-APDs with diameters of 10 to 85 µm at 77 K and room temperature. The modelled 3-dB bandwidths for $W = 3$ and 5 µm plotted for comparison.

It is surprising that the 3-dB bandwidth of both the MR2538 and MR2558 are limited to ~ 3.5 GHz at both 77 K and room temperature. This bandwidth is not *RC*-limited as both the MR2558 and MR2538 have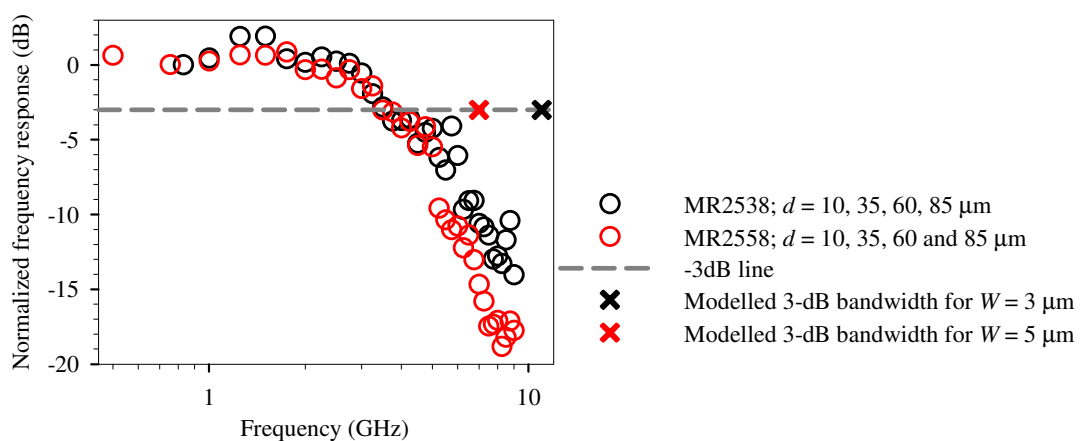 different contact resistance and very different depletion widths, hence the capacitances are different. Furthermore, besides the devices with *d* = 135 and 235 µm which are clearly *RC*-limited, the frequency responses from both the *p-i-n* and *n-i-p* high speed InAs e-APDs with *d* = 10, 35, 60 and 85 µm are very similar. For clarity purpose, these identical results are summarised in figure 7.10.

Gain, *M*	Simulated 3-dB bandwidth (GHz)			
	W = 3 µm	*W* = 4 µm	*W* = 5 µm	*W* = 6 µm
1	12.281	9.181	7.317	5.935
2	11.597	8.734	6.974	5.807
10	10.394	7.786	6.236	5.194
100	10.355	7.765	6.214	5.177

Table 7.1 The modelled 3-dB bandwidths for *k* = 0 APDs with *W* = 3 to 6 µm for *M* = 1 to 100 using the RPL model by assuming v_{se} = 1.5×10^5 m/s and v_{sh} = 0.75×10^5 m/s.

From the discussion in section 7.4, it is expected that MR2538 can produce a higher 3-dB bandwidth than MR2558. This is because the carrier transit time is much shorter in MR2538 due to thinner *W*. To estimate the 3-dB bandwidth of these devices due to carrier transit and avalanche build-up time, the RPL model was used. With the *k* = 0 characteristic and without the effect of the deadspace, devices with *W* = 3 to 6 µm were simulated. The saturation drift velocity of electron v_{se} in InAs was reported to be 1.5×10^5 m/s [30]. Since there is no value reported for holes, the saturation velocity of hole v_{sh} in InGaAs was taken as 0.75×10^5 m/s [31]. Uniform electric fields were assumed across the depletion region and the current pulses were computed. The 3-dB bandwidths were calculated by Fast-Fourier Transform using

the MATLAB software. The simulation was carried out for different M values. The results are summarised in table 7.1.

Clearly, from table 7.1, the bandwidths of the diodes decrease with increasing W. Matching the $k = 0$ characteristics, as M increases, the bandwidths do not roll-off even up to $M = 100$. The bandwidths are not limited by the avalanche build-up time as they are for $k > 0$ material systems at high M. For MR2538 and MR2558 high speed InAs e-APDs with $W = 3$ and 5 µm, respectively, 3-dB bandwidth of ~ 3.5 GHz is definitely way lower than what it is expected, as plotted in figure 7.10. According to the simulated results, these values should be between 7 and 11 GHz. Therefore, the 3.5-GHz measured bandwidth is certainly neither carrier transit nor avalanche build-up time limited despite having very wide W.

Following from the above discussion, the carrier transit time, avalanche build up time and RC time are ruled out as the root cause for limiting the 3-dB bandwidth of the InAs e-APDs. The frequency responses at 77 K and room temperature also show that the 3.5-GHz bandwidth is temperature insensitive. As described in section 4.5, a few different designs of GSG pads were included in the mask set to evaluate the effect of GSG pads on the frequency response of the diodes. These different designs of signal tracks and GSG pads have also proven that the capacitance between the GSG pads and the parasitic capacitance between the signal tracks and the p-type conducting substrate are not the limiting factors. Therefore, the parasitic effect associated to the SU-8 as a dielectric material is considered to be restricting the bandwidth to ~ 3.5 GHz. This is because the material properties of SU-8 at high frequencies are not well studied and understood. However, proofing the infinite GBP with $k = 0$ characteristics of InAs can still be made possible if the APDs can provide very high M and the ~ 3.5 GHz bandwidth remains. Therefore subsequent measurements were done on MR2558 because it could produce much higher M. The suppression of tunnelling current due to the wider W in MR2558 also enabled measurement to be taken up to higher V_b.
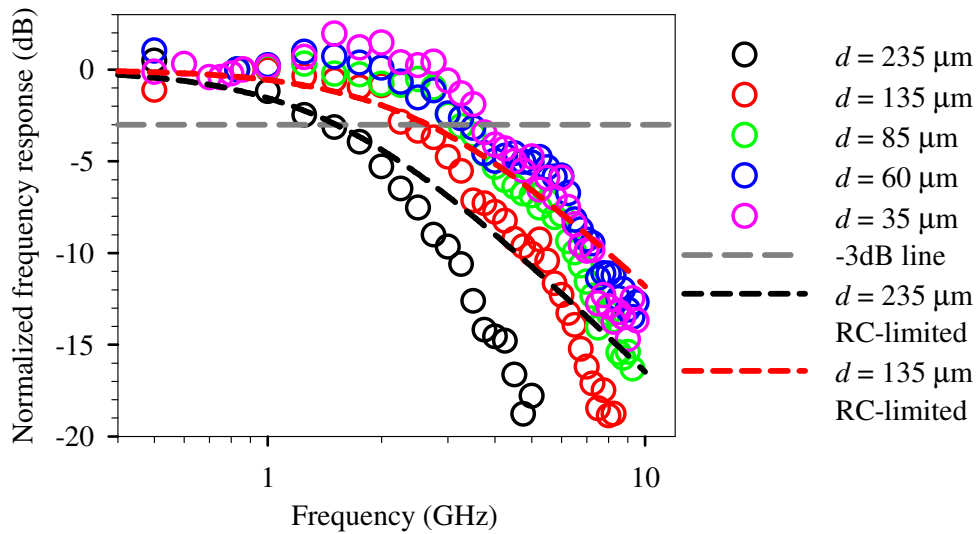
Figure 7.11 The normalised frequency responses of MR2558 high speed InAs e-APDs with d = 35 to 235 µm at V_b = 10 V. Modelled *RC*-limited responses of the d = 235 and 135 µm devices [26].

The frequency responses of all sizes of MR2558 high speed devices were measured at 77 K and room temperature. There is no observable difference in the frequency response at different temperatures. The frequency responses of the devices at V_b = 10 V are shown in figure 7.11. The two largest devices demonstrate bandwidths which are *RC*-limited. The value of *R* has been discussed in section 4.5.2, with *R* = 20 and 70 Ω for devices with d = 235 and 135 µm, respectively. Their capacitances are calculated from the area normalised capacitance presented in section 7.3. The *RC*-limited bandwidths were simulated using LT-SPICE with the fitted and calculated *R* and *C*. The 50 Ω contributed by the system was included into the value of *R* when the simulation was carried out. The modelled results are plotted together in figure 7.11 for comparison.

For devices with $d \leq 85$ µm, the 3-dB bandwidth is limited to ~ 3.5 GHz at low *M*, as shown in figure 7.11. The avalanche gain was measured using phase sensitive detection, as described in section 7.4. The dark current, photocurrent and avalanche gain of the MR2558 InAs e-APDs are shown in figure 7.12.
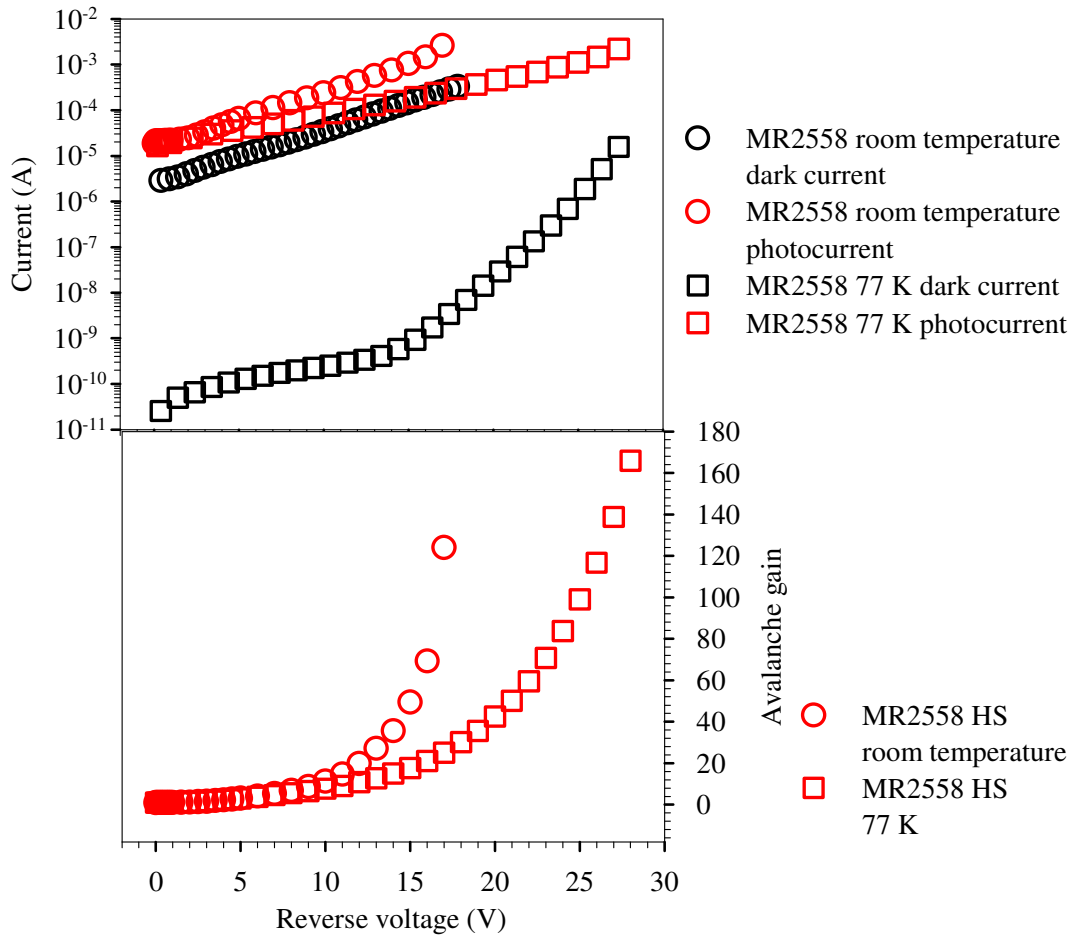
Figure 7.12 The dark currents and photocurrents (top) of a 50-µm diameter MR2558 InAs e-APDs. The avalanche gain (bottom) of the InAs e-APDs at different reverse bias voltages at room temperature and 77 K.

The frequency response and M were measured for each V_b to deduce the GBP of the devices. The 3-dB bandwidths at different M are presented in figure 7.13. Unlike other conventional APDs where the bandwidth rolls-off at high M, the InAs e-APDs possess a bandwidth that is not limited by M, with the highest GBP of ~ 430 and ~ 580 GHz at room temperature and 77 K, respectively [26]. The fluctuation between 3.5 and 4 GHz is mainly due to experimental limitation and should not be treated as the change in 3-dB bandwidth. It is worth noting that these GBP values are limited by the maximum achievable stable M in these InAs prototype diodes. As the technology matures further, especially in terms of growth and fabrication of InAs e-

APD, the leakage current is expected to be lower and higher *M* could be achieved, potentially providing GBP exceeding 1 THz.
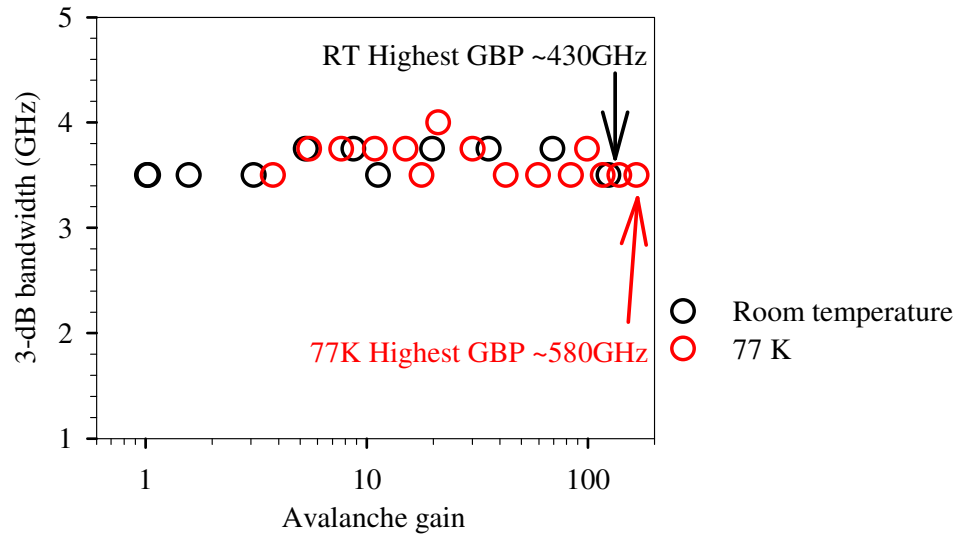
Figure 7.13 The 3-dB bandwidth of the MR2558 high speed InAs e-APD with different avalanche gain at room temperature and 77 K [26].

7.7 Frequency response at > 10 GHz

Although the 3-dB bandwidth of the InAs e-APD is limited to ~ 3.5 GHz, its bandwidth that is unlimited by the avalanche gain will potentially allow it to be utilised for applications at > 10 Gbps while providing sufficiently high internal gain to improve the system sensitivity. To study the frequency response of the InAs e-APD at frequencies > 10 GHz, measurements using the VNA were carried out at room temperature, as discussed in section 3.5. As in other measurement systems, this set-up has a certain noise floor across the whole measured frequency range. Figure 7.14 shows the noise when the GSG probe was open-circuited. It can be seen that at frequencies > 16 GHz, the system noise increases dramatically by > 20 dB and this will be shown later to be the major hindrance in measuring the frequency response at frequencies > 15 GHz.
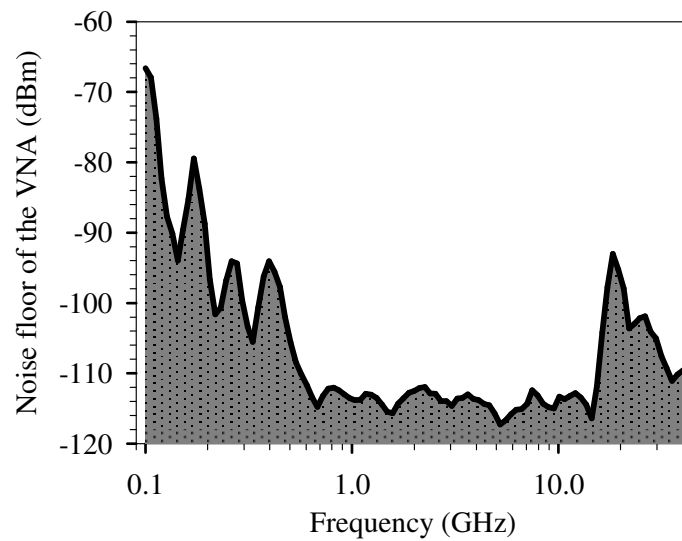
Figure 7.14 The noise floor of the measurement system with the VNA at frequencies from 0.1 to 40 GHz.

The absolute measured power at 200 MHz, 1, 10, 15 and 20 GHz are shown in figure 7.15. It is clear that due to the high noise floor at frequencies > 16 GHz, the signal powers measured at 20 GHz are still within the system noise even at the highest V_b. However, with $M > 4$ at $V_b > 5$ V, the signal powers at 10 and 15 GHz are amplified above the noise floor. At the highest $V_b = 15$ V, the signal power at 15 GHz can still be amplified by ~ 23 dB above the system noise floor. The comparison with the power gain at 200 MHz and 1 GHz also shows that the signal powers are amplified by similar amplitudes regardless of the frequency of the signal. Figure 7.16 shows the avalanche gain measured at $V_b = 15$ V using the LIA and VNA at different frequencies from 270 Hz to 15 GHz. There is a small fluctuation in the calculated gain from VNA due to the limitation of the measurements and derivation of the voltage gain from the power gain. However, the similarity of M regardless of the signal frequency again shows the $k = 0$ characteristics of the InAs e-APDs since the bandwidth is not limited by its avalanche build-up time.
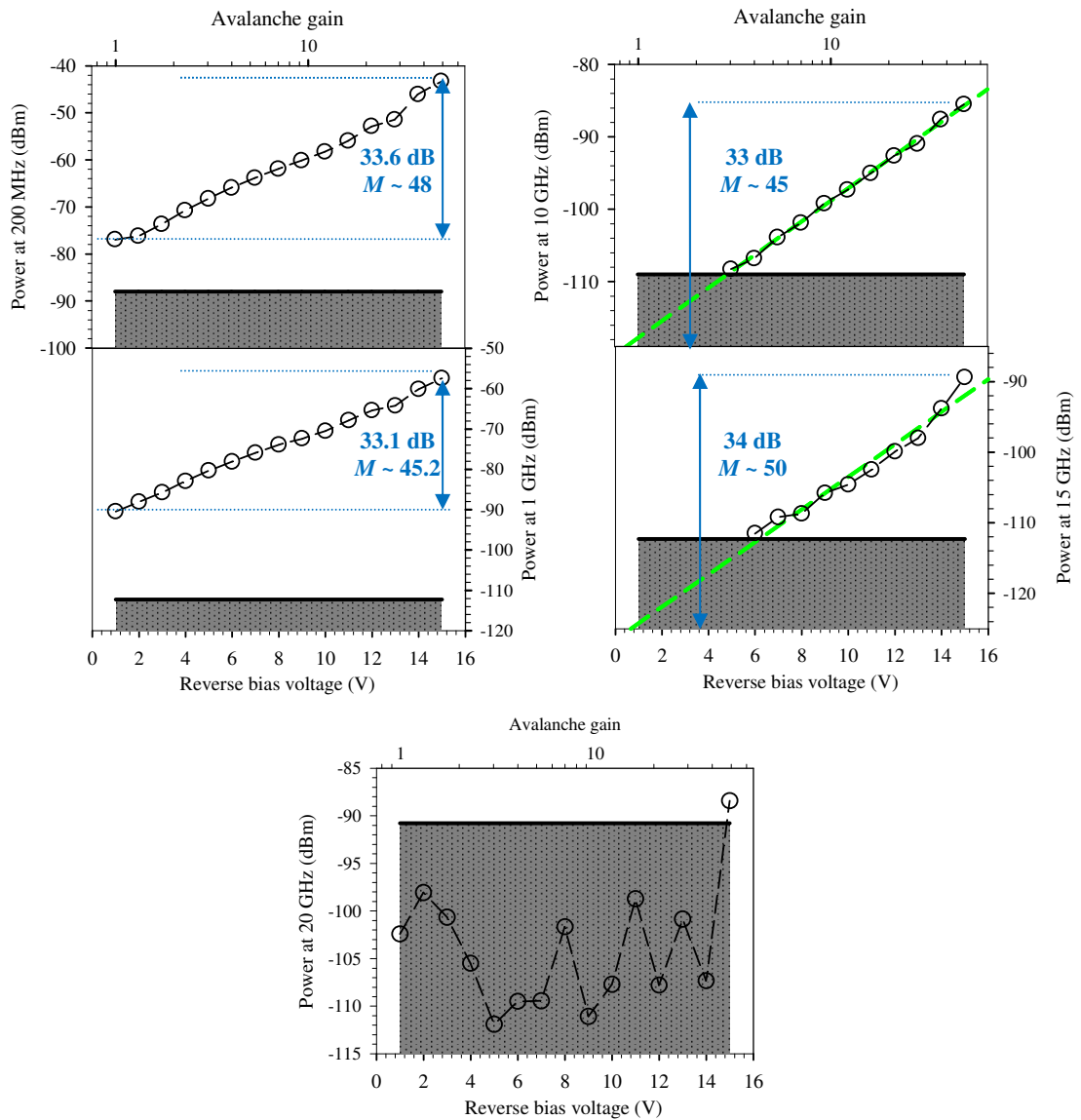
Figure 7.15 The measured power at 200 MHz, 1, 10, 15 and 20 GHz for different bias voltages at room temperature.

This measurement showed that even with a non-optimised device structure and non-ideal dielectric for surface passivation, the InAs e-APDs are still able to provide useful avalanche gain to produce sufficiently high signal power for detection at 15 GHz. Hence it is believed that the InAs e-APDs can be exploited for applications up to 20 Gbps despite the 3-dB bandwidth of ~ 3.5 GHz. In addition, due to the onset of avalanche gain at very low V_b, the InAs e-APDs can be operated at low operating voltage, therefore consuming much less power than the conventional InP-based

APDs. Operating the 20-Gbps InAs e-APDs in 2×20 Gbps parallel integrated optical receiver [32], InAs e-APDs can potentially be used as low noise and low operating power APDs in 40-Gbps optical communication.
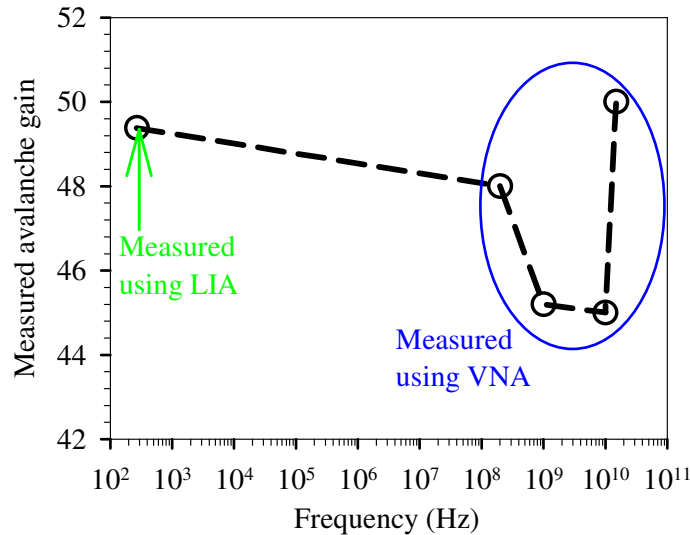
Figure 7.16 The calculated M at V_b = 15 V at room temperature for different frequencies from 270 Hz to 15 GHz.

7.8   Conclusion

High speed InAs e-APDs have been fabricated after identifying SU-8 as the suitable surface passivation of the etched mesa sidewalls. The optimised MOVPE growth conditions have made the growth of thick InAs layers with low background doping possible, producing InAs e-APDs with higher M at a particular V_b. The frequency responses of the e-APDs with $W = 3$ and 5 µm were measured, producing similar 3-dB bandwidth of ~ 3.5 GHz. The transit time, avalanche build up time, RC-time and the design of the signal tracks were ruled out as the factors which limit the bandwidth to 3.5 GHz. Instead, the parasitic effect due to the SU-8 dielectric material was considered to be the limiting factor. Growing the InAs structure on a semi-insulating substrate may be able to eliminate this effect to produce higher bandwidth, as reported recently by Shi *et al*. [33] for InAs photodiodes. However, it involves very

challenging growth of InAs on a lattice-mismatched substrate, causing high leakage current, which inhibits APD operation.

Despite having low 3-dB bandwidth of ~ 3.5 GHz, the avalanche gain and frequency response of the MR2558 InAs e-APDs were demonstrated to produce very high GBPs of ~ 580 GHz and 430 GHz at 77 K and room temperature, respectively. Although it was theoretically made known that materials with $k = 0$ can provide gain-unlimited bandwidth, this is one of the very first practical work that exploits the e-APD's characteristics to achieve extremely high GBP, potentially exceeding 1 THz.

Further characterisation of these high speed InAs e-APDs at frequencies > 10 GHz demonstrate the potential of using InAs e-APDs for 20-Gbps applications. Due to the property of having a bandwidth that is not limited by its avalanche gain, the internal gain provided by the InAs e-APDs is able to amplify the 15-GHz signal by ~ 23 dB above the noise floor. Further improvement in growth and fabrication is likely to reduce the leakage current at room temperature, which can make InAs e-APDs to be more attractive for optical fibre communication. Moreover, the InAs e-APD with thick *W* also allows APDs with larger sizes to be used for non-fibre based imaging and sensing applications without the bandwidth being *RC*-limited.

References

[1]   D. S. Franco, K. Vaccaro, W. R. Clark, W. A. Teynor, H. M. Dauplaise, M. Roland, B. Krejca, and J. P. Lorenzo, "High-performance InGaAs-InP APDs on GaAs," *IEEE Photon. Technol. Lett.,* vol. 17, pp. 873-874, 2005.

[2]   N. Yasuoka, H. Kuwatsuka, M. Makiuchi, T. Uchida, and A. Yasaki, "Large multiplication-bandwidth products in APDs with a thin InP multiplication layer," in *16th Annual Meeting of the IEEE LEOS 2003.*, 2003, pp. 999-1000 vol.2.

[3]   W. R. Clark, A. Margittai, J. P. Noel, S. Jatar, H. Kim, E. Jamroz, G. Knight, and D. Thomas, "Reliable, high gain-bandwidth product InGaAs/InP avalanche photodiodes for 10 Gb/s receivers," in *Optical Fiber Communication Conference, 1999*, 1999, pp. 96-98 vol.1.

[4]   J. C. Campbell, W. T. Tsang, G. J. Qua, and B. C. Johnson, "High-speed InP/InGaAsP/InGaAs avalanche photodiodes grown by chemical beam epitaxy," *IEEE J. Quantum Electron.,* vol. 24, pp. 496-500, 1988.

[5] K. A. Anselm, H. Nie, C. Hu, C. Lenox, P. Yuan, G. Kinsey, J. C. Campbell, and B. G. Streetman, "Performance of thin separate absorption, charge, and multiplication avalanche photodiodes," *IEEE J., Quantum Electron.,* vol. 34, pp. 482-490, 1998.

[6] D. S. G. Ong, N. Jo Shien, M. M. Hayat, S. Peng, and J. David, "Optimization of InP APDs for High-Speed Lightwave Systems," *J. Lightwave Technol.,* vol. 27, pp. 3294-3302, 2009.

[7] Y. L. Goh, D. J. Massey, A. R. J. Marshall, J. S. Ng, C. H. Tan, W. K. Ng, G. J. Rees, M. Hopkinson, J. P. R. David, and S. K. Jones, "Avalanche Multiplication in InAlAs," *IEEE Trans. Electron Devices,,* vol. 54, pp. 11-16, 2007.

[8] M. Lahrichi, G. Glastre, E. Derouin, D. Carpentier, N. Lagay, J. Decobert, and M. Achouche, "240-GHz Gain-Bandwidth Product Back-Side Illuminated AlInAs Avalanche Photodiodes," *IEEE Photon. Technol. Lett. ,* vol. 22, pp. 1373-1375.

[9] N. Li, R. Sidhu, X. Li, F. Ma, X. Zheng, S. Wang, G. Karve, S. Demiguel, A. L. Holmes, and J. C. Campbell, "InGaAs/InAlAs avalanche photodiode with undepleted absorber," *Appl. Phys. Lett.,* vol. 82, pp. 2175-2177, 2003.

[10] G. S. Kinsey, J. C. Campbell, and A. G. Dentai, "Waveguide avalanche photodiode operating at 1.55 μm with a gain-bandwidth product of 320 GHz," *IEEE Photon. Technol. Lett.,* vol. 13, pp. 842-844, 2001.

[11] T. Nakata, T. Takeuchi, K. Makita, Y. Amamiya, Y. Suzuki, and T. Torikai, "An ultra high speed waveguide avalanche photodiode for 40-Gb/s optical receiver," in *27th European Conference on Optical Communication, 2001.*, 2001, pp. 564-565 vol.4.

[12] K. Makita, T. Nakata, I. Watanabe, and K. Taguchi, "High-frequency response limitation of high performance InAlGaAs/InAlAs superlattice avalanche photodiodes," *Electron. Lett.,* vol. 35, pp. 2228-2229, 1999.

[13] C. Lenox, H. Nie, P. Yuan, G. Kinsey, A. L. Homles, Jr., B. G. Streetman, and J. C. Campbell, "Resonant-cavity InGaAs-InAlAs avalanche photodiodes with gain-bandwidth product of 290 GHz," *IEEE Photon. Technol. Lett.,* vol. 11, pp. 1162-1164, 1999.

[14] M. Hayashi, I. Watanabe, T. Nikata, K. Makita, S. Yamakata, and K. Taguchi, "Microlens-integrated large-area InAlGaAs-InAlAs superlattice APD's for eye-safety 1.5-µm wavelength optical measurement use," *IEEE Photon. Technol. Lett.,* vol. 10, pp. 576-578, 1998.

[15] R. B. Emmons, "Avalanche-Photodiode Frequency Response," *J. App. Phys.,* vol. 38, pp. 3705-3714, 1967.

[16] R. J. McIntyre, "Multiplication noise in uniform avalanche diodes," *IEEE Trans. Electron Devices,* vol. 13, pp. 164-168, 1966.

[17] Y. Kang, H.-D. Liu, M. Morse, M. J. Paniccia, M. Zadka, S. Litski, G. Sarid, A. Pauchard, Y.-H. Kuo, H.-W. Chen, W. S. Zaoui, J. E. Bowers, A. Beling, D. C. McIntosh, X. Zheng, and J. C. Campbell, "Monolithic germanium/silicon avalanche photodiodes with 340 GHz gain-bandwidth product," *Nat Photon,* vol. 3, pp. 59-63, 2009.

[18] W. S. Zaoui, H.-W. Chen, J. E. Bowers, Y. Kang, M. Morse, M. J. Paniccia, A. Pauchard, and J. C. Campbell, "Frequency response and bandwidth enhancement in Ge/Si avalanche photodiodes with over 840GHz gain-bandwidth-product," *Opt. Express,* vol. 17, pp. 12641-12649, 2009.

[19] S. Assefa, F. Xia, and Y. A. Vlasov, "Reinventing germanium avalanche photodetector for nanophotonic on-chip optical interconnects," *Nature Lett.,* vol. 464, pp. 80-84, 2010.

[20] A. R. Hawkins, W. Wu, P. Abraham, K. Streubel, and J. E. Bowers, "High gain-bandwidth-product silicon heterointerface photodetector," *Appl. Phys. Lett.,* vol. 70, pp. 303-305, 1997.

[21] J. Beck, C. Wan, M. Kinch, J. Robinson, P. Mitra, R. Scritchfield, F. Ma, and J. Campbell, "The HgCdTe electron avalanche photodiode," *J. Electron. Materials,* vol. 35, pp. 1166-1173, 2006.

[22] A. R. J. Marshall, C. H. Tan, M. J. Steer, and J. P. R. David, "Electron dominated impact ionization and avalanche gain characteristics in InAs photodiodes," *Appl. Phys. Lett.,* vol. 93, pp. 111107-3, 2008.

[23] A. R. J. Marshall, C. H. Tan, M. J. Steer, and J. P. R. David, "Extremely Low Excess Noise in InAs Electron Avalanche Photodiodes," *IEEE Photon. Technol. Lett.,* vol. 21, pp. 866-868, 2009.

[24] A. R. J. Marshall, P. Vines, P. J. Ker, J. P. R. David, and C. H. Tan, "Avalanche Multiplication and Excess Noise in InAs Electron Avalanche Photodiodes at 77 K," *IEEE J. Quantum Electron.,* vol. 47, pp. 858-864, 2011.

[25] G. Perrais, J. Rothman, G. Destefanis, and J.-P. Chamonal, "Impulse response time measurements in $Hg_{0.7}Cd_{0.3}Te$ MWIR avalanche photodiodes," *J. Electron. Materials,* vol. 37, pp. 1261-1273, 2008.

[26] A. R. J. Marshall, P. J. Ker, A. Krysa, J. P. R. David, and C. H. Tan, "High speed InAs electron avalanche photodiodes overcome the conventional gain-bandwidth product limit," *Opt. Express,* vol. 19, pp. 23341-23349, 2011.

[27] P. J. Ker, A. R. J. Marshall, A. B. Krysa, J. P. R. David, and C. H. Tan, "Temperature Dependence of Leakage Current in InAs Avalanche Photodiodes," *IEEE J., Quantum Electron.,* vol. 47, pp. 1123-1128, 2011.

[28] A. R. J. Marshall, J. P. R. David, and C. H. Tan, "Impact Ionization in InAs Electron Avalanche Photodiodes," *IEEE Trans. Electron Devices,* vol. 57, pp. 2631-2638, 2010.

[29] "50 GHz ground-signal-ground high performance microwave probe datasheet, Picoprobe GGB Industries Inc."

[30] G. Satyanadh, R. P. Joshi, N. Abedin, and U. Singh, "Monte Carlo calculation of electron drift characteristics and avalanche noise in bulk InAs," *J. Appl. Phys.,* vol. 91, pp. 1331-1338, 2002.

[31] P. Hill, J. Schlafer, W. Powazinik, M. Urban, E. Eichen, and R. Olshansky, "Measurement of hole velocity in n-type InGaAs," *Appl. Phys. Lett.,* vol. 50, pp. 1260-1262, 1987.

[32] A. Polzer, W. Gaberl, R. Swoboda, P. Brandl, J. M. Fedeli, C. Kopp, L. Vivien, and H. Zimmermann, "High sensitivity 80 Gbps parallel optical receiver for hybrid integrated Ge photodiodes," in *8th IEEE International Conference on Group IV Photonics (GFP), 2011* pp. 86-88.

[33] J. W. Shi, F. M. Kuo, and B. R. Huang, "Zn-Diffusion InAs Photodiodes on a Semi-Insulating GaAs Substrate for High-Speed and Low Dark-Current Performance," *IEEE Photon. Technol. Lett.,* vol. 23, pp. 100-102, 2011.

Chapter 8 Conclusion and proposed further work

8.1   Conclusion

It was reported back in the 1960s that the band structures of InAs and InSb [1] could produce characteristics which are ideal for APDs. However, there is little literature reporting a comprehensive study of their impact ionisation properties, possibly due to the high leakage current at high bias voltages, resulting from their narrow bandgaps. Until recently, Marshall *et al.* have produced a fabrication recipe for InAs diodes [2] to reduce the surface leakage current significantly, such that the avalanche characteristics at room temperature could be investigated. Therefore, the research work reported in this thesis was targeted to further reduce the dark current of InAs APDs by etched mesa surface passivation, to study the avalanche properties of InAs APDs with different designs and operating conditions, and to develop APDs with very high GBP based on the impact ionisation characteristics of InAs.

The fabrication recipe of InAs diodes using wet chemical etchants has been revisited in chapter 4. The surface passivation using different dielectric materials such as SU-8, BCB, SiO_2 and SiN_x were investigated with SU-8 being identified as the most effective dielectric in reducing the surface leakage current, especially below room temperature. The SU-8 surface passivation has also increased the robustness of the InAs APDs such that they can withstand higher bias voltages, which will be proven to be critical when InAs APDs are utilised in practical applications. Without having a semi-insulating substrate that is lattice-matched to InAs, the discovery of this suitable dielectric has made the fabrication of high speed InAs APDs possible by providing a flat insulting film for the deposition of GSG pads. Before fabricating the high speed InAs diodes, Ti/Pt/Au and Ti/Au were identified as the most suitable

metals for the *p-* and *n-*contacts, respectively, after taking into consideration the low contact resistances and low leakage current. A new mask set was designed to suit the isotropic and deep etching profile of InAs diodes. The heat and UV curing of SU-8 dielectric were also optimised. With a set of well-controlled fabrication procedures, the dark current densities of the high speed InAs APDs remained low despite going through a more complicated fabrication process. In addition, the temperature dependence of the spectral responses of a packaged InAs diode was measured using a FTIR spectrometer and the variation of bandgaps with temperatures agreed well with those which were previously reported using photoluminiscene [3].

Chapter 5 analysed the temperature dependence of the leakage current in SU-8 passivated InAs APDs and identified the bulk and surface leakage current mechanisms with their respective activation energies. The analysis also enabled the estimation of the leakage current of InAs diodes with different dimensions at different operating temperatures. By operating the InAs APD at temperatures achievable by thermoelectric cooling, the APD can provide useful gain while satisfying the minimum $R_D A$ requirements of most of the commercially available ROICs. This chapter also discussed and compared the responsivity and detectivity of our InAs diodes with those of the commercial InAs photodiodes. The high responsivity and low dark current density of the InAs diodes led to either higher or comparable detectivity with commercial InAs photodiodes. Furthermore, the ability to provide $M > 20$ with a gain-normalised dark current density of 5×10^{-6} A/cm^2 at 77 K has demonstrated the potential of InAs APDs for infrared sensing applications.

The study of the avalanche gain and excess noise characteristics in chapter 6 aimed at providing a clearer idea in designing and operating an InAs APDs. Within the practical operating temperatures of InAs APDs, the depletion widths do not change with temperatures. This has confirmed that the reduction in M_e with decreasing T was mainly due to the change in ionisation parameters in InAs. The avalanche gains of InAs APDs with different electric field profiles were investigated and the depletion width was determined to be the dominant factor that influenced M_e at a given V_b, instead of the peak electric field and field gradient. To complement the temperature

and field dependent study on avalanche gain, the excess noise of InAs APDs with the same structures were also measured. Within the accuracy of the measurement, the excess noise factors remained low, between 1.45 and 1.6, and the variation with respect to temperatures and electric field gradients were determined to be negligible in practical applications. The discrepancies in previous low temperature noise measurement were explained based on previously non-optimised designs of APD and measurement set-up. F below that predicted by the local model at $k = 0$ were attributed to the effect of the dead space even in APDs with very thick W. Therefore thin W is not needed for APDs with $k = 0$ in order to exploit the dead space effect for lower F. The demonstration of the ability of InAs APDs to provide higher sensitivity or SNR was done by using the APD with a pre-amplifier. Low dark current and pure electron injection were determined to be the important requirements to obtain a high SNR for InAs e-APDs.

Following from the fabrication of high speed InAs diodes, the frequency response of InAs APDs was presented in chapter 7. With a proper and systematic system calibration, the 3-dB bandwidth of the InAs APDs with $W \sim 3$ and 5 µm was measured to be ~ 3.5 GHz, which is much lower than that predicted by modelling (between 7 and 11 GHz). The SU-8 dielectric was determined to be the major limiting factor of this 3-dB bandwidth. Despite this constraint, the high avalanche gain from the InAs APDs has enabled the demonstration of gain-unlimited bandwidth, with record high GBPs of 430 and 580 GHz at 295 and 77 K respectively. This is considered to be a major breakthrough as this is the very first experimentally demonstrated bandwidth that is not affected by its avalanche gain using III-V semiconductors, although it has been theoretically understood since 1960s for APDs with $k = 0$. The frequency responses of the InAs APDs were also measured up to 20 GHz despite the 3-dB bandwidth of ~ 3.5 GHz. With such a high GBP, the InAs APDs could amplify the optical signal at 15 GHz by ~ 23 dB above the equipment noise floor. This has proven the ability of InAs APDs to support 20-Gbps operations, with the advantage of low operating voltages or low power consumption.

8.2   Proposed further work

As discussed in chapter 4 and Appendix A2, most of the recently grown InAs wafers, either by MBE or MOVPE, suffered from high leakage current and unusual breakdown that inhibit APD operation at $V_b > 10$ V. It is not clear to us the actual reasons which lead to low-quality InAs wafers. This problem can be a major stumbling block to further developing InAs APDs, especially for real practical applications such as gas sensing and FPAs for imaging. To achieve this, the growth conditions must be optimised such that the InAs wafers have thick epilayers with low surface defect density, very low UID in the *i*-region and minimum dopant diffusion from the cladding into the *i*-layer. The repeatability of the growth conditions and parameters for InAs wafers is also crucial in exploring different InAs APDs design to increase the avalanche gain of InAs APDs at low V_b.

Currently InAs APDs with the best performance are the mesa-etched diodes with SU-8 surface passivation. In chapter 4 and 5 it is clear that the surface leakage still needs to be reduced, especially for operating temperatures below room temperature and for small pixel devices. Ammonium sulfide $((NH_4)_2S)$ was reported to reduce the surface leakage current of Type-II InAs/GaSb Superlattice photodiodes by ~ 2 orders of magnitude [4]. Since InAs APDs face a similar problem as other narrow bandgap photodiodes where the surface is pinned near the mid-gap, $((NH_4)_2S)$ surface passivation may also help in reducing the surface leakage current. Different $((NH_4)_2S)$-based solution concentrations and sample immersion time shall be used so that optimum passivation condition can be determined. Furthermore, although the mechanism was not well understood, a reduction of ~ 5 orders of magnitude in leakage current was reported for $InAs_{0.91}Sb_{0.09}$ photodiodes by exposing the mesa diodes to argon ion plasma [5]. A further reduction by ~ 2 orders was observed when the samples were illuminated by white light at 0.1 W/cm^2 at room temperature and the samples were cooled to low temperature before withdrawing the white-light illumination [5]. This can be used as one of the surface treatments for etched-mesa InAs diodes. In addition, a technique called epitaxial overgrowth where a lattice-matched wide bandgap material is grown on the etched-mesa surface is also reported

to be capable of reducing the surface leakage current [6]. Wide bandgap materials such as $AlAs_{0.16}Sb_{0.84}$ can be used for InAs diodes to carry out this epitaxial overgrowth. Since Al-containing semiconductors can be oxidised easily, a layer of SiN_x can be deposited onto the overgrowth epilayer to prevent oxidation of the wide bandgap material.

Planar InAs APDs, either by dopant diffusion or ion implantation, can prevent the diode surfaces from exposure to the air, potentially mitigating the surface leakage current. There are 2 groups reporting Zn-diffused InAs *p-n* junctions [7, 8] with high leakage current at $V_b < 1$ V. We have attempted Zn-diffusion at 500 ^{o}C for 60 minutes on a large area InAs sample. Results in Appendix H shows that Zn can be incorporated into InAs up to concentrations of $\sim 1\times10^{19}$ cm^{-3} with a diffused depth of ~ 2 µm. While the fabricated InAs mesa diodes from this large-area Zn-diffused sample show high leakage current at room temperature, there is a reduction of ~ 3 to 5 orders in dark currents at 77 K as shown in Appendix H. Further study on InAs Zn-diffused *p-n* junction shall be carried out with high-quality InAs wafer with low UID. Recently, Sandall *et al.* reported that Helium implantation could be employed to electrically isolate InAs photodiodes such that the implanted areas were made highly resistive [9]. Further annealing of the samples showed leakage current comparable to mesa-etched InAs diodes at low V_b. However, further optimisation of ion implantation such as the implantation profiles, ion concentrations and energy are needed to eliminate the catastrophic breakdown [9] and to allow higher V_b operation.

In chapter 6, it has been shown that the local model and hard dead space non-local model are not appropriate and not sufficient to model InAs e-APDs due to its impact ionisation properties which need soft ionisation threshold modelling. Therefore, an analytical band Monte Carlo model shall be developed to accurately model the results described in chapter 6. Throughout the work presented in this thesis, it is clear that InAs APDs possess many characteristics which are distinctly opposite to conventional III-V semiconductors APDs. The development of a proper modelling technique for InAs e-APDs will definitely assist in further understanding, more so discovering new characteristics of InAs e-APDs.

InAs APDs with a wide depletion width can provide high gain at low V_b while suppressing the tunnelling current. However, it is difficult to obtain large $W > 8$ µm with a single *p-i-n* junction, unless the UID is $< 2\times10^{-14}$ cm^{-3} throughout the *i*-layer. Therefore engineering InAs APDs with different design is needed, such as an APD with cascaded *i*-regions with *p-i-p⁻-i-n* structure. Initial electric field profile modelling, doping calibration for *p⁻*-region, growth and fabrication of InAs APDs with this structure has been carried out. Appendix I shows the SIMS of M4049 wafer, *I-V*s of the double mesa InAs diodes, excess noise factors at room temperature, avalanche gain and depletion width. Unfortunately, this layer still shows high leakage current and unusual device breakdown. It remains unclear if this is due to the crystal quality of the wafer, fabrication or the electric field profile of the diodes. However, it is clear from Appendix I that these APDs with cascaded *i*-regions enable W to grow much quicker than a single *p-i-n* junction diode. Further trials shall be carried out by having more cascaded *i*-regions but the repeatability of high quality growth shall be dealt with prior to exploring more complicated device structures.

While chapter 7 has demonstrated that InAs e-APDs have unlimited GBP due to the $k = 0$ characteristics, the 3-dB bandwidth of the devices are limited to ~ 3.5 GHz. The RPL simulation predicts that InAs APDs with $W \sim 5$ µm can produce a 3-dB bandwidth of ~ 7 GHz. However, the overshoot velocity of electrons above v_{se} can potentially further increase the 3-dB bandwidth [10]. Since the major limiting factor is determined to be the SU-8 dielectric, further work can be done by growing InAs on GaAs semi-insulating substrate [8] such that air-bridge can be employed to deposit the GSG pads onto the semi-insulating substrate. Obviously the strain due to the lattice-mismatch between GaAs and InAs can impose a major challenge to growth and fabrication, which if not properly optimised, will cause high leakage current and inhibit APD operations. Furthermore He-implanted InAs was reported to produce high resistivity of $\sim 1\times10^7$ Ω/square [9]. This technique can be employed so that this high resistivity InAs layer can play the same role as a semi-insulating substrate for GSG pads deposition, without the need of using the SU-8 dielectric. This proposed work is important in determining the actual transit-time limited

bandwidth of InAs e-APDs.

The proposed areas of further work described above have equal degree of importance. However, it shall be noted that having high quality crystals, consistent and repeatable growth of InAs wafers are the key to further exploitation of InAs e-APDs for practical applications.

References

[1] R. B. Emmons, "Avalanche-Photodiode Frequency Response," *J. Appl. Phys.,* vol. 38, pp. 3705-3714, 1967.

[2] A. R. J. Marshall, C. H. Tan, J. P. R. David, J. S. Ng, and M. Hopkinson, "Fabrication of InAs photodiodes with reduced surface leakage current," in *Proc. SPIE Optical Materials in Defence Systems Technology IV*, Florence, Italy, 2007, pp. 67400H-9.

[3] Z. M. Fang, K. Y. Ma, D. H. Jaw, R. M. Cohen, and G. B. Stringfellow, "Photoluminescence of InSb, InAs, and InAsSb grown by organometallic vapor phase epitaxy," *J. Appl. Phys.,* vol. 67, pp. 7034-7039, 1990.

[4] A. Gin, Y. Wei, A. Hood, A. Bajowala, V. Yazdanpanah, M. Razeghi, and M. Tidrow, "Ammonium sulfide passivation of Type-II InAs/GaSb superlattice photodiodes," *Appl. Phys. Lett.,* vol. 84, pp. 2037-2039, 2004.

[5] I. Shafir, M. Katz, A. Sher, A. Raizman, A. Zuessman, and M. Nathan, "Suppression of leakage currents in InAsSb MWIR photodiodes by chemical treatment and illumination," *Semicond. Sci. Technol.,* vol. 25, p. 045004, 2010.

[6] R. Rehm, M. Walther, F. Fuchs, J. Schmitz, and J. Fleissner, "Passivation of InAs/(GaIn)Sb short-period superlattice photodiodes with 10 µm cutoff wavelength by epitaxial overgrowth with $Al_xGa_{1-x}As_ySb_{1-y}$," *Appl. Phys. Lett.,* vol. 86, pp. 173501-3, 2005.

[7] A. Saynatjoki, P. Kostamo, J. Sormunen, J. Riikonen, A. Lankinen, H. Lipsanen, H. Andersson, K. Banzuzi, S. Nenonen, H. Sipila, S. Vaijarvi, and D. Lumb, "InAs pixel matrix detectors fabricated by diffusion of Zn in a metal-organic vapour-phase epitaxy reactor," *Nucl. Instr. Met. Phys. Res. Sec. A: Accelerators, Spectrometers, Detectors and Associated Equipment,* vol. 563, pp. 24-26, 2006.

[8] J. W. Shi, F. M. Kuo, and B. R. Huang, "Zn-Diffusion InAs Photodiodes on a Semi-Insulating GaAs Substrate for High-Speed and Low Dark-Current Performance," *IEEE Photon. Technol. Lett.,* vol. 23, pp. 100-102, 2011.

[9] I. Sandall, C. H. Tan, A. Smith, and R. Gwilliam, "Planar InAs photodiodes fabricated using He ion implantation," *Opt. Express,* vol. 20, pp. 8575-8583, 2012.

[10] S. A. Plimmer, J. P. R. David, B. Jacob, and G. J. Rees, "Impact ionization probabilities as functions of two-dimensional space and time," *J. Appl. Phys.,* vol. 89, pp. 2742-2751, 2001.

Appendices

Appendix A1: InAs wafers details

Wafer ref.	Intrinsic region			*p*-type cladding		*n*-type cladding	
	Nominal width (µm)	Actual width (µm)	doping ($\times 10^{15}$ cm^{-3})	width (µm)	doping ($\times 10^{18}$ cm^{-3})	width (µm)	doping ($\times 10^{18}$ cm^{-3})
M3279 *p-i-n*	1.0	0.9	~ 3	2.3[c]	5.0	1.9	2.0
M3247 *p-i-n*	3.5	3.5	~ 0.2	1.0[c]	6.0	1.9	2.0
MR2558 *n-i-p*	6.0	5.0[a]	~ 0.5[b]	3.5	1.0	1.5	0.5
MR2559 *n-i-p*	6.0	4.5[a]	~ 0.7[b]	3.5	1.0	1.5	0.5
MR2560 *n-i-p*	6.0	3.2[a]	~ 1.5[b]	3.5	1.0	1.5	0.5
MR2537 *n-i-p*	6.0	3.3[a]	~ 1.4[b]	3.0	3.0	2.0	0.5
MR2538 *p-i-n*	6.0	3.0[a]	~ 2.0[b]	2.0	3.0	2.0	0.5
MR2835 *p-i-n*	6.0	3.0[a]	~ 2.0[b]	2.0	3	2.0	0.1
MR2840 *p-i-n*	6.0	4.5[a]	~ 0.7[b]	2.0	3	2.0	0.1
MR2775 *n-i-p*	6.0	3.0[a]	~ 2.0[b]	2.0	1.0	2.0	0.2

[a] The actual depletion widths quoted at a bias voltage of 12 V since the structure was not fully depleted due to the thick *i*-layers and high background doping concentrations.

[b] The unintentional background doping concentrations quoted are the lowest achievable doping concentrations. The doping concentrations across the *i*-layer vary due to the diffusion of dopants from the cladding layers.

[c] The *p*-layer consists of a 200-nm thick $AlAs_{0.16}Sb_{0.84}$ that is capped with a 100-nm thick InAs layer. The *p*-type cladding width quoted includes these layers.
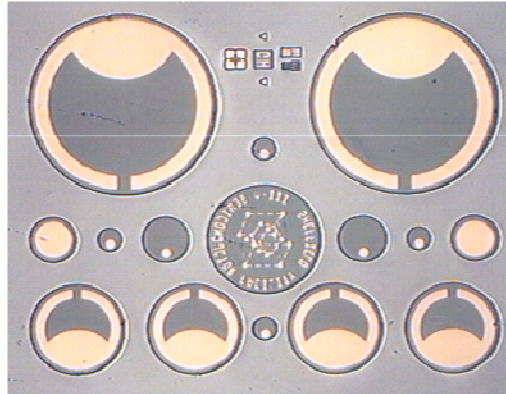

Figure A.1 The NEWPIN mask design which is used for quick evaluation of InAs wafer quality.

Appendix A2: InAs wafers details

Layer number	No. of Wafers	Layer structure (*p/i/n* or *n/i-p*)	Comments
MR2714 (*p-i-n*)	1	2/6/1.5 (μm)	➤ Very high dark current of 10 mA at V_b < 1 V.
MR2715 (*p-i-n*)	1	2/6/1.5 (μm)	➤ Very high dark current of 10 mA at V_b < 1 V.
MR2745 (*p-i-n*)	1	2/6/1.5 (μm)	➤ Very high dark current of 10 mA at V_b < 1 V.
MR2774 (*p-i-n*)	1	2/6/1.5 (μm)	➤ Very high dark current of 10 mA at V_b < 2 V.
MR2776 (*p-i-n*)	1	2/6/1.5 (μm)	➤ Very high dark current of 10 mA at V_b < 5 V.
MR2836 (*p-i-n*)	2	2/6/1.5 (μm)	➤ Show unusual breakdown at V_b < 10 V. ➤ Dark current density ~ 260 mA/cm^2 at 0.1V. ➤ Bad surface property.
MR2837 (*p-i-n*)	2	2/6/1.5 (μm)	➤ Show unusual breakdown at V_b < 10 V. ➤ Dark current density ~ 155 mA/cm^2 at 0.1V.
MR2838 (*p-i-n*)	2	2/6/1.5 (μm)	➤ Show unusual breakdown at V_b < 10 V. ➤ Dark current density ~ 145 mA/cm^2 at 0.1V. ➤ Bad surface property.
MR2841 (*p-i-n*)	2	2/6/1.5 (μm)	➤ Show unusual breakdown at V_b < 10 V. ➤ Dark current density ~ 98 mA/cm^2 at 0.1V.
M3884 (*p-i-n*)	1	2/5/2 (μm)	➤ Unknown catastrophic breakdown at V_b < 7 V. ➤ Dark current density ~ 80 mA/cm^2 at 0.1V.
M3948 (*p-i-n*)	1	2/5/2 (μm)	➤ Show unusual breakdown at V_b < 7 V. ➤ Dark current density ~ 100 mA/cm^2 at 0.1V.
M3954 (*p-i-n*)	1/4	2/5/2 (μm)	➤ Show unusual breakdown at V_b < 7 V. ➤ Dark current density ~ 90 mA/cm^2 at 0.1V.
M3978 (*p-i-n*)	1	2/10/2 (μm)	➤ Very high dark current of 10 mA at V_b < 1 V.
M4049 (*p-i-p-i-n*)	1	2/2.5/0.1/2.5/2 (μm)	➤ High dark current and unusual breakdown at V_b < 6 V.
M3897, M3949, M3977, M4033 (*n-p$^-$-n*)	4	1/1.5/1 (μm)	➤ Used for doping calibration for the MBE machine.

* Wafer numbers start with 'M' are grown by MBE and with 'MR' are grown by MOVPE*

Appendix B: Using the Agilent N8973A noise figure analyser

1. Connect the noise source (model: Agilent 346B; Serial number: MY44420110) to the NFA, with one end connected to the bias-tee and another end to the noise source drive output + 28 V (pulsed).

2. Press <ENR> to make sure that the excess noise ratio (ENR) table matches the noise source. The ENR table specifically for the noise source is as follows:-

Frequency (MHz)	Power (dB)
10	15.51
100	15.42
1000	15.29
2000	15.43
3000	15.43
4000	15.38
5000	15.37
6000	15.34
7000	15.35
8000	15.38
9000	15.38
10000	15.28
11000	15.23
12000	15.16
13000	15.11
14000	15.20
15000	15.26
16000	15.28
17000	15.17
18000	14.57

Table B.1 The noise power of the Agilent 346B MY44420110 noise source at different frequencies.

3. Choose the start and stop frequency by pressing <Frequency/Points> → select the start and stop frequency.

4. Choose number of points between start and stop frequency by pressing <Frequency/Points> → [Start/Stop]

5. Choose number of averaging points by pressing <Averaging/Bandwidth> → select the number of averaging points.

6. Press <sweep> → select [continuous]

7. Press <calibrate> → <calibrate> (to start calibration).

8. Wait until the calibration is completed.

9. Press <Result> → [Phot] :- you should see the graph which matches the ENR table of the noise source.

10. Disconnect the noise source from the NFA.

11. Connect the probe to the bias-tee.

12. Probe the device and bias the device at a desired voltage.

13. Sweep the noise level with ($P_{total,dB}$) and without ($P_{dark,dB}$) laser or radiation.

14. Record data such as dark current, primary photocurrent, photocurrent at a particular bias voltage and the calculated gain.

15. Saving the noise data:- <File> → [save] → [Trace] → type filename (≤ 8 characters) → <Enter>

16. Repeat step 12 to 15 as required.

   <…>   – button on the NFA

   […]   – button on the front panel

Appendix C: Using the HP 8341B RF modulating source and HP 70820A microwave transition analyser

A. Electrical connections between the RF source and MTA (at the back of these equipments)

> ➢ GPIB to GPIB - *MTA has 2 GPIB. Use the centre GPIB.*
> ➢ MTA 10 MHz input to RF Source 10 MHz output

B. To use MTA:-

  i. Instr. Preset – to calibrate all to zero / default

  ii. Main (*L*)

  iii. RF out on (*R*)

  iv. Noise Filter on (*R*)

  v. Sweep(*R*) → Freq → Start (Set freq.) → Stop (Set freq.) → Source Power (<+10 dBm)

  vi. Noise Filter (*R*) → set 50 kHz

  vii. Config(*L*) → Trace Point (*R*) → Adjust trace point/steps

  viii. Scale (*L*) → Autoscale (*R*)

  ix. Trigger (*L*) → Cont or Single (*R*)

  x. Traces (*L*) → avg. Hld. (*R*) → Smooth on (*R*)

  xi. Use Marker (*L*) to check/measure.

*** On the panel: (L) – Left Side; (R) – Right Side ***

To change the freq/div or time/div – Main → Sweep → Time/Freq

To change the P/div or V/div – Scale

Appendix D: Using the 2-port E8364B PNA Series vector network analyser for frequency response measurement

The external connections between the equipments are shown in figure 3.11 in chapter 2 [a]. Here, the step-by-step operation of the set-up is listed below together with a few precaution steps.

i. Set the interested frequency range on the VNA. For example, 10 MHz to 40 GHz. You can choose either a linear or log frequency sweep.

Sweep → Sweep type

ii. Set the number of points throughout the frequency range (Higher number of points will slow down the measurement speed)

Sweep → Number of points

iii. Set the number of averaging points

Channel → Average

iv. Set the IF bandwidth (Lower IF bandwidth settings make higher dynamic range calibrations at the expense of slower measurement speed)

Sweep → IF bandwidth

v. Reverse bias the EAM at -1 V. Set the power at port 1 of the VNA to be +9 dBm and turn on the power [a] (Do not turn on the RF power before reverse biasing the EAM as this will operate it in the forward bias range)

Channel → Power

vi. Turn on the laser [c]. You should see that the current reading of the SMU connected to the EAM increases significantly.

vii. Start the measurement using port 2. Repeat the measurements and save the data in the format of ".prn".

Trace → Measure

Scale → Autoscale or change the scale

viii. When all the measurement is done, turn off the laser.

ix. Turn off the RF power from port 1.

x. Set the d.c bias of the EAM to 0 V [d].

xi.   It is recommended that the VNA and SMU are not powered off as it will risk damaging the EAM due to a voltage spike. Disconnect the EAM from those instruments before powering off the VNA and SMU.

[a] When connecting the EAM and VNA, please wear the electrostatic discharge wrist band to avoid any electrostatic discharge which can damage the equipments.

[b] The reverse bias voltage and the RF power from port 1 can vary to maximise the amplitude of the modulated laser. However, the operating voltage of the EAM is between 0 and -4 V. Make sure that the EAM is biased (d.c. + RF component) within this range so that it is not damaged. Furthermore, it should be noted that the maximum acceptable RF power of the EAM is + 13 dBm. A conversion table between the power in dBm and the peak-to-peak voltage for a 50-Ω system is shown below.
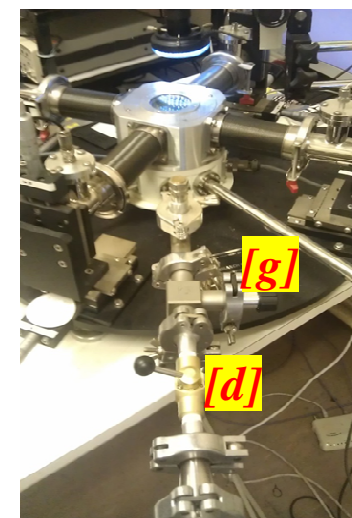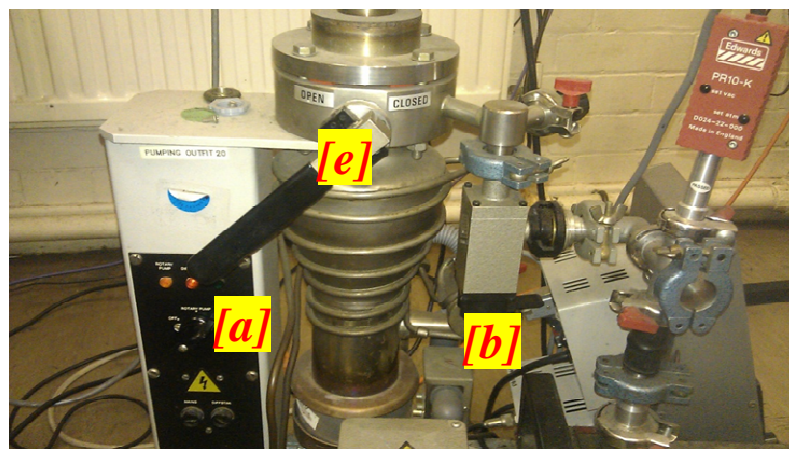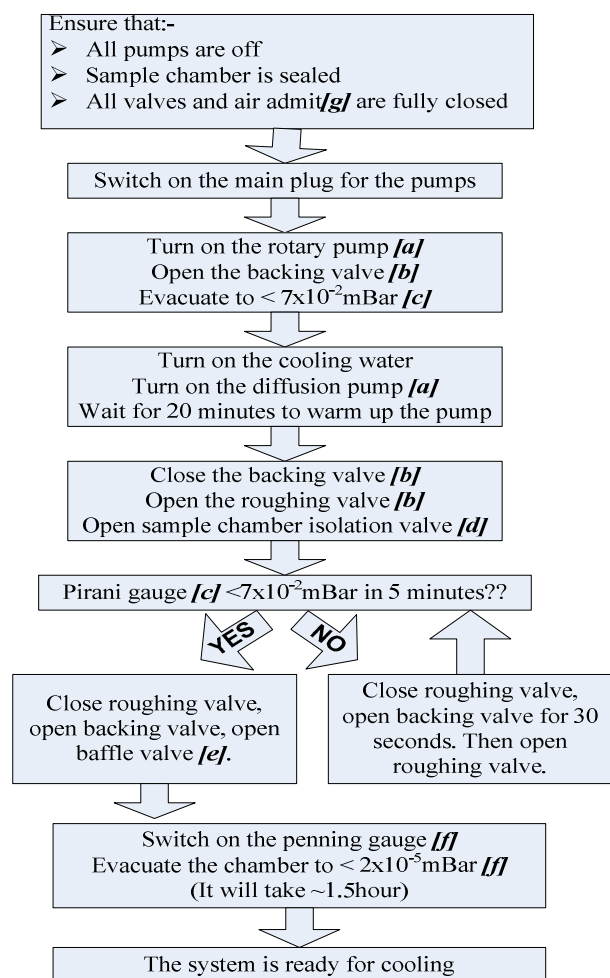
Power (dBm)	Peak-to-peak voltage (V)
-5	0.3557
-4	0.3991
-3	0.4477
-2	0.5024
-1	0.5637
0	0.6325
1	0.7096
2	0.7962
3	0.8934
4	1.0024
5	1.1247
6	1.2619
7	1.4159
8	1.5887
9	1.7825
10	2.0000

Table D.1 The conversion table between power in dBm and the peak-to-peak voltage of a 50-Ω system.
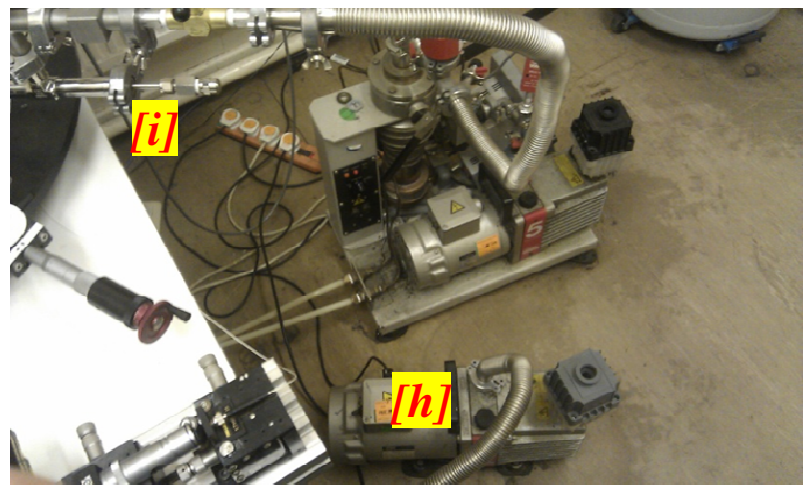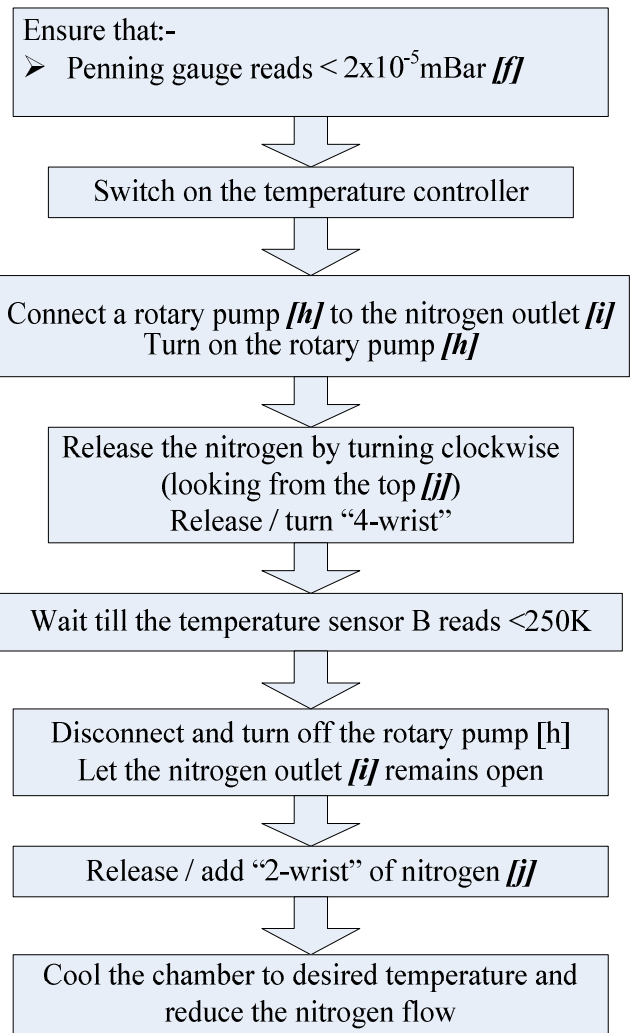
^c The typical current level of the laser is from 35 to 65 mA. Since the maximum optical input rating of the EAM is +14 dBm or 25 mW, it is always a good practice to measure the output power of the laser before connecting it to the EAM to avoid any damage to the EAM.

^d Turn off the RF power first before setting the d.c. bias to 0 V so that the EAM will not be forward biased.
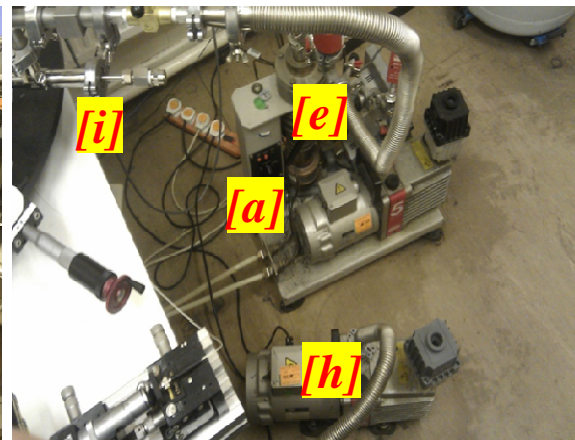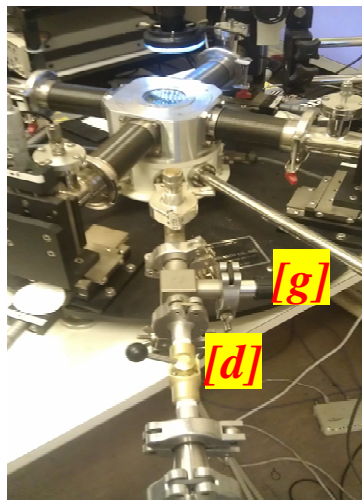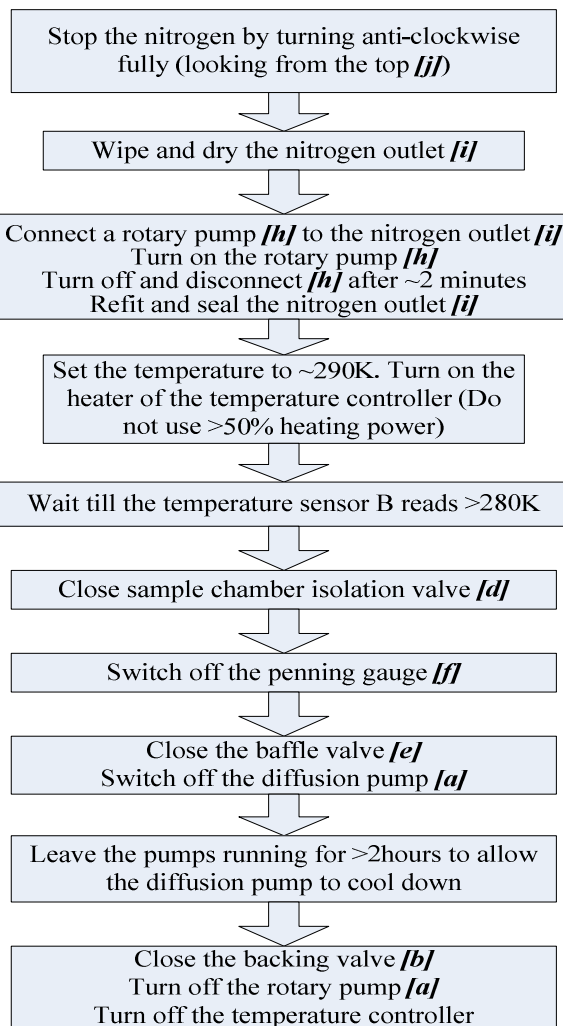
Appendix E: Low temperature probe station

Ensure that:-
➢ All pumps are off
➢ Sample chamber is sealed
➢ All valves and air admit*[g]* are fully closed

↓

Switch on the main plug for the pumps

↓

Turn on the rotary pump *[a]*
Open the backing valve *[b]*
Evacuate to < 7x10^{-2}mBar *[c]*

↓

Turn on the cooling water
Turn on the diffusion pump *[a]*
Wait for 20 minutes to warm up the pump

↓

Close the backing valve *[b]*
Open the roughing valve *[b]*
Open sample chamber isolation valve *[d]*

↓

Pirani gauge *[c]* <7x10^{-2}mBar in 5 minutes??

YES ↓   NO ↓

Close roughing valve, open backing valve, open baffle valve *[e]*.

Close roughing valve, open backing valve for 30 seconds. Then open roughing valve.

↓

Switch on the penning gauge *[f]*
Evacuate the chamber to < 2x10^{-5}mBar *[f]*
(It will take ~1.5hour)

↓

The system is ready for cooling

CHAMBER EVACUATION

Ensure that:-
➢ Penning gauge reads < 2x10^{-5}mBar *[f]*

↓

Switch on the temperature controller

↓

Connect a rotary pump *[h]* to the nitrogen outlet *[i]*
Turn on the rotary pump *[h]*

↓

Release the nitrogen by turning clockwise
(looking from the top *[j]*)
Release / turn "4-wrist"

↓

Wait till the temperature sensor B reads <250K

↓

Disconnect and turn off the rotary pump [h]
Let the nitrogen outlet *[i]* remains open

↓

Release / add "2-wrist" of nitrogen *[j]*

↓

Cool the chamber to desired temperature and
reduce the nitrogen flow

C O O L I N G   P R O C E D U R E

| Stop the nitrogen by turning anti-clockwise fully (looking from the top *[j]*) |
| Wipe and dry the nitrogen outlet *[i]* |
| Connect a rotary pump *[h]* to the nitrogen outlet *[i]*
 Turn on the rotary pump *[h]*
 Turn off and disconnect *[h]* after ~2 minutes
 Refit and seal the nitrogen outlet *[i]* |
| Set the temperature to ~290K. Turn on the heater of the temperature controller (Do not use >50% heating power) |
| Wait till the temperature sensor B reads >280K |
| Close sample chamber isolation valve *[d]* |
| Switch off the penning gauge *[f]* |
| Close the baffle valve *[e]*
 Switch off the diffusion pump *[a]* |
| Leave the pumps running for >2hours to allow the diffusion pump to cool down |
| Close the backing valve *[b]*
 Turn off the rotary pump *[a]*
 Turn off the temperature controller |

SHUTDOWN VACUUM SYSTEM

Ensure that:-
➢ The sample chamber reaches >290K for >4hours

↓

Open the air admit *[g]*

↓

Open both lids of the sample chamber
Remove the sample(s) and close the lids

↓

Close the air admit *[g]*

↓

Turn on the rotary pump *[a]*

↓

Open the roughing valve *[b]*
Open sample chamber isolation valve *[d]*

↓

Evacuate to < $7x10^{-2}$mBar *[c]*

↓

Close sample chamber isolation valve *[d]*

↓

Close the roughing valve *[b]*
Turn off the rotary pump *[a]*

↓

The system is ready for the next user

R E M O V I N G   S A M P L E S

Appendix F: BCB passivation on InAs diodes

1. Take the Cyclotene out from the fridge. (the BCB film will be too thick if it is too cold)
2. Bake sample at 100 ^{o}C for 1 minute to dehydrate the surface.
3. Cool the sample and stick on blue tacky paper.
4. Set the spin speed to 2000 rpm *.
5. Spin the sample.
6. Put Adhesion promoter (AP3000) on the sample then spin it.
7. Put the BCB onto the sample, wait for 15 second, then spin.
8. Remove the sample from the blue tacky paper.
9. Bake the sample for 2 minutes 30 seconds at 100 ^{o}C.
10. Stick the sample on a blue tacky paper and spin BCB onto the sample at 3000 rpm *.
11. Bake the sample for ~ 5 minutes at 100 ^{o}C.
12. Anneal the sample at 300 ^{o}C for 1 minute (Use slow temperature ramp up and down time - 5 minutes each).
13. To open the contact windows, spin the SPR220 onto the sample. Pattern it using the top contact mask and develop using MF26A.
14. RIE etching recipe: $CFH_3:O_2 = 35:12$ (sccm)

    Pressure = 35 mTorr

    RF power = 70 W

    Estimated etch rate ~ 80 to 100 nm/min
15. Clean the sample surface by dipping into 1 % buffered HF for 40 seconds to have better contact resistance.

*Estimated thickness for BCB with different spin speed:

     5000 rpm: ~ 2.35 µm

     3000 rpm: ~ 3.05 µm

     2000 rpm: ~ 3.76 µm

Appendix G: Fabrication of high speed InAs APDs

The fabrication steps of the high speed InAs *p-i-n* and *n-i-p* diodes were almost similar. The only difference is the deposition of the GSG pads where the top mesas of the *n-i-p* diodes were covered by a metal cap whereas the top mesas of the *p-i-n* diodes were opened to enable pure electron injection.

There are basically two major difficulties in fabricating the high speed InAs diodes. Firstly, these InAs wafers were thick, with ~ 6 µm *i*-region and the total etching depth was approaching 10 µm. Due to the isotropic etching profile of the wet chemical etchants, the InAs layers were etched vertically and horizontally, leading to the undercut of the mesa sidewalls. Furthermore, depending on the orientation of the wafer, the undercut is more severe on the facet which is parallel to the minor wafer flat and less severe on the facet which is parallel to the major wafer flat, as shown in figure G.1. Hence the designs of the top contact and surface passivation mask set have taken these factors into account. Besides, starting from the first step of the fabrication, the orientation of the wafer was observed in such a way that the signal tracks could connect the diodes from the facet which has less severe undercutting. This was to make sure that the signal tracks could connect the devices more easily without making into contact with the mesa sidewalls.

Secondly, the UV exposure and baking time of SU-8 were crucial for several reasons. Overexposing the SU-8 to UV was needed so that a gradual slope was formed at the interface between the dielectric and top mesa, and at the interface between the dielectric and lower contact. Since the mesas were etched ~ 10 µm, this was particularly crucial to ensure that the GSG tracks could make contacts with the top and lower contacts. Furthermore, there were instances where the SU-8 cracked when the samples were dipped in acetone. Hence, the SU-8 needed to be fully cured by UV exposure and baking so that the dielectric was sufficiently durable and hard for the subsequent fabrication processes. While the two major considerations mentioned above suggested that overexposing the SU-8 to UV would mitigate these problems, overdose of UV exposure would also cause the smaller mesa diodes to be

fully covered by SU-8, leading to the inability of the signal tracks to make contact. There was therefore a trade-off in the UV exposure dosage. After a series of optimisation trials, the optimum UV exposure time was determined to be 15 seconds (when the UV400 mask aligner has a 1 second optimum exposure time for standard GaAs). The SU-8 was best pre-baked at 65 ^{o}C for 3 minutes, followed by 95 ^{o}C for 7 minutes. The post-exposure baking time was determined to be at 65 ^{o}C for 2 minutes, followed by 95 ^{o}C for 3 minutes. After developing the SU-8 for 1 minute to open the windows for contacts, the sample was again exposed to UV for 115 second, followed by a 1 and 2 minutes baking at 65 ^{o}C and 95 ^{o}C respectively, to harden the SU-8.
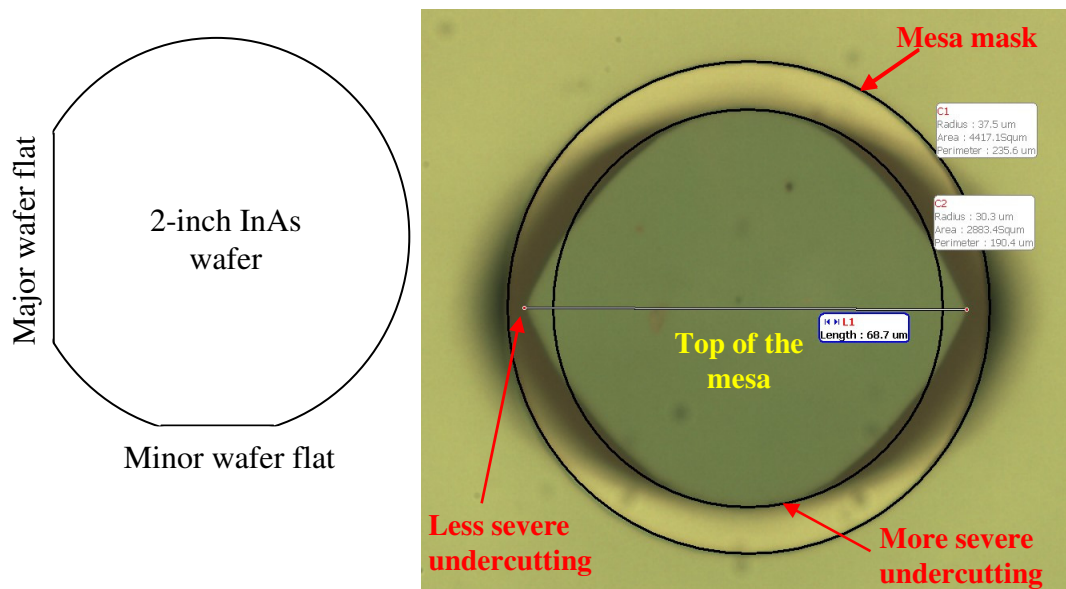
Figure G.1 The schematic diagram of the major and minor flats of a 2-inch InAs wafer (left) and the picture illustrating the etching profile of an InAs diode with an etch depth of ~ 10 µm.

The fabrication steps of the high speed InAs diodes are listed below in the sequence that they were carried out.

Fabrication steps for high speed InAs *p-i-n* and *n-i-p* layers with slight difference in fabrication steps for *n-i-p* diodes (Italics):-

i.   Cleave a sample from the wafer (*p-i-n* or *n-i-p*) and clean in heated n-butyl acetate, acetone and isopropyl alcohol.

ii. Spin the BPRS100 photoresist onto the sample at 4000 rpm and pattern it using the top contact mask [a].

iii. Deposit top contacts with appropriate choice of metal [b] by evaporation.

iv. Lift-off the mask in acetone and clean the sample [c]. Then, spin the BPRS100 onto the sample at 4000 rpm and pattern it using the mesa mask [a].

v. Etch the mesa through to the *n*-type (*p-type*) layer (~ 10 µm in this case) using the wet chemical etchants [d].

vi. Lift-off the mask in acetone. Immediately after this, bake the sample at 100 ^{o}C to dehydrate the surface. Then spin the SU-8 at 2000 rpm onto the sample.

vii. Pre-bake, align the dielectric mask [a], UV expose, post-bake and develop the sample in SU-8 developer followed by a rinse using isopropyl alcohol [e].

viii. Expose the sample to UV for 115 seconds. Then bake it at 65 ^{o}C for 1 minute followed by baking at 95 ^{o}C for 2 minutes.

ix. Spin the SPR220 onto the sample at 4000 rpm.

x. Pattern the photoresist mask using the mask for PIN bondpads (*NIP bondpads*) [a]. The optimum exposure time was ~ 12.4 seconds.

xi. Deposit the GSG pads using Ti/Au = 30/400 nm from both sides [f].

[a] The alignment of each photoresist mask should be within the tolerance of < 2 µm. This is because the misalignment can cause even more severe implication in the following fabrication steps. If the mask is not well aligned, clean the sample in acetone and repeat the process.

[b] The choice of metal is discussed in section 3.5.1. The metal for *p*-type contact is Ti/Pt/Au = 10/20/200 and for *n*-type contact is Ti/Au = 25/200. To ensure better adhesion of metals on semiconductor, the deposition of metal was carried out when the pressure of the chamber was < 2×10^{-6} mBar.

[c] Clean the sample in a heated n-butyl acetate, acetone and isopropyl alcohol.

[d] Wet chemical etchants as described in chapter 4.

[e] The optimum pre-bake, exposure and post-bake time discussed earlier in the beginning of appendix G were used. The time can vary if the thickness of the film is different.
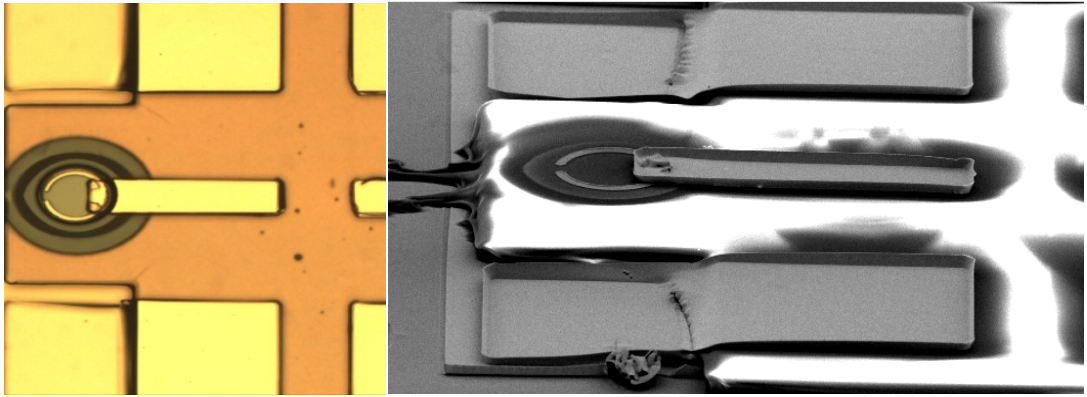
Fig G.2 The picture of a fully fabricated high speed InAs diode with the corresponding SEM image.

Appendix H: Zinc-diffusion
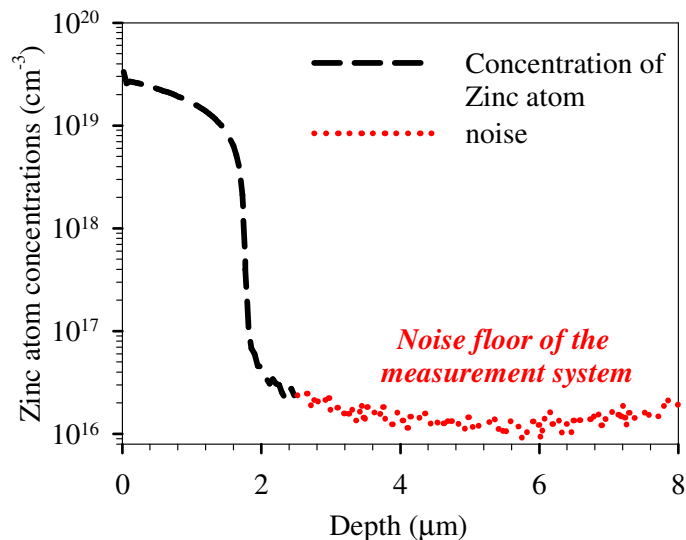

Figure H.1 Zinc diffusion profile on InAs sample at $T = 500\ ^{o}$C for 60 minutes from SIMS.
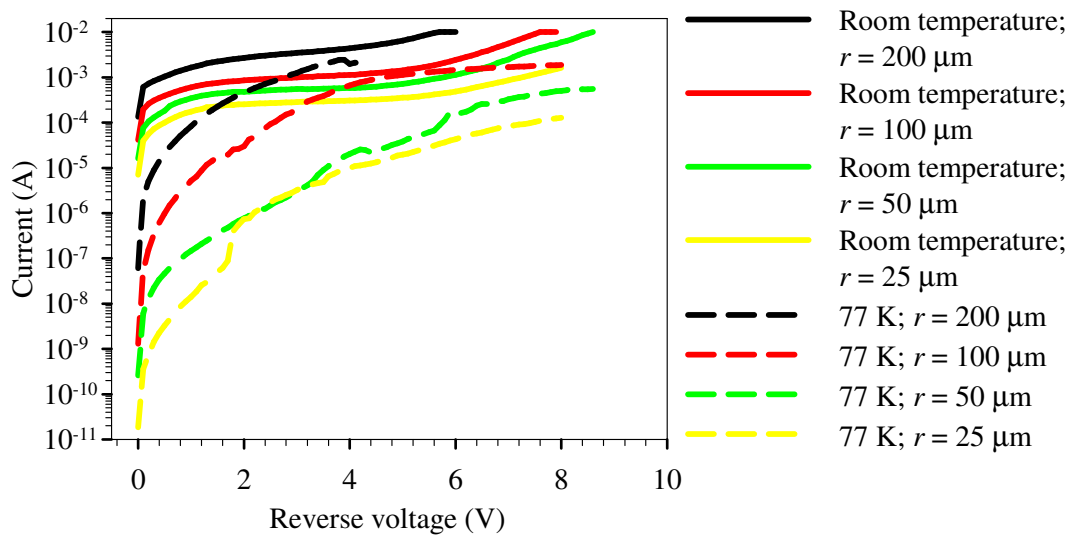

Figure H.2 Dark current characteristics at room temperature and 77 K from fabricated InAs mesa diodes with Zn-diffused *p*-dopant.

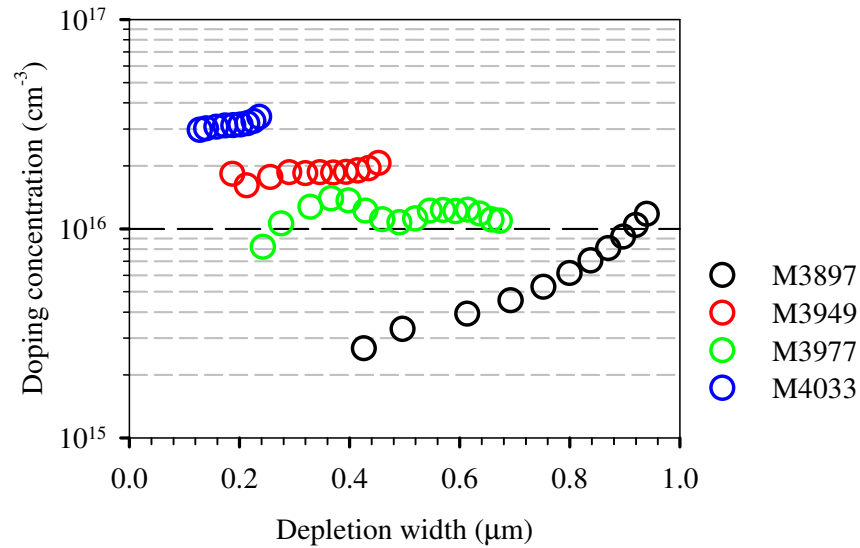## Appendix I: InAs APDs with cascaded *i*-regions (M4049)

Figure I.1 Four layers of InAs wafers to calibrate 2×10^{16} cm^{-3} for p^--region for InAs APDs with cascaded *i*-regions.
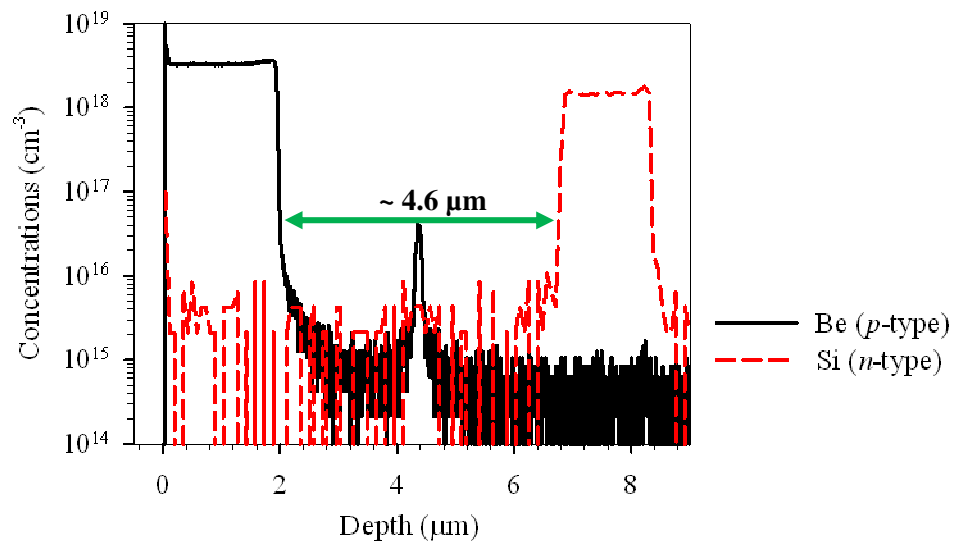
Figure I.2 SIMS for Be (*p*-type) and Si (*n*-type) dopants of the M4049 InAs wafers with cascaded *i*-regions.
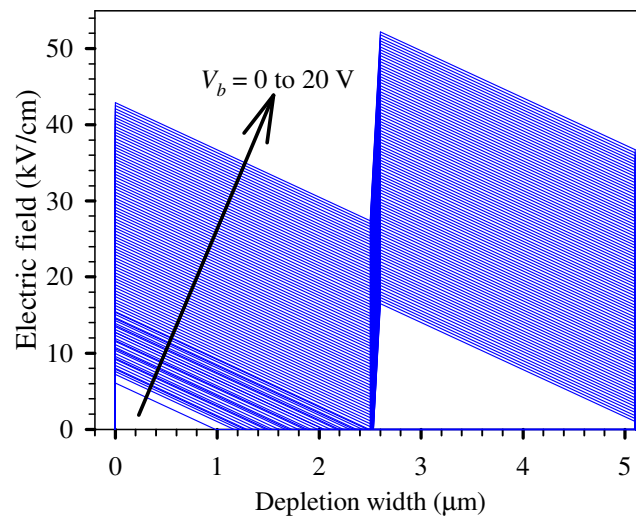
Figure I.3 Simulated electric field profile using Poisson equation based on SIMS.
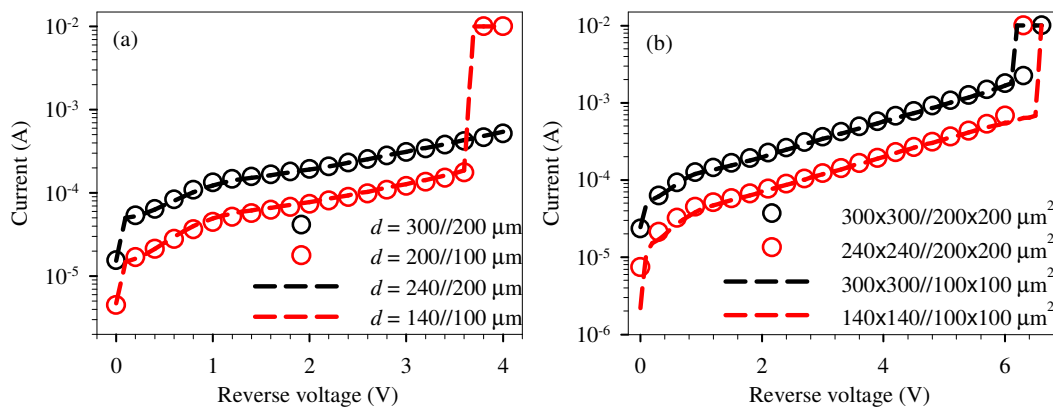
Figure I.4 *I-V*s of the M4049 double mesa diodes with inner size//outer size for (a) circular devices and (b) square devices. *I-V*s show that the reverse current scales with the inner size of the double mesa diodes.
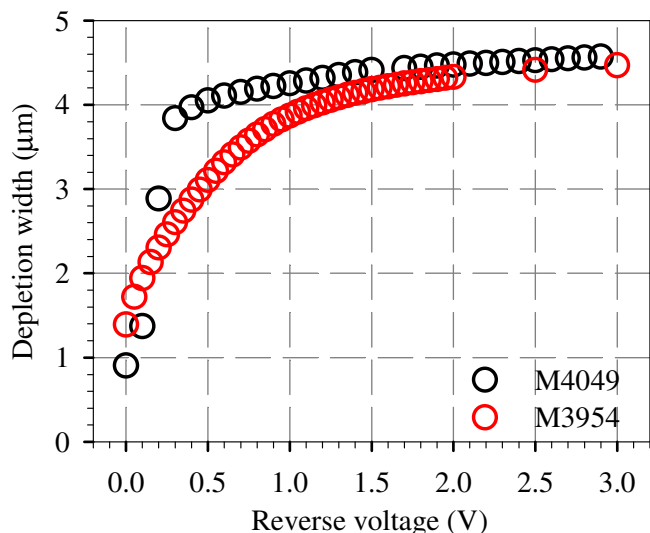
Figure I.5 Depletion widths with increasing V_b for M4049 compared to M3954 which has very similar W as M4049.
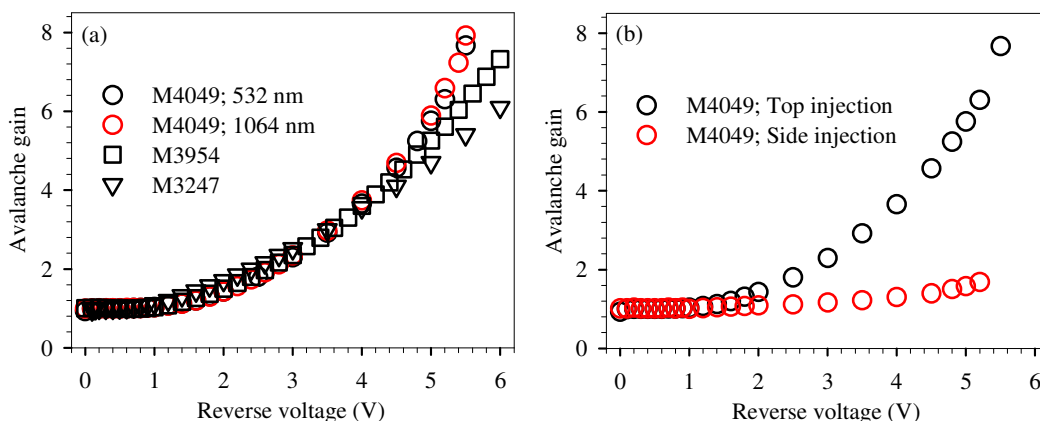

Figure I.6 (a) Pure electron initiated avalanche gain of M4049 (W ~ 4.6 µm) compared to M3954 (W ~ 4.6 µm) and M3247 (W ~ 3.5 µm) at room temperature. (b) Pure electron initiated and mixed injection avalanche gain of M4049 at room temperature.

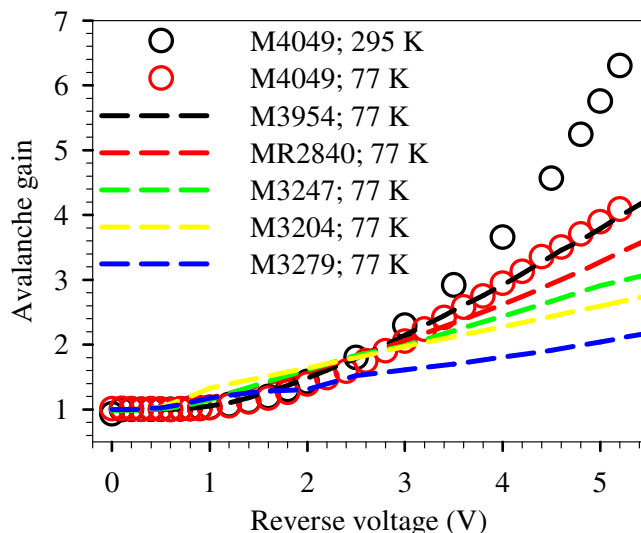Figure I.7 (a) Pure electron initiated avalanche gain of M4049 ($W \sim 4.6$ µm) compared to M3954 ($W \sim 4.6$ µm), MR2840 ($W \sim 4.5$ µm at $V_b = 12$ V), M3247 ($W \sim 3.5$ µm), M3204 ($W \sim 1.9$ µm) and M3279 ($W \sim 0.9$ µm) at 77 K.
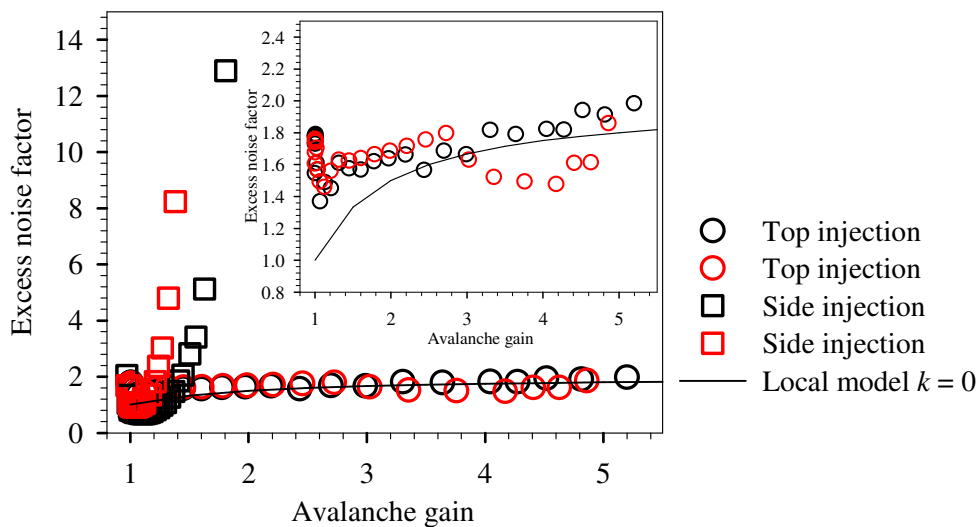

Figure I.8 Pure electron and mixed injections excess noise factors of M4049 InAs APDs at room temperature.